FINAL REPORT FOR PROJECT DE-FG07-021D14325

DEVELOPMENT OF AN ON-LINE, CORE POWER DISTRIBUTION MONITORING SYSTEM

Tunc Aldemir, Don W. Miller
The Ohio State University

ABSTRACT

The objective of the proposed work was to develop a software package that can construct in three-dimensional core power distributions using the signals from constant temperature power sensors distributed in the reactor core. The software developed uses a model-based state/parameter estimation technique that is particularly attractive when there are model uncertainties and/or large signal noise. The software yields the expected value of local power at the detector locations and points in between, as well as the probability distribution of the local power density.

1. PROJECT OBJECTIVES

The objective of the project was to develop a software based method that will construct in real-time, three-dimensional core power distributions using the signals from power sensitive sensors distributed in the reactor core. While power distribution related quantities are used to specify operational thermal limits in nuclear reactors, none of these quantities are measured directly but rather inferred from flux measurements and local material properties. Recent developments in detector technology have lead to sensors that can measure local power directly [1,2]. The research aimed at developing the software that will construct in real-time three-dimensional core power distributions using the signals from such devices distributed in the reactor core. The software yields the expected value of local power at the detector locations and points in between, as well as the probability distribution of the local power density. Such data will be useful for risk-informed regulatory process and may allow reduction in thermal margins (and subsequently increasing power extracted from the core) in view of the reduced uncertainty in the estimated local power densities. The proposed work also investigated using the method to obtain radially averaged axial power distributions in pressurized water reactors (PWRs) using physically discrete, energy-sensitive ex-core flux detectors, such as described in [3].

2. BACKGROUND AND PROBLEM STATEMENT

The measures that are used to specify operational thermal limits in nuclear reactors include quadrant power tilt ratio (QPTR), heat flux hot channel factor (HFHCF) (i.e. maximum fuel rod linear power density divided by the average fuel rod linear power density), nuclear enthalpy rise hot channel factor (i.e. ratio of highest integrated fuel rod power to average integrated fuel rod power), maximum average planar linear heat generation rate, critical power ratio (i.e. ratio of the bundle fuel power to bundle power required to produce onset of transition boiling) all of which are based on local power. However, none of these quantities are directly measured in current applications. For example, the QRPR in PWRs is found from the ratios of the signals received from the flux detectors placed outside the reactor vessel. Again in PWRs, the HFHCF is found from the measured neutron flux, computed local fuel properties, and a computed cycle-dependent function that accounts for power distribution transients encountered during normal operation and is corrected for fuel manufacturing tolerances and uncertainty in the flux measurement through a correction factor [4]. From a safety viewpoint, such an approach is satisfactory because the computations can be performed and correction factors can be chosen as conservatively as needed. On the other hand, an excessive margin in not desirable from an operational viewpoint since it may lead to an unnecessary power derating.

A new in-core reactor power sensor has been under development at The Ohio State University since 1996. This feedback-controlled calorimetric instrument, which is referred to as a constant-temperature power sensor (CTPS), is capable of direct measurement of nuclear energy deposition [1,2]. This type of sensor is ideally suited for use in proposed Generation IV power systems, in which the sensors could become an

integral part of the fuel for the core lifetime. The CTPS concept is based on maintaining the temperature of a small mass of reactor fuel constant by adding heat through resistive dissipation of input electrical energy. Work to date with the CTPS, however, indicates that the observed rate of nuclear energy deposition is sensitive to model uncertainties (e.g. local fuel thermal properties) and signal noise [5]. Although point estimators such as the least squares estimator (LSE) have been used to estimate the effect of model uncertainties and signal noise, they can yield results that are substantially different from the true value, with no indication of the magnitude of the error (LSE may not even converge when correlated noise is present [6])

A technique that provides reliable measures of uncertainty in the estimates is based on the cell-to-cell-mapping (CCMT) approach [7]. The CCMT represents dynamic system evolution in terms of transition probabilities between user specified magnitude intervals of the system variables/parameters to be estimated (cells). These cells are similar to the computational cells used in finite difference and finite element techniques and can be chosen to envelope the noise in the dynamical variables or the uncertainties in the system parameters in general. The CCMT yields the probability of finding the system variables/parameters to be estimated in a given cell. The estimation methodology uses a recursive Bayesian procedure and has been developed into a system independent algorithm called DSD (Dynamic System Doctor) [8]. It can be shown that convergence to the correct value is guaranteed with sufficiently small cell sizes [7].

The report is organized as follows: Section 4 overviews the CTPS. Sections 5 and 6, respectively, describe how DSD is used to estimate the uncertainty in the observed power at in-core CTPS locations and how the uncertainty propagation between CTPS location is tracked. Section 7 describes how power distribution may be inferred from ex-core measurements of physically discrete, energy-sensitive ex-core flux detectors.

3. AN OVERVIEW OF CTPS [9]

The CTPS consists of a UO_2 pellet surrounded by electrical heating resistance wire (Fig.1). The pellet and the wire form the sensor core (Node 2). The core is surrounded by ceramacast which is an alumina based ceramic thermal insulator (Node 1). Both the sensor core and the insulator are coated with thin layers of copper. A feedback control loop is used to provide the exact amount of input electrical energy q_e needed to keep Node 2 temperature T_2 constant in time *(t)*, well above the ambient temperature T_0, regardless of q_n. The sensor operation involves switching between the feedback-controlled constant-temperature mode and the dynamic temperature decay mode following the opening of the feedback loop as described by

$$\begin{aligned} C_1 \frac{dT_2}{dt} &= (q_n + q_e) - \frac{1}{R_1}(T_2 - T_1) \\ C_2 \frac{dT_1}{dt} &= \frac{1}{R_1}(T_2 - T_1) - \frac{1}{R_2}(T_1 - T_0) \end{aligned} \tag{1}$$

$$\frac{1}{R_1} = \frac{2\pi k_{Cu}(T_2)\left[h_s - 2(r_o - r_i)\right]}{\log\left(\frac{r_o}{r_i}\right)} + \frac{2\pi k_{Cu}(T_2)\left(r_o^2 - r_i^2\right)}{\left[h_s - 2(r_o - r_i)\right]}$$

where k_C , r_o (0.575 mm), r_i (0.3mm) are, respectively, the thermal conductivity, outer and inner radius of the copper layer between Node 1 and Node 2, h_s is the height of the sensor, T_2 is Node 2 temperature, and C_1 and C_2 are, respectively, thermal capacitances of Node 1 and Node 2. Other notation in Eq.(1) are as defined previously. The model described by Eq(1) has been validated against a finite element code [3]. At steady-state Eq.(1) yields

$$q_n + q_e = \frac{1}{R_2}\left(T_1 - T_0\right) \tag{2}$$

which corresponds to the constant temperature mode operation of CTPS.

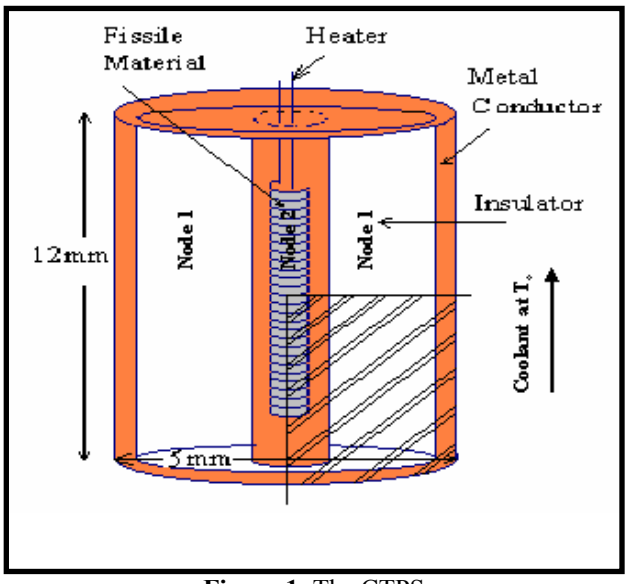

Figure 1: The CTPS

Previous work [9] to determine the local nuclear energy deposition rate q_n with CTPS has used: a) an algebraic model obtained from the solution of the linearized differential equations describing the CTPS operation, and, b) the software package DSD [8] to estimate the operation dependent model parameters. The results of [9] indicated that the model is very sensitive to model and data uncertainties which is the main reason why a model more closely representing the operation of CTPS (i.e. Eqs.(1) and (2)) are being used in this study.

4. AN OVERVIEW OF DSD [8, 10]

The DSD is based on the representation of the system dynamics in terms of transition probabilities between user specified cells that partition the system parameter/state space during user specified time intervals. The DSD recursively

computes the probability $p_k(j,n \mid J_k)$ that the state variables (e.g. $T_1(t)$, $T_2(t)$) are in cell j (j = 1,...,J) and the unknown parameters (e.g. R_2, T_0) are in cell n (n = 1,...,N) during the data-sampling time period $k\tau \le t \le (k+1)\tau$ k (k = 0, 1, 2, ...), given that the possible set of cells the state variables can be in at this time is J_k (as observed from the monitored data), from

$$p_k^*(j,n) \equiv p_k(j,n \mid J_k) = \frac{p_k(j,n)}{\sum_{j' \in J_k} \sum_{n'} p_k(j',n')} \quad (j \in J_k)$$

$$p_k(j,n) = \sum_{j' \in J_{k-1}} g(j \mid j',n) p_{k-1}^*(j',n') \tag{3}$$

where $g(j \mid j',n)$ is the transition probability from state variable cell j' to state variable cell j during the period $k\tau \le t \le (k+1)\tau$ when the system parameters are within cell n. The $g(j \mid j',n)$ can be approximated by: 1) at time $k\tau$, selecting randomly or otherwise (e.g. equidistant) M' starting points from cell j' for a given n, 2) using the given system model (e.g. Eq.(1)) to find the number M of trajectories that arrive within cell j at $t = (k+1)\tau$ (e.g. by integrating Eq.(1) over $k\tau \le t \le (k+1)\tau$ for each of the m' = 1, 2, . . , M' initial conditions), and, c) letting $g(j \mid j',n) = M / M'$. A graphical illustration of this process is given in Fig.2 and some sufficient conditions for the convergence of DSD are given in [11].

5. USE OF DSD TO ESTIMATE THE UNCERTAINTY IN THE OBSERVED POWER AT IN-CORE CTPS LOCATIONS

If the values of the system parameters change in time, the DSD may lose track of the variables to be estimated, i.e. all the obtained from Eq.(3) will be zero. In the original DSD algorithm with this fixed partitioning scheme (FPS), the estimation process will reinitialize itself in this situation by starting from the initial probability and estimate the new parameter by the recursive use of Eq.(3) again by searching over all the cells. This approach may lead to excessive computational time if there are frequent parameter changes during system evolution and a large number of variables/parameters to be estimated. In that respect, a recursive algorithm was developed to overcome this limitation [12, 13]. The recursive partitioning scheme (RPS) reduces the computational time for reinitialization (as well as overall memory requirements for DSD) through following steps:

1. Input parameter and state variable ranges of interest, RPS stopping rules and monitored data uncertainty. Read data from the monitors.
2. Define the cells so as to contain the variation/noise on the monitored data, centered on their median values. Define the cells for the unmonitored variables by bisecting each state variable range of interest and each parameter range of interest.
3. Specify $p_0(j,n)$ to be used to start the estimation process (usually uniform)

4. Determine the cell-to-cell transition probabilities by quadratures or by sampling over the cells specified in Step 2.
5. Find $p_k(j,n)$ from Eq.(3)
6. If all, then bisect the cells and go to Step 3. Otherwise, normalize $p_k(j,n)$ by dividing it by the total probability of finding the system in the search space, increment the time index *k* and go to Step 2.

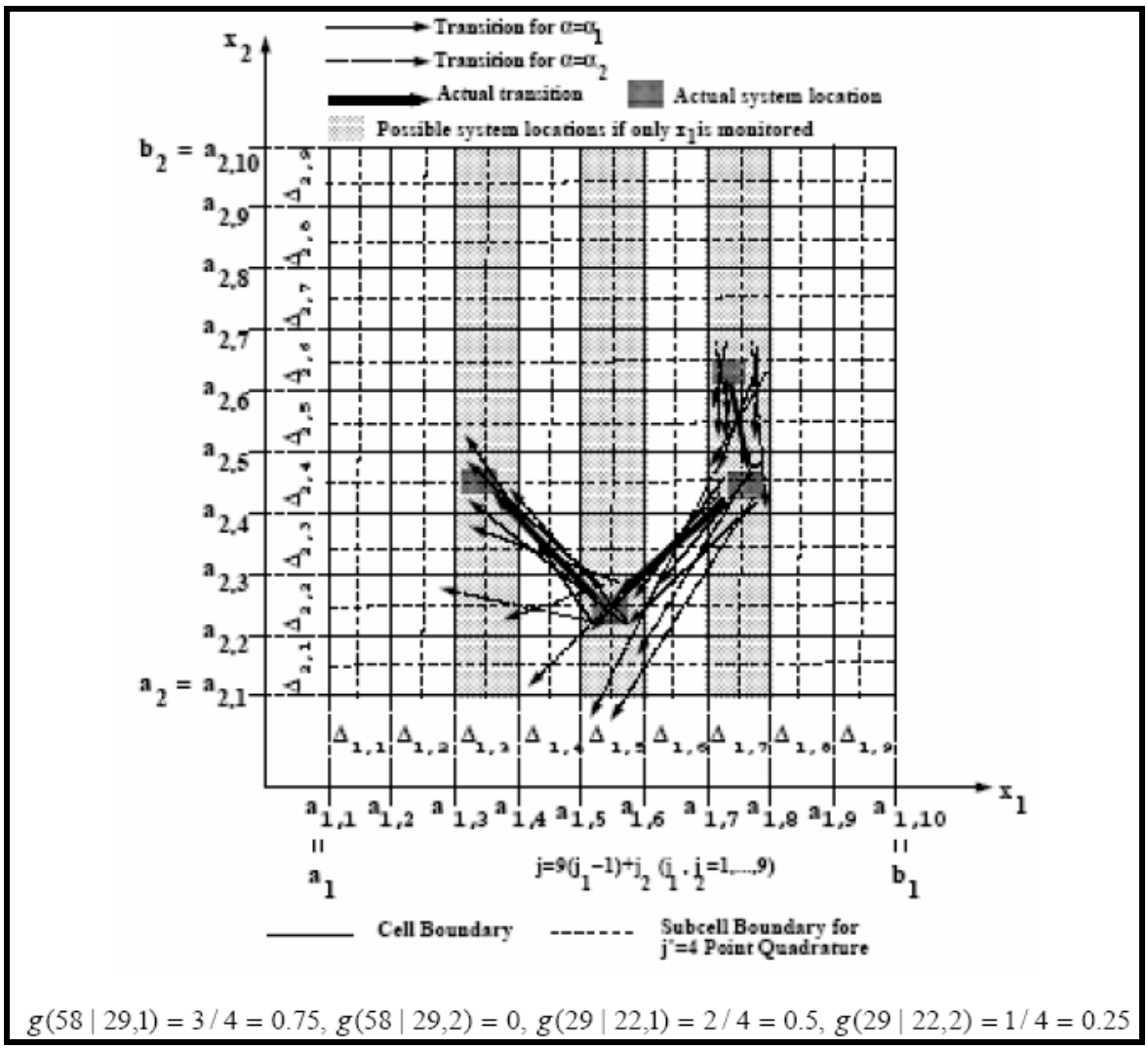

Figure 2: An example partitioning scheme and the illustration of the approximation of *g(j| j', n)* for a hypothetical dynamical system with two state variables x_1, x_2 and one parameter α . The system is in cells j = 9(j_1 − 1) + j_2 = 60,58,29,22 at times kτ , (k + 1)τ , (k + 2)τ , (k + 3)τ respectively. If only x_1 is monitored, the set of possible cells the system can be in are $J_k = J_{k+1}$ = { j = 55, . . . , 63}, J_{k+2} = { j = 37,…,45} and J_{k+3} = { j = 10, . . . , 18} [14].

Steps 2 through 6 are repeated until convergence, i.e. $p_k(j,n)$ are all zero except for the cells containing the actual system locations. It should be mentioned at this point that the algorithm may not converge for rapidly evolving systems during one data sampling interval*)* $k\tau < t < (k+1)\tau$. However, even in this situation [14] shows that the expected

values of the parameters/state variables to be estimated are often found to be close to their actual values. Section 5.1 and 5.2 below describe, respectively, the implementation of the recursive algorithm to single CTPS [12] and a series of CTPS for direct estimation of power distribution in reactors for nuclear thermal space propulsion [13]. The other improvement to DSD was the reformulation of the cell-to-cell transition probabilities to account for the possible non-uniform distribution of the system location within the cells, described Section 5.3 below.

5.1 An Application of DSD with Recursive Partitioning Scheme to Constant Temperature Power Sensors [12]

Two cases were considered, one of normal operation with a switch between the operation modes of the sensor with constant coolant temperature T_0 (Case 1), and a second one, a slow transient with decreasing T_0 (Case 2). Node 1 and 2 temperatures for the estimation process were simulated using Eqs.(1) and (2) with the parameter values given in Table 1.

Table 1: Steady-State Parameter Values Used for the Generation of Simulated CTPS Data

T_0(K)	T_2(K)	C_1(J/K)	C_1(J/K)	R_1(K/W)	R_2(K/W)	q_n(W)	q_e(W)
1000.0	1085.9	0.00804	0.744	5.709	1.857	1.68	9.67

The choice of the temperature data in Table 1 reflects the expected steady-state operational conditions in Generation 4 gas cooled reactors.

Figures 3 and 4, respectively, show the estimation results for Case 1 and Case 2 using RPS. The spikes starting at around t=10 s in both Figs.2 and 3 at around indicate the time at which the initial switch from Mode 1 to Mode 2 is made. The figures show that while DSD temporarily looses track of q_n at the time of the switch, recovery is very rapid and DSD with the RPS is able to estimate q_n with the desired accuracy (within 1% of the range of interest) for the rest of the time interval of interest (i.e. until 100 s). Comparison of the run times and memory requirements to obtain the results in Figs.3 and 4 to those obtained using the original fixed partitioning scheme for comparable accuracy indicates a speedup by a factor of 5 in the run time with RPS and a reduction by a factor of 2 in memory requirements.

5.2 Direct Estimation of Power Distribution in Reactors for Nuclear Thermal Space Propulsion [13]

The example nuclear thermal propulsion reactor concept chosen to illustrate the utilization of the CTPS/DSD combination is the particle bed reactor (PBR) concept used in [15]. Figures 4 and 5, respectively, show a horizontal cross section of the reactor core and an axial cross section of a PBR fuel element. The PBR uses fuel in the form of small diameter particles (100-500 μm) which consist of a highly enriched uranium kernel surrounded by multiple layers of pyrographite and sometimes additional ZrC or SiC

layers. The fuel particles are held between two porous annuli ("frits") to form a fuel element (Fig.4) and the fuel elements are embedded in the moderator block in concentric rings to form the core (Fig.5). The moderator block is surrounded by a pressure vessel, reflected radially and axially for neutron economy. Hydrogen pumped from the propellant tank flows through an annulus located between the radial reflector and the pressure vessel before entering the core. After entering the core, the coolant first passes through the outer cold frit (Zircaloy 2), then directly over the fuel particles and finally through the inner hot frit (ZrC) into the outlet plenum to be ejected through a nozzle to develop thrust. Partial reactivity control is achieved by varying the hydrogen mass flow rate in the annulus.

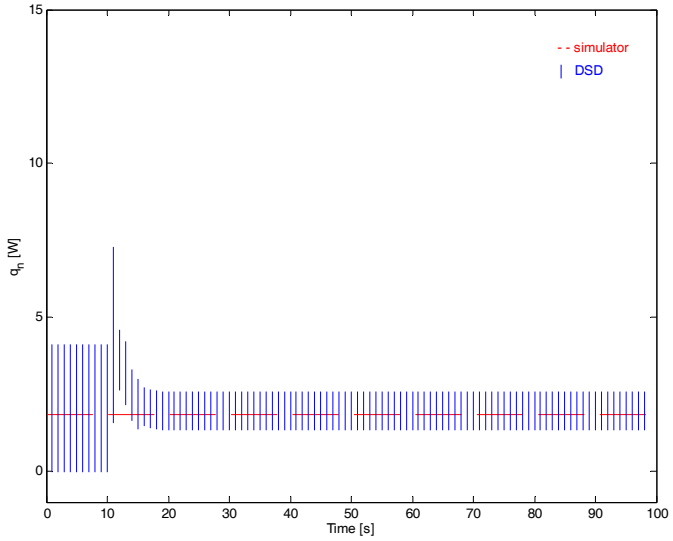

Figure 3: Simulated and Estimated q_n as a Function of Time for Case 1

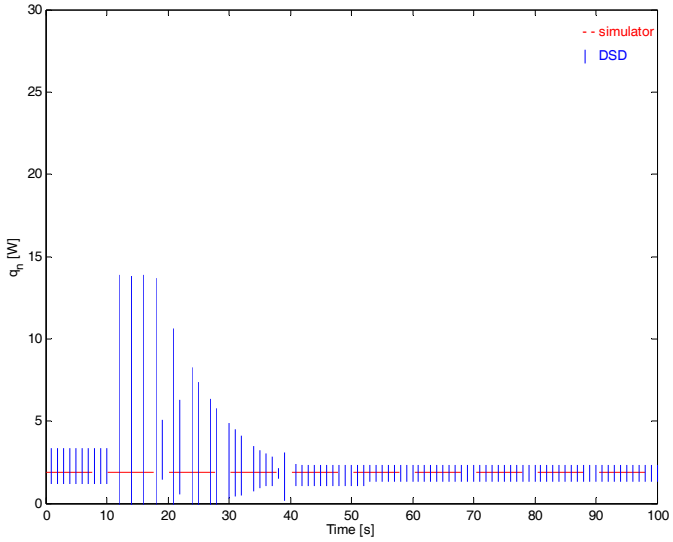

Figure 4: Simulated and Estimated q_n as a Function of Time for Case 2

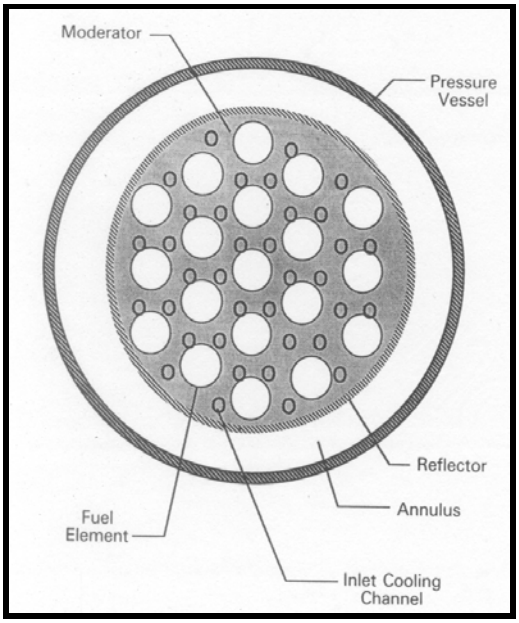

Figure 4: The Particle Bed Reactor Core [15].

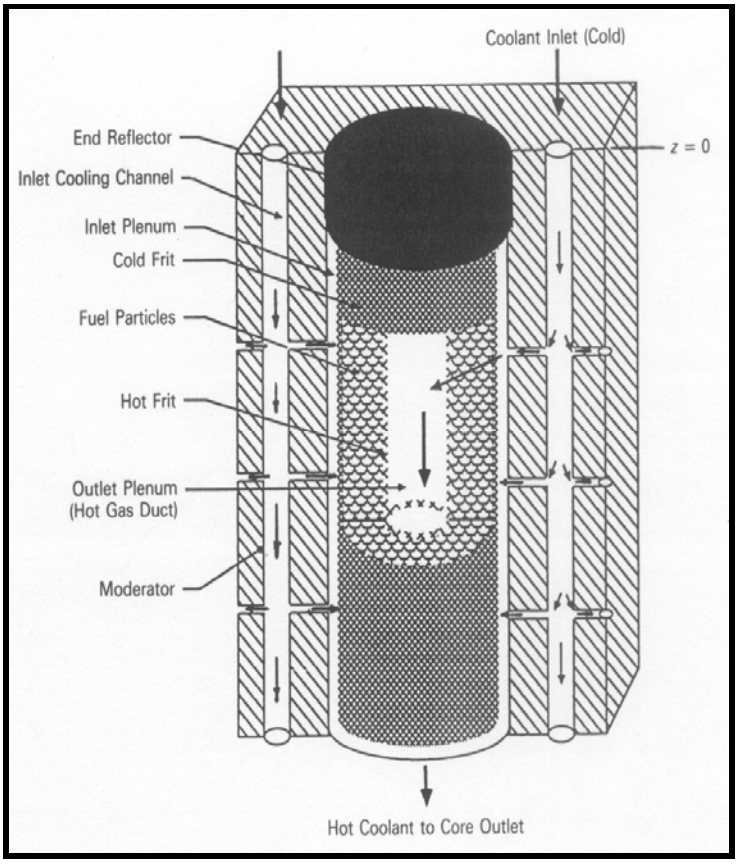

Figure 5: A Particle Bed Reactor Fuel Element [15]

For the PBR application, the CTPS is assumed to be imbedded in the fuel element between the hot and cold frit with sensor core (i.e. Node 2 in Fig.1) consisting of the same type of particles used in the fuel elements. For the purposes of this illustration, the sensor heater wire and the Node 1 and 2 metal coatings were assumed to be tungsten. Table 2 shows the example power and temperature data used for the illustration. The data in Table 2 have been generated with the MCNP [16] and HEATING-5 [17] codes. Figure 6 shows the results of the estimation using DSD, assuming that the monitored variables are $T_1(t), T_2(t)$ (see Eq.(1)) and $q_e(t)$ (see Eq.(2)). The bars in Fig.6 indicate 100% credibility intervals. The data for the estimation process was simulated using Eq.(1) with 1% noise in the monitored variables. Figure 6 indicates that the credibility intervals contain the actual (i.e. simulated data) and also quantify the uncertainty in the estimation process.

Table 2. Example Power and Temperature Data for the Particle Bed Reactor [15]

Distance from Coolant Inlet (cm)	Power Density q_n (W/cm^3)	Solid Temperature $T_1(0)=T_2(0)$ (K)	Coolant Temperature (K)
5	960	480	455
10	1440	635	610
20	1888	1230	1208
30	2040	1580	1560

40	1888	2104	2085
50	1456	2521	2503
55	976	2968	2950

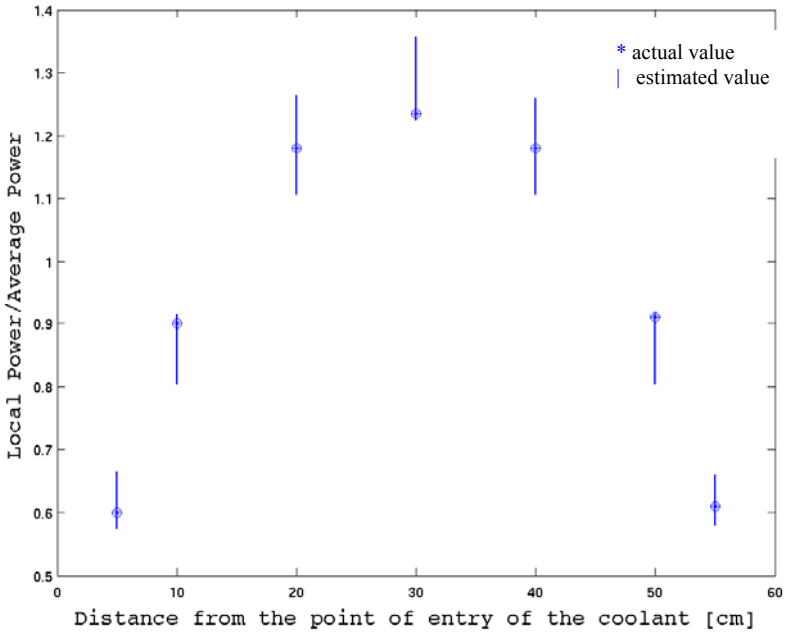

Figure 6: Estimated and Actual Values of the Local Power for the Data in Table 2

5.3 SOME IMPROVEMENTS IN STATE/PARAMETER ESTIMATION USING CCMT [18]

The original DSD estimation algorithm is based on the assumptions that the measurement noise is uniformly distributed and the measured variables are among of the state variables. From an implementation viewpoint, this assumption implies that arbitrary observers and measurement noise or model uncertainties with arbitrary distributions are not allowed. A new theoretical basis for the DSD algorithm was developed which waives these assumptions using a Bayesian interpretation of CCMT based state/parameter estimation. The new theoretical basis expands the applicability range of DSD and leads to improvements in the estimation algorithm, as well as providing a better understanding of the relationship of CCMT based state/parameter estimation to conventional state/parameter estimation techniques and of the origins of some unexplained phenomena encountered in previous work.

The new theoretical basis can be encapsulated as

$$p(\mathbf{j}_{k+1}|\overline{\mathbf{y}}_{k+1}) = \frac{\sum_{\mathbf{j}_k} g(\mathbf{j}_{k+1}|\mathbf{j}_k)\, p(\mathbf{j}_k|\overline{\mathbf{y}}_k)}{\sum_{\mathbf{j}_{k+1}}\sum_{\mathbf{j}_k} g(\mathbf{j}_{k+1}|\mathbf{j}_k)\, p(\mathbf{j}_k|\overline{\mathbf{y}}_k)} \tag{4}$$

with

$$g(\mathbf{j}_{k+1}|\mathbf{j}_k) = \iint_{\mathbf{j}_{k+1},\mathbf{j}_k} p(\mathbf{y}_{k+1}|\mathbf{x}_{k+1})p(\mathbf{x}_{k+1}|\mathbf{x}_k)\frac{p(\mathbf{x}_k|\overline{\mathbf{y}}_k)}{\int_{\mathbf{j}_k} p(\mathbf{x}_k|\overline{\mathbf{y}}_k)d\mathbf{x}_k}d\mathbf{x}_k d\mathbf{x}_{k+1} \quad (5)$$

where $p(\mathbf{j}_{k+1}|\overline{\mathbf{y}}_{k+1})$ is the probability that the system is in cell $\mathbf{j}_{k+1}$ at time $t=(k+1)\tau$ given observations $\mathbf{y}_0, \mathbf{y}_1, \ldots, \mathbf{y}_k$ and $\mathbf{x}_k$ is the true location of the system in the state space at time $t=k\tau$. The $g(\mathbf{j}_{k+1}|\mathbf{j}_k)$ as defined in Eq.(5) allows explicitly accounting for observation uncertainties, modeling uncertainties and noise through $p(\mathbf{y}_{k+1}|\mathbf{x}_{k+1})$, $p(\mathbf{x}_{k+1}|\mathbf{x}_k)$ and $p(\mathbf{x}_k|\overline{\mathbf{y}}_k)/\int_{\mathbf{j}_k} p(\mathbf{x}_k|\overline{\mathbf{y}}_k)d\mathbf{x}_k$, respectively.

6. TRACKING UNCERTAINTY PROPAGATION BETWEEN CTPS LOCATIONS

The two methods were developed for the tracking process with the following assumptions [19]:

- Method 1 assumes that, at every point in the reactor, the expected value of the power density/flux follows the diffusion theory.
- Method 2 imposes the additional constraint that the power density/flux can achieve all possible values at any specified point in the reactor.

Method 1 assumption implies that the origin of the uncertainty at the CTPS locations is random fluctuations in local power. Method 2 accounts for the possibility that the uncertainty may originate from noise or measurement error.

Method 1 yields [

$$p(h|y) = \begin{cases} \frac{1}{\sin(\beta)}\left[p_{n+1}\sin[\beta(1-y)] + p_n \sin(\beta y)\right] & B^2(y) > 0 \\ \frac{1}{\sinh(\beta)}\left[p_{n+1}\sinh[\beta(1-y)] + p_n \sinh(\beta y)\right] & B^2(y) < 0 \end{cases} \quad (6)$$

$$y = \frac{x_{n+1} - x}{x_{n+1} - x_n} \quad (7)$$

where $p(h|y)$ is the probability distribution function (pdf) of power density/flux h at y, h_n is the measured pdf of power density/flux at $x = x_n$ (or $y = 1$), h_{n+1} is the measured power density/flux at $x = x_{n+1}$ (or $y = 0$) and

$$\beta^2 = (x_{n+1} - x_n)^2 B^2 \quad (8)$$

with B being a function of the material properties between x_n and x_{n+1}.

Method 2 is a modification of the procedure proposed by [20] to search for neutral and charged Higgs bosons in electron-positron collisions. Adapted to the problem under consideration in this study, it assumes that power density/flux varies linearly between detector locations and imposes the condition that $F(\infty \mid y) = 1$ at all y. The procedure also requires that the cumulative distribution functions (Cdfs)

$$F(h \mid 1) \equiv F_n(h) = \int_0^h p_n(h')dh' \quad \text{and} \quad F(h \mid 0) \equiv F_{n+1}(h) = \int_0^h p_{n+1}(h')dh' \tag{9}$$

at the two consecutive detector locations x_n and x_{n+1}, respectively, have the same value F as well as at all points between the detector locations, i.e.

$$F_n(h_n) = F_{n+1}(h_{n+1}) = F(h) = F \tag{10}$$

Given $p_n(h)$ and $p_{n+1}(h)$, the $p(h \mid y)$ can then be constructed using the algorithm shown in Fig.7

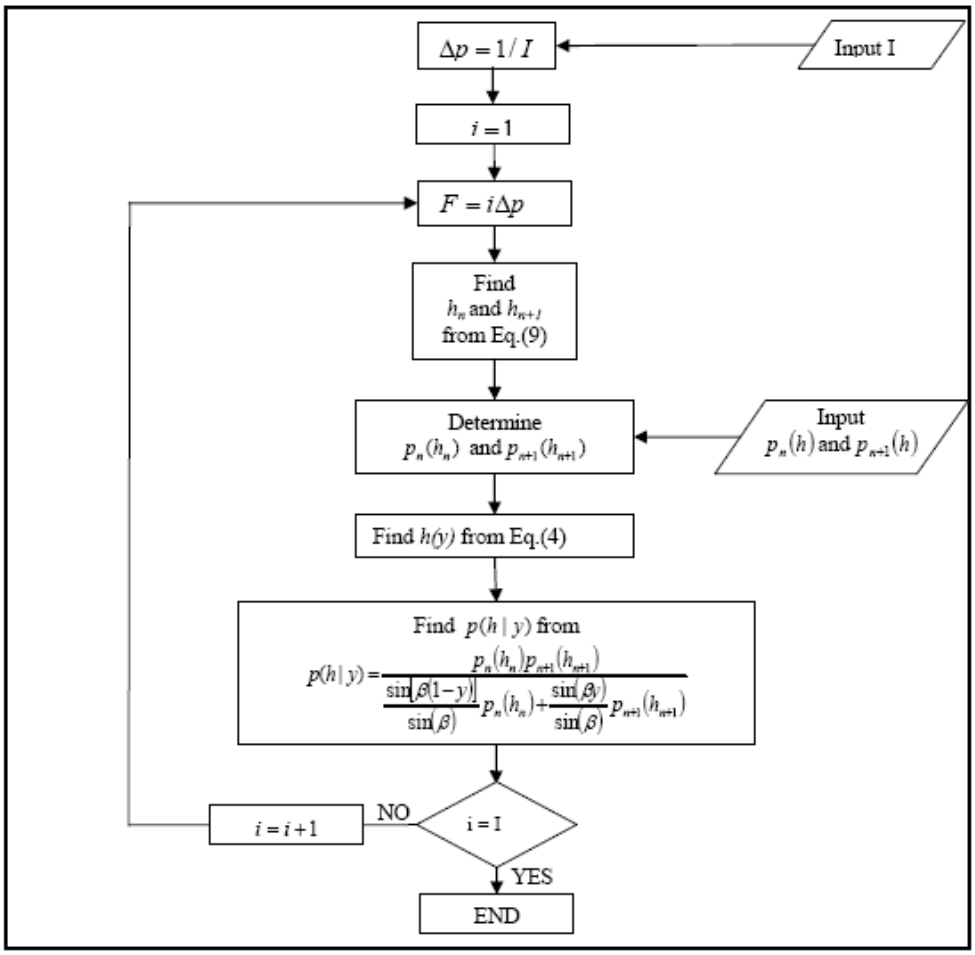

Figure 7: Method 2 Flowchart [19]

A one-dimensional reactor of length $2L$ = 300 cm with material properties given in Table 3 was considered for illustrative implementations. A gray control rod of thickness 2 cm and transmissivity 0.9 was assumed to be inserted in the reactor at x = 50 cm away from the reactor midplane. Data from detectors placed within the core at every 10 cm starting from the reactor midplane were simulated by solving 1 ½ group neutron diffusion equation within $0 \le x \le L$ and with

$$\left.\frac{d\phi_1(x)}{dx}\right|_{x=0} = \left.\frac{d\phi_2(x)}{dx}\right|_{x=0} = 0 \tag{11}$$

$$\phi_1(L) = \phi_2(L) = 0$$

to obtain

$$h(x)/h(0) = \begin{cases} \cos(Bx) & \text{if } x < 49\,\text{cm} \\ 0.488751[\sin(Bx) - \tan(BL)\cos(Bx)] & \text{if } x > 51\,\text{cm} \end{cases} \tag{12}$$

where $\phi_1(x)$ and $\phi_2(x)$ are, respectively, the fast and thermal neutron fluxes and for criticality we must have B = 0.0242 cm^{-1}.

Table 3: Group constants for the example reactor [19]

Group constant	Group	
	1	**2**
$\nu\Sigma_f$ (cm^{-1})	0.008476	0.18514
Σ_a (cm^{-1})	0.01207	0.1210
D (cm)	1.2627	0.3543
$\Sigma_{1->2}$ (cm^{-1})	0.0141	-

The monitored data from the detectors were assumed to be normally distributed with the expected value satisfying Eq.(12) and with a 1% standard deviation. Figure 8(a) shows the probability distributions and the expected values as obtained from Method 1. Figure 8(b) shows the same information, but as obtained by applying Method 2. In the region 40 < x < 60 cm were the existence of a control rod is assumed, the β coefficient in Eq.(8) was obtained through homogenization.

It was noted that although the expected values predicted by both methods matched the simulated data well (see Fig.8), Method 1 may lead to a bimodal distribution and that the predicted expected value between detector locations may fall in a region of low probability. Figures 9 and 10 show the pdfs of reactor power at x = 43 cm and x = 85 cm, respectively. The bimodal shape predicted by Method 1 in Fig.9 has also been observed in other studies [21] and is due to the fact that $p_n(h)$ and $p_{n+1}(h)$ are being concentrated in

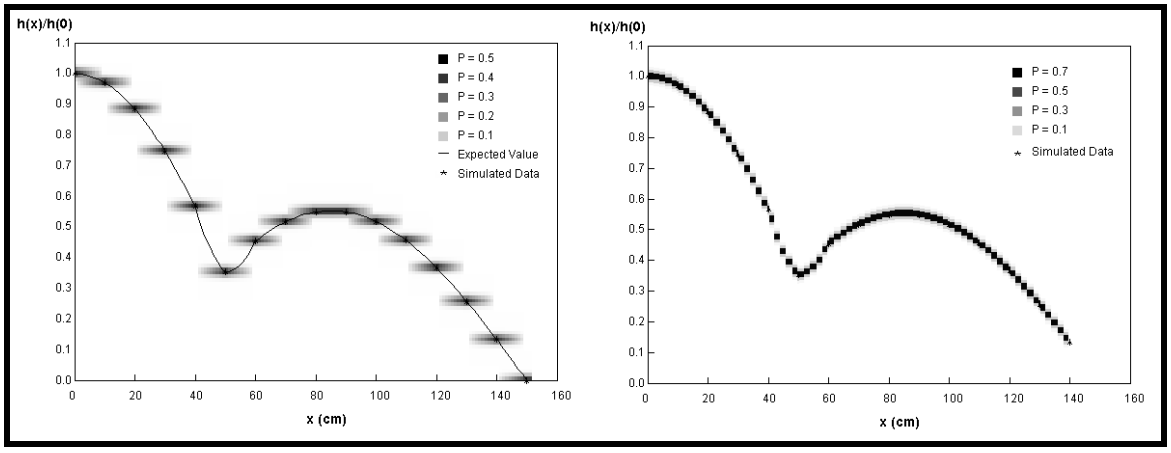

(a) (b)

Figure 8: Relative power distribution *h(x)/h(0)* for the example reactor: a) Method 1, b) Method 2 [19]

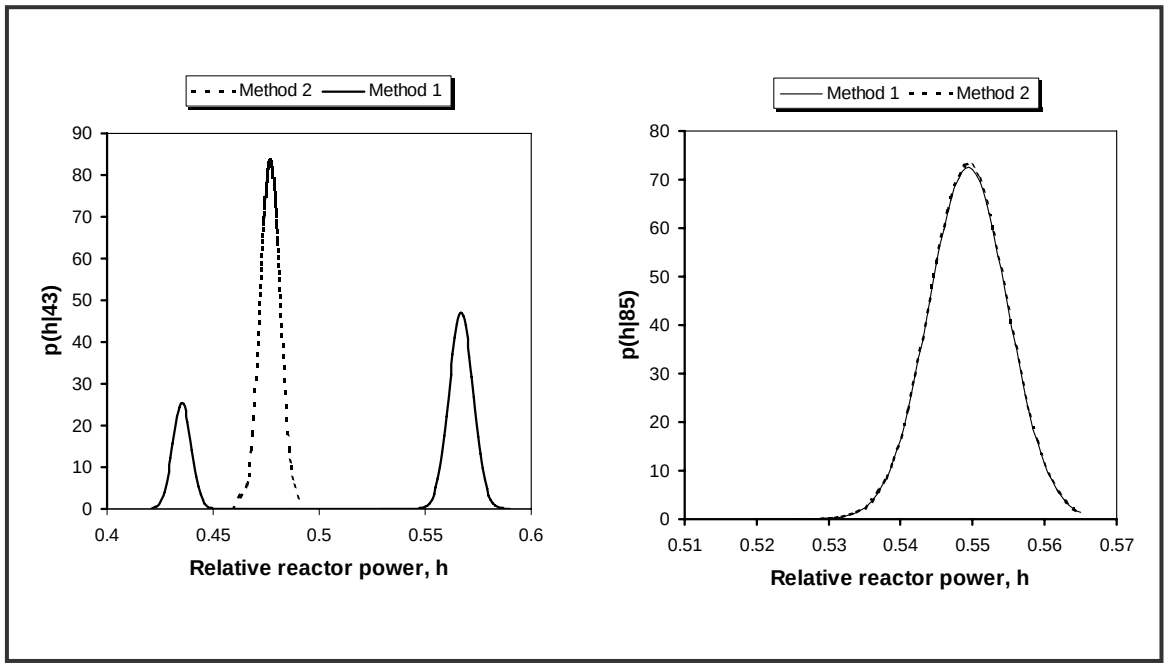

Figure 9: Probability distribution function at location x = 43 cm [19]

Figure 10: Probability distribution function at location x = 85 cm [19]

different regions of the state space. The unimodal shape of $p(h|y)$ is due to the linearity assumption of Method 2. Figure 10 shows that if the variation in the power density/flux is small with distance (e.g. at x = 85 cm as can be seen from Fig.8) and subsequently $h(y)$ is close to linear, then $p(h|y)$ obtained from both Method 1 and Method 2 are similar.

In another study [22], Method 2 was applied to a 300X300X300 cm homogeneous cube, placed in vacuum and with diffusion parameters as given in [22] to illustrate the applicability of these methods to 3-dimensional cases.

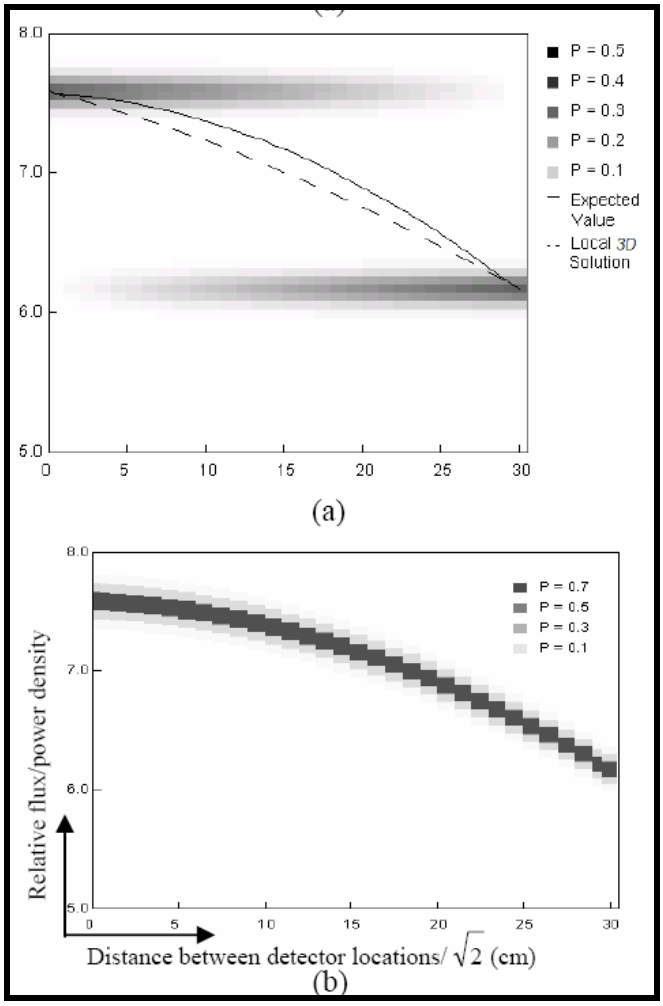

Figure11: Flux comparison for the x-y diagonal direction (a) and corresponding $p(\phi \mid w)$ obtained from Method 1 (a) and Method 2 (b)

Figures 11(a) and 11(b), respectively, show the pdf $p(\phi \mid w)$ of the flux (ϕ) distribution at the normalized distance w between detector locations obtained from Method 1 and Method 2. The bimodal nature of the pdf obtained from Method 1 in Fig.11(a) and the low probability region between detector locations reflects the large uncertainty in the flux value due to lack of observation in this region. The expected value in Fig.11 (a) is still very similar to the local 3-dimensional solution. The difference between Fig.11 (a) and 11(b) results is due to the condition imposed by Eq.(9) which assumes that the cumulative probability distribution of flux/power density is conserved between detector locations. Another interpretation of this assumption is that the uncertainty in flux/power at the detector locations also propagates according to Eq.(4) between detector locations. The assumption is justified if the uncertainty originates from possible flux/power fluctuations but not if it originates from electronic noise in the detection hardware.

7. MATERIAL AND SOURCE IDENTIFICATION IN FINITE CYLINDRICAL GEOMETRIES USING THE SCHWINGER INVERSE METHOD [23]

The objective of this activity was to investigate if burnup and power distribution in nuclear reactors can be inferred through measurements of unscattered gamma leakage from the reactor. Schwinger inverse method was employed to study the feasibility of identifying the material composition and source distribution in finite cylindrical geometries which then would yield level of burnup through the fission product activity and power distribution in the reactor core from the spatial distribution of ^{235}U and Pu gammas.

7.1 Material Identification

The following equation was used for the identification of the composition of an unknown layer with specified dimensions [24]:

$$\Sigma'^{g}_{t,1} = \frac{\int dV \int d\hat{\mathbf{\Omega}} \psi^{*g} q^{g}}{\int_{\Delta r} dV \int d\hat{\mathbf{\Omega}} \psi^{*g} \psi^{g}} \left(\frac{M^{g} - M_0^{g}}{M_0^{g}} \right) + \Sigma_t^{g} . \qquad (13)$$

$$g = 1, \ldots, G.$$

In this equation, Σ_t^g is the total photon cross section in the current iteration for the unknown material at the energy corresponding to line *g* and $\Sigma'^{g}_{t,1}$ is the updated cross section that will be used in the next iteration. The terms ψ^g, ψ^{*g}, and M^g are the forward flux, adjoint flux, and leakage calculated for line *g* in the current iteration; q^g is the source term for line *g* (γ/cm^3-s); and M_0^g is the measured leakage for line *g*. The integral in the numerator in Eq. (13) is over the entire problem, but the integral in the denominator is over the unknown material region only. Once the *G* macroscopic cross sections are found, the unknown material is identified using cross section tables [24].

7.2 Source Weight Fraction Identification

The following equation was used to iteratively determine the unknown weight fractions of a gamma-emitting source [25]:

$$\frac{\rho_S N_A}{\langle \psi^{*g} q^{g} \rangle} \left[\left(\int_{V_S} dV \int d\hat{\mathbf{\Omega}} \psi^{*g} \psi^{g} \sum_{j=1}^{J} \frac{\sigma_{t,j}^{g}}{A_j} \Delta f_j \right) - \frac{M^{g}}{M_0^{g}} \frac{q_i^{g}}{A_i} \int_{V_S} dV \int d\hat{\mathbf{\Omega}} \psi^{*g} \Delta f_i \right] = \frac{M^{g} - M_0^{g}}{M_0^{g}} \qquad (14)$$

$$g = 1, \ldots, G.$$

In Eq.(14), ρ_S is the mass density of the source material, N_A is Avogadro's number, $\sigma_{t,j}^g$ is the total microscopic cross section for source isotope *j* and line energy *g*, and A_j is the

gram atomic weight of source isotope j. The term $\Delta f_j \equiv f_j' - f_j$ is the update to the weight fraction in the current iteration to obtain the weight fraction to use in the next.

7.3 Test Problem

The methods for source and shield identification were tested on the finite cylindrical geometry shown in Fig. 12. A highly enriched uranium source is surrounded by a shield consisting of aluminum on the bottom and side of the cylindrical shield and nickel on the top. The top of the shield is twice as thick as the bottom. This axial asymmetry allows for more physically realistic test problems than were possible with the one-dimensional spherical problems of [24] and [25] .

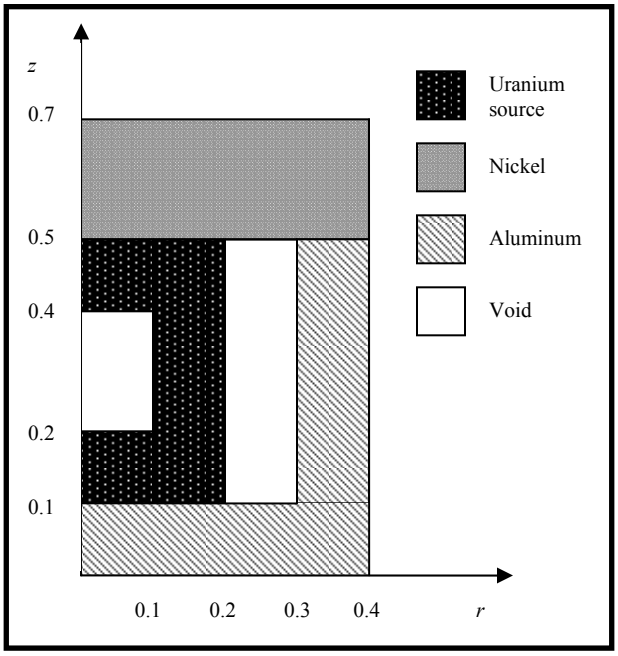

Fig. 12. Geometry for numerical test problems. Dimensions are in cm.

The quantities of interest were the total leakage (into 4π of four decay lines from natural uranium, 144, 186, 766, and 1001 keV. The forward and adjoint angular fluxes of Eqs. (13) and (14) were calculated for each line using the PARTISN discrete-ordinates code [26] with no scattering.

Leakage measurements were simulated in two ways. The first was by using PARTISN with the same angular (S_8) and spatial discretizations as used to calculate the flux in the iterative calculation. Thus, these "measured" and calculated leakages were exactly consistent. The second way of simulating measured leakages was by using a Monte Carlo code, which simulated a real measurement of the total leakage. These measurements are shown in Table 4.

Table 4: Measured Leakages

Line (keV)	S_8	Monte Carlo
144	3.05349E+2	3.360E+2±5.45%
186	9.99298E+3	1.029E+4±1.02%
766	1.41914E+3	1.458E+3±2.65%
1001	3.53495E+1	4.60E+1±14.74%

7.4 Results

7.4.1 Material Identification

Converged cross sections on the left side of Eq. (13) were compared to known cross sections from a library of 40 candidate materials using a root-mean-squared (RMS) difference, where the RMS difference for material *m* is

$$(\mathrm{RMS})_m = \sqrt{\frac{1}{G}\sum_{g=1}^{G}(\Sigma_t'^g - \Sigma_{t,m}^g)^2}. \tag{15}$$

The materials with the lowest RMS differences were considered candidates for the unknown.

When S_8 measurements in Table 4 were used, nickel was successfully identified as the only suitable candidate for the unknown layer, having an RMS difference two orders of magnitude smaller than any other material (see Table 5). With Monte Carlo measurements, nickel was one of seven possible candidate materials.

Table 5: Materials with the Lowest RMS Difference in the Shield Identification Problem (Actual Material Was Nickel, Initial Guess Was Lead)

	S_8 Measurements		Monte Carlo Measurements	
1	Nickel	8.612E-04	Cobalt	2.947E-01
2	Copper	2.952E-02	SS316	3.159E-01
3	Cobalt	8.705E-02	Nickel	3.232E-01
4	SS316	1.967E-01	Iron	3.299E-01
5	Iron	2.390E-01	SS304	3.312E-01
			Carbon Steel	3.429E-01
			Copper	3.495E-01

7.4.2 Source Weight Fraction Identification

Initial guesses for the weight fractions of uranium in the source were: ^{235}U: 0.5000, ^{238}U: 0.5000. When S_8 measurements were used, the actual source weight fractions (^{235}U: 0.9473, ^{238}U: 0.0527) were found in one iteration of Eq.(14). With Monte Carlo measurements, slightly less accurate weight fractions of ^{235}U: 0.9524, ^{238}U: 0.0476 were calculated in one iteration.

8. CONCLUSION

The project achieved all its objectives. The main contribution of the project to the state-of-the-art are is the development of an algorithm that can be used to determine the power distribution directly in a nuclear reactor core using the signals obtained from CTPS, as well as quantifying the uncertainty associated with the estimated power distribution. The project results also indicate that it may be possible to determine burnup and power distribution in nuclear reactor cores using ex-core measurements of discrete gamma lines.

The project led to the completion of 4 M.S. theses [27-30] and initiated research that will lead to 2 Ph.D. degrees. The publications resulting from the study are given in [10-14, 18, 19, 22-24, 31-36].

REFERENCES

1. T. D. RADCLIFF, D. W. MILLER AND A. C. KAUFFMAN, "Modeling of a Constant-Temperature Power Sensor", *ICONE8*, Paper #8263, American Society of Mechanical Engineers, New York, N.Y. (May 2000)
2. T. D. RADCLIFF, D. W. MILLER AND A. C. KAUFFMAN, "Constant Temperature Calorimetry for In-Core Power Measurement," *Nucl.Technol*., **132**, 240-255 (2000)
3. F. H. Ruddy F.H., A. R. Duloo, J. G. Seidel, F. W. Hantz, L. R. Grobmyer L.R., "Nuclear Reactor Power Monitoring Using Silicon Carbide Semiconductor Radiation Detectors, *Proceedings of the ANS Topical Meeting on Nuclear Power Plant Instrumentation and Control and Human-Machine Interface Technology (HPIC&HMIT'2000)*, November 2000, Washington, DC.
4. AP600 Standard Safety Analysis Report, Volume 10, B 3.2.3, Westinghouse Electric Corporation, Monroeville, PA (1998)
5. I. MUNTEANU, H.B. ZHOU, T. D. RADCLIFF, T. ALDEMIR, D. W. MILLER, "In-Core Power Detection Using DSD", *Trans. Am. Nucl. Soc*., **83**, 279-281 (2000)
6. Z-S. Liu, "QR Methods of O(N) Complexity in Adaptive Parameter Estimation," *IEEE Transactions on Signal Processing*, **43**, 720, (1995).
7. L. DINCA, T. ALDEMIR, "Parameter Estimation Towards Fault Diagnosis in Non-Linear Systems Using a Markov Model of System Dynamics", *Nucl.Sci.Eng*, **127**, 199-219 (October 1997)
8. X.M. CHEN, P. WANG, T. ALDEMIR, "DSD: A Parameter/State Estimation Tool for Model-based Fault Diagnosis in Non-linear Dynamic Systems", *Dynamic Reliability : Future Directions*, C . Smidts, J. Devooght, P. E. Labeuau (Eds), 251-276, International Workshop Series on Advanced Topics in Reliability and Risk Analysis, Center for Reliability Engineering, University of Maryland (October 2000)
9. T. D. RADCLIFF, D. W. MILLER AND A. C. KAUFFMAN, "Modeling of a Constant-Temperature Power Sensor", *ICONE8*, Paper #8263, American Society of Mechanical Engineers, New York, N.Y. (May 2000)

10. P. WANG, X. M. CHEN, T. ALDEMIR, "DSD: A Generic Software Package For Model-based Fault Diagnosis in Dynamic Systems", *Reliab. Engng & System Safety*, **75**, 31-39 (January 2002)
11. P. WANG, T. ALDEMIR, "Real Time Xenon Estimation in Nuclear Power Plants", *Trans. Am. Nucl. Soc.,81*, 154-156 (November 1999)
12. A. Burghelea, T. Aldemir, "An Application of DSD with Recursive Partitioning Scheme to Constant Temperature Power Sensors", *Probabilistic Safety Assessment and Management: PSAM 7-ESREL'04*, C. Spitzer, U. Schmocker, V. N. Dang (Eds.), 1821-1827, Springer – Verlag, London, U.K. (June 2004)
13. T. ALDEMIR, D.W. MILLER, A. BURGHALEA, "Direct Estimation of Power Distribution in Reactors for Nuclear Thermal Space Propulsion", *Space Technology and Applications International Forum—STAIF 2004*, M. S. El-Genk (Ed.), 582-589, American Institute of Physics, Melville, N.Y. (February 2004)
14. A. BURGHELEA, I. MUNTEANU, T. ALDEMIR, "A Recursive Partitioning Approach to DSD", *PSA2002: Proceedings of the International Topical Meeting on Probabilistic Safety Assessment, G*. E. Apostolakis, T. Aldemir (Eds), 630-635, American Nuclear Society, La Grange Park, IL (2002)
15. S. M. AITHAL, T. ALDEMIR, K. VAFAI "Assessment of the Impact of Neutronic/Thermal-Hydraulic Coupling on the Design and Performance of Nuclear Reactors for Space Propulsion," *Nucl. Technol*. 106, 15-30 (1994).
16. J. S. BREIMEISTER, "MCNP-A General Monte Carlo Code For Neutron and Photon Transport, Version 3B," LA 7396-M, Los Alamos National Laboratory, New Mexico (1989).
17. W. D. TURNER, W, D. ELROD, I. I. SIMAN-TOV, "HEATING-5," ORNL/CSD/TM-15, Oak Ridge National Laboratory, Oak Ridge, Tennessee (1977).
18. P. WANG, T. ALDEMIR, "Some Improvements in State/Parameter Estimation Using the Cell-to-Cell-Mapping Technique", *Nucl.Sci.Eng.*, **147**, 1-25 (May 2004)
19. M. BIRO, T. ALDEMIR, "Quantifying the Measurement Uncertainty Propagation In Flux/Power Reconstruction", *Proceedings of NPIC&HMIT 2004*, 1246-1253, American Nuclear Society, LaGrange Park, IL (September 2004)
20. L. READ, "Linear Interpolation of Histograms", *Nuclear Instruments & Methods in Physics Research* A 425, 357-360 (1999)
21. F. H. BURSAL, "On Interpolating between Probability Distributions", *Applied Mathematics and Computation*, 77, 213-244 (1996).
22. A. HAKOBYAN, M. BIRO, T. ALDEMIR, "Representation of Measurement Uncertainty in Flux/Power Shape Construction From Monitored Data", *Trans. Am. Nucl. Soc*., **92,** 555-557 (June 2005)
23. K. C. BLEDSOE, J. A. FAVORITE, T. ALDEMIR, "Material Identification in Finite Cylindrical Geometries Using the Schwinger Inverse Method", *Trans. Am. Nucl. Soc.*, **95,** 545 - 547 (June 2007)
24. J. A. FAVORITE and K.C. BLEDSOE, "Identification of an Unknown Material in a Radiation Shield Using the Schwinger Inverse Method," *Nucl. Sci. Eng.*, **152**, 106-117 (2006).
25. J. A. FAVORITE, "Using the Schwinger Variational Functional for the Solution of Inverse Transport Problems," *Nucl. Sci. Eng.*, **146**, 51-70 (2004).

26. R. E. ALCOUFFE et al., "PARTISN," LA-CC-98-62, Los Alamos National Laboratory (1997).
27. R KENNEDY, "A Computational Benchmark of Sn And Monte Carlo Codes Using The Ohio State University Nuclear Reactor Laboratory", M.S. Thesis, The Ohio State University (2007)
28. K. C. BLEDSOE, "Using the Schwinger Inverse Method for Material Identification in One- and Two-Dimensional Cylindrical Radiation Shields", M.S. Thesis, The Ohio State University (2006)
29. M. BIRO, "The Development of a Self-Calibrating Power Monitoring System for Nuclear Reactors", M.S. Thesis, The Ohio State University (2005)
30. A. E. BURGHELEA, "Applications of the DSD Algorithm with Recursive Partitioning to Nuclear Systems" , M.S. Thesis, The Ohio State University (2003)
31. M. BIRO, T. ALDEMIR, "The Development of a Self-Calibrating Power Monitoring System for Nuclear Reactors", *Proc.ISAS-CITSA 2005*, II, J. Aguilar, H.-A. Chu, E. D. Gugiu, I. Miloucheva, N. Rishe (Eds.), 4-8, International Institute of Informatics and Systemics, Orlando, FL (July 2005)
32. A. BURGHELEA, T. ALDEMIR, "In-Core Power Detection with CTPS Using a Non-Linear Model", *Trans. Am. Nucl. Soc*., **88**, 314-316 (June 2003)
33. A. BURGHELEA, T. ALDEMIR, "A Parametric Investigation of the Recursive Partitioning Approach to DSD for Implementation with CTPS", *Trans. Am. Nucl. Soc*., **89,** 493-495 (November 2003)
34. M. BIRO, T. ALDEMIR, "A Model Based Probabilistic Scheme for Flux/Power Shape Construction from Monitored Data", *Trans. Am. Nucl. Soc*., **90**, 59-61 (June 2004)
35. M. BIRO, T. ALDEMIR, "Implementation of an On-Line Reactor Power Monitoring System Using CTPS", *Trans. Am. Nucl. Soc*., **93,** 575-577 (November 2006)

Probabilistic Safety Assessment and Management: PSAM 7-ESREL'04,
C. Spitzer, U. Schmocker, V. N. Dang (Eds.), 1809-1814, Springer – Verlag, London, U.K. (June 2004)

The DSD and Conventional State/Parameter Estimation

Peng Wang and Tunc Aldemir
The Ohio State University, 206 West 18th Avenue,
Columbus, OH 43210, U.S.A.

Abstract

The DSD (Dynamic System Doctor) is system independent, state/parameter estimation software that can be used for both point and interval estimation. The DSD also yields useful information for risk informed regulation and risk monitoring of nuclear power plants. The relationship of DSD to some conventional estimation techniques is described and illustrated using a linearized model for the on-line calibration of the constant temperature power sensor, recently proposed for direct core power density distribution measurement in Generation IV reactors.

1 Introduction

The DSD (Dynamic System Doctor) is system independent, state/parameter estimation software [1]. The DSD uses a system representation scheme based on the transition probabilities between user specified computational cells that partition the system state space (cell-to-cell mapping). These transition probabilities are obtained from the user supplied system model. The theoretical basis of the DSD and the current DSD algorithm are described in a companion paper [2]. The main advantage of the DSD over conventional estimators is that DSD is both a point and an interval estimator. In addition, the DSD yields the probability distribution of the system variables/parameters within the estimated bounds which provides a probabilistic measure to rank the likelihood of system faults in view of modeling uncertainties and/or signal noise. Such information is particularly useful for risk informed regulation and risk monitoring of nuclear power plants.

The current DSD algorithm is based on the assumptions that: a) the measurement noise is uniformly distributed, and, b) the measured variables are part of the state variable vector. Recent theoretical developments [3] have extended the applicability range of DSD to arbitrarily distributed (but known) signal noise and modeling uncertainties and arbitrary observers. The new theoretical developments have also provided the framework which clarifies the previously unexplained relationship between DSD and conventional state/parameter estimation techniques. The paper describes and illustrates the relationship of DSD to the generalized maximum likelihood estimator (MLE),

least squares estimator (LSE) and the Kalman filter approach.

2 Overview of the Recent Developments

The extended DSD algorithm accepts system equations of the form

$$\boldsymbol{x}_{k+1} = \tilde{\boldsymbol{x}}(\boldsymbol{x}_k) + \boldsymbol{v}_k \quad (k = 0,1,2,\cdots) \tag{1}$$

and observers of the form

$$\boldsymbol{y}_k = \boldsymbol{h}(\boldsymbol{x}_k) + \boldsymbol{w}_k \quad (k = 0,1,2,\cdots) \tag{2}$$

where

$\boldsymbol{x}$ L-dimensional vector whose elements are the state variables or unknown model parameters x_l $(l = 1,...,L)$ of the dynamic system

$\boldsymbol{v}_k$ system noise at time step $k\tau$ $(k = 0,1,2,...)$ (e.g. due to stochastic variation of system parameters) or a measure of modelling uncertainties, in general

$\boldsymbol{x}_k$ state vector at time step $k\tau$ $(k = 0,1,2,...)$

$\boldsymbol{y}_k$ M-dimensional vector whose elements y_k are the measured data at time step $k\tau$ $(k = 0,1,2,...)$

$\boldsymbol{w}_k$ measurement uncertainty

$\tilde{\boldsymbol{x}}$ a L- dimensional rule that maps $\boldsymbol{x}_k$ onto $\boldsymbol{x}_{k+1}$ (such as by the integration of a set of L ordinary differential equations)

$\boldsymbol{h}$ M - dimensional vector whose elements are known nonlinear functions

The estimation process takes place in the discretized state/parameter space partitioned through the user-defined intervals

$$\Delta_{l,j_l} = \{x_l : a_{l,j_l} \le x < a_{l,j_l+1}; a_{l,1} = a_l, a_{l,J_l} = b_l\} \tag{3}$$
$$j_l = 1,...,J_l; l = 1,...,L.$$

The specification of these intervals may be, for example, based on the uncertainty/noise in the monitored x_l. The Δ_{l,j_l} constitute the computational cells $\boldsymbol{V}_j = \{\Delta_{1,j_1}, \Delta_{2,j_2}, ...\Delta_{L,j_L}\}$ $(j = 1,...,J = \prod_{l=1}^{L} J_l)$ which partition the

range of interest $a_l \le x_l \le b_l (l = 1,...,L)$ in the state/parameter space in a similar manner to those used by finite difference and finite element methods. If $\boldsymbol{j} = \{j_1 j_2 ... j_L\}$ denotes the location of the cell $\boldsymbol{V}_j$ in the discretized state-space, then it can be shown that [3] the probability

$$p(\boldsymbol{j}_k | \bar{\boldsymbol{y}}_k) = \int_{\boldsymbol{j}_k} p(\boldsymbol{x}_k | \bar{\boldsymbol{y}}_k) d\boldsymbol{x}_k \tag{4}$$

of finding the system in the cell $\boldsymbol{j}_k$ at time $t = k\tau$ is recursively calculated from

$$p(\boldsymbol{j}_{k+1} | \bar{\boldsymbol{y}}_{k+1}) = \frac{\sum_{\boldsymbol{j}_k} g(\boldsymbol{j}_{k+1} | \boldsymbol{j}_k) p(\boldsymbol{j}_k | \bar{\boldsymbol{y}}_k)}{\sum_{\boldsymbol{j}_{k+1}} \sum_{\boldsymbol{j}_k} g(\boldsymbol{j}_{k+1} | \boldsymbol{j}_k) p(\boldsymbol{j}_k | \bar{\boldsymbol{y}}_k)} \tag{5}$$

$$g(\boldsymbol{j}_{k+1} | \boldsymbol{j}_k) = \iint_{\boldsymbol{j}_{k+1}, \boldsymbol{j}_k} p(\boldsymbol{y}_{k+1} | \boldsymbol{x}_{k+1}) p(\boldsymbol{x}_{k+1} | \boldsymbol{x}_k) \frac{p(\boldsymbol{x}_k | \bar{\boldsymbol{y}}_k)}{\int_{\boldsymbol{j}_k} p(\boldsymbol{x}_k | \bar{\boldsymbol{y}}_k) d\boldsymbol{x}_k} d\boldsymbol{x}_k d\boldsymbol{x}_{k+1} \tag{6}$$

where $g(\boldsymbol{j}_{k+1} | \boldsymbol{j}_k)$ is the probability that the system will move from cell $\boldsymbol{j}_k$ to cell $\boldsymbol{j}_{k+1}$ during $k\tau \le t < (k+1)\tau$. It can be also shown that [3]:

1. Eqs.(5) and (6) constitute a recursive Bayesian estimator (the original DSD algorithm is based on the Chapman-Kolmogorov equation),
2. if $\boldsymbol{j}_{s,k}$ denotes the actual cell the system is in at time $t = k\tau$ and $g(\boldsymbol{j}_{k+1} | \boldsymbol{j}_k) < g(\boldsymbol{j}_{s,k+1} | \boldsymbol{j}_k)$ for all $\boldsymbol{j}_{k+1} \ne \boldsymbol{j}_{s,k+1}$, $p(\boldsymbol{j}_{k+1} | \bar{\boldsymbol{y}}_{k+1})$ converges to the correct cell $\boldsymbol{j}_{s,k+1}$ irrespective of the initial distribution used, and,
3. if
   - $\boldsymbol{v}_k = 0$ for all $k = 0,1,2,\cdots$,
   - the probability $p(\boldsymbol{x}_k | \bar{\boldsymbol{y}}_k)$ is uniform over each cell $\boldsymbol{j}_k$,
   - $\boldsymbol{h}(\boldsymbol{x}_k) = \boldsymbol{x}_k$,
   - the integrals in Eq.(6) are approximated by a quadrature scheme,

   Eqs.(5) and (6) reduce to the current DSD algorithm [2].

The $p(\boldsymbol{j}_k | \bar{\boldsymbol{y}}_k)$ from Eq.(5) can be used to find all the statistical properties of the variables to be estimated at times $t = k\tau$, including expected values, standard deviations and credibility intervals. Item 3 above indicates the limitations of the current DSD algorithm with respect to Eqs.(5) and (6). Item 1 implies that [3]

1. For constant $\boldsymbol{x}_k = \boldsymbol{\theta}$ $(k = 0,1,\cdots)$, the mode of $p(\boldsymbol{\theta} | \bar{\boldsymbol{y}}_k)$ yields the maximum likelihood estimate (MLE) of $\boldsymbol{\theta}$.

2. If in Eq.(1) and $\boldsymbol{w}_k$ in Eq.(2) are both white Gaussian noise and Eq.(1) originates from a linear model for the evolution of $\boldsymbol{x}$, then the mean and covariance of $p(\boldsymbol{x}_k|\bar{\boldsymbol{y}}_k)$ obtained from Eq.(6) are equivalent to those obtained from a Kalman filter.
3. The mean of $p(\boldsymbol{\theta}|\bar{\boldsymbol{y}}_k)$ is also the least-squares estimate (LSE) of $\boldsymbol{\theta}$.

These implications are illustrated below using a linearized version of the model in [2] for the on-line calibration of the constant temperature power sensor (CTPS), proposed for direct core power density distribution measurement in Generation 4 reactors.

3 Implementation and Results

The CTPS [2] can directly measure the local nuclear energy deposition and heat transfer rate. This design concept is based on the idea of adding heat through resistive dissipation of input electrical energy to a small mass of actual reactor fuel pellet analogue which constitutes the sensor core (Node 2). The core is surrounded by ceramacast, which is an alumina based ceramic thermal insulator (Node 1). In Mode 1 operation, Node 2 is kept at constant temperature T_2 by providing the exact amount of input electrical energy q_e (in kW) through a feedback control loop irrespective of the nuclear energy q_n (in kW) generated in Node 2. At steady state [2]

$$q_e + q_n = \frac{T_2 - T_1}{R_1} = \frac{T_1 - T_0}{R_2} = \frac{T_2 - T_0}{R_1 + R_2} \tag{7}$$

where T_i is the Node i (i=1,2) temperature (K), T_0 is the temperature of the surrounding coolant, R_1 (in K/kW) is the contact resistance between Node 1 and Node 2 and R_2 (in K/kW) is the contact resistance between Node 1 and the coolant. In Eq.(7), q_n, R_2 and T_0 are not known. In the current design, only T_2 is measured. The calibration of the senor is accomplished through the determination of R_2 and T_0. Then q_n can be found from Eq.(7) with the measured q_e, T_2 and known R_1. For calibration, the sensor is temporarily taken out of the control loop (Mode 2 operation), or practically, the supplied electrical current is reduced to 1% of the steady state value in Mode 1 operation. Then R_2 and T_0 can be obtained from the dynamic characteristics of the sensor temperature in decaying back from the steady state value in Mode 1 to its original level through [2]

$$T_{2k} \equiv T_2(t_k) = T_0 + \theta_1 e^{-\theta_2 t_k} + \theta_3 e^{-\theta_4 t_k} \tag{8}$$

In Eq.(8), $T_2(t_k)$ is Node 2 temperature at time t_k The parameters θ_1 through θ_4 are known functions of q_n, q_e, sensor properties and Mode 1 node temperatures. Once θ_1 or θ_4 are estimated, then R_2 can be found from [2]

$$\theta_2 = \frac{1}{2}\left[\gamma + \sqrt{\gamma^2 - 4}\right] \qquad \theta_4 = \frac{1}{2}\left[\gamma - \sqrt{\gamma^2 - 4}\right] \tag{9}$$

with

$$\gamma = \frac{1}{C_1 R_1} + \frac{1}{C_2 R_2} + \frac{1}{C_2 R_1}. \tag{10}$$

For this study, the data T_k with k=1,…,250 were generated using a finite element CTPS model [4]. The noise $\boldsymbol{w_k}$ in Eq.(2) was assumed to be Gaussian noise with mean 0 and the variance was calculated by the sample variance of T_k which was found to be 0.1.

Table 1 below summarizes the results of the comparison of DSD with LSE, MLE and Kalman filters.

Parameter/Estimator	$\hat{\theta}_1$	$\hat{\theta}_2$	$\hat{\theta}_3$	$\hat{\theta}_4$
LSE	5.4854	0.2833	19.6994	2.7906
MLE	5.4825	0.2831	19.7017	2.7897
Kalman Filter	6.9525	0.3464	18.4278	3.2104
DSD (Mode)[1]	5.4326	0.2798	19.6685	2.7865
DSD (Mean)[2]	5.4663	0.2865	19.7247	2.7978

[1]For comparison to LSE and MLE [2]For comparison to Kalman Filter

Table 1. Comparison of the Results for Different Estimators

Table 1 shows that there is good agreement between DSD, LSE and MLE results, as expected. In general, the differences between the DSD, LSE and MLE are small (within 0.1% to 1.2%). The larger differences between the Kalman filter and other estimator results originate from the white Gaussian noise requirement of the Kalman filter. The data generated for the estimation process using the finite difference model of [4] do not necessarily conform to the functional form of Eq.(7). Subsequently, the differences between data behaviour and the functional form of Eq.(7) exhibit themselves as correlated noise.

4 Conclusion

The new theoretical developments show that DSD is equivalent to LSE, MLE and Kalman filter approach for stat/parameter estimation under certain conditions.

The advantage of DSD is that it is both a point and interval estimator whereas the other estimators are only point estimators. In addition, the DSD yields the probability distributions of the estimated quantities over their respective intervals which are useful information for risk informed regulation and risk monitoring of nuclear power plants.

References

1. Wang P, Chen X-M, Aldemir T. DSD: a generic software package for model-based fault diagnosis in dynamic systems. Reliab Engn & System Safety 2002; 28, 31-39
2. Burghalea A, Aldemir T. An application of DSD with recursive partitioning scheme to constant temperature power sensors. These proceedings
3. Wang P. Some improvements in state/parameter estimation using the cell to-cell mapping technique. Ph.D. thesis, The Ohio State University, 2002
4. Radcliff TD, Miller DW, Kauffman AC. Modeling of A Constant-Temperature Power Sensor. In: ICONE-8, Proceedings of 8th International Conference on Nuclear Engineering. American Society of Mechanical Engineers, New York, 2000

Probabilistic Safety Assessment and Management: PSAM 7-ESREL'04,
C. Spitzer, U. Schmocker, V. N. Dang (Eds.), 1809-1814, Springer – Verlag, London, U.K. (June 2004)

The DSD and Conventional State/Parameter Estimation

Peng Wang and Tunc Aldemir
The Ohio State University, 206 West 18th Avenue,
Columbus, OH 43210, U.S.A.

Abstract

The DSD (Dynamic System Doctor) is system independent, state/parameter estimation software that can be used for both point and interval estimation. The DSD also yields useful information for risk informed regulation and risk monitoring of nuclear power plants. The relationship of DSD to some conventional estimation techniques is described and illustrated using a linearized model for the on-line calibration of the constant temperature power sensor, recently proposed for direct core power density distribution measurement in Generation IV reactors.

1 Introduction

The DSD (Dynamic System Doctor) is system independent, state/parameter estimation software [1]. The DSD uses a system representation scheme based on the transition probabilities between user specified computational cells that partition the system state space (cell-to-cell mapping). These transition probabilities are obtained from the user supplied system model. The theoretical basis of the DSD and the current DSD algorithm are described in a companion paper [2]. The main advantage of the DSD over conventional estimators is that DSD is both a point and an interval estimator. In addition, the DSD yields the probability distribution of the system variables/parameters within the estimated bounds which provides a probabilistic measure to rank the likelihood of system faults in view of modeling uncertainties and/or signal noise. Such information is particularly useful for risk informed regulation and risk monitoring of nuclear power plants.

The current DSD algorithm is based on the assumptions that: a) the measurement noise is uniformly distributed, and, b) the measured variables are part of the state variable vector. Recent theoretical developments [3] have extended the applicability range of DSD to arbitrarily distributed (but known) signal noise and modeling uncertainties and arbitrary observers. The new theoretical developments have also provided the framework which clarifies the previously unexplained relationship between DSD and conventional state/parameter estimation techniques. The paper describes and illustrates the relationship of DSD to the generalized maximum likelihood estimator (MLE),

least squares estimator (LSE) and the Kalman filter approach.

2 Overview of the Recent Developments

The extended DSD algorithm accepts system equations of the form

$$\boldsymbol{x}_{k+1} = \tilde{\boldsymbol{x}}(\boldsymbol{x}_k) + \boldsymbol{v}_k \quad (k = 0,1,2,\cdots) \tag{1}$$

and observers of the form

$$\boldsymbol{y}_k = \boldsymbol{h}(\boldsymbol{x}_k) + \boldsymbol{w}_k \quad (k = 0,1,2,\cdots) \tag{2}$$

where

$\boldsymbol{x}$ L-dimensional vector whose elements are the state variables or unknown model parameters x_l $(l = 1,...,L)$ of the dynamic system

$\boldsymbol{v}_k$ system noise at time step $k\tau$ $(k = 0,1,2,...)$ (e.g. due to stochastic variation of system parameters) or a measure of modelling uncertainties, in general

$\boldsymbol{x}_k$ state vector at time step $k\tau$ $(k = 0,1,2,...)$

$\boldsymbol{y}_k$ M-dimensional vector whose elements y_k are the measured data at time step $k\tau$ $(k = 0,1,2,...)$

$\boldsymbol{w}_k$ measurement uncertainty

$\tilde{\boldsymbol{x}}$ a L- dimensional rule that maps $\boldsymbol{x}_k$ onto $\boldsymbol{x}_{k+1}$ (such as by the integration of a set of L ordinary differential equations)

$\boldsymbol{h}$ M - dimensional vector whose elements are known nonlinear functions

The estimation process takes place in the discretized state/parameter space partitioned through the user-defined intervals

$$\Delta_{l,j_l} = \{x_l : a_{l,j_l} \le x < a_{l,j_l+1}; a_{l,1} = a_l, a_{l,J_l} = b_l\} \tag{3}$$
$$j_l = 1,...,J_l; l = 1,...,L.$$

The specification of these intervals may be, for example, based on the uncertainty/noise in the monitored x_l. The Δ_{l,j_l} constitute the computational cells $\boldsymbol{V}_j = \{\Delta_{1,j_1}, \Delta_{2,j_2}, ...\Delta_{L,j_L}\}$ $(j = 1,...,J = \prod_{l=1}^{L} J_l)$ which partition the

range of interest $a_l \le x_l \le b_l (l = 1,...,L)$ in the state/parameter space in a similar manner to those used by finite difference and finite element methods. If $\boldsymbol{j} = \{j_1 j_2 ... j_L\}$ denotes the location of the cell $\boldsymbol{V}_j$ in the discretized state-space, then it can be shown that [3] the probability

$$p(\boldsymbol{j}_k | \bar{\boldsymbol{y}}_k) = \int_{\boldsymbol{j}_k} p(\boldsymbol{x}_k | \bar{\boldsymbol{y}}_k) d\boldsymbol{x}_k \tag{4}$$

of finding the system in the cell $\boldsymbol{j}_k$ at time $t = k\tau$ is recursively calculated from

$$p(\boldsymbol{j}_{k+1} | \bar{\boldsymbol{y}}_{k+1}) = \frac{\sum_{\boldsymbol{j}_k} g(\boldsymbol{j}_{k+1} | \boldsymbol{j}_k) p(\boldsymbol{j}_k | \bar{\boldsymbol{y}}_k)}{\sum_{\boldsymbol{j}_{k+1}} \sum_{\boldsymbol{j}_k} g(\boldsymbol{j}_{k+1} | \boldsymbol{j}_k) p(\boldsymbol{j}_k | \bar{\boldsymbol{y}}_k)} \tag{5}$$

$$g(\boldsymbol{j}_{k+1} | \boldsymbol{j}_k) = \iint_{\boldsymbol{j}_{k+1}, \boldsymbol{j}_k} p(\boldsymbol{y}_{k+1} | \boldsymbol{x}_{k+1}) p(\boldsymbol{x}_{k+1} | \boldsymbol{x}_k) \frac{p(\boldsymbol{x}_k | \bar{\boldsymbol{y}}_k)}{\int_{\boldsymbol{j}_k} p(\boldsymbol{x}_k | \bar{\boldsymbol{y}}_k) d\boldsymbol{x}_k} d\boldsymbol{x}_k d\boldsymbol{x}_{k+1} \tag{6}$$

where $g(\boldsymbol{j}_{k+1} | \boldsymbol{j}_k)$ is the probability that the system will move from cell $\boldsymbol{j}_k$ to cell $\boldsymbol{j}_{k+1}$ during $k\tau \le t < (k+1)\tau$. It can be also shown that [3]:

1. Eqs.(5) and (6) constitute a recursive Bayesian estimator (the original DSD algorithm is based on the Chapman-Kolmogorov equation),
2. if $\boldsymbol{j}_{s,k}$ denotes the actual cell the system is in at time $t = k\tau$ and $g(\boldsymbol{j}_{k+1} | \boldsymbol{j}_k) < g(\boldsymbol{j}_{s,k+1} | \boldsymbol{j}_k)$ for all $\boldsymbol{j}_{k+1} \ne \boldsymbol{j}_{s,k+1}$, $p(\boldsymbol{j}_{k+1} | \bar{\boldsymbol{y}}_{k+1})$ converges to the correct cell $\boldsymbol{j}_{s,k+1}$ irrespective of the initial distribution used, and,
3. if
   - $\boldsymbol{v}_k = 0$ for all $k = 0,1,2,\cdots$,
   - the probability $p(\boldsymbol{x}_k | \bar{\boldsymbol{y}}_k)$ is uniform over each cell $\boldsymbol{j}_k$,
   - $\boldsymbol{h}(\boldsymbol{x}_k) = \boldsymbol{x}_k$,
   - the integrals in Eq.(6) are approximated by a quadrature scheme,

   Eqs.(5) and (6) reduce to the current DSD algorithm [2].

The $p(\boldsymbol{j}_k | \bar{\boldsymbol{y}}_k)$ from Eq.(5) can be used to find all the statistical properties of the variables to be estimated at times $t = k\tau$, including expected values, standard deviations and credibility intervals. Item 3 above indicates the limitations of the current DSD algorithm with respect to Eqs.(5) and (6). Item 1 implies that [3]

1. For constant $\boldsymbol{x}_k = \boldsymbol{\theta}$ $(k = 0,1,\cdots)$, the mode of $p(\boldsymbol{\theta} | \bar{\boldsymbol{y}}_k)$ yields the maximum likelihood estimate (MLE) of $\boldsymbol{\theta}$.

2. If in Eq.(1) and $\boldsymbol{w}_k$ in Eq.(2) are both white Gaussian noise and Eq.(1) originates from a linear model for the evolution of $\boldsymbol{x}$, then the mean and covariance of $p(\boldsymbol{x}_k|\bar{\boldsymbol{y}}_k)$ obtained from Eq.(6) are equivalent to those obtained from a Kalman filter.
3. The mean of $p(\boldsymbol{\theta}|\bar{\boldsymbol{y}}_k)$ is also the least-squares estimate (LSE) of $\boldsymbol{\theta}$.

These implications are illustrated below using a linearized version of the model in [2] for the on-line calibration of the constant temperature power sensor (CTPS), proposed for direct core power density distribution measurement in Generation 4 reactors.

3 Implementation and Results

The CTPS [2] can directly measure the local nuclear energy deposition and heat transfer rate. This design concept is based on the idea of adding heat through resistive dissipation of input electrical energy to a small mass of actual reactor fuel pellet analogue which constitutes the sensor core (Node 2). The core is surrounded by ceramacast, which is an alumina based ceramic thermal insulator (Node 1). In Mode 1 operation, Node 2 is kept at constant temperature T_2 by providing the exact amount of input electrical energy q_e (in kW) through a feedback control loop irrespective of the nuclear energy q_n (in kW) generated in Node 2. At steady state [2]

$$q_e + q_n = \frac{T_2 - T_1}{R_1} = \frac{T_1 - T_0}{R_2} = \frac{T_2 - T_0}{R_1 + R_2} \tag{7}$$

where T_i is the Node i (i=1,2) temperature (K), T_0 is the temperature of the surrounding coolant, R_1 (in K/kW) is the contact resistance between Node 1 and Node 2 and R_2 (in K/kW) is the contact resistance between Node 1 and the coolant. In Eq.(7), q_n, R_2 and T_0 are not known. In the current design, only T_2 is measured. The calibration of the senor is accomplished through the determination of R_2 and T_0. Then q_n can be found from Eq.(7) with the measured q_e, T_2 and known R_1. For calibration, the sensor is temporarily taken out of the control loop (Mode 2 operation), or practically, the supplied electrical current is reduced to 1% of the steady state value in Mode 1 operation. Then R_2 and T_0 can be obtained from the dynamic characteristics of the sensor temperature in decaying back from the steady state value in Mode 1 to its original level through [2]

$$T_{2k} \equiv T_2(t_k) = T_0 + \theta_1 e^{-\theta_2 t_k} + \theta_3 e^{-\theta_4 t_k} \tag{8}$$

In Eq.(8), $T_2(t_k)$ is Node 2 temperature at time t_k The parameters θ_1 through θ_4 are known functions of q_n, q_e, sensor properties and Mode 1 node temperatures. Once θ_1 or θ_4 are estimated, then R_2 can be found from [2]

$$\theta_2 = \frac{1}{2}\left[\gamma + \sqrt{\gamma^2 - 4}\right] \qquad \theta_4 = \frac{1}{2}\left[\gamma - \sqrt{\gamma^2 - 4}\right] \tag{9}$$

with

$$\gamma = \frac{1}{C_1 R_1} + \frac{1}{C_2 R_2} + \frac{1}{C_2 R_1}. \tag{10}$$

For this study, the data T_k with k=1,…,250 were generated using a finite element CTPS model [4]. The noise $\boldsymbol{w_k}$ in Eq.(2) was assumed to be Gaussian noise with mean 0 and the variance was calculated by the sample variance of T_k which was found to be 0.1.

Table 1 below summarizes the results of the comparison of DSD with LSE, MLE and Kalman filters.

Parameter/Estimator	$\hat{\theta}_1$	$\hat{\theta}_2$	$\hat{\theta}_3$	$\hat{\theta}_4$
LSE	5.4854	0.2833	19.6994	2.7906
MLE	5.4825	0.2831	19.7017	2.7897
Kalman Filter	6.9525	0.3464	18.4278	3.2104
DSD (Mode)[1]	5.4326	0.2798	19.6685	2.7865
DSD (Mean)[2]	5.4663	0.2865	19.7247	2.7978

[1]For comparison to LSE and MLE [2]For comparison to Kalman Filter

Table 1. Comparison of the Results for Different Estimators

Table 1 shows that there is good agreement between DSD, LSE and MLE results, as expected. In general, the differences between the DSD, LSE and MLE are small (within 0.1% to 1.2%). The larger differences between the Kalman filter and other estimator results originate from the white Gaussian noise requirement of the Kalman filter. The data generated for the estimation process using the finite difference model of [4] do not necessarily conform to the functional form of Eq.(7). Subsequently, the differences between data behaviour and the functional form of Eq.(7) exhibit themselves as correlated noise.

4 Conclusion

The new theoretical developments show that DSD is equivalent to LSE, MLE and Kalman filter approach for stat/parameter estimation under certain conditions.

The advantage of DSD is that it is both a point and interval estimator whereas the other estimators are only point estimators. In addition, the DSD yields the probability distributions of the estimated quantities over their respective intervals which are useful information for risk informed regulation and risk monitoring of nuclear power plants.

References

1. Wang P, Chen X-M, Aldemir T. DSD: a generic software package for model-based fault diagnosis in dynamic systems. Reliab Engn & System Safety 2002; 28, 31-39
2. Burghalea A, Aldemir T. An application of DSD with recursive partitioning scheme to constant temperature power sensors. These proceedings
3. Wang P. Some improvements in state/parameter estimation using the cell to-cell mapping technique. Ph.D. thesis, The Ohio State University, 2002
4. Radcliff TD, Miller DW, Kauffman AC. Modeling of A Constant-Temperature Power Sensor. In: ICONE-8, Proceedings of 8th International Conference on Nuclear Engineering. American Society of Mechanical Engineers, New York, 2000

Trans. Am. Nucl. Soc., 92, 555-557 (June 2005)

Representation of Measurement Uncertainty in Flux/Power Shape Construction From Monitored Data

Aram Hakobyan, Mihaela Biro, Tunc Aldemir

The Ohio State University, Nuclear Engineering Program,
Bldg 1, Rm 130B, Suite 255, 650 Ackerman Road, Columbus, OH 43202

INTRODUCTION

Different techniques have been developed and used to predict the flux/power density between measurement points, namely, using cubic splines to interpolate between measured data [1], fittings by modal expansions [2, 3], artificial neural networks [4], and, finally, least-square fittings [5]. Also, there have been few attempts to directly incorporate the measurement uncertainty into the flux/power shape reconstruction process [6-9].

Recent work [8,9] has described such a one-dimensional (1-D) reconstruction procedure which leads to computational simplicity when there are a large number of observations. This procedure can be also used with a wide range of fitting schemes, from simple linear interpolation between data points to model based fittings, as well as a variety of probability distribution functions (pdfs) to represent the measurement uncertainty.

The objective of this paper is to demonstrate that the 1-D procedures of [8] and [9] can be used for three dimensional (3-D) power/flux shape construction by decomposing the reconstruction process into three 1-D problems locally.

PROCEDURE

Consider a cube whose vertices are detector locations and which also contains another detector at its center. We will assume that thermal neutron flux/power density satisfies the Helmholtz equation within the cube, i.e.

$$\nabla^2\varphi(\boldsymbol{r})+B^2\varphi(\boldsymbol{r})=0 \tag{1}$$

where the vector $\boldsymbol{r}$ denotes the spatial location within the cube and

$$B^2=\frac{\left[\nu\frac{\Sigma_{f,1}}{\Sigma_{a,1}}-1\right]\Sigma_{a,1}+\left[\nu\frac{\Sigma_{f,2}}{\Sigma_{a,2}}-1\right]\Sigma_{1\to 2}}{D_1} \tag{2}$$

for 1 ½ group diffusion theory representation of the flux/power distribution under uniform material composition within the cube (e.g. through a homogenization process). The symbols in Eq.(2) have their conventional definitions. The solution of Eq.(1) using separation of variables yields

$$\begin{aligned}&\left[A_1\cos(B_x x_i)+C_1\sin(B_x x_i)\right]\times\\&\left[A_2\cos(B_y y_i)+C_2\sin(B_y y_i)\right]\times\\&\left[A_3\cos(B_z z_i)+C_3\sin(B_z z_i)\right]=\phi_i\end{aligned} \tag{3}$$

where ϕ_i is the measured flux/power density at detector location i = 1,…,9 and x_i, y_i, z_i are the coordinates of the measurement point i. The other quantities in Eq.(3) are arbitrary constants. These constants are determined from the system of 9 non-linear equations given by Eq(3) using non-linear least squares estimation and the mean values of the measured pdfs for ϕ_i (e.g. by taking repeated measurements for steady-state operation or for slow transients or using the procedure described in [10]). Once these constants are determined, then two methods can be used to move to the probabilistic domain and interpolate between the measured pdfs. Method 1 [8] assumes that the expected value $\varphi(s)$ of the flux/power at a point $0\le s\le d$ between two detector locations i and j satisfies again the Helmholtz equation

$$\nabla^2\varphi(s)+B^2\varphi(s)=0 \tag{4}$$

with ϕ_i and ϕ_j as boundary conditions and: a) $B = B_x$, B_y ,B_z if the detectors are placed on the x-, y-and z-edges of the cube, respectively, b) $B^2=B_x^2+B_y^2$, $B^2=B_x^2+B_z^2$ and $B^2=B_y^2+B_z^2$ if the detectors are placed on the diagonals of the x-y, x-z and y-z surfaces of the cube, respectively, and, c) $B^2=B_x^2+B_y^2+B_x^2$ if the detectors are placed on the diametrically opposite vertices of the cube. For Eq.(4) with ϕ_i and ϕ_j as boundary conditions it can be shown that [8]

$$p(\phi\,|\,w)=\frac{1}{\sin(B)}\begin{bmatrix}p(\phi_i\,|\,0)\sin[B(1-w)]\\+p(\phi_j\,|\,1)\sin(Bw)\end{bmatrix} \tag{5}$$

with $w = s/d$ ($w=0$ at location i), where $p(\phi\,|\,w)$ is the pdf of ϕ at w. Method 2 [9] imposes the additional condition

$$F=\int_0^{\phi_i}d\phi' p(\phi'\,|\,0)=\int_0^{\phi_j}d\phi' p(\phi'\,|\,1)=\int_0^{\phi}d\phi' p(\phi'\,|\,w) \tag{6}$$

for all w, where ϕ_i, ϕ_j and ϕ denote the corresponding quantities in Eq.(5) for specified $0 \le F \le 1$.

IMPLEMENTATION

The hypothetical assembly considered for illustration was a 300X300X300 cm homogeneous cube, placed in vacuum and with diffusion parameters as given in [8]. The overall flux distribution in the cube was determined analytically from Eqs.(1) and (2). Then the ϕ_i in Eq.(3) were determined from this flux distribution for a 30X30X30 cm virtual test cube randomly placed in the assembly.

The comparison of the overall flux/power distribution (S1) with the flux/power distribution obtained from the solution of Eq.(3) (S2) was carried out for a fixed plane 10cm above the mid *x-y* plane. Figure 1 below shows that the maximum relative error (S1-S2)/S1 did not exceed 0.8%.

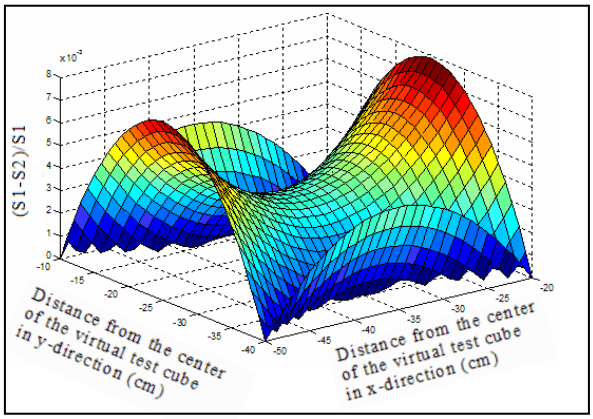

Fig.1: Relative error (S1-S2)/S1 10cm above the mid *x-y* plane of the virtual test cube

Figure 2(a) shows comparison of the solutions obtained from Eqs.(3) and (4) for the *x-y* diagonal on the same plane and indicates good agreement (less than 2.5%) difference between the 3-D and 1-D solutions.

For the $p(\phi \mid w)$, it was assumed that the $p_i(\phi)$ and $p_j(\phi)$ in Eq.(5) are Gaussian with means equal to ϕ_i and ϕ_j, respectively, and 1% standard deviation. Figures 2(b) and 2(c), respectively, show the $p(\phi \mid w)$ obtained from Method 1 and Method 2. The bimodal nature of the pdf obtained from Method 1 in Fig.2(b) and the low probability region between detector locations reflects the large uncertainty in the flux value due to lack of observation in this region. Note that expected value in Fig.2 (b) is still very similar to the local 3D solution shown in Fig.2 (a).

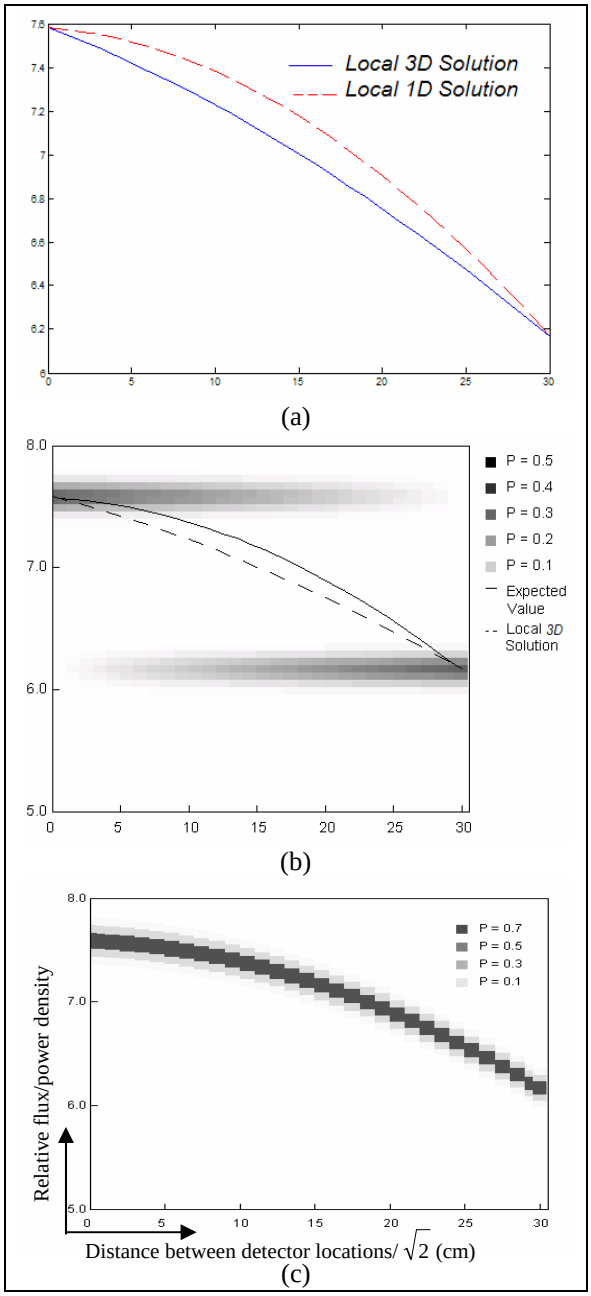

Fig.2: Flux comparison for the *x-y* diagonal direction (a) and corresponding $p(\phi \mid w)$ obtained from Method 1 (b) and Method 2 (c)

The difference between Fig.2(b) and 2(c) results is due to the condition imposed by Eq.(6) which assumes that the cumulative probability distribution of flux/power density is conserved between detector locations. Another interpretation

of this assumption is that the uncertainty in flux/power at the detector locations also propagates according to Eq.(4) between detector locations. The assumption is justified if the uncertainty originates from possible flux/power fluctuations but not if it originates from electronic noise in the detection hardware.

CONCLUSION

This study shows that uncertainty on the flux/power density between detector locations in a 3-D problem can be quantified by:

- locally decomposing in flux/power density construction into three 1-D problems, and,
- using Method 1 or Method 2.

It is not clear at this point in time whether Method 1 or 2 should be the method of choice. Work is underway to study Methods 1 and 2 with simulated data obtained from actual production codes.

REFERENCES

1. S. HAN, U. S. KIM, P. H. SEONG "A Methodology for Benefit Assessment of Using In-core Neutron Detector Signals in Core Protection Calculator System (CPCS) for Korea Standard Nuclear Power Plants (KSNPP)", *Annals of Nuclear Energy*, **26**, 471-488 (1999).
2. M. E. Pomerantz, C.R. Calabrese, C. Grant, "Nuclear Reactor Power and Flux Distribution Fitting from a Diffusion Theory Model and Experimental Data", *Annals of Nuclear Energy*, **29,** 1073–1083 (2002).
3. L. Fu, L. Zhengpei, H. Yongming "Harmonics Synthesis Method for Core Flux Distribution Reconstruction", *Progress in Nuclear Energy*, **31**, 369-372 (1997).
4. G.-C. Lee, W-P. Baek, S. H. Chang. "Improved Methodology for Generation of Axial Flux Shapes in Digital Core Protection Systems", *Annals of Nuclear Energy*, **29**, 805–819 (2002).
5. K. Lee, C. H. Kim, "The Least-Squares Method for Three-Dimensional Core Power Distribution Monitoring in Pressurized Water Reactors"**,** *Nucl.Sci.Eng*, **143,** 268 (2003).
6. J. W. Bryson, J. C. Lee, and J. A. Hassberger, "Optimal Flux Map Generation Through Parameter Estimation Techniques", *Nucl.Sci.Eng*, **114**, 238 (1993).
7. R.A. Bonalumi, N.P.Kherani "Rational Mapping (RAM) of In-Core Data", *Nucl.Sci.Eng*, **90**, 47 (1985).
8. M. Biro, T. Aldemir, "A Model Based Probabilistic Scheme for Flux/Power Shape Construction from Monitored Data**",** *Trans. Am. Nucl. Soc*., **90,** 59-61 (June 2004)
9. M. Biro, T. Aldemir, "Quantifying The Measurement Uncertainty Propagation In Flux/Power Reconstruction", *Proceedings of NPIC&HMIT 2004*, 1246-1253, American Nuclear Society, LaGrange Park, IL (September 2004)
10. A. Burghelea, T. Aldemir, "An Application of DSD with Recursive Partitioning Scheme to Constant Temperature Power Sensors", *Probabilistic Safety Assessment and Management: PSAM 7-ESREL'04*, C. Spitzer, U. Schmocker, V. N. Dang (Eds.), 1821-1827, Springer – Verlag, London, U.K. (June 2004)

Space Technology and Applications International Forum—STAIF 2004,
M. S. El-Genk (Ed.), 582-589, American Institute of Physics, Melville, N.Y. (February 2004)

Direct Estimation of Power Distribution in Reactors for Nuclear Thermal Space Propulsion

Tunc Aldemir, Don W. Miller, and Andrei Burghelea

The Ohio State University, Nuclear Engineering Program, 206 West 18th Avenue, Columbus, Ohio 43210
(614)292-4627; aldemir.1@osu.edu

Abstract. A recently proposed constant temperature power sensor (CTPS) has the capability to directly measure the local power deposition rate in nuclear reactor cores proposed for space thermal propulsion. Such a capability reduces the uncertainties in the estimated power peaking factors and hence increases the reliability of the nuclear engine. The CTPS operation is sensitive to the changes in the local thermal conditions. A procedure is described for the automatic on-line calibration of the sensor through estimation of changes in thermal .conditions.

INTRODUCTION

Substantial effort has been spent since the 1950s on the design and testing of highly enriched uranium fuelled, graphite moderated reactor cores for nuclear thermal space propulsion. Due to their compact size and high operating temperatures, very strong coupling exists between the nuclear and thermal hydraulic behavior of such cores (Aithal, Aldemir, and Vafai, 1994). Accurate modeling of this coupling in both ground testing of the cores and in-flight operation is usually difficult because of the uncertainties in local material compositions, coolant flow paths, reactor operation history and possibly nuclear data. On the other hand, accurate prediction of core power distribution is important to determine the local power peaking factors and hence the operating limits of the nuclear engine. A recently proposed constant temperature power sensor (CTPS) (Radcliff, Miller, and Kauffman, 2000a) has the capability to measure local core power directly. While the measurement process is sensitive to local temperature and flow variations, such variations can be accounted for using the estimation procedure DSD (Dynamic System Doctor) (Wang, Chen, and Aldemir, 2002). This paper describes how the CTPS-DSD combination can be applied to space reactors for accurate prediction of core power distribution. Three important features of the CTPS-DSD combination for space reactors are the following:

- The sensor core can blend with the fuel matrix of a number of reactor concepts proposed for nuclear thermal propulsion, such as the particle bed concept (Powell et al., 1991) or cermet fuel (Kruger, 1991), reducing material compatibility problems at high temperatures and high temperature gradients.
- The measurement procedure is self-calibrating. This feature is particularly important for space reactors where sensor calibration though external means may not be feasible.
- The measurement process yields point estimates for the power densities as well as credibility intervals for these point estimates so that the uncertainty in the estimated quantities is an automatic output of the estimation process. Such data provide useful inputs for pre-launch determination mission reliability and for decision making during the mission.

THE SENSOR

As designed for testing purposes, the sensor consists of a fuel pellet surrounded by electrical heating resistance wire (see Fig.1). (Radcliff, Miller, and Kauffman, 2000a) The pellet and the wire form the sensor core (Node 2). The core is surrounded by ceramacast which is an alumina based ceramic thermal insulator (Node 1). Both the sensor core and the insulator are coated with thin layers of copper. A feedback control loop is used to provide the exact

amount of input electrical energy q_e needed to keep Node 2 temperature T_2 constant in time t, well above the ambient temperature T_0, regardless of nuclear energy deposited (q_n). The CTPS is ideally suited for use in the proposed nuclear thermal space systems in which the sensors need to be an integral part of the core for the mission duration and where sensor calibration though external means may not be feasible.

The sensor operation involves switching between the feedback-controlled constant-temperature mode (Mode 1) and the dynamic temperature decay mode following the opening of the feedback loop (Mode 2) as described by (Burghelea and Aldemir, 2003; Liu, Miller, Li, and Radcliff, 2002; Radcliff, Miller, and Kauffman, 2000a)

$$\begin{aligned} C_1 \frac{dT_2}{dt} &= (q_n + q_e) - \frac{1}{R_1}(T_2 - T_1), \\ C_2 \frac{dT_1}{dt} &= \frac{1}{R_1}(T_2 - T_1) - \frac{1}{R_2}(T_1 - T_0), \\ \frac{1}{R_1} &= \frac{2\pi k(T_2)[h_s - 2(r_o - r_i)]}{\log\left(\frac{r_o}{r_i}\right)} + \frac{2\pi k(T_2)(r_o^2 - r_i^2)}{[h_s - 2(r_o - r_i)]}. \end{aligned} \tag{1}$$

Equation (1) has been validated against the results from a finite element code (Liu, Miller, Li, and Radcliff, 2002).

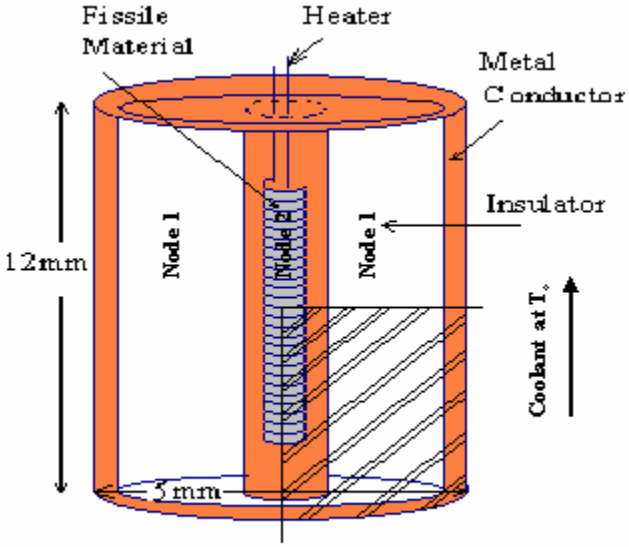

FIGURE 1. The Constant Temperature Power Sensor.

At steady-state Eq.(1) yields:

$$q_n + q_e = \frac{1}{R_2}(T_1 - T_0), \tag{2}$$

which corresponds to the constant temperature mode (i.e. Mode 1) operation of the CTPS. Under linearity assumptions Eq.(1) yields for Mode 2

$$T_2(t) = \theta_0 + \theta_1 e^{-\theta_2 t} + \theta_3 e^{-\theta_4 t}, \tag{3}$$

where θ_0 through θ_4 are known functions of T_0, $T_2(0)$ and the parameters of Eq.(1). In the implementation, C_1, C_2, R_1 in Eq.(1) are assumed to be known. The estimation of q_n consists of the following steps:

1. In Mode 1, measure q_e, $T_1(0)$ and $T_2(0)$
2. Switch to Mode 2 and measure $T_1(t)$, $T_2(t)$
3. Assume a value q_n' for nuclear energy deposition rate.
4. Estimate T_0 and R_2 from Eq.(1) or θ_0 through θ_4 from Eq.(3) using Step 1 through Step 3 results and the estimation software described in the next section. Once θ_0 through θ_4 are estimated, T_0 and R_2 can be determined from these estimates and given C_1, C_2 and R_1 (Radcliff, Miller, and Kauffman, 2000b).
5. Determine q_n from Eq.(2) using Step 4 results.
6. Compare q_n from Step 5 to its Step 3 value q_n'.
7. If $(q_n - q_n')/q_n < 0.01$ stop (convergence), otherwise go to Step 3 with $q_n' = q_n$.

Steps 1 though 4 account for changes in the local temperature and flow variations which affect T_0 and R_2 in Eq.(1) and hence are equivalent to the on-line calibration of the sensor

THE ESTIMATON SOFTWARE

The DSD is based on the representation of the system dynamics in terms of transition probabilities between user specified cells that partition the system parameter/state space during user specified time intervals $k\tau \le t \le (k+1)\tau$ (k = 0, 1, 2, ...), such as between data sampling times. These cells are obtained by partitioning the range of interest $a_l \le x_l \le b_l$ for the state variable $x_l (l = 1, \cdots, L)$ into $j_l = 1, \cdots, J_l - 1$ intervals $a_{l,j_1} \le x < a_{l,j_l+1}$ and the range of interest $\widetilde{a}_m \le \alpha_m \le \widetilde{b}_m$ for the parameter $\alpha_m (m = 1, \cdots, M)$ into $n_m = 1, \cdots, N_m - 1$ intervals $\widetilde{a}_{m,n_m} \le x < \widetilde{a}_{m,n_m+1}$, in a manner similar to those used in finite difference or finite difference methods. The partitionings are provided as user input to DSD. The DSD recursively computes the probability $p_k(j, n \mid J_k)$ that the state variables (e.g. $T_1(t)$, $T_2(t)$) are in cell j ($j = 1,...J=J_1J_2...J_L$) and the unknown parameters (e.g. R_2, T_0) are in cell n ($n = 1,...,N=N_1N_1...N_M$) during $k\tau \le t \le (k+1)\tau$, given that the possible set of cells the state variables can be in at this time is J_k (as observed from the monitored data), from

$$
\begin{aligned}
p_k^*(j,n) &\equiv p_k(j,n \mid J_k) \\
&= \frac{p_k(j,n)}{\sum_{j' \in J_k} \sum_{n'} p_k(j',n')} \quad (j \in J_k), \\
p_k(j,n) &= \sum_{j' \in J_{k-1}} g(j \mid j', n) p_{k-1}^*(j',n'),
\end{aligned}
\tag{4}
$$

where

$$g(j \mid j', n') =$$

$$\begin{cases} \int_{a_1, j_1}^{a_1, j_1+1} \frac{dx'_1}{a_{1,j'_1+1} - a_{1,j'_1}} e_{j_1}(\tilde{\boldsymbol{x}}(\boldsymbol{x}', \boldsymbol{\alpha}_{n'}, \tau)) \ldots \int_{a_L, j_L}^{a_L, j_{L1}+1} \frac{dx'_L}{a_{L,j'_L+1} - a_{L,j'_L}} e_{j_{L1}}(\tilde{\boldsymbol{x}}(\boldsymbol{x}', \boldsymbol{\alpha}_{n'}, \tau)), \\ \quad \text{if} \quad a_l \le x'_l \le b_l \\ \quad 0 \quad \text{otherwise} \end{cases} \tag{5}$$

with

$$e_{j_l} = \begin{cases} 1 & \text{if} \quad a_{1,j_1} \le x \le a_{1,j_1+1}, \\ 0 & \text{otherwise} \end{cases} \tag{6}$$

is the transition probability from state variable cell j' to state variable cell j during the period $k\tau \le t \le (k+1)\tau$ while the system parameters remain within cell n'. The quantity $\tilde{\boldsymbol{x}}(\boldsymbol{x}', \boldsymbol{\alpha}_{n'}, \tau)$ in Eq.(5) indicates the arrival point in the state-space at time $(k+1)\tau$ of the trajectory that has departed at time $k\tau$ from point $\boldsymbol{x}'$ in cell j' with the system parameters at $\boldsymbol{\alpha}_{n'}$ within cell n', as determined from a user provided system model (e.g. Eq.(1)). In applications, the $g(j \mid j', n)$ are usually approximated using a $\tilde{j}'$ -point quadrature scheme, i.e.

1) at time $k\tau$, selecting randomly or otherwise (e.g. equidistant) $\tilde{j}'$ starting points from cell j' for a given n,

2) from the user provided system model, find the number $\tilde{j}$ of trajectories that arrive within cell j at $t = (k+1)\tau$ (e.g. by integrating Eq.(1) over $k\tau \le t \le (k+1)\tau$ for each of the $\tilde{j}'$ initial conditions), and,

3) letting $g(j \mid j', n) = \tilde{j} / \tilde{j}'$.

A graphical illustration of this process, along with an example partitioning scheme, is shown in Fig.2 for a second order system where only one state variable is monitored. Some sufficient conditions for the convergence of Eq.(4) are given in (Wang and Aldemir, 1999) An important advantage of DSD is that it yields point estimates of the system variables to be determined as well as credibility intervals for these point estimates (i.e. state variable and parameter ranges inferred from j and n with $p_k(j, n) \ne 0$) so that the uncertainty in the estimated quantities is an automatic output of the estimation process.

IMPLEMENTATION

The example nuclear thermal propulsion reactor concept chosen to illustrate the utilization of the CTPS/DSD combination is the particle bed reactor (PBR) concept used in (Aithal, Aldemir, and Vafai, 1994). Figures 3 and 4, respectively, show a horizontal cross section of the reactor core and an axial cross section of a PBR fuel element. The PBR uses fuel in the form of small diameter particles (100-500 μm) which consist of a highly enriched uranium kernel surrounded by multiple layers of pyrographite and sometimes additional ZrC or SiC layers. The fuel particles are held between two porous annuli ("frits") to form a fuel element (Fig.4) and the fuel elements are embedded in the moderator block in concentric rings to form the core (Fig.3). The moderator block is surrounded by a pressure vessel, reflected radially and axially for neutron economy. Hydrogen pumped from the propellant tank flows through an annulus located between the radial reflector and the pressure vessel before entering the core. After

entering the core, the coolant first passes through the outer cold frit (Zircaloy 2), then directly over the fuel particles and finally through the inner hot frit (ZrC) into the outlet plenum to be ejected through a nozzle to develop thrust. Partial reactivity control is achieved by varying the hydrogen mass flow rate in the annulus.

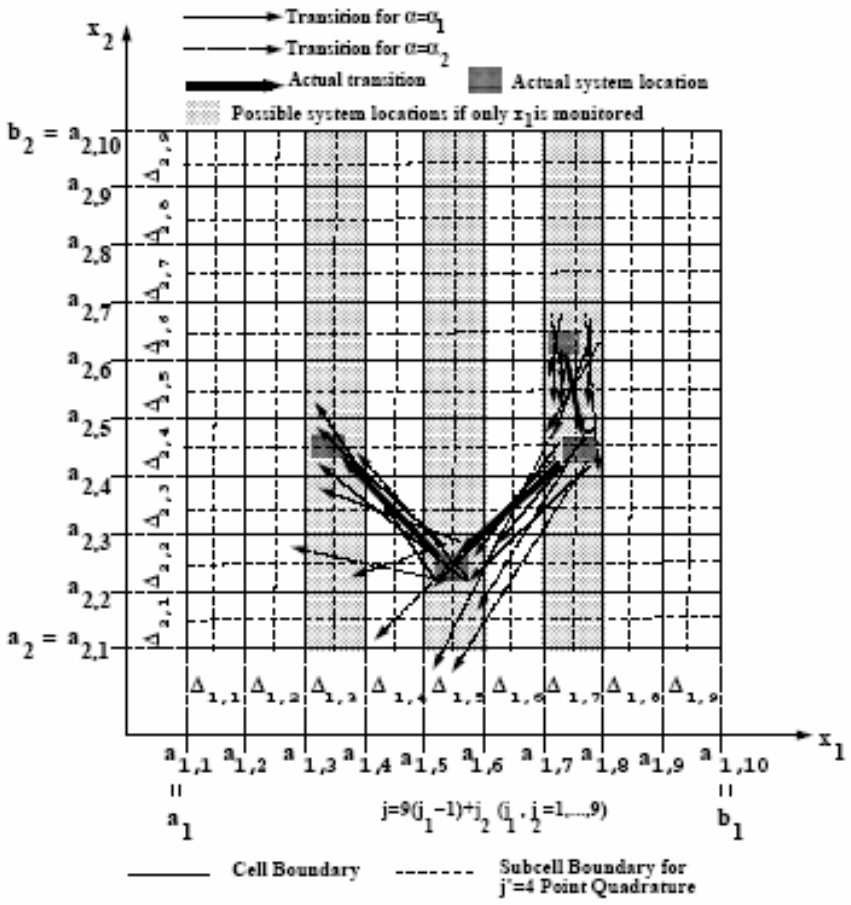

$$g(58 \mid 29,1) = 3/4 = 0.75,\ g(58 \mid 29,2) = 0,\ g(29 \mid 22,1) = 2/4 = 0.5,\ g(29 \mid 22,2) = 1/4 = 0.25$$

FIGURE 2. An example partitioning scheme and the illustration of the approximation of *g(j| j', n)* for a hypothetical dynamical system with two state variables x_1, x_2 and one parameter α. The system is in cells $j = 9(j_1 - 1) + j_2 = 60,58,29,22$ at times $k\tau, (k+1)\tau, (k+2)\tau, (k+3)\tau$ respectively. If only x_1 is monitored, the set of possible cells the system can be in are $J_k = J_{k+1} = \{j = 55, \ldots, 63\}$, $J_{k+2} = \{j = 37,\ldots,45\}$ and $J_{k+3} = \{j = 10, \ldots, 18\}$ (adapted from Dinca, 1997).

For the PBR application, the CTPS is assumed to be imbedded in the fuel element between the hot and cold frit with sensor core (i.e. Node 2 in Fig.1) consisting of the same type of particles used in the fuel elements. For the purposes of this illustration, the sensor heater wire and the Node 1 and 2 metal coatings were assumed to be tungsten. Table 1 shows the example power and temperature data used for the illustration. The data in Table 1 have been generated with the MCNP (Breimeister, 1989) and HEATING-5 (Turner, Elrod, and Siman-Tov, 1977) codes. Figure 5 shows the results of the estimation using DSD, assuming that the monitored variables are $T_1(t), T_2(t)$ and $q_e(t)$. The bars in Fig.5 indicate 100% credibility intervals. The data for the estimation process was simulated using Eq.(1) with 1% noise in the monitored variables. Figure 5 indicates that the credibility intervals contain the actual (i.e. simulated data) and also quantify the uncertainty in the estimation process.

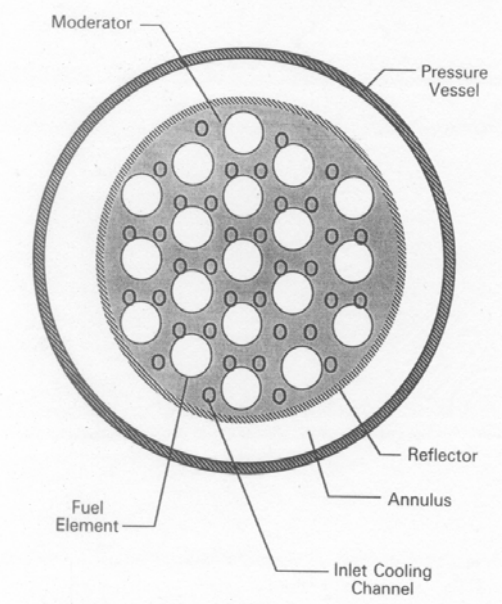

FIGURE 3. The Particle Bed Reactor Core (Aithal, Aldemir, and Vafai, 1994).

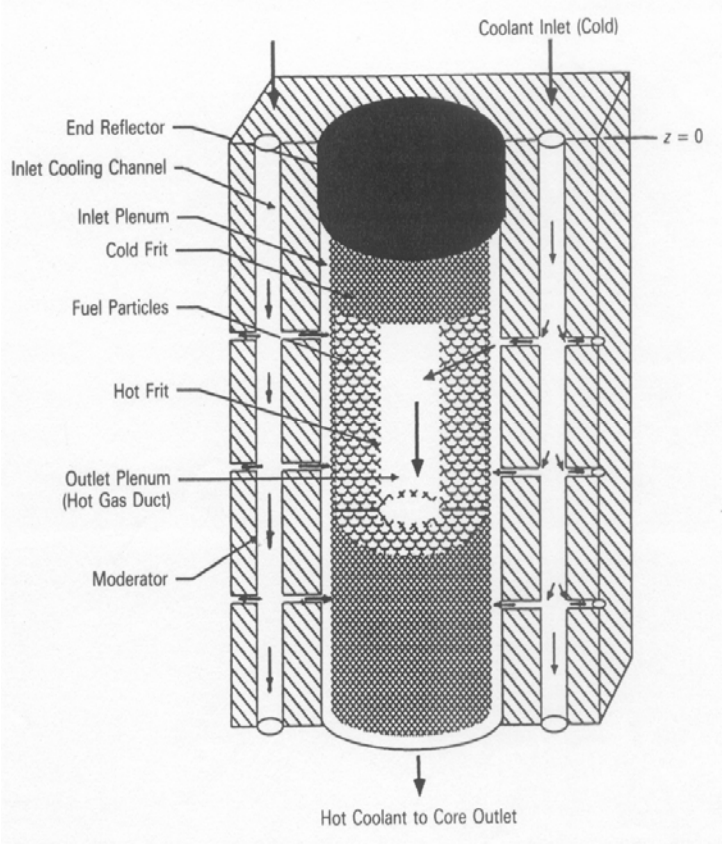

FIGURE 4. A Particle Bed Reactor Fuel Element (Aithal, Aldemir, and Vafai, 1994).

TABLE 1. Example Power and Temperature Data for the Particle Bed Reactor (Aithal, Aldemir, and Vafai, 1994).

Distance from Coolant Inlet (cm)	Power Density q_n (W/cm^3)	Solid Temperature $T_1(0)=T_2(0)$ (K)	Coolant Temperature (K)
5	960	480	455
10	1440	635	610
20	1888	1230	1208
30	2040	1580	1560
40	1888	2104	2085
50	1456	2521	2503
55	976	2968	2950

CONCLUSION

Obtaining accurate power profiles in both ground testing and in-flight operation or reactor cores for nuclear thermal propulsion is usually difficult because the strong neutronic-thermal hydraulic coupling of the cores and uncertainties in local material compositions, coolant flow paths, reactor operation history and possibly nuclear data. This study shows that using CTPS modeled through Eq.(1) and DSD may be a feasible option to obtain direct estimates of the power distribution as well as quantifying the uncertainty in the estimated power profiles. The advantages of the CTPS-DSD combination with respect to space reactors are: a) it reduces material compatibility problems at high

temperatures and high temperature gradients, b) the measurement procedure is self-calibrating, and, c) it provides useful inputs for pre-launch determination mission reliability and for decision making during the mission.

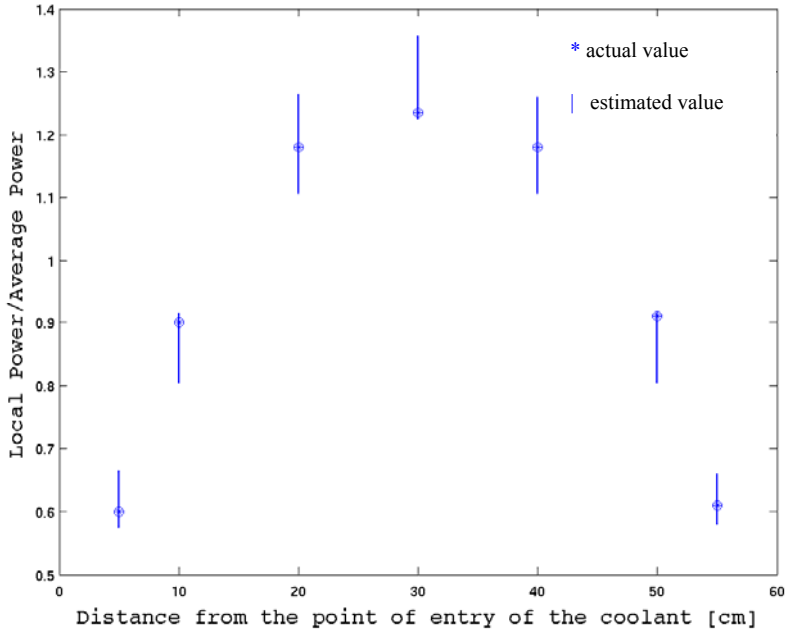

FIGURE 5. Estimated and Actual Values of the Local Power for the Data in Table 1.

NOMENCLATURE

C_i	=	thermal capacitance of Node i (i =1,2) (J/m^{3}K)
$g(j,n\|j',n')$	=	transition probability from cell pair (j',n') to cell pair (j,n) during $k\tau < t < (k+1)\tau$ (k=0,1,2,..)
h	=	sensor height (m)
k	=	thermal conductivity of the contact layer between Node 1 and 2 (W/m.K)
$p_k(j,n)$	=	probability that the system variables are in cell j ($j=1,...,J$) and the system parameters are in cell n ($n=1,...,N$) at time $t=k\tau$
q_n	=	nuclear energy deposition rate (W/m^3)
q_e	=	electrical energy deposition rate (W/m^3)
r_i	=	inner radius of the layer between Node 1 and Node 2(m)
r_0	=	outer radius of the layer between Node 1 and Node 2 (m)
R_1	=	thermal resistance between Node 1 and 2 (K.m^3/W)
R_2	=	thermal resistance between Node 1 and the coolant (K.m^3/W)
t	=	time (s)
T_i	=	temperature of Node i (i =1,2) (K)
T_0	=	coolant temperature (K)
x_l	=	system state variable ($l=1,...,L$)
α_m	=	system parameter ($m=1,...,M$)

REFERENCES

Aithal, S.M., Aldemir, T., and Vafai, K., "Assessment of the Impact of Neutronic/Thermal-Hydraulic Coupling on the Design and Performance of Nuclear Reactors for Space Propulsion," *Nucl. Technol*. 106, 15-30 (1994).

Breimeister, J. S. "MCNP-A General Monte Carlo Code For Neutron and Photon Transport, Version 3B," LA 7396-M, Los Alamos National Laboratory, New Mexico (1989).

Burghelea, A., and Aldemir, T., "In-Core Power Detection with CTPS Using a Non-Linear Model," *Trans. Am. Nucl. Soc*., **88**, 314-316 (2003).

Dinca, L., "A Probabilistic Approach to Parameter Estimation towards Fault Diagnosis in Non-Linear Dynamic Systems," Ph.D Thesis, The Ohio State University (1997).

Kruger,G., "A Cermet Fuel Reactor for Nuclear Thermal Propulsion," *Nuclear Thermal Propulsion*, NASA Conference Publication 10079, 165-184 (1991).

Liu, H.-Y., Miller, D. W., Li, D.-X., and Radcliff, T. D., "A Novel Method to On-Line Monitor Reactor Nuclear Power and In-Core Thermal Environments," *Proceedings of the International Congress on Advanced Nuclear Power Plants (ICAPP),* Paper #1212, CD-ROM, American Nuclear Society, La Grange, IL (2002).

Powell, J., Ludewig, H., Mughabghab, S., Perkins, K. Selcow, E., Schmidt, E., and, Horn, F., "A Nuclear Thermal Rocket Engine Design Based on the Particle Bed Reactor Suitable for a Mars Mission," AIAA-91-3508, AIAA/NASA/OAI Conference on SEI Technologies, Cleveland, Ohio (1991).

Radcliff, T. D., Miller, D. W., and Kauffman, A. C., "Constant-Temperature Calorimetry for In-Core Power Measurement", *Nucl. Technol.,* **132,** 240-255 (2000a).

Radcliff, T. D., Miller, D. W., and Kauffman, A. C., "Modeling Of A Constant-Temperature Power Sensor", *Proceeding of 8th International Conference on Nuclear Engineering (ICONE-8)*, Paper #8098, American Society of Mechanical Engineers, New York, N.Y. (2000b).

Turner, W. D., Elrod, D. C., Siman-Tov, I. I., "HEATING-5," ORNL/CSD/TM-15, Oak Ridge National Laboratory, Oak Ridge, Tennessee (1977).

Wang, P., and Aldemir, T., "Real Time Xenon Estimation in Nuclear Power Plants," *Trans. Am. Nucl. Soc.,* **81**, 154-156 (1999).

Wang, P., Chen, X. M., and Aldemir, T., "DSD: A Generic Software Package For Model-based Fault Diagnosis in Dynamic Systems," *Reliab. Engng & System Safety,* **75**, 31-39 (2002).

Proceedings of NPIC&HMIT 2004, 1246-1253, American Nuclear Society, LaGrange Park, IL (September 2004)

Forth American Nuclear Society International Topical Meeting on Nuclear Plant Instrumentation, Controls and Human-Machine Interface Technologies (NPIC&HMIT 2004), Columbus, Ohio, September, 2004

QUANTIFYING THE MEASUREMENT UNCERTAINITY PROPAGATION IN FLUX/POWER RECONSTRUCTION

Mihaela Biro, Tunc Aldemir
The Ohio State University, Nuclear Engineering Program
Bldg 1, Rm 130B, Suite 255, 650 Ackerman Road, Columbus, OH 43202
biro.6@osu.edu; aldemir.1@osu.edu

Keywords: diffusion theory, core power distribution, probability distribution function

ABSTRACT

This paper presents a theoretical approach combining the 1 ½ group diffusion theory with statistical techniques to estimate the flux/power shape probability distribution based on statistical interpolation between measured data. Two methods for estimating the statistical properties of power density/flux between measurement points are described and illustrated on a hypothetical steady state one-dimensional reactor. Results are reported using simulated measured data from 15 hypothetical power sensors placed within the core.

1. INTRODUCTION

In nuclear reactors, it is important to have knowledge of the power/flux shape at all times during the reactor lifetime. This information is, for example, used for determining fuel burnup history and is strictly necessary for ensuring safe operation of the reactor. Currently, in power reactors, the flux/power map is reconstructed based on the signals from out of core or in-core detectors, using diffusion codes and employing different methods of flux reconstruction, such as: piecewise cubic splines to interpolate between measured data (Han, 1999), fittings based on modal expansions (Pomerantz, 2002; Fu, 1997), artificial neural networks (Lee, 2002) and least-squares fittings (Lee, 2003).

There have been relatively few studies that explicitly consider the probability distribution of the measurement uncertainty in the flux/power shape construction process (Bryson, 1993). The proposed approaches are limited to linear relationships between flux/power and location, often requiring long computation times and large memory (Bryson, 1993).

The objective of this research is to develop an approach that can be used to obtain the probability distribution function (pdf) of the flux/power distribution at all points in the reactor using monitored data from in-core power detectors. The proposed approach yields all the statistical properties of the flux/power distribution in the core, including expected values and credibility intervals. Such data could be useful for risk-informed regulatory process and may allow reduction in operational thermal margins (and

subsequently increasing the power extracted from the core) in view of the reduced uncertainty in the estimated local power densities.

Two possible methods of obtaining the pdfs between detectors locations are investigated in this study, both combining the diffusion theory with statistical techniques.

Section 2 describes the theoretical basis. Application on a hypothetical steady state one-dimensional reactor is presented in Section 3. A discussion of the results is given in Section 4.

2. METHODS

The two methods considered in this study differ in the assumptions made:

- Method 1 assumes that, at every point in the reactor, the expected value of the power density/flux follows the diffusion theory.
- Method 2 imposes the additional constraint that the power density/flux can achieve all possible values at any specified point in the reactor.

2.1 Method 1

Consider a one–dimensional steady state reactor as described by 1 ½ group diffusion theory:

$$\frac{d}{dx}\left[D_1(x)\frac{d\phi_1(x)}{dx}\right] + B^2(x)\phi_1(x) = 0 \tag{1}$$

$$\Sigma_{1\to 2}(x)\phi_1(x) = [\Sigma_{a,2}(x) + \Sigma_b(x)]\phi_2(x)$$

with

$$B^2(x) = \frac{\nu}{D_1}\left[\Sigma_{f,1}(x) + \Sigma_{f,2}(x)\frac{\Sigma_{1\to 2}(x)}{\Sigma_{a,2}(x) + \Sigma_b(x)}\right] - [\Sigma_{a,1}(x) + \Sigma_{1\to 2}(x)] \quad (0 \le x \le L) \tag{2}$$

where $\Sigma_b(x)$ denotes the reactivity control cross section (poison and/or control rods) and all the other symbols have their conventional definitions. Solution of Eq.(1) for constant $B^2(x) > 0$ and $B^2(x) < 0$ (e.g. in the vicinity of a control rod) within $x_n < x < x_{n+1}$ yields the power density $h(y)$ at location

$$y = \frac{x_{n+1} - x}{x_{n+1} - x_n} \tag{3}$$

as

$$h(y)=\begin{cases}\dfrac{1}{\sin(\beta)}\left[h_{n+1}\sin[\beta(1-y)]+h_n\sin(\beta y)\right] & B^2(y)>0\\ \dfrac{1}{\sinh(\beta)}\left[h_{n+1}\sinh[\beta(1-y)]+h_n\sinh(\beta y)\right] & B^2(y)<0\end{cases} \tag{4}$$

where h_n is the measured power density/flux at $x = x_n$ (or $y = 1$), h_{n+1} is the measured power density/flux at $x = x_{n+1}$ (or $y = 0$) and

$$\beta^2 = (x_{n+1} - x_n)^2 B^2 \tag{5}$$

Imposing the condition that the expected values of ϕ_1 and ϕ_2 satisfy Eq.(1), the pdf of the power density/flux, $p(h \mid y)$, for given $p(h \mid 1) = p_n$, $p(h \mid 0) = p_{n+1}$ and at a given $0 < y < 1$ can be written as

$$p(h\mid y)=\begin{cases}\dfrac{1}{\sin(\beta)}\left[p_{n+1}\sin[\beta(1-y)]+p_n\sin(\beta y)\right] & B^2(y)>0\\ \dfrac{1}{\sinh(\beta)}\left[p_{n+1}\sinh[\beta(1-y)]+p_n\sinh(\beta y)\right] & B^2(y)<0\end{cases} \tag{6}$$

It can be seen from Eq.(6) that the resulting inferred pdf of power density/flux at location $x_n < x < x_{n+1}$ is a weighted sum of the pdfs of power density/flux at locations x_n and x_{n+1}. This result may be extended for the multigroup case, where energy discriminant detectors need to be used to determine the boundary conditions.

2.2 Method 2

Integration of Eq.(6) over all possible values of h yields

$$F(\infty \mid y)=\int_0^\infty dh\,p(h\mid y)=\begin{cases}\dfrac{1}{\sin(\beta)}\left[\sin[\beta(1-y)]+\sin(\beta y)\right] & B^2(y)>0\\ \dfrac{1}{\sinh(\beta)}\left[\sinh[\beta(1-y)]+\sinh(\beta y)\right] & B^2(y)<0\end{cases} \tag{7}$$

where $F(h|y)$ is the cumulative distribution function (Cdf) for power density/flux at a specified y. It can be seen from Eq.(7) that, for all y, $F(\infty \mid y) = 1$ only for small β, and not for all β values as would be intuitively expected. Method 2 is a modification of the procedure proposed by Read (1999) to search for neutral and charged Higgs bosons in electron-positron collisions. Adapted to the problem under consideration in this study, it assumes that power density/flux varies linearly between detector locations and imposes the condition that $F(\infty \mid y) = 1$ at all y. The procedure also requires that the Cdfs

$$F(h\mid 1)\equiv F_n(h)=\int_0^h p_n(h')dh' \quad \text{and} \quad F(h\mid 0)\equiv F_{n+1}(h)=\int_0^h p_{n+1}(h')dh' \tag{8}$$

at the two consecutive detector locations x_n and x_{n+1}, respectively, have the same value F as well as at all points between the detector locations, i.e.

$$F_n(h_n) = F_{n+1}(h_{n+1}) = F(h) = F \tag{9}$$

Given $p_n(h)$ and $p_{n+1}(h)$, the $p(h \mid y)$ can then be constructed using the algorithm shown in Fig.1

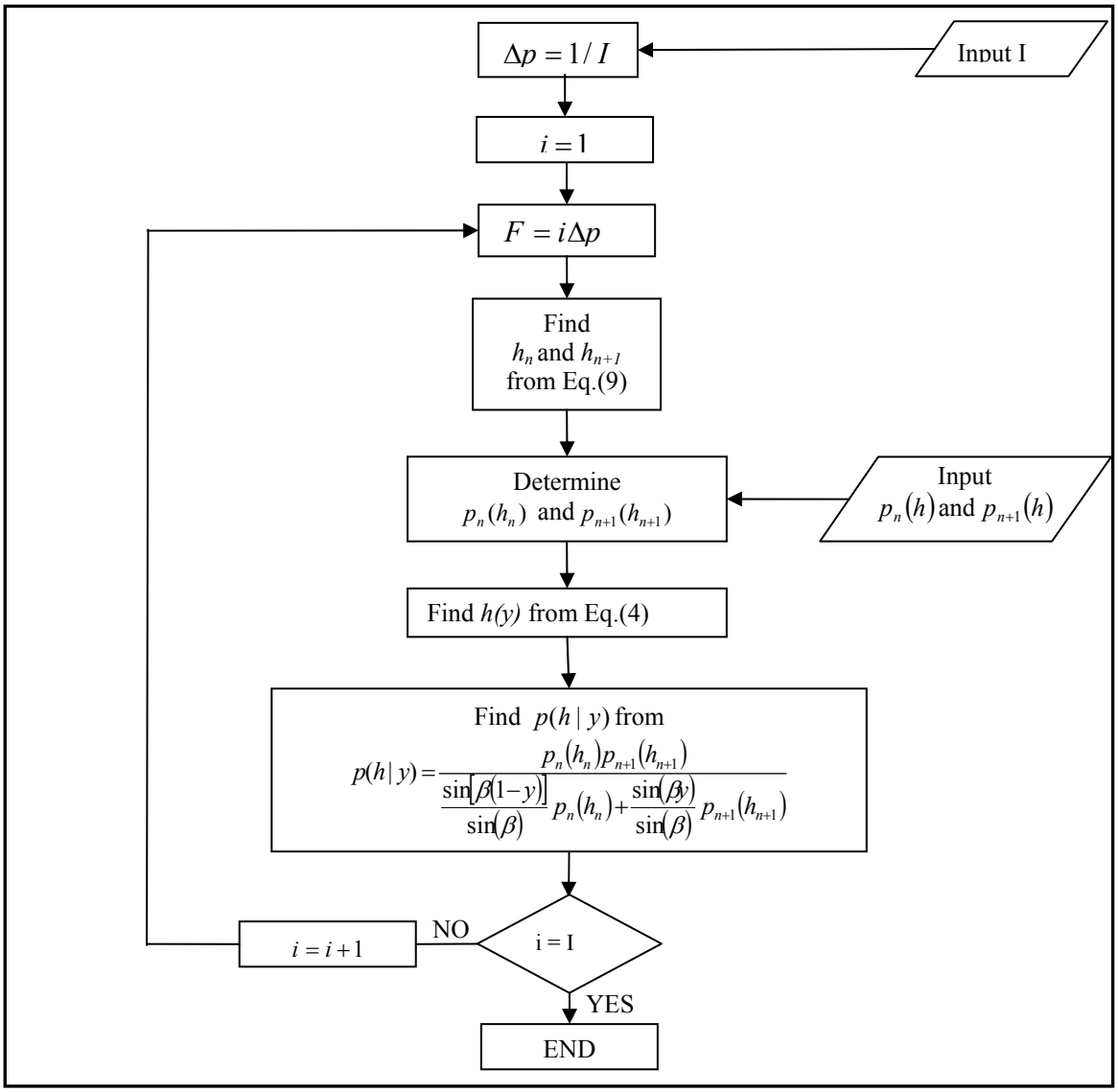

Fig.1: Method 2 Flowchart

3. EXAMPLE RESULTS

A one-dimensional reactor of length $2L$ = 300 cm with material properties given in Table 1 was considered. A gray control rod of thickness 2 cm and transmissivity 0.9

was assumed to be inserted in the reactor at x = 50 cm away from the reactor midplane. Data from detectors placed within the core at every 10 cm starting from the reactor midplane were simulated by solving Eqs.(1) and (2) within $0 \le x \le L$ and with

$$\left.\frac{d\phi_1(x)}{dx}\right|_{x=0} = \left.\frac{d\phi_2(x)}{dx}\right|_{x=0} = 0 \tag{10}$$

$$\phi_1(L) = \phi_2(L) = 0$$

to obtain

$$h(x)/h(0) = \begin{cases} \cos(Bx) & \text{if } x < 49\,\text{cm} \\ 0.488751[\sin(Bx) - \tan(BL)\cos(Bx)] & \text{if } x > 51\,\text{cm} \end{cases} \tag{11}$$

where for criticality we must have B = 0.0242 cm^{-1}.

Table 1 Group constants for the example reactor

Group constant	**Group**	
	1	**2**
$\nu\Sigma_f$ (cm^{-1})	0.008476	0.18514
Σ_a (cm^{-1})	0.01207	0.1210
D (cm)	1.2627	0.3543
$\Sigma_{1->2}$ (cm^{-1})	0.0141	-

The monitored data from the detectors were assumed to be normally distributed with the expected value satisfying Eq.(11) and with a 1% standard deviation. Figure 2(a) shows the probability distributions and the expected values as obtained from Method 1. Figure 2(b) shows the same information, but as obtained by applying Method 2. In the region 40 < x < 60 cm were the existence of a control rod is assumed, the β coefficient in Eq.(4) was obtained through homogenization.

It was noted that although the expected values predicted by both methods matched the simulated data well (see Fig.2), Method 1 may lead to a bimodal distribution and that the predicted expected value between detector locations may fall in a region of low probability. Figures 3 and 4 show the pdfs of reactor power at x = 43 cm and x = 85 cm, respectively. The bimodal shape predicted by Method 1 in Fig.3 has also been observed in other studies (Bursal, 1996) and is due to the fact that $p_n(h)$ and $p_{n+1}(h)$ are being concentrated in different regions of the state space. The unimodal shape of $p(h|y)$ is due to the linearity assumption of Method 2. Figure 4 shows that if the variation in the power density/flux is small with distance (e.g. at x = 85 cm as can be seen from Fig.2)

and subsequently *h(y)* is close to linear, then *p(h|y)* obtained from both Method 1 and Method 2 are similar.

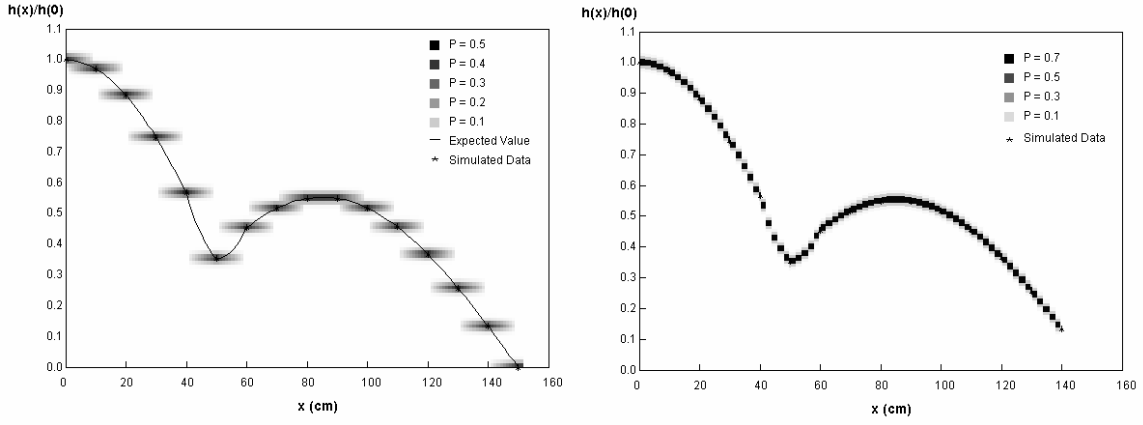

(a) (b)

Fig. 2 Relative power distribution *h(x)/h(0)* for the example reactor: a) Method 1, b) Method 2

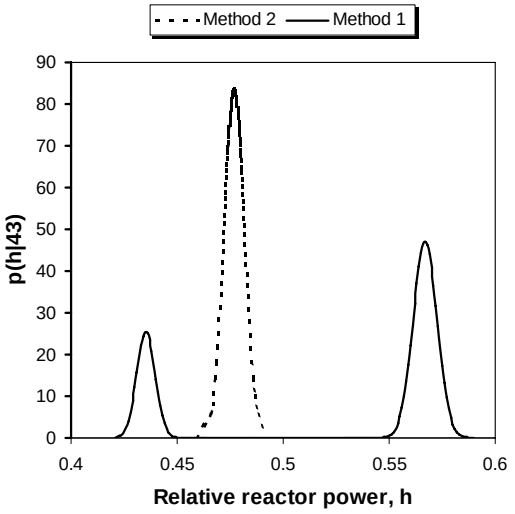

Fig.3 Probability distribution function at location x = 43 cm

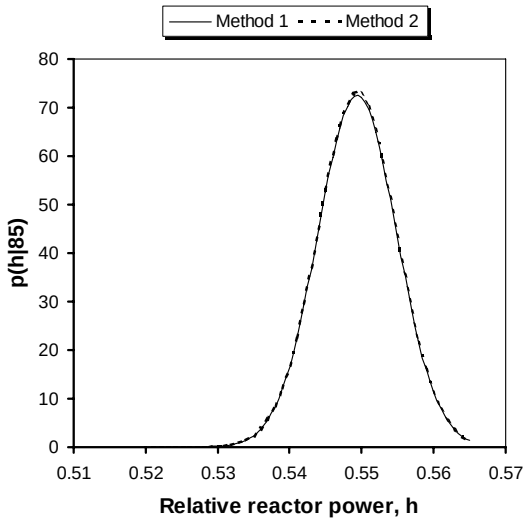

Fig. 4 Probability distribution function at location x = 85 cm

4. CONCLUSIONS

Two methods for estimating the statistical properties of power density/flux between measurement points are described and illustrated in a 1-dimensional reactor assuming steady state behavior and 1 ½ group diffusion theory. Such data may be useful

for risk informed regulation, as well as for establishing meaningful margins on operational power levels and setpoints.

The results of the study show the following:

1. Both Method 1 and Method 2 estimate the expected value of the power density/flux between measurement points well.

2. Method 1 may lead to a bimodal distribution with the uncertainty on the expected value being very large at the midpoint between detector locations.

3. Method 2 always leads to a unimodal distribution with the mode of the distribution close to the expected value.

Considering the fact that the midpoint between detector locations is the one furthest away from the detectors, Result 2 is not counter-intuitive. However, it leads to difficulties from a practical viewpoint since credibility intervals for the expected value of power density/flux in reactor regions away from the detector locations cannot be obtained in a meaningful manner. While Method 2 does not have this problem, it is not clear how the linearity assumption affects the results. One conclusion that arises from these results is that comparison of Method 1 and Method 2 results as a function of x_n allows the optimal choice of detector locations.

NOMENCLATURE

D	diffusion coefficient
ν	number of neutrons emitted per fission
$\phi_i(x)$	neutron flux
$\Sigma_f(x)$	fission cross section
$\Sigma_a(x)$	absorption cross-sections
$\Sigma_{1\to 2}(x)$	group transfer cross-section
$\Sigma_b(x)$	reactivity control cross section
h	power density
p	probability distribution function
F	cumulative distribution function

Subscripts

1	fast neutrons group
2	thermal neutrons group

REFERENCES

J. W. Bryson, J. C. Lee, and J. A. Hassberger, 1993. Optimal Flux Map Generation through Parameter Estimation Techniques, *Nucl.Sci.Eng,* **114**, 238.

F. H. Bursal, 1996. On Interpolating between Probability Distributions, *Applied Mathematics and Computation*, 77, 213-244.

J. J. Duderstadt, L. J. Hamilton, 1976. *Nuclear Reactor Analysis,* John Wiley & Sons.

S. Han, U. S. Kim, P. H. Seong, 1999. A Methodology for Benefit Assessment of Using In-core Neutron Detector Signals in Core Protection Calculator System (CPCS) for Korea Standard Nuclear Power Plants (KSNPP). *Annals of Nuclear Energy*, **26**, 471-488.

G.-C. Lee, W-P. Baek, S. H. Chang, 2002. Improved Methodology for Generation of Axial Flux Shapes in Digital Core Protection Systems, *Annals of Nuclear Energy*, **29**, 805–819.

K. Lee, C. H. Kim, 2003. The Least-Squares Method for Three-Dimensional Core Power Distribution Monitoring in Pressurized Water Reactors**,** *Nucl.Sci.Eng*, **143,** 268.

M. E. Pomerantz, C.R. Calabrese, C. Grant, 2002. Nuclear Reactor Power and Flux Distribution Fitting from a Diffusion Theory Model and Experimental Data, *Annals of Nuclear Energy*, **29,** 1073–1083.

L. Read, 1999. Linear Interpolation of Histograms, *Nuclear Instruments & Methods in Physics Research* A 425, 357-360.

L. Fu, L. Zhengpei, H. Yongming, 1997. Harmonics Synthesis Method for Core Flux Distribution Reconstruction, *Progress in Nuclear Energy*, **31**, 369-372.

Trans. Am. Nucl. Soc., 88, 314-316 (June 2003)

In-Core Power Detection with CTPS Using a Non-Linear Model

Andrei Burghelea, Tunc Aldemir*

The Ohio State University, Nuclear Engineering Program, 206 West 18th Avenue,
Columbus, Ohio 43210

*Author to whom correspondence should be addressed

1. INTRODUCTION

A new in-core reactor power sensor has been under development at The Ohio State University since 1996. This feedback-controlled calorimetric instrument, which is referred to as a constant-temperature power sensor (CTPS), is capable of direct measurement of nuclear energy deposition [1]. The CTPS is ideally suited for use in the proposed Generation IV power systems in which the sensors become an integral part of the fuel for the core lifetime. Previous work [2] to determine the local nuclear energy deposition rate q_n with CTPS has used: a) an algebraic model obtained from the solution of the linearized differential equations describing the CTPS operation, and, b) the software package DSD [3] to estimate the operation dependent model parameters. The results of [2] indicated that the model is very sensitive to model and data uncertainties. This study directly uses the non-linear differential equations describing the CTPS behavior and DSD to estimate the operation dependent model parameters as well q_n. Sections 2 and 3, respectively, describe the sensor model and give an overview of the estimation procedure. Section 4 presents the implementation and results.

2. THE CTPS

The CTPS consists of a UO_2 pellet surrounded by electrical heating resistance wire. The pellet and the wire form the sensor core (Node 2). The core is surrounded by ceramacast which is an alumina based ceramic thermal insulator (Node 1). Both the sensor core and the insulator are coated with thin layers of copper. A feedback control loop is used to provide the exact amount of input electrical energy q_e needed to keep Node 2 temperature T_2 constant in time *(t)*, well above the ambient temperature T_0, regardless of q_n. The sensor operation involves switching between the feedback-controlled constant-temperature mode and the dynamic temperature decay mode following the opening of the feedback loop as described by

$$
\begin{aligned}
C_1 \frac{dT_2}{dt} &= \left(q_n + q_e\right) - \frac{1}{R_1}\left(T_2 - T_1\right) \\
C_2 \frac{dT_1}{dt} &= \frac{1}{R_1}\left(T_2 - T_1\right) - \frac{1}{R_2}\left(T_1 - T_0\right) \\
\frac{1}{R_1} &= \frac{2\pi k_{Cu}(T_2)\left[h_s - 2(r_o - r_i)\right]}{log\left(\frac{r_o}{r_i}\right)} + \frac{2\pi k_{Cu}(T_2)\left(r_o^2 - r_i^2\right)}{\left[h_s - 2(r_o - r_i)\right]}
\end{aligned}
\tag{1}
$$

where k_C , r_o (0.575 mm), r_i (0.3mm) are, respectively, the thermal conductivity, outer and inner radius of the copper layer between Node 1 and Node 2, h_s is the height of the sensor, T_2 is Node 2 temperature, and C_1 and C_2 are, respectively, thermal capacitances of Node 1 and Node 2. Other notation in Eq.(1) are as defined previously. The model described by Eq(1) has been validated against a finite element code [3]. At steady-state Eq.(1) yields

$$
q_n + q_e = \frac{1}{R_2}\left(T_1 - T_0\right) \tag{2}
$$

which corresponds to the constant temperature mode operation of CTPS.

3. AN OVERVIEW OF DSD [4]

The DSD is based on the representation of the system dynamics in terms of transition probabilities between user specified cells that partition the system parameter/state space during user specified time intervals. The DSD recursively computes the probability $p_k(j,n \mid J_k)$ that the state variables (e.g. $T_1(t)$, $T_2(t)$) are in cell j (j = 1,...,J) and the unknown parameters (e.g. R_2, T_0) are in cell n (n = 1,...,N) during the data-sampling time period $k\tau \le t \le (k+1)\tau$ k (k = 0, 1, 2, ...), given that the possible set of cells the state variables can be in at this time is J_k (as observed from the monitored data), from

$$
\begin{aligned}
p_k^*(j,n) &\equiv p_k(j,n \mid J_k) = \frac{p_k(j,n)}{\sum_{j' \in J_k}\sum_{n'} p_k(j',n')} \quad (j \in J_k) \\
p_k(j,n) &= \sum_{j' \in J_{k-1}} g(j \mid j',n)\, p_{k-1}^*(j',n')
\end{aligned}
\tag{3}
$$

where $g(j \mid j',n)$ is the transition probability from state variable cell j' to state variable cell j during the period $k\tau \le t \le (k+1)\tau$ when the system parameters are within cell n. The $g(j \mid j',n)$ can be approximated by: 1) at time $k\tau$, selecting randomly or otherwise (e.g. equidistant) M' starting points from

cell j' for a given n, 2) using the given system model (e.g. Eq.(1)) to find the number M of trajectories that arrive within cell j at $t = (k+1)\tau$ (e.g. by integrating Eq.(1) over $k\tau \le t \le (k+1)\tau$ for each of the $m' = 1, 2, \ldots, M'$ initial conditions), and, c) letting $g(j \mid j', n) = M / M'$. A graphical illustration of this process is given in [5] and some sufficient conditions for the convergence of DSD are given in [6].

4. IMPLEMENTATION AND RESULTS

In the implementation, C_1, C_2, R_1 in Eq.(1) are assumed to be known. T_1, T_2 and q_e are assumed to be measured. The estimation of q_n for each data sampling time $t = k\tau$ (see Section 3) was carried out iteratively through the following steps: 1) Assume q_n; 2) Estimate T_0 and R_2 from Eq.(1); 3) Determine q_n from Eq.(2) using Step 2 results; 4) Compare q_n to its previous value q_n'; 5) If $(q_n - q_n')/q_n < 0.01$ stop (convergence), otherwise go to Step 2 with q_n. The $T_1(t)$ and $T_2(t)$ data for the estimation were generated from Eq.(1) with T_0=700 K, $T_1(0)$=721.095 K, $T_2(0)$=782.538 K, C_1=0.008041 J/K, C_2=0.744024 J/K, R_1=5.41 K/W, R_2=1.85 K/W, q_n=1.68 W q_e=9.6766 W and superimposed 1%random noise on the observed data (i.e. T_1 and T_2). The k_{Cu} as a function of T_2 was represented by a third order polynomial. Figure 1 shows the estimation results, as well as the partitioning scheme used with Eq.(3). Convergence on q_n was obtained in 12 iterations on the average per data sampling interval. The results indicate that the estimation scheme works well for both constant and time-varying ambient temperature T_0.

5. CONCLUSION

The results of the study show that DSD be used with CTPS to estimate the local power density in nuclear reactor cores both for steady-state and transient conditions with noisy data.

REFERENCES

1. T. D. Radcliff, D. W. Miller and A. C. Kauffman, "Modeling of a Constant-Temperature Power Sensor", *ICONE8*, Paper #8263, American Society of Mechanical Engineers, New York, N.Y. (May 2000)
2. I. Munteanu, H.B. Zhou, T. D. Radcliff, T. Aldemir, D. W. Miller, "In-Core Power Detection Using DSD", *Trans. Am. Nucl. Soc*., **83**, 279-281 (November 2000)
3. H.-Y. Liu, D. W. Miller, D.-X. Li, T. D. Radcliff, "A Novel Method to On-Line Monitor Reactor Nuclear Power and In-Core Thermal Environments", *ICAPP: Proceedings of the International Congress on Advanced Nuclear Power Plants,* Paper #1212, CD-ROM, American Nuclear Society, La Grange, IL (June 2002).

4. P. Wang, X. M. Chen, T. Aldemir, "DSD: A Generic Software Package For Model-based Fault Diagnosis in Dynamic Systems", *Reliab. Engng & System Safety*, **75**, 31-39 (January 2002)
5. M. Gadioli, M. Marseguerra, E. Zio, "Fast Integration by Neural Nets in DSD: Probabilistic State Estimation", *Trans. Am. Nucl. Soc., 81*, 151-153 (November 1999)
6. P. Wang, T. Aldemir, "Real Time Xenon Estimation in Nuclear Power Plants", *Trans. Am. Nucl. Soc.,81*, 154-156 (November 1999)

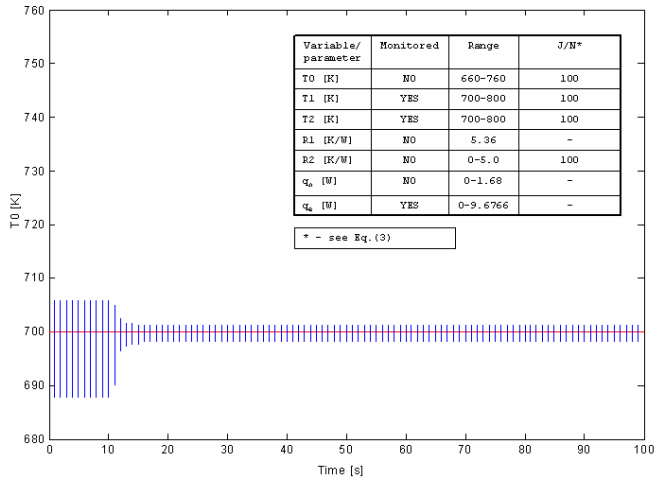

(a)

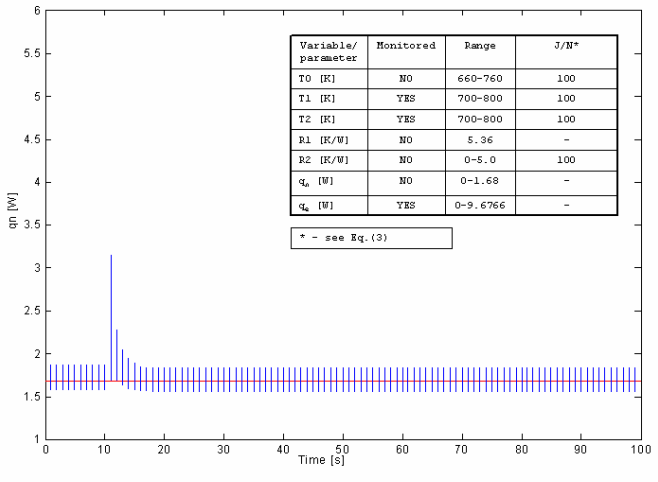

(b)

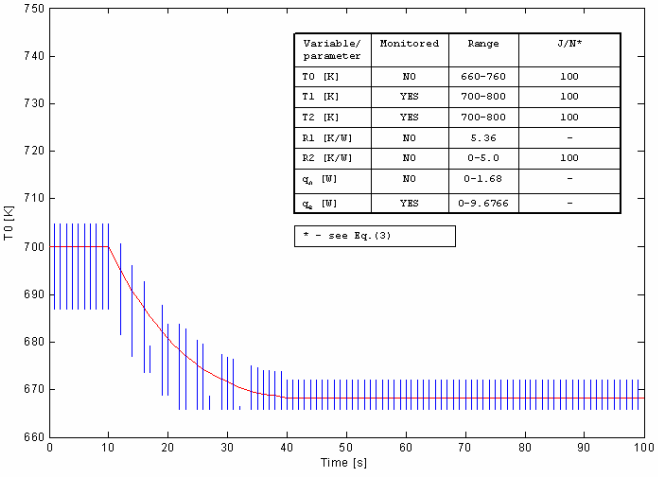

(c)

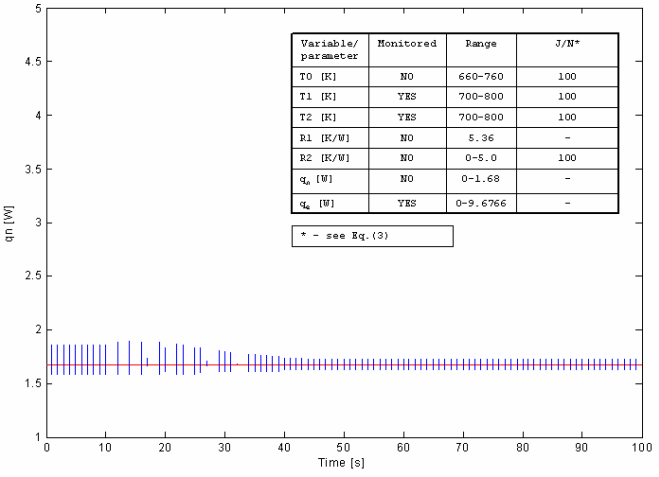

(d)

Fig.1: Estimation results (bars) for constant and time-varying T_0: a) constant T_0; b) q_n for constant T_0; c) time-varying T_0; b) q_n for time-varying T_0. Solid lines indicates the true values.

Trans. Am. Nucl. Soc., 89, 493-495 (November 2003)

A Parametric Investigation of the Recursive Partitioning Approach to DSD for Implementation with CTPS

Andrei Burghelea, Tunc Aldemir*

The Ohio State University, Nuclear Engineering Program, 206 West 18th Avenue, Columbus, Ohio 43210

*Author to whom correspondence should be addressed

INTRODUCTION

The DSD (Dynamic System Doctor) is dynamic system state/parameter estimation software [1] that can automatically account for modeling uncertainties/signal noise in the estimation process. This capability is accomplished through the representation of system evolution in terms of probability of transitions within a user specified time interval τ (e.g. data sampling interval) between sets of user defined parameter/state variable magnitude intervals (or cells) that partition the search space. The DSD yields the probability $p_k(n,j)$ that the parameters are in cell n and the state variables are in cell j at time $t = k\tau$. Then $p_k(n,j)$ can be used to determine the lower and upper bounds on the estimated values of state variables/parameters, as well as their probability distribution within these bounds.

A potential limitation in the implementation of DSD is that excessively long run times and large memory requirements may result for large or rapidly evolving systems if the cell definitions are provided as fixed initial input. Recently a recursive partitioning scheme (RPS) for cell definitions was proposed that substantially reduces the estimation time and memory requirements [2]. This paper investigates the sensitivity of the RPS to the ranges of interest for the state variables/parameters to be estimated using the constant temperature power sensor (CTPS) [3]. The CTPS has been proposed for direct measurement of local power density in nuclear reactor cores and requires the on-line estimation of ambient conditions for reliable operation. A practical implication of such a parametric search is the determination of the power range the CTPS can be operated in.

OVERVIEW OF DSD WITH RPS

The RPS philosophy is to progressively eliminate the regions of the search space where $p_k(n,j) = 0$ through the on-line definition of the cells. Figure 1 shows the DSD algorithm with RPS. The DSD assumes that a system model is available which can be used the system location is state space at time $t = (k+1)\tau$ $(k = 0,1,2\cdots)$ from the knowledge of its location at time $t = k\tau$ and the known values of the system parameters. The algorithm consists of the following steps:

1. *Specify, respectively, the state variable and parameter ranges of interest, RPS stopping rules and monitored data uncertainty*. The parameter and state variable ranges of interest define the search space for the estimation process. The RPS stopping rules define the smallest cell size that needs to be used for the estimation of the unmonitored state variables/parameters. The choice of such a cell is usually based on the accuracy level desired for the variables/parameters to be estimated.
2. *Read data from the monitors* at each time point $t = k\tau$ $(k = 0,1,2\cdots)$.
3. *Define the intervals for the monitored variables* so as to contain the variation/noise on the monitored data, centered on their median values.
4. *Define the intervals for the unmonitored variables and the parameters by bisecting each range of interest*. Along with the intervals defined in Step 3, these intervals form the cells that partition the search space.
5. *Input the initial probability distribution $p_0(n,j)$ to be used to start the estimation process*. The $p_0(n,j)$ is usually chosen as the uniform distribution, however, results of the estimation are not dependent on the choice of $p_0(n,j)$.

6. *Determine the cell-to-cell transition probabilities* $g(j \mid j', n')$ by: a) selecting J' points in cell j' at time $t = k\tau$, b) finding the number of arrival points J in cell j at time $t = (k+1)\tau$ from the system model, assuming that the system parameters remain in their cell n' at time $t = k\tau$, and, c) letting $g(j \mid j', n') = J' / J$.
7. *Find* $p_k(n, j)$ from

$$p_k(n, j) = \sum_{j'} \sum_{n'} g(j \mid j', n') p_{k-1}(n', j')$$

8. *If all* $p_k(n, j) = 0$, *then subdivide each and go to Step 3. Otherwise, normalize* $p_k(n, j)$ *by dividing it by the total probability of finding the system in the search space, increment the time index k and go to Step 2.* The probability of finding the system in the search space is not necessarily 1, because the system may leave the search space during $k\tau \le t < (k+1)\tau$ depending on its location at $t = k\tau$.

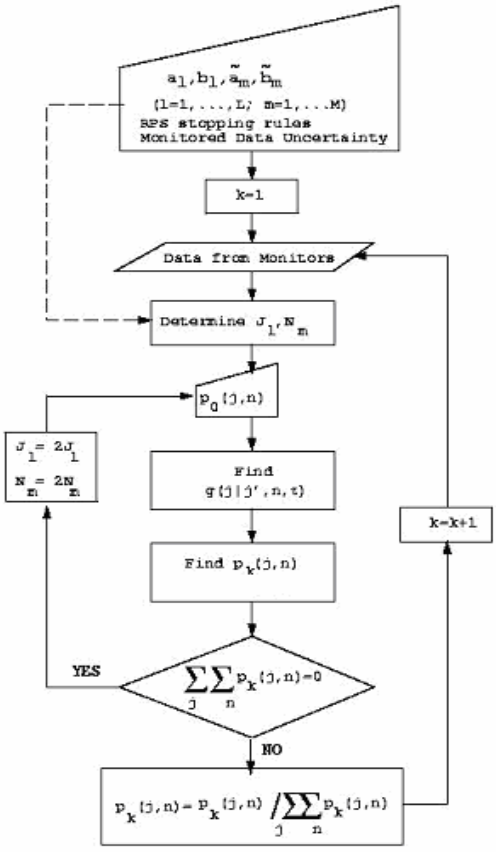

Fig.1: DSD Algorithm with RPS

Steps 2 through 8 are repeated until $p_k(n, j)$ converges in the probability sense, i.e. $p_k(n, j)$ are all zero except for the cells containing the actual system locations in the system state and parameter spaces It should be mentioned at this point that the algorithm may not converge for rapidly evolving systems during one data sampling interval $k\tau \le t < (k+1)\tau$. However, even in this situation, previous work shows that the expected values of the parameters/state variables to be estimated are often found to be close to their actual values [4].

THE CTPS

The CTPS consists of a UO_2 pellet surrounded by electrical heating resistance wire. The pellet and the wire form the sensor core (Node 2). The core is surrounded by ceramacast which is an alumina based ceramic thermal insulator (Node 1). Both the sensor core and the insulator are coated with thin layers of copper. A feedback control loop is used to provide the exact amount of input electrical energy q_e needed to keep Node 2 temperature T_2 constant in time, well above the ambient temperature T_0, regardless of q_n. The sensor operation involves switching between the feedback-controlled constant-temperature mode (Mode 1) and the dynamic temperature decay mode (Mode 2) following the opening of the feedback loop as shown below in Fig.2.

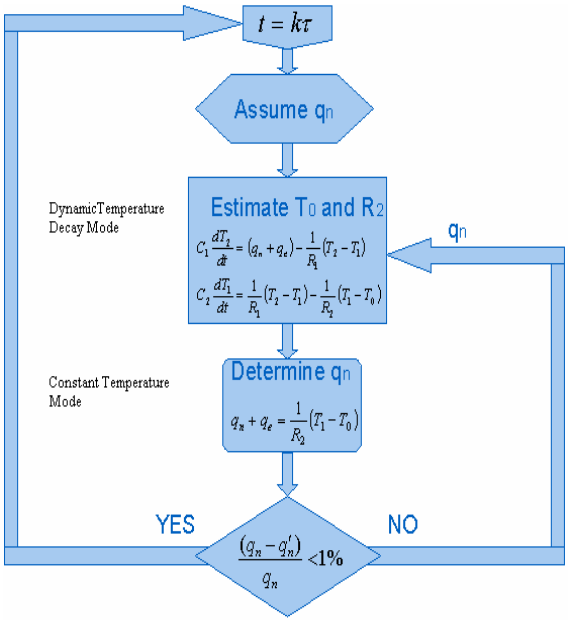

Fig.2: CTPS Operation

The quantities C_1, C_2 and R_1 in Fig.2 are assumed to be known. T_1, T_2 and q_e are assumed to be measured.

IMPLEMENTATION AND RESULTS

In the implementation, the estimation of q_n for each data sampling time $t = k\tau$ was carried out iteratively as shown in Fig.2. The $T_1(t)$ and $T_2(t)$ data for the estimation were generated from the equations describing the dynamic temperature decay mode in Fig. 2 with T_0=700 K, $T_1(0)$=721.095 K, $T_2(0)$=782.538 K, C_1=0.008041 J/K, C_2=0.744024 J/K, R_1=5.41 K/W, R_2=1.85 K/W, q_n=1.68 W q_e=9.6766 W and superimposed 1% random noise on the monitored data (i.e. T_1 and T_2). The noise level is substantially larger than the anticipated measurement uncertainty during the operation of the sensor. The k_{Cu} in Fig.2 as a function of T_2 was represented by a third order polynomial. Table 1 shows the estimation results. The last row shows the average number of switches between Mode 1 and Mode 2 for convergence in q_n and indicates that the computational demand for RPS is relatively insensitive to the size of the search space, however, increases with the refinement of the stopping rule as also expected from DSD applications with progressively refined fixed partitioning schemes.

CONCLUSION

The results of the study show that DSD with RPS be used with CTPS to estimate the local power density in nuclear reactor cores for fuel temperature ranges within 300 K to 1000 K. Similarly, the estimation scheme works within the coolant temperature range of (i.e. T_0) of 300 – 1000K. While these temperatures ranges include most of the operational range of current reactors, further studies are needed to investigate the suitability of measurement scheme to high temperature, gas cooled Generation IV reactors.

Table 1
Estimation Results for RPS

	Case		
	1	2	3
T_0 Range (K)	650-850	500-900	300-1000
T_1/T_2 Range (K)	50-1250	300-900	300-1000
R_2 Range (K/W)	0-5	0-5	0-5
Stopping Rule (%of range)	1	2.0/1.0	1.5
Average Number of Intermodal Iterations	7.25	8.94/11.47	8.63

REFERENCES

1. P. WANG, X. M. CHEN, T. ALDEMIR, "DSD: A Generic Software Package For Model-based Fault Diagnosis in Dynamic Systems", *Reliab. Engng & System Safety*, **75**, 31-39 (January 2002)
2. A. BURGHELEA, I. MUNTEANU, T. ALDEMIR, "A Recursive Partitioning Approach to DSD", *PSA2002: Proceedings of the International Topical Meeting on Probabilistic Safety Assessment, G*. E. Apostolakis, T. Aldemir (Eds), 630-635, American Nuclear Society, La Grange Park, IL (2002)
3. A. BURGHELEA, T. ALDEMIR, "In-Core Power Detection with CTPS Using a Non-Linear Model", *Trans. Am. Nucl. Soc*., **88**, 314-316 (June 2003)
4. P. WANG, T. ALDEMIR, "Some Improvements in State/Parameter Estimation Using the Cell-to-Cell-Mapping Technique", submitted to *Nucl.SciEng* .

TRANSACTIONS

OF THE
AMERICAN NUCLEAR SOCIETY

June 24–28, 2007
Boston Marriott Copley Place
Boston, Massachusetts

Volume 96
TANSAO 96 1–882 (2007)
ISSN: 0003-018X

Raymond T. Klann (ANL)
Technical Program Chair

Stephen P. LaMont (LANL)
Jess Gehin (ORNL)
Assistant Technical Program Chairs

Julie B. Rule (ANS)
Editor

Ellen M. Leitschuh (ANS)
Coordinator

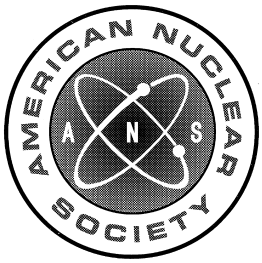

CLICK HERE TO START

AMERICAN NUCLEAR SOCIETY HOME PAGE

Material Identification in Finite Cylindrical Geometries Using the Schwinger Inverse Method, invited

Keith C Bledsoe,* Jeffrey A. Favorite,** and Tunc Aldemir***

*Nuclear Engineering Program, The Ohio State University, Columbus, OH 43210 USA, bledsoe.12@osu.edu
**X-4-TAR, MS T082, Los Alamos National Laboratory, Los Alamos, NM 87545 USA, fave@lanl.gov
***Nuclear Engineering Program, The Ohio State University, Columbus, OH 43210 USA, aldemir.1@osu.edu

INTRODUCTION

The Schwinger inverse method [1], a novel solution method for solving inverse transport problems, was recently developed and tested in one-dimensional spherical geometries [1, 2]. In this paper, the method is applied to solving the inverse problems of source weight fraction identification and shield composition identification in finite two-dimensional cylindrical geometries.

THE SCHWINGER INVERSE METHOD

The Schwinger inverse method [1] was derived from a perturbation-theory approach to the inverse transport problem. Instead of calculating the effect of a system perturbation on a quantity of interest (the usual use of the Schwinger functional), the quantity of interest was assumed to be given (from a measurement) and the Schwinger functional was manipulated to produce an equation for the system perturbation. The equation is applied iteratively. The quantity of interest is the leakage of a discrete gamma-ray line from radioactive decay, which implies that the scattering term in the transport equation can be ignored.

Shield Material Identification

The method was used to derive the following equation for the composition of an unknown shield layer [2]:

$$\Sigma_t'^g = \frac{\int dV \int d\hat{\mathbf{\Omega}} \psi^{*g} q^g}{\int_{V_{unk.}} dV \int d\hat{\mathbf{\Omega}} \psi^{*g} \psi^g} \left(\frac{M^g - M_0^g}{M_0^g} \right) + \Sigma_t^g, \qquad g = 1, \ldots, G. \tag{1}$$

In this equation, Σ_t^g is the total photon cross section in the current iteration for the unknown material at the energy corresponding to line g and $\Sigma_t'^g$ is the updated cross section that will be used in the next iteration. The terms ψ^g, ψ^{*g}, and M^g are the forward flux, adjoint flux, and leakage calculated for line g in the current iteration; q^g is the source for line g (γ/cm^3·s); and M_0^g is the measured leakage for line g. The integral in the numerator in Eq. (1) is over the entire problem, but the integral in the denominator is over the unknown material region only. Once the G macroscopic cross sections are found, the unknown material is identified using cross section tables [2].

Source Weight Fraction Identification

The method was also used to derive an equation for unknown isotope weight fractions in a gamma-emitting source material [1]:

$$\frac{\rho_S N_A}{\left\langle \psi^{*g} q^g \right\rangle} \left[\left(\int_{V_S} dV \int d\hat{\mathbf{\Omega}} \psi^{*g} \psi^g \right) \sum_{j=1}^{J} \frac{\sigma_{t,j}^g}{A_j} \Delta f_j - \left(\frac{M^g}{M_0^g} \frac{q_i^g}{A_i} \int_{V_S} dV \int d\hat{\mathbf{\Omega}} \psi^{*g} \right) \Delta f_i \right] = \frac{M^g - M_0^g}{M_0^g}, \qquad g = 1, \ldots, G. \tag{2}$$

In this equation, ρ_S is the mass density of the source material, N_A is Avogadro's number, $\sigma_{t,j}^g$ is the total microscopic cross section for source isotope j and line energy g, q_i^g is the source strength of isotope i for line g, and A_j is the gram atomic weight of isotope j. The term $\Delta f_j \equiv f_j' - f_j$ is the update to the weight fraction in the current iteration to obtain the weight fraction to use in the next.

TEST PROBLEM

The methods for source and shield identification were tested on the finite cylindrical geometry shown in Fig. 1. A highly enriched uranium source is surrounded by a shield consisting of aluminum on the bottom and side of the cylindrical shield and nickel on the top. The top of the shield is twice as thick as the bottom. This axial asymmetry allows for more physically realistic test problems than were possible with the one-dimensional spherical problems of Refs. 1 and 2.

The quantities of interest were the total leakage (into 4π) of four decay lines from uranium, 144, 186, 766, and 1001 keV. The forward and adjoint angular fluxes of Eqs. (1) and (2) were calculated for each line using the PARTISN discrete-ordinates code [3] with no scattering.

Leakage measurements were simulated in two ways. The first was by using PARTISN with the same angular (S_8) and spatial discretizations as used to calculate the flux in the iterative calculation. Thus, these "measured" and calculated leakages were exactly consistent. The second way of simulating measured leakages was by using a Monte Carlo code, which simulated a real measurement of the total leakage. These measurements are shown in Table I.

Schwinger iterations were run until the calculated line leakages were within 0.01% of the measurements.

RESULTS

Shield Material Identification

Converged cross sections on the left side of Eq. (1) were compared to known cross sections from a library of 40 candidate materials using a root-mean-squared (rms) difference, where the rms difference for material m is

$$(\text{rms})_m = \sqrt{\frac{1}{G}\sum_{g=1}^{G}(\Sigma_t'^g - \Sigma_{t,m}^g)^2}. \quad (3)$$

The materials with the lowest rms differences were considered candidates for the unknown.

When S_8 measurements were used, nickel was successfully identified as the only suitable candidate for the unknown layer, having an rms difference two orders of magnitude smaller than any other material (see Table II). With Monte Carlo measurements, nickel still had the smallest rms difference, but was one of nine possible shield materials.

Source Weight Fraction Identification

Initial guesses for the weight fractions of uranium in the source were ^{235}U: 0.5000, ^{238}U: 0.5000. When S_8 measurements were used, the actual source weight fractions (^{235}U: 0.9473, ^{238}U: 0.0527) were found in one iteration of Eq. (2). With Monte Carlo measurements, slightly less accurate weight fractions of ^{235}U: 0.9300, ^{238}U: 0.0700 were calculated in one iteration.

CONCLUSIONS

The Schwinger inverse method has previously been applied to the separate problems of determining unknown source [1] and shield compositions [2] in one-dimensional spherical geometries. In this paper, the method was successfully applied to these problems in a more physically realistic two-dimensional cylindrical geometry.

In this work, the total leakage into 4π was the quantity of interest. To model more realistic scenarios, the quantity of interest should be the gamma-ray flux at a particular detector location outside the object. We are currently studying ways to mitigate the discrete-ordinates ray effects in order to allow such calculations to be made accurately.

REFERENCES

1. J. A. FAVORITE, "Using the Schwinger Variational Functional for the Solution of Inverse Transport Problems," *Nucl. Sci. Eng.*, **146**, 51-70 (2004).
2. J. A. FAVORITE and K.C. BLEDSOE, "Identification of an Unknown Material in a Radiation Shield Using the Schwinger Inverse Method," *Nucl. Sci. Eng.*, **152**, 106-117 (2006).
3. R. E. ALCOUFFE et al., "PARTISN," LA-CC-98-62, Los Alamos National Laboratory (1997).

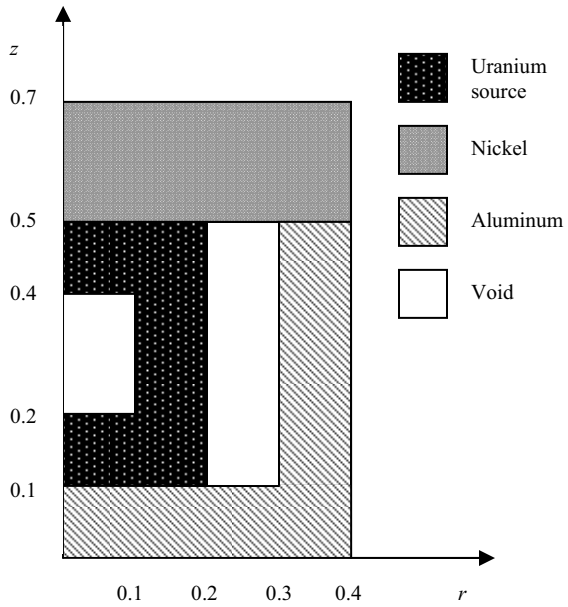

Fig. 1. Geometry for numerical test problems. Dimensions are in cm.

TABLE I. Measured Leakages.

Line (keV)	S_8	Monte Carlo
144	4.58897E+2	4.274E+2 ± 7.79%
186	4.54920E+3	4.577E+3 ± 5.40%
766	1.22674E+0	1.193E+0 ± 2.15%
1001	3.47231E+0	3.393E+0 ± 2.06%

TABLE II. Materials with the Lowest rms Difference in the Shield Identification Problem (Actual Material Was Nickel, Initial Guess Was Lead).

	S_8 Measurements			Monte Carlo Measurements	
1	Nickel	8.612E-04	1	Nickel	1.636E-01
2	Copper	2.952E-02	2	Copper	1.694E-01
3	Cobalt	8.705E-02	3	Cobalt	1.831E-01
4	SS316	1.967E-01	4	SS316	2.191E-01
5	Iron	2.390E-01	5	Cadmium	2.193E-01
			6	Iron	2.287E-01
			7	SS304	2.293E-01
			8	Carbon Steel	2.321E-01
			9	Silver	2.781E-01

Trans. Am. Nucl. Soc., 93, 575-577 (November 2006)

Implementation of an on-line reactor power monitoring system using CTPS

Mihaela Biro, Tunc Aldemir*

T*he Ohio State University, Nuclear Engineering Program, 650 Ackerman Road, Columbus, Ohio 43202*

*Author to whom correspondence should be addressed

INTRODUCTION

The constant-temperature power sensor (CTPS) [1, 2] is a feedback-controlled calorimetric instrument capable of direct measurement of nuclear energy deposition. A conceptual system for power measurements in reactor cores using such sensors has been developed using DSD [3]. The DSD is state/parameter estimation technique for dynamic systems. It yields the probability distribution functions (pdfs) of the quantities to be estimated in their discretized space from a user-provided system model and using monitored system data along with their associated uncertainties. The data uncertainties provide inputs for the discretization process which partitions space of the quantities to be estimated into computational cells, in a similar manner to those used by the finite difference or finite element methods. It has been shown that a probabilistic map of core power distribution can be constructed with DSD using simulated signals from an array of sensors distributed in a hypothetical reactor core [4].

This paper investigates the computational feasibility of the estimation algorithm proposed in [4]. The goal is to have an estimation engine able to construct the probabilistic map of core power distribution in real-time. Parallel implementation of the algorithm is investigated on multiple processors, attempting to determine the minimum number of processors necessary to run the estimation algorithm under real-time constraints.

THE CTPS

The CTPSs [1, 2] are sensors capable of direct measurement of nuclear power density (q_n). The CTPS concept is based on control of the energy balance about a small mass of fissionable material. The sensor core is a UO_2 pellet (Node 2) surrounded by an insulator material (Node 1). An electrical heating resistance wire is wound on Node 2. A feedback control loop is provided that adjusts the necessary input of electrical energy (q_e) such that the Node 2 temperature is maintained constant.

The sensor behavior is described by [5]:

$$C_1\frac{dT_2}{dt} = (q_n + q_e) - \frac{1}{R_1}(T_2 - T_1)$$
$$C_2\frac{dT_1}{dt} = \frac{1}{R_1}(T_2 - T_1) - \frac{1}{R_2}(T_1 - T_0) \quad (1)$$

where T_1 and T_2 are the temperatures of Node 1 and Node 2, respectively, T_0 is the temperature of the coolant in contact with Node 1, C_1 and C_2 are the thermal capacitances of Nodes 1 and Node 2, respectively, R_1 is the thermal resistance between Node 2 and Node 1 and R_2 is the thermal resistance between Node 1 and the coolant.

At steady-state conditions, the energy balance around Node 2 is described by

$$q_n + q_e = (T_2 - T_0)/(R_1 + R_2). \quad (2)$$

By measuring q_e and T_2, q_n can be estimated from Eq. (2) if R_2 and T_0 are known.

As can be seen from Eq. (2), an accurate estimation of q_n in the measuring mode depends on the accurate estimation of T_0 and R_2. The CTPS has two modes of operation: i) power measurement mode when q_e is measured and q_n is estimated using Eq.(2), and, ii) calibration mode during which R_2 and T_0 are estimated from Eq.(1). In the power measurement mode, q_e is such that T_1 and T_2 are constant. In the calibration mode, q_e is interrupted. Then T_1 and T_2 decrease to steady-state values as described by Eq.(1). In Eq.(1), T_1, T_2 and q_e are measured quantities. The R_2, T_0 and q_n parameters are to be estimated. All the other quantities in Eq.(1) are assumed to be known (e.g. through previous off-line measurements)

THE DSD

The DSD uses a representation of system evolution in time in terms of probability of transitions between sets of magnitude intervals of system state-variables (i.e. T_1 and T_2 for Eqs.(1) and (2)) and parameters (i.e. R_2,T_0, q_n for Eqs.(1) and (2)) within the user specified

time intervals $k\tau \le t \le (k+1)\tau$ $(k=0,1,..)$. These sets form computational cells that partition the system state and parameter spaces. If location of the system in the state-space is known for specified system parameters (such as for the problem under consideration since T_1 and T_2 are measured), the DSD generates the transition probability $g(j \mid j', n, \tau)$ from cell j' to j in the state-space within $k\tau \le t \le (k+1)\tau$ given that the system parameters are in cell n at time $k\tau$ from

$$g(j \mid j', n, \tau) = \frac{1}{v_{j'}} \frac{1}{v_n} \int_n d\boldsymbol{\alpha} \int_{j'} d\boldsymbol{x}' e_j[\tilde{\boldsymbol{x}}(\boldsymbol{x}', \boldsymbol{\alpha}, k\tau)]$$
$$e_j(\boldsymbol{x}) = \begin{cases} 1 & \text{if } \boldsymbol{x} \text{ is within } j \\ 0 & \text{otherwise} \end{cases} \quad (3)$$

In Eq.(3), the elements of the vectors $\boldsymbol{x}$ and $\boldsymbol{\alpha}$ are the state variables and system parameters, respectively. The vector $\tilde{\boldsymbol{x}}(\boldsymbol{x}', \boldsymbol{\alpha}, k\tau)$ denotes the location of the system in the state-space at time $t = (k+1)\tau$ given that it departed from point $\boldsymbol{x}'$ at time $t = k\tau$ for specified $\boldsymbol{\alpha}$, $v_{j'}$ is the volume of cell j' and v_n is the volume of cell n. The point $\tilde{\boldsymbol{x}}(\boldsymbol{x}', \boldsymbol{\alpha}, k\tau)$ is determined from a user provided system model describing system evolution in time, such as Eqs.(1) and (2). If the system parameters do not change within $k\tau \le t \le (k+1)\tau$, the DSD determines the joint pdf $p_k(j,n)$ for the mean value of the state-variables and parameters over cell pair j,n at time $t = k\tau$ recursively from

$$p_k(j,n) = \sum_{j'} g(j \mid j', n, \tau) p_{k-1}(j', n) \quad (k = 0,1,\cdots). \quad (4)$$

DETERMINATION OF POWER DISTRIBUTION

Figure 1 shows schematically the procedure for the determination of power distribution. First, the $g(j \mid j', n, \tau)$ in Eq.(4) are determined from Eqs.(1) and (3), monitored $T_1(k\tau)$, $T_2(k\tau)$ and q_e. Then the joint pdf $p_k(R_2, T_0, q_n) \equiv p_k(\hat{j}, n)$, where n denotes the cells in the R_2-T_0-q_n space, and $\hat{j}$ denotes the observed system location in the discretized T_1-T_2 space, is updated using Eq.(4). The following steps are used for the estimation of q_n at each CTPS location:

1. $p(R_2, T_0, q_n)$ is integrated (or summed in the discretized R_2-T_0-q_n space) over all possible values of q_n to obtain the joint pdf $p(R_2, T_0)$.
2. $p(R_2, T_0)$ from Step 1 yields a probability for R_2 and T_0 being in each set of intervals partitioning the R_2-T_0 space.
3. Using the boundaries of these intervals as inputs for Eq.(2), upper and lower bounds are found for q_n for the probabilities identified in Step 2.
4. Superimposition of the intervals and the corresponding probabilities from Step 3 yields the pdf for q_n.

Once the pdfs for q_n is found at CTPS locations, the approach described in [6] can be used to generate the pdfs for q_n between these locations.

PARALLEL IMPLEMENTATION

Parallel implementation of the above-described monitoring scheme was investigated on multiple processors, attempting to determine the minimum number of processors necessary to run the estimation algorithm under the real-time constraints. The algorithm was implemented in C/C++ and ran on multiple processors using Message Passing Interface (MPI) directives for assigning jobs and coordinating communication between the parallel processes. Computation time measurements were taken by running the algorithm on the Pentium IV Cluster of the Ohio Supercomputing Center for different problem sizes (i.e. the number of cells partitioning the estimated parameter space) and for different numbers of processors.

The power monitoring scheme was implemented on an example application taken from [5]. It consisted of seven sensors axially distributed within a cylindrical reactor core of a pebble bed type reactor. A reactor transient in which the coolant temperature decreases exponentially with 1 hour period was assumed.

RESULTS

The computation time needed for the estimation algorithm was assumed to be 6 seconds of real time (duration of the calibration mode). For a problem size of 64x64x64 cells partitioning the R_2-T_0-q_n space, the computation time was 23 s for 1 processor, 15 s on 2 processors, 7 s on 4 processors and 4 s on 8 processors. At the same time, the parallelization efficiency (serial time/parallel time/number of processors) decreased from about 80% on 2 processors to about 70% on 8 processors.

CONCLUSION

This study shows that the DSD algorithm is computationally feasible for implementation for an on-line, real-time power monitoring system using parallel processing.

The optimum number of processors needed depends on how fast the sensors need to be calibrated and on the available processor resources. For 4 processors, the computation time is the nearest to real-time for the assumed transient used for this study, but fewer number processors may be adequate for steady-state operation where the parameters to be estimated would not change rapidly.

REFERENCES

1. T. D. RADCLIFF, S. P LIU, D. W. MILLER, "Modeling and Optimization of a Constant-Temperature In-Core Power Sensor", *Nuclear Technology*, **140**, 209-221 (2002).
2. T. D. RADCLIFF, D. W. MILLER, A. C. KAUFFMAN, Constant-Temperature Calorimetry for In-Core Power Measurement", *Nuclear Technology*, **132**, 40-254 (2000).
3. P. WANG, X. M. CHEN, T. ALDEMIR, "DSD: A Generic Software Package For Model-based Fault Diagnosis in Dynamic Systems", *Reliab. Engng & System Safety*, **75**, 1-39 (2002).
4. M. BIRO, T. ALDEMIR, "The Development of a Self-Calibrating Power Monitoring System for Nuclear Reactors", *Proc.ISAS-CITSA 2005*, II, J. Aguilar, H.-A. Chu, E. D. Gugiu, I. Miloucheva, N. Rishe (Eds.), 4-8, International Institute of Informatics and Systemics, Orlando, FL (July 2005)
5. T. ALDEMIR, D. W. MILLER, A. BURGHELEA, "Direct Estimation of Power Distribution in Reactors for Nuclear Thermal Space Propulsion", *Space Technology and Applications International Forum—STAIF 2004*, M. S. El-Genk (Ed.), 582-589, American Institute of Physics, Melville, N.Y. (February 2004).
6. M. BIRO, T. ALDEMIR, "Quantifying the Measurement Uncertainty Propagation In Flux/Power Reconstruction", *Proceedings of NPIC&HMIT 2004*, 1246-1253, American Nuclear Society, LaGrange Park, IL (September 2004)

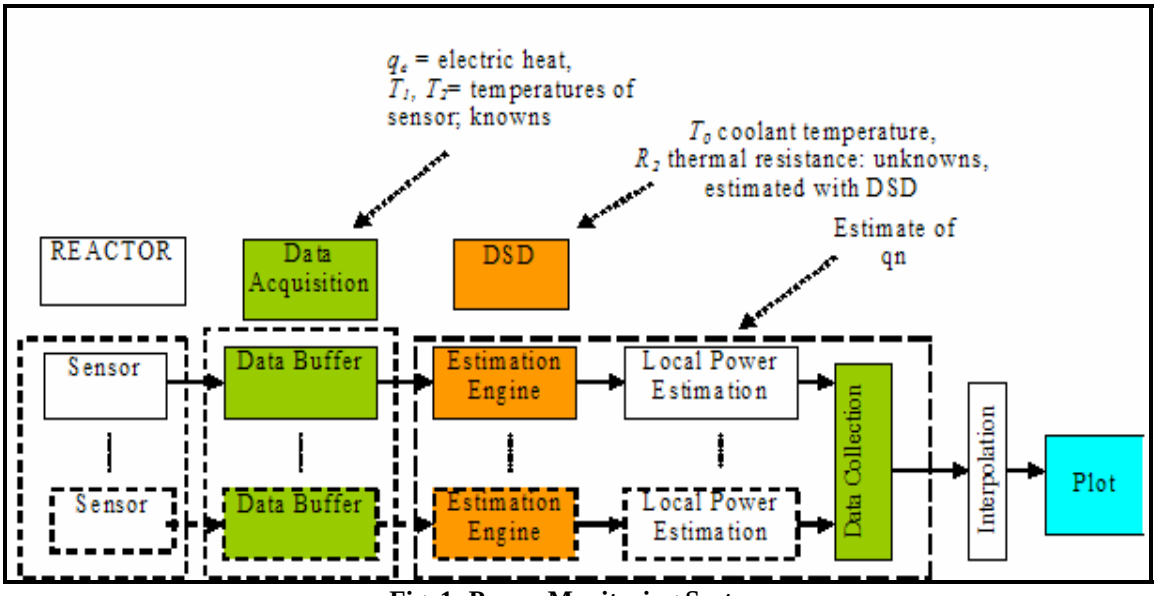

Fig. 1: Power Monitoring System

Trans. Am. Nucl. Soc., 90, 59-61 (June 2004)

A Model Based Probabilistic Scheme for Flux/Power Shape Construction from Monitored Data

Mihaela Biro, Tunc Aldemir*

T*he Ohio State University, Nuclear Engineering Program,*
Bldg 1, Rm 130B, Suite 255, 650 Ackerman Road, Columbus, OH 43202.

*Author to whom correspondence should be addressed

INTRODUCTION

The evolution of flux and power distributions in nuclear reactor cores is usually tracked using diffusion codes. Due to modeling as well as operational uncertainties, it is often necessary to validate/improve the predicted distributions through in-core flux and temperature measurements. A variety of techniques have been developed for this purpose, including using cubic splines to interpolate between measured data [1], fittings based on modal expansions [2,3], artificial neural networks [4] and least-squares fittings [5].

There have been few attempts to directly incorporate the measurement uncertainty into flux/power shape construction process [6, 7]. This paper describes a procedure which approaches the problem in the spirit of [6] and explicitly represents measurement uncertainty through user specified probability distribution functions (pdfs) in the construction process. The difference is that the procedure presented here is a probabilistic interpolation scheme rather than fitting scheme which maximizes the conditional pdf of the estimated flux/power shape given the observations [6]. The proposed procedure is not restricted to linear relationships between flux/power and location [6] and also leads to computational simplicity for a large number of observations. The procedure can be also used with a wide range of approaches to power/flux shape construction, from simple linear interpolation between data points to model based fittings, as well as a variety of pdfs to represent measurement uncertainty. The procedure is illustrated using 1½ group diffusion theory model for a hypothetical one-dimensional reactor.

THE PROCEDURE

Consider a one dimensional reactor with length 2*L* whose steady-state neutronic behavior is described by 1½ group diffusion theory, i.e.

$$\frac{d}{dx}\left[D_1(x)\frac{d\phi_1(x)}{dx}\right]+B^2(x)\phi_1(x)=0$$
$$\Sigma_{1\to2}(x)\phi_1(x)=[\Sigma_{a,2}(x)+\Sigma_b(x)]\phi_2(x) \quad (1)$$
$$B^2(x)=\nu\left[\Sigma_{f,1}(x)+\Sigma_{f,2}(x)\frac{\Sigma_{1\to2}(x)}{\Sigma_{a,2}(x)+\Sigma_b(x)}\right]$$
$$-[\Sigma_{a,1}(x)+\Sigma_{1\to2}(x)] \quad (0\le x\le L)$$

where $\Sigma_b(x)$ indicates the control poison cross section at location *x* and the rest of the symbols have their conventional definitions. We will assume that: 1) group parameters of Eq.(1) are known functions of *x*, 2) the pdfs $p(\phi_1 \mid x_n)=p_n(\phi_1)$ of $\phi_1(x_n)$ at x_n are known for n = 1,…,N on $0\le x\le 2L$, and, 3) expected value

$$<\phi_1(x)>=\int d\phi_1\ \phi_1\ p(\phi_1 \mid x) \quad (2)$$

of $\phi_1(x)$ satisfies Eq.(1). Then it can be shown that

$$\int d\phi_1\ \phi_1\left\{\begin{matrix}\frac{\partial}{\partial x}\left[D(x)\frac{\partial p(\phi_1 \mid x)}{\partial x}\right]+\\ B^2(x)\,p(\phi_1 \mid x)\end{matrix}\right\}=0 \quad (3)$$

which means that a sufficient condition for $p(\phi_1 \mid x)$ to satisfy is

$$\frac{\partial}{\partial x}\left[D(x)\frac{\partial p(\phi_1 \mid x)}{\partial x}\right]+B^2(x)\,p(\phi_1 \mid x)=0 \quad (4)$$

The solution of Eq.(4) with specified $p(\phi_1 \mid x_n)=p_n(\phi_1)$ and $p(\phi_1 \mid x_{n+1})=p_{n+1}(\phi_1)$ yields $\phi_1(x)$ in $x_n<x\le x_{n+1}$ (n = 1,…,N-1). If power is directly measured [8], it can be also shown from Eq.(1)in a similar manner that , for

constant material properties within $x_n < x \le x_{n+1}$,

$$\frac{\partial^2 p(h \mid y)}{\partial y^2} + \beta^2 p(h \mid y) = 0$$

$$\beta^2 = (x_{n+1} - x_n)^2 \frac{B^2}{D_1} \qquad (0 \le y \le 1) \quad (5)$$

$$y = \frac{x_{n+1} - x}{x_{n+1} - x_n}$$

where $p(h \mid y)$ is the pdf of power density h at y. For specified $p(h \mid 0) = p_{n+1}(h)$ and $p(h \mid 1) = p_n(h)$ we get

$$p(h \mid y) = \frac{1}{\sin(\beta)} \begin{bmatrix} p_{n+1}(h) \sin[\beta(1-y)] \\ + p_n(h) \sin(\beta y) \end{bmatrix} \quad (6)$$

or

$$< h(y) >= \frac{1}{\sin(\beta)} \begin{bmatrix} < h(0) > \sin[\beta(1-y)] \\ + < h(1) >= \sin(\beta y) \end{bmatrix} (7)$$

for the expected value $< h(y) >$ of power density at y. For small β (e.g. small interval $[x_{n+1}, x_n]$), Eq.(6) yields

$$p(h \mid y) \approx p_{n+1}(h)(1-y) + p_n(h) y \qquad (8)$$

which is the result from the statistics literature for $< h(y) >$ varying linearly within $0 \le y \le 1$ [11].

Although Eqs.(4) and (5) are in principle partial differential equations, they become ordinary differential equations once the numerical values of the boundary conditions are specified and subsequently can be solved using standard code packages for non-uniform material distributions. It is not difficult to see that equations similar to Eq.(4) can be generated for a multi-group counterpart of Eq.(1). In the multi-group case, energy discriminant sensors need to be used to determine the boundary conditions, such as the SiC detectors developed by Westinghouse [10].

AN EXAMPLE ILLUSTRATION

For the purposes of illustration, we will assume that power density is directly measured in a hypothetical, one dimensional reactor placed in vacuum with uniform material distribution as given in Table 1 and L = 150 cm.

From Eq.(1) and the relationship between power and flux, we have

$$h(x) = h(0) \cos(\beta x) \qquad (0 \le x \le L) \quad (9)$$

For criticality, we must have $\beta \approx \pi / 300\ \text{cm}^{-1}$ (or $\Sigma_b = 0.0707\ \text{cm}^{-1}$ from Eq.(4) and Table 1 data).

Table 1
Group Constants for the Example Reactor [11]

Group Constant	Group	
	1	2
$\nu\Sigma_f$ (cm^{-1})	0.008476	0.18514
Σ_a (cm^{-1})	0.01207	0.1210
D (cm)	1.2627	0.3543
$\Sigma_{1->2}$ (cm^{-1})	0.0141	-

Figure 1 shows: a) the data $h_1, h_2, \cdots h_{10}$ from 10 hypothetical power sensors placed at $0 \le x_1 < x_2 < \cdots x_{10} \le L$, generated from Eq.(9) assuming 1% random error, b) $p(h \mid x)$ obtained from Eqs.(5) and (6) assuming

$$p_n(h) = \frac{1}{0.01\sqrt{2\pi}} \exp\left(-\frac{(h - h_n)^2}{2(0.01)^2} \right), \qquad (10)$$

$$(n = 1, \cdots, 10)$$

and, c) $< h(x) >$ obtained from Eqs.(5) and (7).

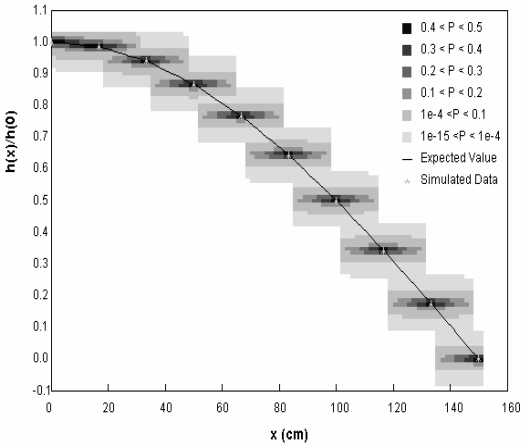

Fig.1: Relative Power Distribution *h(x)/h*(0) for the Example Reactor

Figure 1 indicates that the match between the simulated data and $< h(x) >$ is excellent. Figure 1 also shows how the $p(h \mid y)$ yields the uncertainty ranges for the estimated power between measurement points. The $p(h \mid y)$ can be used to obtain other statistical properties of $h(x)$ as well. For example, the probability that power is within 10% of the expected value can be found from

$$\int_{09<h(y)>}^{1.1<h(y)>} dh\, p(h \mid y) .$$

Similarly, 90% confidence interval for the expected value of power at y can be found from the solution of $p(< h >| y) = 0.9$ for $<h>$.

CONCLUSION

The proposed procedure provides a fast way to estimate the expected value as well as all other statistical properties of power/flux between measurement points. The accuracy of estimation depends on the assumed pdfs at the measurement points and the core model used with the procedure (i.e. Eq.(5))

REFERENCES

1. S. HAN, U. S. KIM, P. H. SEONG "A Methodology for Benefit Assessment of Using In-core Neutron Detector Signals in Core Protection Calculator System (CPCS) for Korea Standard Nuclear Power Plants (KSNPP)", *Annals of Nuclear Energy*, **26**, 471-488 (1999).
2. M. E. Pomerantz, C.R. Calabrese, C. Grant, "Nuclear Reactor Power and Flux Distribution Fitting from a Diffusion Theory Model and Experimental Data", *Annals of Nuclear Energy*, **29,** 1073–1083 (2002).
3. L. Fu, L. Zhengpei, H. Yongming "Harmonics Synthesis Method for Core Flux Distribution Reconstruction", *Progress in Nuclear Energy*, **31**, 369-372 (1997).
4. G.-C. Lee, W-P. Baek, S. H. Chang. "Improved Methodology for Generation of Axial Flux Shapes in Digital Core Protection Systems", *Annals of Nuclear Energy*, **29**, 805–819 (2002).
5. K. Lee, C. H. Kim, "The Least-Squares Method for Three-Dimensional Core Power Distribution Monitoring in Pressurized Water Reactors"**,** *Nucl.Sci.Eng*, **143,** 268 (2003).
6. J. W. Bryson, J. C. Lee, and J. A. Hassberger, "Optimal Flux Map Generation Through Parameter Estimation Techniques", *Nucl.Sci.Eng*, **114**, 238 (1993).
7. R.A. Bonalumi, N.P.Kherani "Rational Mapping (RAM) of In-Core Data", *Nucl.Sci.Eng*, **90**, 47 (1985).
8. T. D. Radcliff, D. W. Miller, A. C. Kauffman,"Constant - Temperature Calorimetry for In-Core Power Measurement", *Nucl. Technol*., **132**, 240-255 (2000).
9. F. H. Bursal, "On Interpolating between Probability Distributions", *Applied Mathematics and Computation*, **77**, 213-244 (1996).
10. F. H. Ruddy, A. R. Dulloo, J. G. Seidel, F. W. Hantz, L. R. Grobmyer, "Nuclear Reactor Power Monitoring Using Silicon Carbide Semiconductor Radiation Detectors", *Nucl. Technol*., **140**, 198-208 (2002).
11. J. J. Duderstadt and L. J. Hamilton, *Nuclear Reactor Analysis*, John Wiley & Sons (1976).

Proc.ISAS-CITSA 2005, II, J. Aguilar, H.-A. Chu, E. D. Gugiu, I. Miloucheva,
N. Rishe (Eds.), 4-8, International Institute of Informatics and Systemics, Orlando, FL (July 2005)

The Development of a Self-Calibrating Power Monitoring System for Nuclear Reactors

Mihaela Biro, Tunc Aldemir
Nuclear Engineering Program, The Ohio State University
Columbus, OH 43202, U.S.A.

ABSTRACT

The constant-temperature power sensor (CTPS) is a feedback-controlled calorimetric instrument capable of direct measurement of nuclear energy deposition. The CTPS simulates a section of the nuclear fuel element. The sensor operation is sensitive to the ambient coolant temperature and contact resistance. A procedure is described which estimates these quantities on-line for an array of sensors and constructs a map of probabilistic core power distribution.

Keywords: nuclear reactors, power distribution, parameter estimation.

1. INTRODUCTION

The constant-temperature power sensor (CTPS) [1] is a feedback-controlled calorimetric instrument capable of direct measurement of nuclear energy deposition. The CTPS simulates a section of the nuclear fuel element. In that respect, is especially suitable for high temperature environments of the planned Generation IV reactors and reactors for nuclear thermal propulsion.

This paper describes a conceptual system for power measurements in the reactor core using such sensors. The monitoring system will process sensor signals from the reactor core in such a manner that probabilistic information, in the form of probability distribution function (pdf) of reactor power density (q_n) is obtained at the sensor location. This signal processing would be in addition and independent of the normal signal processing that is normally performed in a nuclear power plant, and it would be used for informational purposes only, to assist the operator; it would not have any control over the reactor core.

The paper shows how a map of probabilistic core power distribution can be constructed using simulated signals from an array of sensors distributed in a hypothetical reactor core. An estimation algorithm, called DSD (Dynamic System Doctor) [2] is implemented that processes the sensor signals to obtain the power density pdfs at sensor locations.

2. THE MONITORING SYSTEM

The monitoring system will consist of: (a) an array of sensors distributed in the reactor core and associated circuitry, (b) an estimation engine, (c) a module to interpolate the pdf for q_n between sensors locations [3], and, (d) a scheduler to manage data acquisition and multi-thread/distributed processing. All the components of the monitoring system except the interpolation module presented in an earlier publication [3] are described below.

Sensor – The CTPS

The CTPS concept is based on control of the energy balance about a small mass of fissionable material. Figure 1 shows the structure of a CTPS for current electricity generating nuclear power plants. The sensor core (Node 2) is UO_2 pellet. An electrical heating resistance wire surrounds the core. Energy in the sensor core is deposited through nuclear interactions and from resistive dissipation through the wire, while energy is removed through conductive and convective heat transfer to the reactor coolant. A feedback control loop is provided that adjusts the necessary input of electrical energy such that the Node 2 temperature is maintained constant. At steady-state conditions, the energy balance around the core is described by

$$q_n + q_e = (T_2 - T_0)/R_2 \qquad (1)$$

where q_n denotes the nuclear energy deposited (or the reactor power density), q_e is the electrical energy input, R_2 is the thermal resistance between sensor and coolant, T_2 is the temperature of Node 2 and T_0 is the coolant temperature. By measuring q_e and T_2, q_n can be estimated from Eq. (1) above if R_2 and T_0 are known.

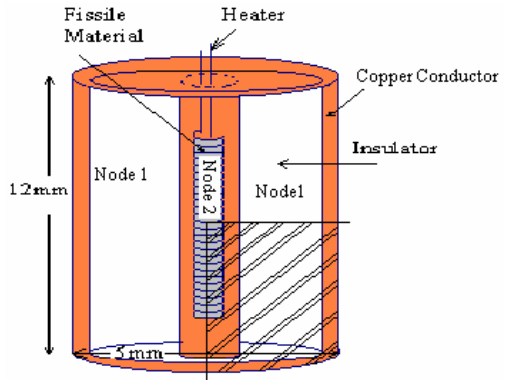

Fig. 1 Constant Temperature Power Sensor

The CTPS has two modes of operation: i) power measurement mode when q_e is measured and q_n is

estimated using Eq.(1), and, ii) calibration mode during which R_2 and T_0 are estimated.

As it can be seen from Eq. (1), an accurate estimation of q_n in the measuring mode depends on the accurate estimation of T_0 and R_2. Coolant temperature T_0 is typically measured at coolant inlet and outlet from the reactor core and it is not measured at each sensor location. The thermal resistance R_2 depends on the coolant temperature, flow speed and local geometry and it is impossible to be measured directly. The calibration mode is designed to provide information on these two variables.

In the calibration mode, the electrical current through the resistive wire that surrounds the sensor core is interrupted. The sensor temperature then decreases to a steady-state value directly dictated by the input of nuclear energy, the coolant temperature and the thermal resistance between the sensor and coolant. T_0 and R_2 are estimated by observing the dynamic behavior of Node 1 and Node 2 temperatures.

The estimation is done through DSD [4,5] which uses a representation of system evolution in time in terms of probability of transitions between sets of magnitude intervals of system state-variables within the user specified time intervals $k\tau \le t \le (k+1)\tau$ $(k=0,1,..)$. These sets form computational cells that partition the system state-space in a similar manner to those used by finite difference and finite element methods. The DSD generates the transition probability $g(j \mid j', \tau)$ from cell j' to j from

$$g(j \mid j', \tau) = \frac{1}{v_{j'}} \int_{j'} d\mathbf{x}' e_j[\tilde{\mathbf{x}}(\mathbf{x}', k\tau)]$$
$$e_j(\mathbf{x}) = \begin{cases} 1 & \text{if } \mathbf{x} \text{ is within } j \\ 0 & \text{otherwise} \end{cases} \quad (2)$$

In Eq.(2), the elements of the vector $\mathbf{x}$ are the state variables, $\tilde{\mathbf{x}}(\mathbf{x}', k\tau)$ denotes the location of the system in the state-space at time $t = (k+1)\tau$ given that it departed from point $\mathbf{x}'$ at time $t = k\tau$ and $v_{j'}$ is the volume of cell j'. The point $\tilde{\mathbf{x}}(\mathbf{x}', k\tau)$ is determined from a user provided system model describing system evolution in time. The DSD determines the joint pdf $p_k(j)$ for the mean value of the state-variables over cell j at time $t = k\tau$ recursively from

$$p_k(j) = \sum_{j'} g(j \mid j', \tau) p_{k-1}(j') \quad (k = 0,1,\cdots). \quad (3)$$

A two node lumped parameter model has been developed for the CTPS [3], representing Node 1 and 2 (see Fig.1) temperature behavior during the calibration mode. By writing the energy conservation equations for the two nodes, the system equations are obtained as [3]:

$$C_1 \frac{dT_2}{dt} = (q_n + q_e) - \frac{1}{R_1}(T_2 - T_1)$$
$$C_2 \frac{dT_1}{dt} = \frac{1}{R_1}(T_2 - T_1) - \frac{1}{R_2}(T_1 - T_0) \quad (4)$$

where T_1 indicates Node 1 temperature; C_1, C_2 are, respectively, thermal capacitance of Nodes 1 and 2; R_1 is the thermal resistance between Node 2 and Node 1. The other notation in Eq.(2) is as defined previously.

Estimation Engine

In Eq.(4) all the variables except R_2, T_0 and q_n are assumed to be known. A flowchart of the estimation engine for these parameters is shown in Fig. 2.

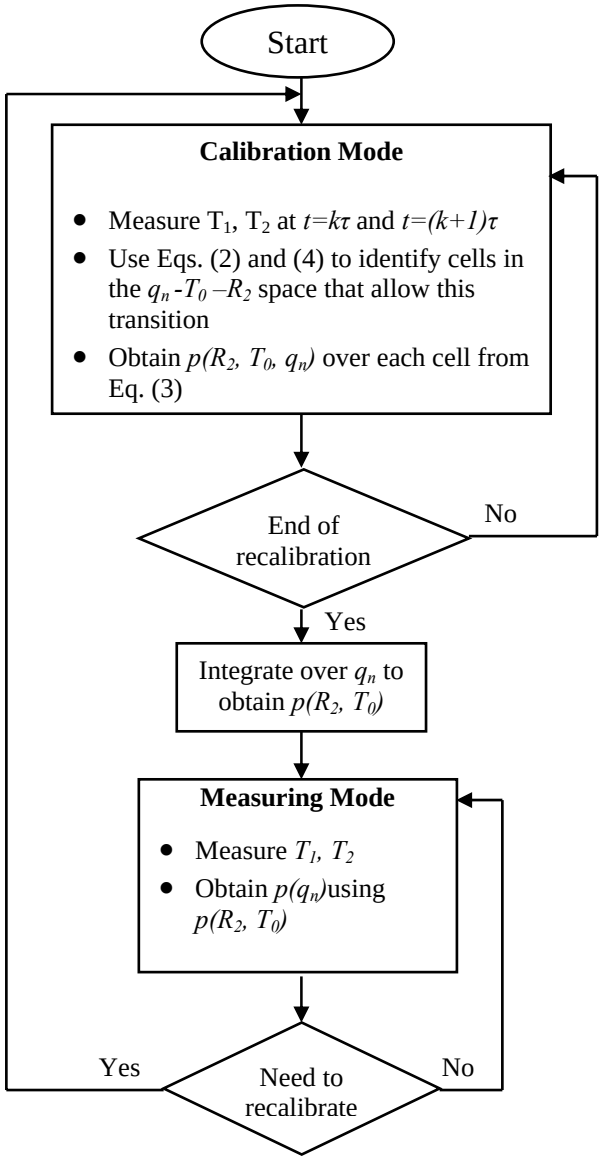

Fig. 2 Estimation engine

In the calibration mode, DSD is run to estimate the values for T_0, R_2 and q_n, in terms of joint pdf $p(R_2,T_0, q_n)$ over the discretized R_2-T_0-q_n space by measuring T_1 and T_2 and using Eqs.(2)-(4). At the end of calibration, $p(R_2,T_0, q_n)$ is integrated over all values of q_n to obtain joint pdf of $p(R_2,T_0)$.

Before the actual algorithm is started, the following are defined for each of the three unknown parameters (R_2, T_0, q_n): a) the ranges of interest (minimum and maximum values $R_{2,min}$, $R_{2,max}$, $T_{0,min}$, $T_{0,max}$, $q_{n,min}$, $q_{n,max}$), b) the number of intervals for each range that will discretize the q_n-T_0-R_2 space into cells, and, c) error σ for the temperature measurements T_1 and T_2. A three dimensional matrix which represents the cells in terms of cell-centered values of R_2, T_0, q_n and which will store $p_k(j)$ (see Eq.(3)) is created and initialized to a uniform distribution $p_0(j)$ (Figure 3(a)).

At t = 0, the sensor starts in the calibration mode trying to estimate the values for T_0, R_2, q_n. Values of T_1, T_2 and q_e for $t=0$ and $t=1$ seconds are read from an input file that simulates the actual sensor signals. Since CTPS is in the calibration mode, q_e = 0 in Eq.(4). Using the simulated $T_1(0)$, $T_2(0)$, $T_1(1)$ and $T_2(1)$, the DSD then searches for the cells that would make this transition possible within the error σ for the temperature measurements from Eqs.(2) - (4) using an equal-weight 4-point quadratures scheme to evaluate the integral in Eq.(2).

The algorithm continues for t = 2, 3... 6 seconds. The temperature signals are read again, the cell—to-cell transition probabilities are recomputed from Eq.(2) based on the current time step and used for recalculating the cell-averaged values of p_k (R_2, T_0, q_n) from Eq.(3) for k=2, 3…6. After each time step the probabilities are rescaled such that they sum to unity over all cells. After 6 seconds, the sensor is switched back to the measurement mode.

At the end of calibration mode, cell-averaged values of $p(R_2, T_0, q_n)$ for each cell j in the q_n-T_0-R_2 space are obtained in the form of $p_6(j)$ from Eq.(3). Integration of $p(R_2, T_0, q_n)$ over q_n yields the joint pdf for R_2 and T_0.

Using this probability distribution function of R_2 and T_0 obtained at the end of the calibration mode, a probability distribution function of q_n can be obtained. By using the minimum and maximum values for R_2 and T_0 in a cell of nonzero probability P, the cell minimum and maximum values for q_n ($q_{n,min}$ and $q_{n,max}$) can be obtained from Eq. (1). It results that q_n is in interval ($q_{n,min}$, $q_{n,max}$) with a probability P. Repeating the calculation for all cells in the R_2 - T_0 space, a pdf of q_n is derived.

Fig.3 shows graphically how this estimation engine works in the discretized q_n-T_0-R_2 space. Fig. 3(a) shows the initial q_n-T_0-R_2 space, where all cells have assigned equal nonzero probabilities (i.e. $p_0(j)$). Then using Eqs.(2) – (4) at successive time steps, the number of cells that have nonzero probabilities narrows down (Fig. 3(b) and Fig. 3(c)).

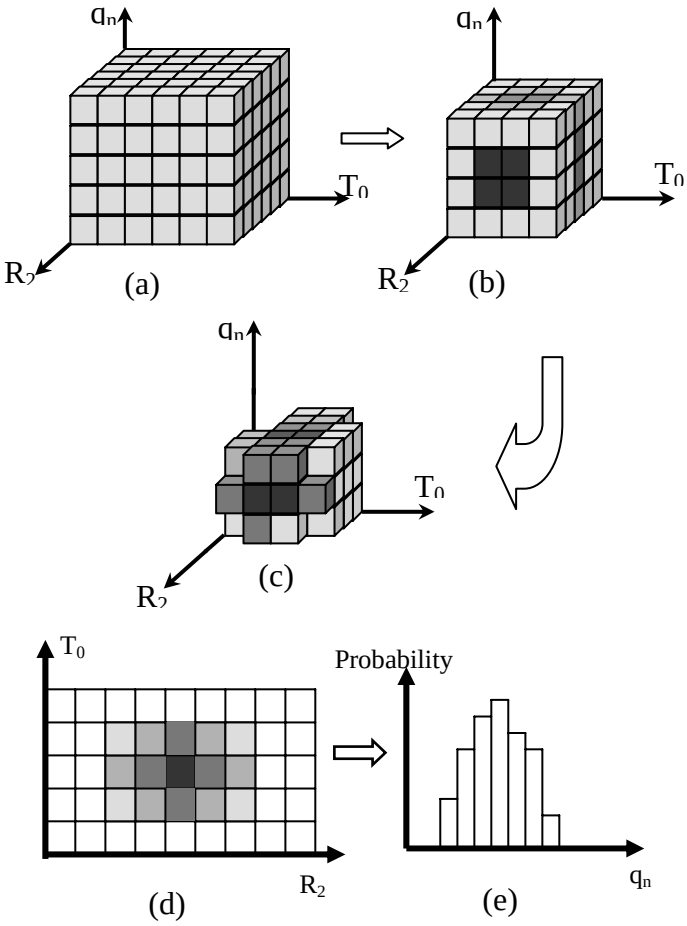

Fig. 3 A graphical illustration of the estimation engine

The different shades of gray represent different probabilities, darker gray represent higher probability than lighter gray. Figure 3(d) shows the probability distribution function of R_2 and T_0 that is obtained at the end of calibration mode and which is used for obtaining the pdf $p(q_n)$ in the measuring mode (Fig. 3(e)).

Scheduler

The estimation engine has been implemented in Java, taking advantage of the modularization capabilities of object-oriented programming. A thread class, running the estimation engine was created. The purpose of the scheduler is synchronize the threads such that data for all sensors at same moment in time can be collected, put together, analyzed and interpolated. Figure 4 shows the conceptual scheduler structure as it would be implemented in a plant. The pdf for q_n between sensor locations (local power estimation) will be estimated using the procedure described in [3].

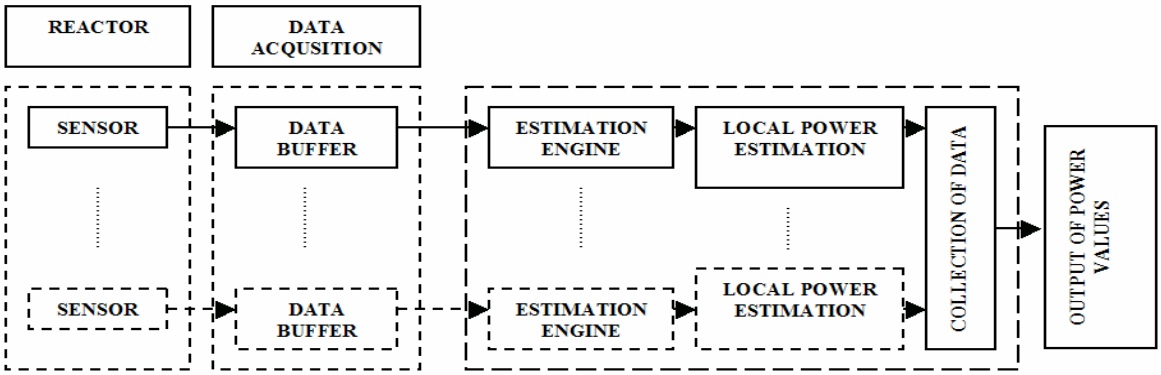

Fig.4 The conceptual scheduler structure

3. EXAMPLE SYSTEM AND RESULTS

Since real sensor data cannot be obtained at this point of the research, a simulation of sensors signals was performed. It was assumed that seven sensors are axially distributed within the core of a pebble bed type reactor [6]. The power/flux is assumed to follow a cosine function axially. The coolant temperature increases continuously from the inlet to the outlet. Data for steady-state power conditions were taken from [6] and are shown in Table 1. The sensors locations and normal power densities and coolant temperatures are shown in Table 1.

Sensor #	Distance from Coolant Inlet (cm)	Deposited Nuclear Energy q_n (W)	Coolant Temperature (K)
1	5	3.09	455
2	10	4.63	610
3	20	6.07	1208
4	30	6.56	1560
5	40	6.07	2085
6	50	4.68	2503
7	55	3.14	2950

Table 1 Simulated data for the example system

From steady-state conditions, it is assumed that a cooling transient occurs in which the coolant temperature start decreasing, while the power density q_n and the thermal resistance R_2 remain constant. The coolant temperature follows

$$T_0(t) = T_0(0)\, e^{-(t-10)/3600} \qquad (5)$$

where the time t is given in seconds [6].

The sensor recalibration is performed every minute, for a six seconds time interval. During these six seconds $q_e = 0$. Since the thermal energy input to the sensor core consists only of the nuclear heat, decay in the sensor temperature will be observed. After the decay, the electric current is switched on again, the sensor temperature increases back to its setpoint value (which is indicated in the last column of Table 1).

The estimation engine was run with 7 parallel threads, each thread handling one sensor. Because of the relatively long computation times, a parallel implementation on multiple processors of the estimation algorithm was also created, this time using C++ and MPI. It was observed that reasonable computation times were achieved when the estimation algorithm it is run on more than two processors.

The results in terms of pdfs of q_n are shown in Fig. 6 and 7. Figure 6 shows a sample pdf for all sensors at a given moment in time. Fig. 7 shows the pdf for Sensor 1 at different moments in time. Both figures represent results for a transient in which the nuclear energy remains constant, while the coolant temperature decreases. In both cases, it can be seen that the probability distribution functions are centered around the expected value for q_n (listed in column 3 of Table 1). In Figure 6, it can be seen that since q_n at detector locations do not vary with time, neither do the pdf's.

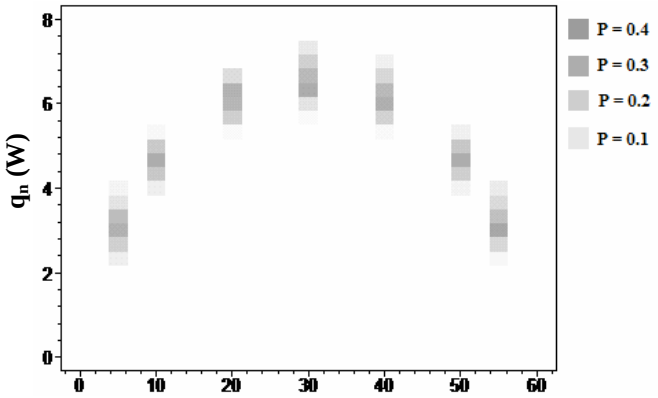

Fig. 5 Pdf of power density at all sensor locations, at $t=7$ seconds

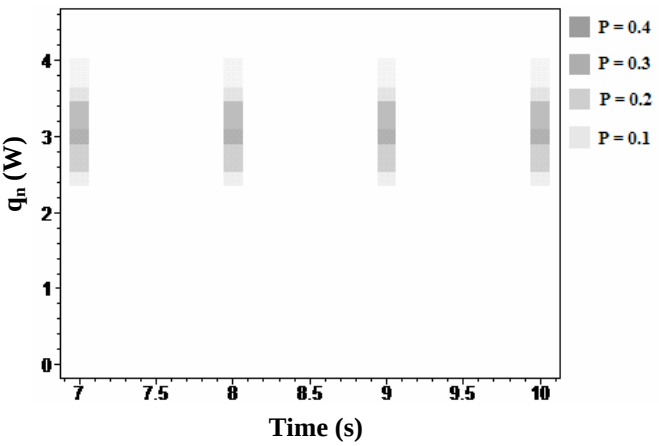

Fig 6 Evolution in time of pdf of power density for Sensor #1

4. CONCLUSIONS

This study illustrates how the CTPS can be used with DSD for an array of sensors to construct a probabilistic map of power distribution in a nuclear reactor. The study also extends the work reported in [6] from the estimation of R_2 and T_0 to the estimation of q_n as well as R_2 and T_0 using Eq.(2). The results of the study indicate that the estimation engine described in Fig.2 can be implemented in a computationally feasible manner to obtain probabilistic maps of power distribution in nuclear reactor under steady-state operation as well as transients.

5. REFERENCES

[1] T. D. Radcliff, S. Liu, D. Miller, "Modeling and Optimization of a Constant-Temperature In-Core Power Sensor", **Nuclear Technology**, Vol. 140, 2002, pp. 209-221.

[2] P. Wang, X. M. Chen, T. Aldemir, "DSD: A Generic Software Package For Model-based Fault Diagnosis in Dynamic Systems", **Reliab. Engng & System Safety**, Vol. 75, January 2002, pp. 1-39.

[3] M. Biro, T. Aldemir, "Quantifying the Measurement Uncertainty Propagation In Flux/Power Reconstruction", **Proceedings of NPIC&HMIT 2004**, pp. 1246-1253, American Nuclear Society, LaGrange Park, IL (September 2004)

[4] I. Munteanu, H.B. Zhou, T. D. Radcliff, T. Aldemir, D. W. Miller, "In-Core Power Detection Using DSD", **Trans. Am. Nucl. Soc**., Vol. 83, November 2000, pp. 279-281.

[5] A. Burghelea, T. Aldemir "A Parametric Investigation of the Recursive Partitioning Approach to DSD for Implementation with CTPS", **Trans. Am. Nucl. Soc.**, Vol. 89**,** November 2003, pp. 493-495.

[6] T. Aldemir, D. W, Miller, A. Burghelea, "Direct Estimation of Power Distribution in Reactors for Nuclear Thermal Space Propulsion", **Space Technology and Applications International Forum—STAIF 2004**, M. S. El-Genk (Ed.), pp. 582-589, American Institute of Physics, Melville, N.Y. (February 2004)

Probabilistic Safety Assessment and Management: PSAM 7-ESREL'04,
C. Spitzer, U. Schmocker, V. N. Dang (Eds.), 1821-1827, Springer – Verlag,
London, U.K. (June 2004)

An Application of DSD with Recursive Partitioning Scheme to Constant Temperature Power Sensors

Andrei Burghelea and Tunc Aldemir
The Ohio State University, 206 West 18th Avenue,
Columbus, OH 43210, U.S.A.

Abstract

The DSD (Dynamic System Doctor) is system independent, state/parameter estimation software. The DSD is based on the modeling of system evolution in terms of probability of transitions within user specified time intervals between sets of user defined parameter/state variable magnitude intervals that partition the system state space. Recently a recursive partitioning scheme has been developed for DSD that reduces the estimation time and memory requirements, as well as making DSD more user friendly. The scheme is illustrated using a non-linear model for the constant temperature power sensor, proposed for direct core power distribution monitoring in Generation 4 nuclear power reactors

1 Introduction

The DSD (Dynamic System Doctor) is a system independent, state/parameter estimation software [1] based on the cell-to-cell mapping technique (CCMT). The CCMT models the system evolution in terms of probability of transitions in time between sets of user defined parameter/state variable magnitude intervals (cells) within a user specified time interval (e.g. data sampling interval). It yields the lower and upper bounds on the estimated values of system variables/parameters (which may be important in the determination of the operational safety margins for the system), as well as the probability distribution of the variables/parameters within these bounds which provides a probabilistic measure to rank the likelihood of system faults in view of modeling uncertainties and/or signal noise.

The original DSD algorithm requires the cell definitions as input to the estimation process which may lead to long run times and large memory requirements. Recently a recursive scheme for cell definitions was proposed for DSD that reduces the estimation time and memory requirements [2]. This paper illustrates the estimation time and memory savings using a non-linear model for

the constant temperature power sensor (CTPS), proposed for direct core power distribution monitoring in Generation 4 nuclear power reactors [3].

2 Overview of the DSD Algorithm with Recursive Partitioning [2]

The DSD estimation algorithm is based on the representation of the system dynamics in terms of transition probabilities between user specified cells that partition the system parameter/state space during user specified time intervals $k\tau \le t < (k+1)\tau$ (k = 0, 1,…). These cells are obtained by dividing the range of interest $a_l \le x_l \le b_l$ for the state variable $x_l (l = 1,\cdots,L)$ into $j_l = 1,\cdots,J_l$ intervals Δ_{l,j_l} and the range of interest $\tilde{a}_m \le \alpha_m \le \tilde{b}_m$ for the parameter $\alpha_m (m = 1,\cdots,M)$ into $n_m = 1,\cdots,N_m$ intervals $\tilde{\Delta}_{m,n_m}$, in a manner similar to those used in finite difference or finite element methods. Such partitionings are provided as user input to DSD. A sample partitioning for a second order system where only one of the state variables is monitored is shown in [2], as well as how the cell-to-cell transition probability $g(j \mid j',n',\tau)$ from cell j' to cell j during $k\tau \le t < (k+1)\tau$ while the system parameters remain in cell n' can be approximated using a 4-point quadrature scheme. The DSD yields the *a posteriori* probabilities $p_{k+1}(j,n)$ that $x_l[(k+1)\tau] \in \Delta_{l,j_l}$ and $\alpha_m \in \tilde{\Delta}_{m,n_m}$ at $t = (k+1)\tau$ $(j_l = 1,...,J_l; l = 1,...L)$ from

$$p_{k+1}(j,n) = \frac{\sum_{j' \in J_k} g(j \mid j',n',\tau)\, p_k(j',n')}{\sum_{n'} \sum_{j' \in J_k} p_k(j',n')} \quad (j \in J_{k+1})(k = 0,1,...) \qquad (1)$$

using the $p_k(j,n)$ estimated at time $t = k\tau$ as *a priori* probabilities The $p_k(j,n)$ determined from Eq.(1) can then be used to determine all the statistical properties of the system state, such as expected values and credibility intervals of the system variables.

If the values of the system parameters change in time, the estimation procedure may lose track of the variables to be estimated, i.e. all the $p_k(j,n)$ obtained from Eq.(1) will be zero. In the original DSD algorithm with this fixed partitioning scheme (FPS), the estimation process will reinitialize itself in this situation by starting from the initial probability $p_0(j,n)$ and estimate the new parameter by the recursive use of Eq.(1) again by searching over all the cells. This approach may lead to excessive computational time if there are frequent parameter changes during system evolution and a large number of variables/parameters to be estimated. The recursive partitioning scheme (RPS)

reduces the computational time for reinitialization (as well as overall memory requirements for DSD) through following steps:

1. Input parameter and state variable ranges of interest (i.e. $a_l \le x_l \le b_l$ and $\tilde{a}_m \le \alpha_m \le \tilde{b}_m$), RPS stopping rules and monitored data uncertainty. Read data from the monitors.
2. Define the intervals Δ_{l,j_l} for the monitored variables so as to contain the variation/noise on the monitored data, centred on their median values. Define the cells for the unmonitored variables by bisecting each state variable range of interest $a_l \le x_l \le b_l$ and each parameter range of interest $\tilde{a}_m \le \alpha_m \le \tilde{b}_m$ (i.e. $J_l = 2, N_m = 2$ for all l and m to be estimated).
3. Specify $p_0(n, j)$ to be used to start the estimation process (usually uniform)
4. Determine the cell-to-cell transition probabilities $g(j \mid j', n', \tau)$ by quadratures or by sampling over the cells specified in Step 2.
5. Find $p_k(n, j)$ from Eq.(1).
6. If all $p_k(n, j) = 0$, then bisect each Δ_{l,j_l} and go to Step 3. Otherwise, normalize $p_k(n, j)$ by dividing it by the total probability of finding the system in the search space, increment the time index *k* and go to Step 2.

Steps 2 through 6 are repeated until convergence, i.e. $p_k(n, j)$ are all zero except for the cells containing the actual system locations. It should be mentioned at this point that the algorithm may not converge for rapidly evolving systems during one data sampling interval $k\tau \le t < (k+1)\tau$. However, even in this situation, previous work a with reduced order reactor dynamics model shows that the expected values of the parameters/state variables to be estimated are often found to be close to their actual values [4].

3 The CTPS

The CTPS consists of a UO_2 pellet surrounded by an electrical heating resistance wire. The pellet and the wire form the sensor core (Node 2). The core is surrounded by ceramacast, which is an alumina based ceramic thermal insulator (Node 1). Both the sensor core and the insulator are coated with thin layers of copper to provide a pathway for heat transfer from the sensor core to the surrounding coolant. A feedback control loop is used to provide the exact amount of input electrical energy q_e (in kW) needed to keep the temperature T_2 (in K) of the Node 2 constant in time (*t*), well above the surrounding coolant temperature T_0 (in K), regardless of the nuclear energy q_n (in kW) deposited into Node 2 (Mode 1 operation). In Mode 1 operation we have

$$q_e + q_n = \frac{T_2 - T_1}{R_1} = \frac{T_1 - T_0}{R_2} = \frac{T_2 - T_0}{R_1 + R_2} \tag{2}$$

where T_1 is the temperature of the ceramacast insulator, R_1 (in K/kW) is the contact resistance between Node 1 and Node 2 and R_2 (in K/kW) is the contact resistance between Node 1 and the coolant.

A mode-switching algorithm has been proposed to accomplish the compensation of the change in the sensor response with the change in R_2 as a function of T_0 and other coolant properties. In Mode 2 operation, the sensor is temporarily taken out of the control loop, or practically, the supplied electrical current is reduced to 1% of the steady state value. In this mode of operation, the time rates of change in Node 1 and Node 2 temperatures are described by

$$C_1 \frac{dT_2}{dt} = (q_n + q_e) - \frac{1}{R_1}(T_2 - T_1)$$

$$C_2 \frac{dT_1}{dt} = \frac{1}{R_1}(T_2 - T_1) - \frac{1}{R_2}(T_1 - T_0) \qquad (3)$$

where C_i is the thermal capacitance (in KJ/K) of Node i (i=1,2). For constant q_n, q_e, C_i and R_i, Eq.(3) yields

$$T_i(t) = T_0 + \theta_{1i} e^{-\theta_2 t} + \theta_{3i} e^{-\theta_4 t} \quad (i = 1,2) \qquad (4)$$

where θ_{1i} and θ_{3i} are known functions of q_n, q_e, sensor properties and Mode 1 sensor temperatures,

$$\theta_2 = \frac{1}{2}\left[\gamma + \sqrt{\gamma^2 - 4}\right] \qquad \theta_4 = \frac{1}{2}\left[\gamma - \sqrt{\gamma^2 - 4}\right] \qquad (5)$$

with

$$\gamma = \frac{1}{C_1 R_1} + \frac{1}{C_2 R_2} + \frac{1}{C_2 R_1}. \qquad (6)$$

The resistance R_1 and the capacitances C_1 and C_2 is a function of the sensor properties only and can be determined off-line. Then the nuclear energy deposition rate q_n and the resistance R_2 can be estimated directly through Eq.(3) and measured $T_i(t)$ (i =1 and/or 2) and q_e or, for constant sensor properties, through Eqs.(4), (5) (6) and the measured $T_i(t)$ and q_e. The sensor operation

involves switching between the feedback-controlled constant-temperature mode (i.e. Mode 1) and the dynamic temperature decay mode following the opening of the feedback loop (i.e. Mode 2).

4 Implementation and Results

Two cases were considered, one of normal operation with a switch between the operation modes of the sensor with constant coolant temperature T_0 (Case 1), and a second one, a slow transient with decreasing T_0 (Case 2). Node 1 and 2 temperatures for the estimation process were simulated using Eq.(3) with the parameter values given in Table 1.

T_0(K)	T_2(K)	C_1(J/K)	C_1(J/K)	R_1(K/W)	R_2(K/W)	q_n(W)	q_e(W)
1000.0	1085.9	0.00804	0.744	5.709	1.857	1.68	9.67

Table 1. Steady-State Parameter Values Used for the Generation of Simulated CTPS Data

The choice of the temperature data in Table 1 reflects the expected steady-state operational conditions in Generation 4 gas cooled reactors.

Figures 1 and 2, respectively, show the estimation results for Case 1 and Case 2 using RPS. The spikes starting at around t=10 s in both Figs.2 and 3 at around indicate the time at which the initial switch from Mode 1 to Mode 2 is made. The figures show that while DSD temporarily looses track of q_n at the time of the switch, recovery is very rapid and DSD with the RPS is able to estimate q_n with the desired accuracy (within 1% of the range of interest) for the rest of the time interval of interest (i.e. until 100 s). Comparison of the run times and memory requirements to obtain the results in Figs.2-4 to those obtained using the original FPS for comparable accuracy indicates a speedup by a factor of 5 in the run time with RPS and a reduction by a factor of 2 in memory requirements.

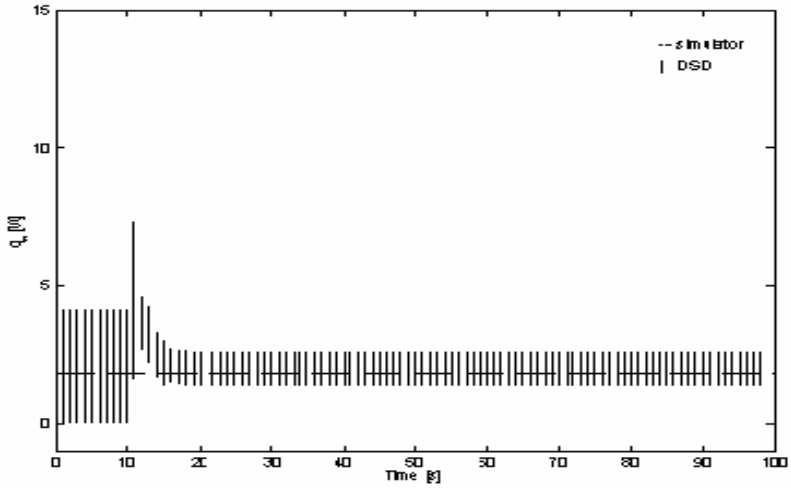

Figure 1. Simulated and Estimated q_n as a Function of Time for Case 1

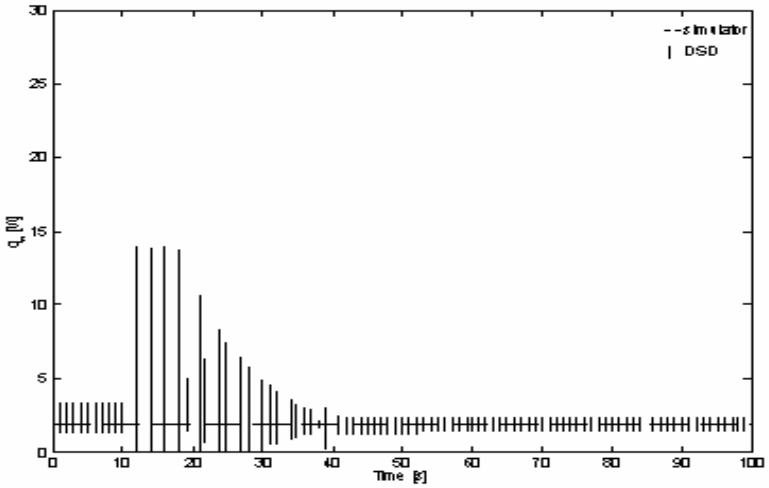

Figure 2. Simulated and Estimated q_n as a Function of Time for Case 2

5 Conclusion

The results of this study show that the DSD with RPS leads to substantial run time and memory savings compared to the original FPS. The results of the study also show that the use of CTPS with DSD may be a feasible option for direct measurement of power distribution in Generation 4 reactors.

References

1. Wang P, Chen X-M, Aldemir T. DSD: a generic software package for model-based fault diagnosis in dynamic systems. Reliab Engn & System Safety 2002; 28, 31-39
2. Burghelea A, Munteanu I, Aldemir T. A Recursive Partitioning Approach to DSD”**,** *PSA2002:* Proceedings of the International Topical Meeting on Probabilistic Safety Assessment, Apostolakis G E, Aldemir T (Eds), 630-635, American Nuclear Society, La Grange Park, IL , 2002
3. Radcliff TD, Miller DW, Kauffman AC. Modeling of A Constant-Temperature Power Sensor. In: ICONE-8, Proceedings of 8th International Conference on Nuclear Engineering. American Society of Mechanical Engineers, New York, 2000
4. Wang P. Some improvements in state/parameter estimation using the cell to-cell mapping technique. Ph.D. thesis, The Ohio State University, 2002

NUCLEAR SCIENCE AND ENGINEERING: **147**, 1–25 (2004)

Some Improvements in State/Parameter Estimation Using the Cell-to-Cell Mapping Technique

Peng Wang and Tunc Aldemir*

The Ohio State University
206 West 18th Avenue
Columbus, Ohio 43210

Received May 6, 2002
Accepted November 3, 2003

Abstract—*The cell-to-cell-mapping technique (CCMT) models system evolution in terms of probability of transitions within a user-specified time interval (e.g., data-sampling interval) between sets of user-defined parameter/state variable magnitude intervals (cells). The cell-to-cell transition probabilities are obtained from the given linear or nonlinear plant model. In conjunction with monitored data and the plant model, the Dynamic System Doctor (DSD) software package uses the CCMT to determine the probability of finding the unmonitored parameter/state variables in a given cell at a given time recursively from a Markov chain. The most important feature of the methodology with regard to model-based fault diagnosis is that it can automatically account for uncertainties in the monitored system state, inputs, and modeling uncertainties through the appropriate choice of the cells, as well as providing a probabilistic measure to rank the likelihood of faults in view of these uncertainties. Such a ranking is particularly important for risk-informed regulation and risk monitoring of nuclear power plants. The DSD estimation algorithm is based on the assumptions that (a) the measurement noise is uniformly distributed and (b) the measured variables are part of the state variable vector. A new theoretical basis is presented for CCMT-based state/parameter estimation that waives these assumptions using a Bayesian interpretation of the approach and expands the applicability range of DSD, as well as providing a link to the conventional state/parameter estimation schemes. The resulting improvements are illustrated using a point reactor xenon evolution model in the presence of thermal feedback and compared to the previous DSD algorithm. The results of the study show that the new theoretical basis (a) increases the applicability of methodology to arbitrary observers and arbitrary noise distributions in the monitored data, as well as to arbitrary uncertainties in the model parameters; (b) leads to improvements in the estimation speed and accuracy; and (c) allows the estimator to be used for noise reduction in the monitored data. The connection between DSD and conventional state/parameter estimation schemes is shown and illustrated for the least-squares estimator, maximum likelihood estimator, and Kalman filter using a recently proposed scheme for directly measuring local power density in nuclear reactor cores.*

I. INTRODUCTION

State/parameter estimation techniques play an important role in dynamic system analysis for fault detection, system identification, and adaptive control. Although parameter estimation in linear systems is by now a well-established field, nonlinear system parameter estimation is still a popular research area.

Among the large number of conventional parameter estimation techniques used for nonlinear dynamic systems, the largest category is based on optimizing the value of the estimates by minimizing a predefined objective function or loss function (i.e., least squares, weighted least square, minimum mean square error). These techniques usually involve solving a linear or nonlinear minimization problem with or without constrains. Closed-form solution of the nonlinear minimization problem is often not available, and numerical methods (e.g., dynamic programming, discrete Euler-Lagrange equations, the

*E-mail: aldemir.1@osu.edu

Gauss-Newton method) have been proposed and widely used in parameter estimation. Mook[1] considers the optimal state and parameter estimation under model error for nonlinear dynamic systems. The unknown parameters are estimated using the least-squares method by minimizing the model error estimate. The minimization problem is solved as a two-point boundary-value problem. The method is shown to be accurate and robust with respect to large errors in system model and measured data, but the model error estimate may contain discontinuities in case of noisy measurement. In Albuquerque and Biegler's[2] paper, the objective function is defined as the sum of a set of functions that depend on the states and inputs at one time, and the constrains are differential equations. A nonlinear dynamic programming (NLP) problem is defined by discretizing the differential equations. Even though the paper presents a faster solver for the NLP problem, the major limitation of this approach is that the size of the NLP problems grows linearly with the number of data sets and the heavy computational load makes it difficult to solve larger problems directly. Guay and McLean[3] present a method for estimation of parameters in nonlinear dynamic systems described by a set of ordinary differential equations by optimization of the Box and Draper (or least-squares) criterion. The decoupled direct method is applied to evaluate the gradient and Hessian matrix of the objective function with respect to the parameters. The authors state that using second-order sensitivity coefficients to evaluate the Hessian matrix can lead to more accurate and reliable results. However, the computation of higher-order sensitivity coefficients increases drastically the computational time and storage. The computational load and storage are also the major problem associated with Hjelmstad's method[4] in order to obtain acceptable accuracy. Another least-squares method, developed by Liu,[5] includes a fast adaptive least-squares algorithm for parameter estimation that is based on Householder transformations. The author indicates that this algorithm requires computation and storage load in the order of $O(N)$ instead of $O(N^2)$, where N is the number of parameters to be estimated. One limitation of this algorithm is that it requires the system to be linear with respect to the unknown parameters. In addition, the estimated parameters may not converge to the true value in case of correlated noise. Dimogianopoulos and Lozano[6] propose a least-squares–based nonrecursive identification algorithm in their paper. The authors chose the L_2 norm of the identification error with a forgetting factor as the minimization criterion. This technique is capable of dealing with slowly time-varying parameters without explicit knowledge of the noise bound or the region where the true parameters lie. However, the bounds on the noise and the parameter variations should be small to obtain meaningful properties of the estimates.

Another widely used technique in parameter estimation problems is to use linearized system models about an operating point. Hopkins and Van Landingham[7,8] propose a method of simultaneous parameter and state estimation called pseudolinear identification (PLID) for stochastic linear time-invariant discrete-time systems with single input single output[7] and multiple inputs multiple outputs.[8] The authors state that the PLID is known to converge, but in the presence of a large amount of noise, this convergence may be practically impossible or so slow as to be useless. Douce and Zhu[9] describe a method for the modeling of nonlinear single-input single-output systems using a modified least-squares method. The application of this method requires that the nonlinear systems be perturbed only in a restricted operating range and the system can be linearized inside this operating range. An autoregressive moving average model is used in order to approximate a wide range of nonlinear systems. A weighted least-squares algorithm for parameter estimation is proposed in order to handle the nonlinearity of the dynamic system. Recently, Lyashevskiy and Chen[10] have developed an innovative identification procedure by applying the harmonic linearization method. Using this technique, the nonlinearity of the system is replaced by a set of harmonic linearized elements, which is obtained through the describing function method. The unknown parameters are solved from a set of algebraic equations that are obtained from the self-oscillations. One limitation of this technique is that it can be applied only for dynamic systems with limit cycles.

A technique that can perform parameter estimation and also deal with unobservable states and variables in nonlinear dynamic systems is to generate observers. Ricardo and Tomei[11] demonstrate adaptive observers that guarantee fast exponential convergence. However, the method is only applicable for a class of nonlinear dynamic systems that are linear with respect to unknown parameters, and the construction of the observers requires the system to be in adaptive observer form. Sliding-mode control and estimation techniques have also been shown to be an effective tool in parameter/state estimation problems. The sliding-mode approach to state/parameter estimation in nonlinear dynamic systems consists of designing the model with discontinuous parameters and enforcing sliding modes such that the model and plant outputs coincide. Then, the average values of the discontinuous parameters depend on the unknown states/parameters and can be used for their evaluation. McCann and Islam[12] have applied the sliding-mode observer method to the operation of a switched reluctance motor to estimate the rotor position and velocity. Sliding-mode observers have also been used in nuclear reactivity and xenon concentration estimation problems by Wang, Aldemir, and Utkin.[13] Kim, Rizzoni, and Utkin[14] apply the sliding-mode estimation idea to an automotive engine diagnosis and control problem. The unknown charge efficiency, mean mass flow rate of air, and throttle angle are estimated through a well-designed sliding-mode observer. The results show that

the observer estimates the actual states within reasonable accuracy.

Statistical parameter estimation methods are also used in dynamic system analysis. The advantage of statistical methods is that these methods deal with uncertainty and noise directly. One commonly used statistical parameter estimation technique is Bayesian estimation. Bolviken et al.[15] use Bayesian state estimation in nonlinear systems. The unknown state vectors are drawn many times from the posterior distribution, and the average is used to be the approximate of the posterior mean. The authors apply the Monte Carlo technique to randomly select points in the range of interest and argue that the Monte Carlo uncertainty is small compared to the inherent uncertainty in the optimal Bayesian estimate. A limitation of this technique is that it gives only sample points of the posterior distribution; the actual posterior distribution is unavailable. Charalambous and Logothetis[16] apply the maximum-likelihood idea to the nonlinear stochastic system parameter estimation problems. The expectation maximization algorithm, an interactive numerical method, is used to generate the parameter estimates by computing the log-likelihood ratio restricted to the measured data. However, the technique is still a point estimator without providing an efficient way to evaluate the uncertainty of the estimation results. Also, the estimation algorithm is system specific and needs to be individually set up for a given system.

Expert systems, neural networks and genetic algorithms have been also used for parameter estimation. Parlos and Atiya[17] use artificial neural networks for the identification of a nonlinear model for a U-tube steam generator. The system identification consists of estimating unknown parameters and/or system variables, which cannot be monitored, in order to obtain a complete model for the system. A similar work by Patton, Lopez-Toribio, and Uppal[18] uses artificial intelligence techniques for fault detection and identification in process systems. Marseguerra and Zio[19] apply a genetic algorithm for estimating the effective nuclear parameters and the initial conditions in tracking xenon evolution using measured power and reactivity. The authors state that the estimation results given by this approach are very close to the true values.

The literature survey shows that the parameter/state estimation of nonlinear systems seems to have the following difficulties:

1. Heavy computational load and large computer memory are required if accurate estimates of the parameters are desired. This requirement usually reduces the capability of most methods for on-line implementation.

2. Noise is difficult to handle, especially when the noise is large.

3. Most methods cannot account for random variations in the parameters.

4. Most estimators are point estimators without providing likelihood of possible parameter values, which renders their implementation difficult for probabilistic risk analysis.

5. Often, the algorithms are system specific and need to be designed for the given system.

The recent developments in state/parameter estimation show that the representation of system dynamics via the cell-to-cell mapping technique[20] (CCMT) may reduce these difficulties. The CCMT models the system evolution in terms of probability of transitions in time between sets of user-defined parameter/state variable magnitude intervals (cells) within a user-specified time interval (e.g., data-sampling interval). The cell-to-cell transition probabilities are obtained from the given system model. Then, using the Chapman-Kolmogorov equation, the probability of finding the system in a given cell at a given time interval is recursively determined from a Markov chain. The most important feature of the methodology with regard to model-based fault diagnosis is that it can automatically account for uncertainties in the monitored system state, inputs, and modeling uncertainties through the appropriate choice of the cells, as well as providing a probabilistic measure to rank the likelihood of faults in view of these uncertainties. Such a ranking is particularly important for risk-informed regulation and risk monitoring of nuclear power plants. Other important features of this methodology are as follows:

1. It does not require a linearization of the system.

2. It allows flexibility in system representation. Differential or difference equations[21,22] as well as almost any type of input/output model (e.g., neural net,[23] response surface) can be used to generate the cell-to-cell transition probabilities.

3. The discrete-time nature of the methodology is directly compatible with a lookup table implementation, which is very convenient for the use of data that may be available from tests or actual incidents.

4. It does not require model inversion (which may lead to singularity problems) or inverse models (which usually have a limited range of applicability).

5. It is both an interval and a point estimator. Subsequently, it yields the lower and upper bounds on the estimated values of state variables/parameters as well as their expected values. A knowledge of such bounds is particularly important in the determination of safety margins during operation.

The Dynamic System Doctor[24] (DSD) software package has been developed for the on-line implementation of this methodology in a system-independent and user-transparent manner. The software has been successfully

tested on a variety of nuclear and mechanical dynamic systems.[20–22] An interactive demonstration version of DSD is available from the internet.[25]

The DSD estimation algorithm is based on the assumptions that the measurement noise is uniformly distributed and the measured variables are among the state variables. From an implementation viewpoint, this assumption implies that arbitrary observers and measurement noise or model uncertainties with arbitrary distributions are not allowed. This paper presents a new theoretical basis for the DSD algorithm that waives these assumptions using a Bayesian interpretation of CCMT-based state/parameter estimation (Sec. II). The new theoretical basis expands the applicability range of DSD and leads to improvements in the estimation algorithm (Sec. III), as well as providing a better understanding of the relationship of CCMT-based state/parameter estimation to conventional state/parameter estimation techniques (Sec. IV) and of the origins of some unexplained phenomena encountered in previous work (Sec. II.B). Section V gives the conclusions of the study.

II. A NEW THEORETICAL BASIS FOR CCMT-BASED STATE/PARAMETER ESTIMATION

The new theoretical basis is developed in two steps. In Sec. II.A, a continuous Bayesian state/parameter estimator is presented for an arbitrary dynamical system. Section II.B applies this Bayesian estimator to a discretized representation of the system used by CCMT and develops a generalized algorithm applicable to arbitrary stochastic variations in the dynamical system variables and parameters. Section II.B also shows that this generalized algorithm reduces to the previous DSD algorithm under the assumptions that the measured variables are part of the state variable vector and the measurement noise is uniformly distributed.

II.A. A Continuous Bayesian Estimator

Consider the dynamic system

$$\dot{\boldsymbol{x}} = \boldsymbol{f}(\boldsymbol{x}) + \boldsymbol{v}$$

and

$$\boldsymbol{y}_k = \boldsymbol{h}(\boldsymbol{x}_k) + \boldsymbol{w}_k \quad (k = 0,1,2,\ldots) \ , \tag{1}$$

where

$\boldsymbol{x}$ = L-dimensional vector whose elements are the state variables $x_l (l = 1,\ldots,L)$ of the dynamic system

$\boldsymbol{v}$ = system noise (e.g., due to stochastic variation of system parameters) or a measure of modeling uncertainties, in general

$\boldsymbol{x}_k$ = state vector at time step $k\tau$ $(k = 0,1,2,\ldots)$

$\boldsymbol{y}_k$ = M-dimensional vector whose elements $y_{m,k}$ $(m = 1,2,\ldots,M)$ are the measured data at time step $k\tau$ $(k = 0,1,2,\ldots)$

$\boldsymbol{w}_k$ = measurement uncertainty

$\boldsymbol{h}$ = M-dimensional vector whose elements are known nonlinear functions

$\boldsymbol{f}$ = L-dimensional vector whose elements are known nonlinear functions.

Equation (1) does not exclude parameter estimation problems because we can always define an unknown set of constant parameters $\boldsymbol{\theta}$ as a set of state variables that satisfy the equation

$$\dot{\boldsymbol{\theta}} = 0 \ . \tag{2}$$

Similarly, systems whose dynamics explicitly depend on time can be described by Eq. (1) by regarding time as another state variable satisfying

$$\dot{t} = 1 \ . \tag{3}$$

Subsequently, Eqs. (1) and (2) allow system parameters that are functions of time. Then, by defining the following new state variables:

$$\boldsymbol{z} = \begin{bmatrix} \boldsymbol{x} \\ \boldsymbol{\theta} \end{bmatrix} \ , \tag{4}$$

the new dynamic system can be described as

$$\dot{\boldsymbol{z}} = \begin{bmatrix} \dot{\boldsymbol{x}} \\ \dot{\boldsymbol{\theta}} \end{bmatrix} = \begin{bmatrix} \boldsymbol{f}(\boldsymbol{x}) + \boldsymbol{v} \\ \boldsymbol{0} \end{bmatrix}$$

and

$$\boldsymbol{y}_k = \boldsymbol{h}(\boldsymbol{C}\boldsymbol{z}_k) + \boldsymbol{w}_k \quad (k = 0,1,2\ldots) \ , \tag{5}$$

where $\boldsymbol{C}$ is a matrix with $\boldsymbol{C} = [\boldsymbol{I} \quad \boldsymbol{0}]$ and $\boldsymbol{I}$ is the $L \times L$ identity matrix.

Let $\boldsymbol{x}_k$ denote the state variable value at time step $t = k\tau$. The estimation problem is stated as the following:

> Given an initial guess $p(\boldsymbol{x}_0|\boldsymbol{y}_0)$ of the probability distribution function (pdf) of the unknown state variable vector $\boldsymbol{x}_0$ at time $t = 0$, estimate the conditional distribution $p(\boldsymbol{x}_k|\boldsymbol{y}_k,\boldsymbol{y}_{k-1},\ldots,\boldsymbol{y}_0) = p(\boldsymbol{x}_k|\bar{\boldsymbol{y}}_k)$ of $\boldsymbol{x}_k$ given the measurements $\boldsymbol{y}_k$ from time step $t = 0$ until time step $t = k\tau$. The $\bar{\boldsymbol{y}}_k = [\boldsymbol{y}_k\boldsymbol{y}_{k-1}\ldots\boldsymbol{y}_0]$ is called the information vector that includes all the measurements from the initial time step until time step $t = k\tau$.

While the main motivation for this problem statement is to lay the groundwork for a more generalized theoretical basis for DSD that will be developed in Sec. II.B, the problem statement also addresses the issue of signal validation as will be illustrated later in this section.

Proposition 1:

Assume

1. $p(\boldsymbol{y}_{k+1}|\boldsymbol{x}_{k+1})$ and $p(\boldsymbol{x}_{k+1}|\boldsymbol{x}_k)$ are, respectively, known pdf's for $\boldsymbol{w}_k$ and for $\boldsymbol{v}$ in Eq. (1) or (5) .

2. $\boldsymbol{w}_k$ are statistically independent for all k.

3. $\boldsymbol{v}$ does not depend on the system history.

4. $p(\boldsymbol{y}_{k+1}, \boldsymbol{x}_{k+1}|\bar{\boldsymbol{y}}_k)$ are Borel measurable over $\boldsymbol{x}_{k+1} \in \Omega_{k+1}$, and $p(\boldsymbol{x}_k|\bar{\boldsymbol{y}}_k)$ are Borel measurable over $\boldsymbol{x}_k \in \Omega_k$, where Ω_k is the set of all possible $\boldsymbol{x}_k$ at time step $k\tau (k = 0,1,2\ldots)$.

Then, $p(\boldsymbol{x}_k|\bar{\boldsymbol{y}}_k)$ can be recursively determined from

$$p(\boldsymbol{x}_{k+1}|\bar{\boldsymbol{y}}_{k+1}) = \frac{\displaystyle\int_{\Omega_k} p(\boldsymbol{y}_{k+1}|\boldsymbol{x}_{k+1})p(\boldsymbol{x}_{k+1}|\boldsymbol{x}_k)p(\boldsymbol{x}_k|\bar{\boldsymbol{y}}_k)\, d\boldsymbol{x}_k}{\displaystyle\int_{\Omega_{k+1}} d\boldsymbol{x}_{k+1} p(\boldsymbol{y}_{k+1}|\boldsymbol{x}_{k+1}) \int_{\Omega_k} p(\boldsymbol{x}_{k+1}|\boldsymbol{x}_k)p(\boldsymbol{x}_k|\bar{\boldsymbol{y}}_k)\, d\boldsymbol{x}_k} \quad , \tag{6a}$$

or since $L(\boldsymbol{x}_{k+1}|\boldsymbol{y}_{k+1}) \equiv p(\boldsymbol{y}_{k+1}|\boldsymbol{x}_{k+1})$ can be regarded also as the likelihood of $\boldsymbol{x}_{k+1}$ given the observation $\boldsymbol{y}_{k+1}$, equivalently,

$$p(\boldsymbol{x}_{k+1}|\bar{\boldsymbol{y}}_{k+1}) = \frac{L(\boldsymbol{x}_{k+1}|\boldsymbol{y}_{k+1})p^{prior}(\boldsymbol{x}_{k+1}|\bar{\boldsymbol{y}}_k)}{\displaystyle\int_{\Omega_{k+1}} d\boldsymbol{x}_{k+1} L(\boldsymbol{x}_{k+1}|\boldsymbol{y}_{k+1})p^{prior}(\boldsymbol{x}_{k+1}|\bar{\boldsymbol{y}}_k)} \tag{6b}$$

with

$$p^{prior}(\boldsymbol{x}_{k+1}|\bar{\boldsymbol{y}}_k) = \int_{\Omega_k} p(\boldsymbol{x}_{k+1}|\boldsymbol{x}_k)p(\boldsymbol{x}_k|\bar{\boldsymbol{y}}_k)\, d\boldsymbol{x}_k \quad ,$$

where $\bar{\boldsymbol{y}}_{k+1} = [\boldsymbol{y}_{k+1}\boldsymbol{y}_k \ldots \boldsymbol{y}_0]$.

A practically important situation that satisfies assumptions 1, 2, and 3 is when $\boldsymbol{v}$ represents random fluctuations in system parameters and $\boldsymbol{w}_k$ corresponds to white noise. However, these assumptions do not exclude correlated noise since correlated noise can be regarded as the transformation of a white noise process through a linear filter (when the power spectral density of the correlated noise is in rational form).[26] Assumption 4 implies that

1. all $\Omega_{k+1}\, k = 0,1,\ldots$ must be closed under finite intersection and union of some open subintervals in the ranges of interest $a_l \le x_l \le b_l\ (l = 1,\ldots,L)$ for the state variables/parameters

2. for a given $0 < p(\boldsymbol{y}_{k+1}, \boldsymbol{x}|\bar{\boldsymbol{y}}_k) < 1, \boldsymbol{x} \in \Omega_{k+1}$

and is important for the existence of the integrals in Eq. (6). Since for given initial conditions within the ranges of interest $a_l \le x_l \le b_l$, the system motion is restricted to trajectories generated by Eq. (1), neither of these implications may need be true in the case of nonlinear systems.

Proof:

From the definition of conditional probability and the information vector $\bar{\boldsymbol{y}}_k$,

$$p(\boldsymbol{y}_{k+1}, \boldsymbol{x}_{k+1}|\bar{\boldsymbol{y}}_k) = \frac{p(\boldsymbol{y}_{k+1}, \boldsymbol{x}_{k+1}, \bar{\boldsymbol{y}}_k)}{p(\bar{\boldsymbol{y}}_k)} = \frac{p(\boldsymbol{x}_{k+1}, \bar{\boldsymbol{y}}_{k+1})}{p(\bar{\boldsymbol{y}}_k)} \tag{7}$$

$$p(\boldsymbol{y}_{k+1}|\bar{\boldsymbol{y}}_k) = \frac{p(\bar{\boldsymbol{y}}_{k+1})}{p(\bar{\boldsymbol{y}}_k)}$$

$$\Rightarrow p(\boldsymbol{x}_{k+1}|\bar{\boldsymbol{y}}_{k+1}) = \frac{p(\boldsymbol{y}_{k+1}, \boldsymbol{x}_{k+1}|\bar{\boldsymbol{y}}_k)}{\displaystyle\int_{\Omega_{k+1}} p(\boldsymbol{y}_{k+1}, \boldsymbol{x}_{k+1}|\bar{\boldsymbol{y}}_k)\, d\boldsymbol{x}_{k+1}} \quad . \tag{8}$$

Assumption 4 needs to be used[27] in the decomposition of $p(\bar{\boldsymbol{y}}_{k+1}|\bar{\boldsymbol{y}}_k)$ to obtain Eq. (8) from Eq. (7). Now, consider the following conditional pdf's:

$$p(\boldsymbol{y}_{k+1}|\boldsymbol{x}_{k+1}, \boldsymbol{x}_k, \bar{\boldsymbol{y}}_k) = \frac{p(\boldsymbol{y}_{k+1}, \boldsymbol{x}_{k+1}, \boldsymbol{x}_k, \bar{\boldsymbol{y}}_k)}{p(\boldsymbol{x}_{k+1}, \boldsymbol{x}_k, \bar{\boldsymbol{y}}_k)} \quad ,$$

$$p(\boldsymbol{x}_{k+1}|\boldsymbol{x}_k, \bar{\boldsymbol{y}}_k) = \frac{p(\boldsymbol{x}_{k+1}, \boldsymbol{x}_k, \bar{\boldsymbol{y}}_k)}{p(\boldsymbol{x}_k, \bar{\boldsymbol{y}}_k)} \quad ,$$

and

$$p(\boldsymbol{x}_k|\bar{\boldsymbol{y}}_k) = \frac{p(\boldsymbol{x}_k,\bar{\boldsymbol{y}}_k)}{p(\bar{\boldsymbol{y}}_k)} \quad . \tag{9}$$

From Eq. (8) and assumption 4, the joint pdf $p(\boldsymbol{y}_{k+1},\boldsymbol{x}_{k+1}|\bar{\boldsymbol{y}}_k)$ can be written as

$$\begin{aligned} p(\boldsymbol{y}_{k+1},\boldsymbol{x}_{k+1}|\bar{y}_k) &= \int_{\Omega_k} p(\boldsymbol{y}_{k+1},\boldsymbol{x}_{k+1},\boldsymbol{x}_k|\bar{\boldsymbol{y}}_k)\,d\boldsymbol{x}_k \\ &= \int_{\Omega_k} \frac{p(\boldsymbol{y}_{k+1},\boldsymbol{x}_{k+1},\boldsymbol{x}_k,\bar{\boldsymbol{y}}_k)}{p(\bar{\boldsymbol{y}}_k)}\,d\boldsymbol{x}_k \\ &= \int_{\Omega_k} \frac{p(\boldsymbol{y}_{k+1},\boldsymbol{x}_{k+1},\boldsymbol{x}_k,\bar{\boldsymbol{y}}_k)}{p(\boldsymbol{x}_{k+1},\boldsymbol{x}_k,\bar{\boldsymbol{y}}_k)}\,\frac{p(\boldsymbol{x}_{k+1},\boldsymbol{x}_k,\bar{\boldsymbol{y}}_k)}{p(\boldsymbol{x}_k,\bar{\boldsymbol{y}}_k)}\,\frac{p(\boldsymbol{x}_k,\bar{\boldsymbol{y}}_k)}{p(\bar{\boldsymbol{y}}_k)}\,d\boldsymbol{x}_k \\ &= \int_{\Omega_k} p(\boldsymbol{y}_{k+1}|\boldsymbol{x}_{k+1},\boldsymbol{x}_k,\bar{\boldsymbol{y}}_k)p(\boldsymbol{x}_{k+1}|\boldsymbol{x}_k,\bar{\boldsymbol{y}}_k)p(\boldsymbol{x}_k|\bar{\boldsymbol{y}}_k)\,d\boldsymbol{x}_k \quad . \end{aligned} \tag{10}$$

Note that the conditional probabilities in Eq (9) have the following properties:

$$p(\boldsymbol{y}_{k+1}|\boldsymbol{x}_{k+1},\boldsymbol{x}_k,\bar{\boldsymbol{y}}_k) = p(\boldsymbol{y}_{k+1}|\boldsymbol{x}_{k+1})$$

and

$$p(\boldsymbol{x}_{k+1}|\boldsymbol{x}_k,\bar{\boldsymbol{y}}_k) = p(\boldsymbol{x}_{k+1}|\boldsymbol{x}_k) \quad . \tag{11}$$

Equation (11) holds because $\boldsymbol{y}_{k+1}$ only depends on the value of $\boldsymbol{x}_{k+1}$ and $\boldsymbol{w}_{k+1}$ by Eq. (1). When $\boldsymbol{x}_{k+1}$ is given, the probability of $\boldsymbol{y}_{k+1}$ will be determined by the value of $\boldsymbol{w}_{k+1}$, whose value does not depend on any previous system states by assumption 2. Similarly, $p(\boldsymbol{x}_{k+1}|\boldsymbol{x}_k)$ only depends on $\boldsymbol{x}_k$ and $\boldsymbol{v}$ by Eq. (1), and $\boldsymbol{v}$ is independent of system history by assumption 3. Using Eqs. (10) and (11), Eq. (8) can be written as

$$p(\boldsymbol{x}_{k+1}|\bar{\boldsymbol{y}}_{k+1}) = \frac{\displaystyle\int_{\Omega_k} p(\boldsymbol{y}_{k+1}|\boldsymbol{x}_{k+1})p(\boldsymbol{x}_{k+1}|\boldsymbol{x}_k)p(\boldsymbol{x}_k|\bar{\boldsymbol{y}}_k)\,d\boldsymbol{x}_k}{\displaystyle\int_{\Omega_{k+1}} d\boldsymbol{x}_{k+1}\,p(\boldsymbol{y}_{k+1}|\boldsymbol{x}_{k+1})\int_{\Omega_k} p(\boldsymbol{x}_{k+1}|\boldsymbol{x}_k)p(\boldsymbol{x}_k|\bar{\boldsymbol{y}}_k)\,d\boldsymbol{x}_k} \quad ,$$

which completes the proof.

Equation (6) constitutes a Bayesian rule for recursive determination of $p(\boldsymbol{x}_{k+1}|\bar{\boldsymbol{y}}_{k+1})$ for known $p(\boldsymbol{y}_{k+1}|\boldsymbol{x}_{k+1})$ and $p(\boldsymbol{x}_{k+1}|\boldsymbol{x}_k)$. Convergence properties of Eq. (6) will be discussed within the context of its discrete formulation in Sec. II.B and also in Sec. IV. Note that if $\boldsymbol{h}(\boldsymbol{x}_k) = \boldsymbol{x}_k$, then Eq. (6) can be used as a recursive rule for signal validation as illustrated in Secs. III.B and III.C. Also, as indicated in Proposition 1, a practically important situation is when the modeling uncertainties and the measurement uncertainties are represented by zero mean random white Gaussian noise. In this situation,

$$\boldsymbol{x}_{k+1} = \tilde{\boldsymbol{x}}(\boldsymbol{x}_k) + \Delta\boldsymbol{B}_\tau \quad , \tag{12}$$

where

$$\Delta\boldsymbol{B}_\tau = \int_{k\tau}^{(k+1)\tau} d\boldsymbol{B}_t = \int_{k\tau}^{(k+1)\tau} \boldsymbol{v}(t)\,dt$$

$$\tilde{\boldsymbol{x}}(\boldsymbol{x}_k) = \int_{k\tau}^{(k+1)\tau} \boldsymbol{f}(\boldsymbol{x}(s))\,ds + \boldsymbol{x}_k$$

and $\mathbf{B}_t$ denotes the Brownian motion[28] whose pdf is the joint normal distribution of the elements of $\Delta\boldsymbol{B}_\tau$. Then, from Eq. (12) we have

$$p(\boldsymbol{x}_{k+1}|\boldsymbol{x}_k) = \frac{1}{(2\pi\sigma_p^2)^{L/2}}\,e^{-\frac{(\boldsymbol{x}_{k+1}-\tilde{\boldsymbol{x}}(\boldsymbol{x}_k))'(\boldsymbol{x}_{k+1}-\tilde{\boldsymbol{x}}(\boldsymbol{x}_k))}{2\sigma_p^2}} \quad , \tag{13}$$

where σ_p is the standard deviation of the modeling uncertainty. Similarly, when $\boldsymbol{w}_k$ is white Gaussian noise, from Eq. (1) we can write

$$p(\boldsymbol{y}_{k+1}|\boldsymbol{x}_{k+1}) = \frac{1}{(2\pi\sigma_m^2)^{M/2}}\,e^{-\frac{(\boldsymbol{y}_{k+1}-\boldsymbol{h}(\boldsymbol{x}_{k+1}))'(\boldsymbol{y}_{k+1}-h(\boldsymbol{x}_{k+1}))}{2\sigma_m^2}} \quad , \tag{14}$$

where again σ_m is the standard deviation of the noise. In Eqs. (13) and (14), the standard deviations σ_p and σ_m are assumed to be constant for all $k\tau$ $(k = 0,1,2,\ldots)$. Substituting Eqs. (13) and (14) into Eq. (6) yields the Bayesian rule for the recursive estimation of the conditional distribution $p(\boldsymbol{x}_k|\bar{\boldsymbol{y}}_k)$ when the modeling and measurement uncertainties are random white Gaussian noise:

$$
\begin{aligned}
&p(\boldsymbol{x}_{k+1}|\bar{\boldsymbol{y}}_{k+1}) \\
&= \frac{\dfrac{1}{(2\pi\sigma_p^2)^{L/2}(2\pi\sigma_m^2)^{M/2}} \displaystyle\int_{\Omega_k} e^{-\left[\frac{(\boldsymbol{x}_{k+1}-\tilde{\boldsymbol{x}}(\boldsymbol{x}_k))'(\boldsymbol{x}_{k+1}-\tilde{\boldsymbol{x}}(\boldsymbol{x}_k))}{2\sigma_p^2}+\frac{(\boldsymbol{y}_{k+1}-\boldsymbol{h}(\boldsymbol{x}_{k+1}))'(\boldsymbol{y}_{k+1}-\boldsymbol{h}(\boldsymbol{x}_{k+1}))}{2\sigma_m^2}\right]} p(\boldsymbol{x}_k|\bar{\boldsymbol{y}}_k)\,d\boldsymbol{x}_k}{\dfrac{1}{(2\pi\sigma_p^2)^{L/2}(2\pi\sigma_m^2)^{M/2}} \displaystyle\int_{\Omega_{k+1}} d\boldsymbol{x}_{k+1} \int_{\Omega_k} e^{-\left[\frac{(\boldsymbol{x}_{k+1}-\tilde{\boldsymbol{x}}(\boldsymbol{x}_k))'(\boldsymbol{x}_{k+1}-\tilde{\boldsymbol{x}}(\boldsymbol{x}_k))}{2\sigma_p^2}+\frac{(\boldsymbol{y}_{k+1}-\boldsymbol{h}(\boldsymbol{x}_{k+1}))'(\boldsymbol{y}_{k+1}-\boldsymbol{h}(\boldsymbol{x}_{k+1}))}{2\sigma_m^2}\right]} p(\boldsymbol{x}_k|\bar{\boldsymbol{y}}_k)\,d\boldsymbol{x}_k} \\
&\equiv \frac{\dfrac{1}{(2\pi\sigma_m^2)^{M/2}} e^{-\left[\frac{(\boldsymbol{y}_{k+1}-\boldsymbol{h}(\boldsymbol{x}_{k+1}))'(\boldsymbol{y}_{k+1}-\boldsymbol{h}(\boldsymbol{x}_{k+1}))}{2\sigma_m^2}\right]} p^{prior}(\boldsymbol{x}_{k+1}|\bar{\boldsymbol{y}}_k)}{\dfrac{1}{(2\pi\sigma_m^2)^{M/2}} \displaystyle\int_{\Omega_{k+1}} d\boldsymbol{x}_{k+1} e^{-\left[\frac{(\boldsymbol{y}_{k+1}-\boldsymbol{h}(\boldsymbol{x}_{k+1}))'(\boldsymbol{y}_{k+1}-\boldsymbol{h}(\boldsymbol{x}_{k+1}))}{2\sigma_m^2}\right]} p^{prior}(\boldsymbol{x}_{k+1}|\bar{\boldsymbol{y}}_k)}
\end{aligned}
\tag{15}
$$

with

$$
p^{prior}(\boldsymbol{x}_{k+1}|\bar{\boldsymbol{y}}_k) = \frac{1}{(2\pi\sigma_p^2)^{L/2}} \int_{\Omega_k} e^{-\left[\frac{(\boldsymbol{x}_{k+1}-\tilde{\boldsymbol{x}}(\boldsymbol{x}_k))'(\boldsymbol{x}_{k+1}-\tilde{\boldsymbol{x}}(\boldsymbol{x}_k))}{2\sigma_p^2}\right]} p(\boldsymbol{x}_k|\bar{\boldsymbol{y}}_k)\,d\boldsymbol{x}_k \ .
$$

In the case there are no system noise and/or modeling uncertainties and $\tilde{\boldsymbol{x}}(\boldsymbol{x}_k)$ [see Eq. (12)] is invertible, then $\boldsymbol{v} = \boldsymbol{0}$ and

$$
p(\boldsymbol{x}_{k+1}|\boldsymbol{x}_k) = \delta(\boldsymbol{x}_{k+1} - \tilde{\boldsymbol{x}}(\boldsymbol{x}_k)) = \delta(l(\boldsymbol{x}_{k+1}) - \boldsymbol{x}_k) \ , \tag{16}
$$

where $l(\boldsymbol{x}_{k+1})$ is the inverse of $\tilde{\boldsymbol{x}}(\boldsymbol{x}_k)$ and δ denotes the Dirac delta function; i.e.,

$$
\int_{\varepsilon} \delta(\boldsymbol{x} - \hat{\boldsymbol{x}})\,d\boldsymbol{x} = 1
$$

with ε as an infinitesimally small ball around $\hat{\boldsymbol{x}}$ and $\delta(\boldsymbol{x} - \hat{\boldsymbol{x}}) = 0$ for $\boldsymbol{x} \neq \hat{\boldsymbol{x}}$. As an example for the inverse function $l(\boldsymbol{x}_{k+1})$ and measurable sets $\boldsymbol{x_k} \in \Omega_k$, consider the system

$$
\dot{x} = x \ .
$$

Then,

$$
x_{k+1} = \tilde{x}(x_k) = \frac{x_k}{e^{t_k}}\, e^{t_{k+1}}
$$

and

$$
x_k = l(x_{k+1}) = \frac{x_{k+1}}{e^{t_{k+1}}}\, e^{t_k} \ .
$$

The sets $\boldsymbol{x_k} \in \Omega_k$ are measurable because each x_k is a continuous function of and any continuous function is (Borel) measurable.[27] Continuing on with the case where there is no system noise/or modeling uncertainties and $\tilde{\boldsymbol{x}}(\boldsymbol{x}_k)$ is invertible, from Eqs. (6) and (16) we have

$$
\begin{aligned}
&p(\boldsymbol{x}_{k+1}|\bar{\boldsymbol{y}}_{k+1}) \\
&= \frac{\displaystyle\int_{\Omega_k} p(\boldsymbol{y}_{k+1}|\boldsymbol{x}_{k+1})p(\boldsymbol{x}_{k+1}|\boldsymbol{x}_k)p(\boldsymbol{x}_k|\bar{\boldsymbol{y}}_k)\,d\boldsymbol{x}_k}{\displaystyle\int_{\Omega_{k+1}} d\boldsymbol{x}_{k+1} p(\boldsymbol{y}_{k+1}|\boldsymbol{x}_{k+1}) \int_{\Omega_k} p(\boldsymbol{x}_{k+1}|\boldsymbol{x}_k)p(\boldsymbol{x}_k|\bar{\boldsymbol{y}}_k)\,d\boldsymbol{x}_k} \\
&= \frac{\displaystyle\int_{\Omega_k} p(\boldsymbol{y}_{k+1}|\boldsymbol{x}_{k+1})\delta(l(\boldsymbol{x}_{k+1}) - \boldsymbol{x}_k)p(\boldsymbol{x}_k|\bar{\boldsymbol{y}}_k)\,d\boldsymbol{x}_k}{\displaystyle\int_{\Omega_{k+1}} d\boldsymbol{x}_{k+1} p(\boldsymbol{y}_{k+1}|\boldsymbol{x}_{k+1}) \int_{\Omega_k} \delta(l(\boldsymbol{x}_{k+1}) - \boldsymbol{x}_k)p(\boldsymbol{x}_k|\bar{\boldsymbol{y}}_k)\,d\boldsymbol{x}_k} \\
&\equiv \frac{L(\boldsymbol{x}_{k+1}|\boldsymbol{y}_{k+1})p^{prior}(l(\boldsymbol{x}_{k+1})|\bar{\boldsymbol{y}}_k)}{\displaystyle\int_{\Omega_{k+1}} L(\boldsymbol{x}_{k+1}|\boldsymbol{y}_{k+1})p^{prior}(l(\boldsymbol{x}_{k+1})|\bar{\boldsymbol{y}}_k)\,d\boldsymbol{x}_{k+1}} \ .
\end{aligned}
\tag{17}
$$

Equation (17) is the special case of Eq. (6) for the situation where there is no model uncertainty [i.e., $\boldsymbol{v} = 0$ in Eq. (1)]. If Eq. (1) has no closed-form solution or the closed-form solution is not invertible, Eq. (6) needs to be evaluated numerically. Section II.B shows how such a numerical evaluation can be performed using the CCMT.

II.B. Application of the Continuous Bayesian Estimator to the Discretized Representation of the System Used by CCMT

The CCMT describes the dynamic system evolution in terms of probability of transitions between user-specified variable magnitude intervals or cells in the system parameter/state-space during user-specified time intervals $k\tau \leq t \leq (k+1)\tau$ $(k = 0,1,2\ldots)$. The cell sizes may correspond to the desired estimation accuracy in

unknown state variables or may be defined to contain the signal noise.

Assume that the l'th component x_l of the state variable vector $\boldsymbol{x} = [x_1, x_2, \ldots, x_L]$ falls within the range of interest $a_l \le x_l \le b_l (l = 1, \ldots, L)$ at all times. This range of interest is partitioned into $J_l (l = 1, \ldots, L)$ user-defined intervals

$$\Delta_{l,j_l} = \{x_l : a_{l,j_l} \le x_l < a_{l,j_l+1}; a_{l,1} = a_l, a_{l,J_l+1} = b_l\}$$
$$j_l = 1, \ldots, J_l; l = 1, \ldots, L \quad . \qquad (18)$$

The sets $\boldsymbol{V}_j = \{\Delta_{1,j_1}, \Delta_{2,j_2}, \ldots, \Delta_{L,j_L}\} (j = 1, \ldots, J = \prod_{l=1}^{L} J_l)$ at locations $\boldsymbol{j} = (j_1, j_2, \ldots, j_L)$ in the discretized L-dimensional state-space constitute computational cells in a similar manner to those used by finite difference and finite element methods. The cell $x_k \in \boldsymbol{V}_{j,k} \equiv \boldsymbol{V}_k$ that the system is in at time $t = k\tau$ contains a subset $\tilde{\Omega}_k$ of Ω_k but may also include points that are not within $\tilde{\Omega}_k$, i.e., points that may not be achievable by the system under any initial condition since $\boldsymbol{V}_k$ consists of a union of semiopen subintervals within $a_l \le x_l \le b_l (l = 1, \ldots, L)$. Figure 1 illustrates such a possible partitioning for a hypothetical second-order system with three trajectories corresponding to three sets of initial conditions and indicates the possible cells the system can be in if one of the state variables is directly measured. As Fig. 1 shows, the set $\tilde{\Omega}_k$ contains the system locations within cell (7,6) for trajectories 1 and 2 at $t = k\tau$ [and possibly other points of cell (7,6) that the system could have reached under other initial conditions]. On the other hand, cell (7,6) may contain points that are never achievable by the system under any initial condition due to the

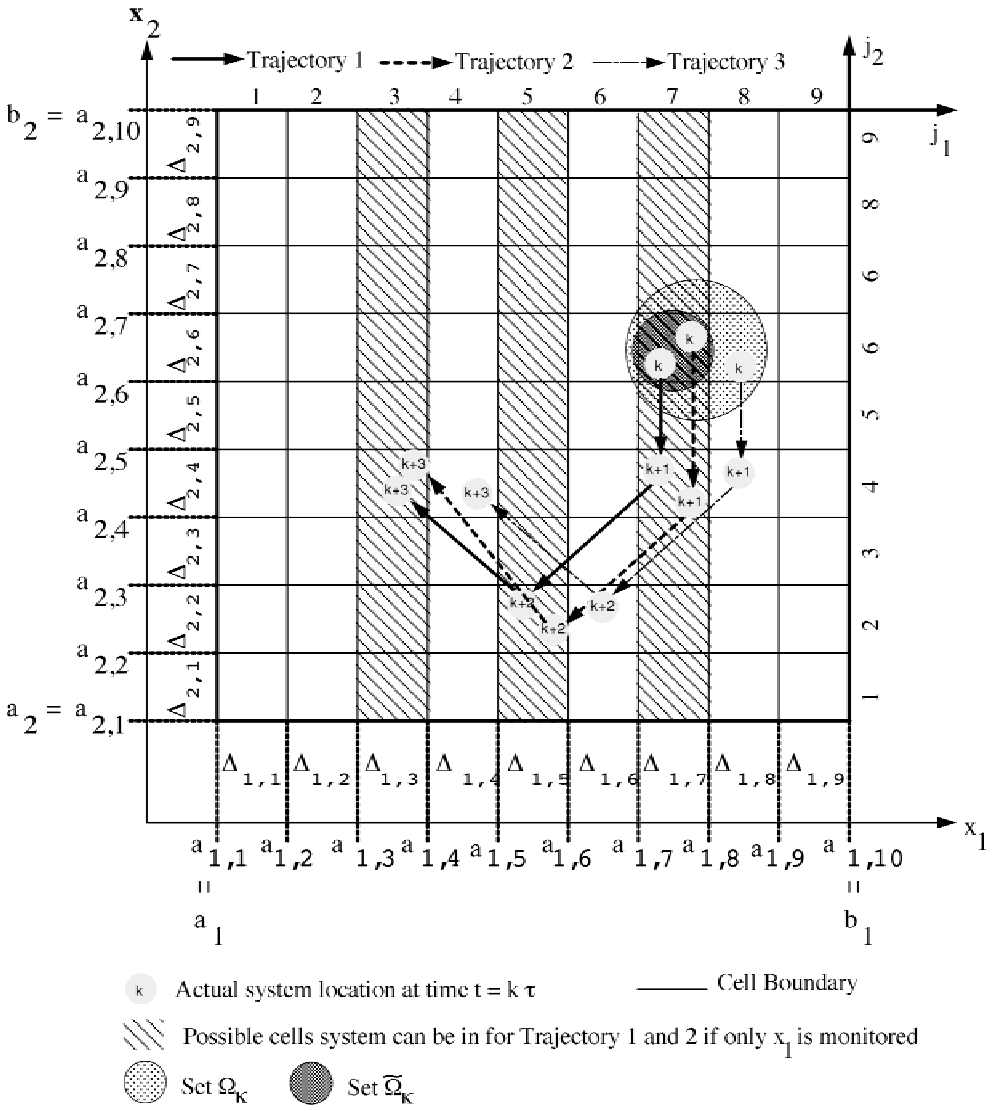

Fig. 1. A possible partitioning for a second-order system.

equations governing the dynamics of the system, just as the trajectory 3 location at $t = k\tau$ is not within cell (7,6) but rather in cell (8,6). Subsequently, cell $\boldsymbol{V}_k$ provides a subcover[27] for $\tilde{\Omega}_k$ (but not for Ω_k).

Integrating both sides of Eq. (6) over the possible cells $\boldsymbol{j}_{k+1}$ where the system might be in at time $t = (k+1)\tau$, we obtain

$$p(\boldsymbol{j}_{k+1}|\bar{\boldsymbol{y}}_{k+1}) = \frac{\displaystyle\int_{\boldsymbol{j}_{k+1}} d\boldsymbol{x}_{k+1} \int_{\Omega_k} d\boldsymbol{x}_k \; p(\boldsymbol{y}_{k+1}|\boldsymbol{x}_{k+1}) p(\boldsymbol{x}_{k+1}|\boldsymbol{x}_k) p(\boldsymbol{x}_k|\bar{\boldsymbol{y}}_k)}{\displaystyle\sum_{\boldsymbol{j}_{k+1}} \int_{\boldsymbol{j}_{k+1}} d\boldsymbol{x}_{k+1} \int_{\Omega_k} d\boldsymbol{x}_k \; p(\boldsymbol{y}_{k+1}|\boldsymbol{x}_{k+1}) p(\boldsymbol{x}_{k+1}|\boldsymbol{x}_k) p(\boldsymbol{x}_k|\bar{\boldsymbol{y}}_k)} \;, \tag{19}$$

where

$$p(\boldsymbol{j}_{k+1}|\bar{\boldsymbol{y}}_{k+1}) = \int_{\boldsymbol{j}_{k+1}} p(\boldsymbol{x}_{k+1}|\bar{\boldsymbol{y}}_{k+1})\, d\boldsymbol{x}_{k+1} \tag{20}$$

is the probability that the system is in cell $\boldsymbol{j}_{k+1}$ at time $(k+1)\tau$. Note that from the definition of $p(\boldsymbol{j}_k|\bar{\boldsymbol{y}}_k)$ in Eq. (20), we can write

$$\int_{\Omega_k} p(\boldsymbol{y}_{k+1}|\boldsymbol{x}_{k+1}) p(\boldsymbol{x}_{k+1}|\boldsymbol{x}_k) p(\boldsymbol{x}_k|\bar{\boldsymbol{y}}_k)\, d\boldsymbol{x}_k = \sum_{\boldsymbol{j}_k} \frac{\displaystyle\int_{\boldsymbol{j}_k} p(\boldsymbol{y}_{k+1}|\boldsymbol{x}_{k+1}) p(\boldsymbol{x}_{k+1}|\boldsymbol{x}_k) p(\boldsymbol{x}_k|\bar{\boldsymbol{y}}_k)\, d\boldsymbol{x}_k}{\displaystyle\int_{\boldsymbol{j}_k} p(\boldsymbol{x}_k|\bar{\boldsymbol{y}}_k)\, d\boldsymbol{x}_k} p(\boldsymbol{j}_k|\bar{\boldsymbol{y}}_k) \;. \tag{21}$$

Substituting Eq. (21) into Eq. (19) we obtain

$$\begin{aligned}
p(\boldsymbol{j}_{k+1}|\bar{\boldsymbol{y}}_{k+1}) &= \frac{\displaystyle\int_{\boldsymbol{j}_{k+1}} d\boldsymbol{x}_{k+1} \int_{\Omega_k} d\boldsymbol{x}_k\, p(\boldsymbol{y}_{k+1}|\boldsymbol{x}_{k+1}) p(\boldsymbol{x}_{k+1}|\boldsymbol{x}_k) p(\boldsymbol{x}_k|\bar{\boldsymbol{y}}_k)}{\displaystyle\sum_{\boldsymbol{j}_{k+1}} \int_{\boldsymbol{j}_{k+1}} d\boldsymbol{x}_{k+1} \int_{\Omega_k} d\boldsymbol{x}_k\, p(\boldsymbol{y}_{k+1}|\boldsymbol{x}_{k+1}) p(\boldsymbol{x}_{k+1}|\boldsymbol{x}_k) p(\boldsymbol{x}_k|\bar{\boldsymbol{y}}_k)} \\
&= \frac{\displaystyle\int_{\boldsymbol{j}_{k+1}} \sum_{\boldsymbol{j}_k} \frac{\displaystyle\int_{\boldsymbol{j}_k} p(\boldsymbol{y}_{k+1}|\boldsymbol{x}_{k+1}) p(\boldsymbol{x}_{k+1}|\boldsymbol{x}_k) p(\boldsymbol{x}_k|\bar{\boldsymbol{y}}_k)\, d\boldsymbol{x}_k}{\displaystyle\int_{\boldsymbol{j}_k} p(\boldsymbol{x}_k|\bar{\boldsymbol{y}}_k)\, d\boldsymbol{x}_k} p(\boldsymbol{j}_k|\bar{\boldsymbol{x}}_k)\, d\boldsymbol{x}_{k+1}}{\displaystyle\sum_{\boldsymbol{j}_{k+1}} \int_{\boldsymbol{j}_{k+1}} \sum_{\boldsymbol{j}_k} \frac{\displaystyle\int_{\boldsymbol{j}_k} p(\boldsymbol{y}_{k+1}|\boldsymbol{x}_{k+1}) p(\boldsymbol{x}_{k+1}|\boldsymbol{x}_k) p(\boldsymbol{x}_k|\bar{\boldsymbol{y}}_k)\, d\boldsymbol{x}_k}{\displaystyle\int_{\boldsymbol{j}_k} p(\boldsymbol{x}_k|\bar{\boldsymbol{y}}_k)\, d\boldsymbol{x}_k} p(\boldsymbol{j}_k|\bar{\boldsymbol{y}}_k)\, d\boldsymbol{x}_{k+1}} \\
&= \frac{\displaystyle\sum_{\boldsymbol{j}_k} p(\boldsymbol{j}_k|\bar{\boldsymbol{y}}_k) \iint_{\boldsymbol{j}_{k+1},\boldsymbol{j}_k} p(\boldsymbol{y}_{k+1}|\boldsymbol{x}_{k+1}) p(\boldsymbol{x}_{k+1}|\boldsymbol{x}_k) \frac{p(\boldsymbol{x}_k|\bar{\boldsymbol{y}}_k)}{\displaystyle\int_{\boldsymbol{j}_k} p(\boldsymbol{x}_k|\bar{\boldsymbol{y}}_k)\, d\boldsymbol{x}_k} d\boldsymbol{x}_k\, d\boldsymbol{x}_{k+1}}{\displaystyle\sum_{\boldsymbol{j}_{k+1}} \sum_{\boldsymbol{j}_k} p(\boldsymbol{j}_k|\bar{\boldsymbol{y}}_k) \iint_{\boldsymbol{j}_{k+1},\boldsymbol{j}_k} p(\boldsymbol{y}_{k+1}|\boldsymbol{x}_{k+1}) p(\boldsymbol{x}_{k+1}|\boldsymbol{x}_k) \frac{p(\boldsymbol{x}_k|\bar{\boldsymbol{y}}_k)}{\displaystyle\int_{\boldsymbol{j}_k} p(\boldsymbol{x}_k|\bar{\boldsymbol{y}}_k)\, d\boldsymbol{x}_k} d\boldsymbol{x}_k\, d\boldsymbol{x}_{k+1}} \;.
\end{aligned} \tag{22}$$

The fundamental difference between Eqs. (6) and (22) is that the integrations in Eq. (6) are carried over the possible system locations at times $t = k\tau$ and $t = (k+1)\tau$ as determined from Eq. (1) and given initial conditions and represented, respectively, by the sets Ω_k and Ω_{k+1}, whereas the integrations in Eq. (22) are carried over cell $\boldsymbol{V}_k$ at $\boldsymbol{j}_k$ and cell $\boldsymbol{V}_{k+1}$ at $\boldsymbol{j}_{k+1}$, which the system is in at these times and which contain the subsets $\tilde{\Omega}_k \subset \Omega_k$ $(k = 0,1,\ldots)$. In view of the explanation given above for the difference between $\boldsymbol{V}_k$ and $\tilde{\Omega}_k$, the $p(\boldsymbol{j}_k|\bar{\boldsymbol{y}}_k)$ as defined by Eq. (20) can be regarded as an outer measure[27] for $\tilde{\Omega}_k$. The limitations and advantages of this approximation will be discussed later in this section.

Now, define the cell-to-cell transition probability as

$$g(\boldsymbol{j}_{k+1}|\boldsymbol{j}_k) = \iint\limits_{\boldsymbol{j}_{k+1},\boldsymbol{j}_k} p(\boldsymbol{y}_{k+1}|\boldsymbol{x}_{k+1})p(\boldsymbol{x}_{k+1}|\boldsymbol{x}_k) \times \frac{p(\boldsymbol{x}_k|\bar{\boldsymbol{y}}_k)}{\int_{\boldsymbol{j}_k} p(\boldsymbol{x}_k|\bar{\boldsymbol{y}}_k)\,d\boldsymbol{x}_k}\,d\boldsymbol{x}_k\,d\boldsymbol{x}_{k+1} \quad . \tag{23}$$

The $g(\boldsymbol{j}_{k+1}|\boldsymbol{j}_k)$ does not include $\boldsymbol{y}_{k+1}$ and $\bar{\boldsymbol{y}}_k$ as arguments for notational simplicity and also because $\boldsymbol{y}_{k+1}$ and $\bar{\boldsymbol{y}}_k$ are measured data points (and hence fixed), whereas $\boldsymbol{j}_{k+1}$ and $\boldsymbol{j}_k$ are arbitrary cells (i.e., variables). Then, Eqs. (22) and (23) yield the discrete counterpart of Eq. (6) as

$$p(\boldsymbol{j}_{k+1}|\bar{\boldsymbol{y}}_{k+1}) = \frac{\sum_{\boldsymbol{j}_k} g(\boldsymbol{j}_{k+1}|\boldsymbol{j}_k)p(\boldsymbol{j}_k|\bar{\boldsymbol{y}}_k)}{\sum_{\boldsymbol{j}_{k+1}}\sum_{\boldsymbol{j}_k} g(\boldsymbol{j}_{k+1}|\boldsymbol{j}_k)p(\boldsymbol{j}_k|\bar{\boldsymbol{y}}_k)} \quad . \tag{24}$$

The cell-to-cell transition probabilities can be calculated numerically from

$$\begin{aligned} g(\boldsymbol{j}_{k+1}|\boldsymbol{j}_k) &= \iint\limits_{\boldsymbol{j}_{k+1}\boldsymbol{j}_k} f_w(\boldsymbol{y}_{k+1} - \boldsymbol{h}(\boldsymbol{x}_{k+1})) \times f_{\Delta B}(\boldsymbol{x}_{k+1} - \tilde{\boldsymbol{x}}(\boldsymbol{x}_k)) \times \frac{p(\boldsymbol{x}_k|\bar{\boldsymbol{y}}_k)}{\int_{\boldsymbol{j}_k} p(\boldsymbol{x}_k|\bar{\boldsymbol{y}}_k)\,d\boldsymbol{x}_k}\,d\boldsymbol{x}_k\,d\boldsymbol{x}_{k+1} \\ &\approx \sum_r\sum_q f_w(\boldsymbol{y}_{k+1} - \boldsymbol{h}(\hat{\boldsymbol{x}}^r_{k+1})) \times f_{\Delta B}(\hat{\boldsymbol{x}}^r_{k+1} - \tilde{\boldsymbol{x}}(\hat{\boldsymbol{x}}^q_k)) \times \frac{p(\hat{\boldsymbol{x}}^q_k|\bar{\boldsymbol{y}}_k)}{\int_{\boldsymbol{j}_k} p(\boldsymbol{x}_k|\bar{\boldsymbol{y}}_k)\,d\boldsymbol{x}_k}\,\Delta\hat{\boldsymbol{x}}^q_k\Delta\hat{\boldsymbol{x}}^r_{k+1} \quad , \end{aligned} \tag{25}$$

where

$f_{\Delta B}, f_w$ = user-specified pdf's for the system noise [e.g., see Eq. (13)] and measurement noise [e.g., see Eq. (14)], respectively

$\hat{\boldsymbol{x}}^q_k$ = quadrature points selected in cell $\boldsymbol{j}_k$ with $\Delta\hat{\boldsymbol{x}}^q_k$ denoting small volumes that surrounds $\hat{\boldsymbol{x}}^q_k$

$\hat{\boldsymbol{x}}^r_{k+1}$ = quadrature points selected in cell $\boldsymbol{j}_{k+1}$ with $\Delta\hat{\boldsymbol{x}}^r_{k+1}$ denoting the small volume that surrounds $\hat{\boldsymbol{x}}^r_{k+1}$.

Equation (25) constitutes a quadrature rule for the numerical approximation of $g(\boldsymbol{j}_{k+1}|\boldsymbol{j}_k)$; however, Monte Carlo sampling can be also used for the approximation of the integrals in Eq. (25). The $\tilde{\boldsymbol{x}}(\hat{\boldsymbol{x}}^q_k)$ can be evaluated by any numerical integration technique from Eq. (1). At this point it should be mentioned that the equations describing the evolution of the system do not have to be differential equations as assumed in Eq. (1). All that is needed is a rule $\tilde{\boldsymbol{x}}(\boldsymbol{x}_k)$ that yields the system location in the state-space at time $(k+1)\tau$ given its location at time $k\tau$, such as difference equations, neural nets, response surfaces, tabular data, or algebraic equations.

If there is no modeling uncertainty, Eq. (25) can be simplified using Eq. (16). In this situation,

$$\begin{aligned} g(\boldsymbol{j}_{k+1}|\boldsymbol{j}_k) &= \iint\limits_{j_{k+1}j_k} p(\boldsymbol{y}_{k+1}|\boldsymbol{x}_{k+1})\delta(\boldsymbol{x}_{k+1} - \tilde{\boldsymbol{x}}(\boldsymbol{x}_k)) \times \frac{p(\boldsymbol{x}_k|\bar{\boldsymbol{y}}_k)}{\int_{j_k} p(\boldsymbol{x}_k|\bar{\boldsymbol{y}}_k)\,d\boldsymbol{x}_k}\,d\boldsymbol{x}_k\,d\boldsymbol{x}_{k+1} \\ &= \int_{j_k} p(\boldsymbol{y}_{k+1}|\tilde{\boldsymbol{x}}(\boldsymbol{x}_k)) \times \frac{p(\boldsymbol{x}_k|\bar{\boldsymbol{y}}_k)}{\int_{j_k} p(\boldsymbol{x}_k|\bar{\boldsymbol{y}}_k)\,d\boldsymbol{x}_k}\,e_{k+1}(\tilde{\boldsymbol{x}}(\boldsymbol{x}_k))\,d\boldsymbol{x}_k \\ &= \int_{j_k} f_w(\boldsymbol{y}_{k+1} - \boldsymbol{h}(\tilde{\boldsymbol{x}}(\boldsymbol{x}_k))) \times \frac{p(\boldsymbol{x}_k|\bar{\boldsymbol{y}}_k)}{\int_{j_k} p(\boldsymbol{x}_k|\bar{\boldsymbol{y}}_k)\,d\boldsymbol{x}_k}\,e_{k+1}(\tilde{\boldsymbol{x}}(\boldsymbol{x}_k))\,d\boldsymbol{x}_k \\ &\approx \sum_i f_w(\boldsymbol{y}_{k+1} - \boldsymbol{h}(\tilde{\boldsymbol{x}}(\hat{\boldsymbol{x}}^i_k))) \times \frac{p(\hat{\boldsymbol{x}}^i_k|\bar{\boldsymbol{y}}_k)}{\int_{j_k} p(\boldsymbol{x}_k|\bar{\boldsymbol{y}}_k)\,d\boldsymbol{x}_k}\,e_{k+1}(\tilde{\boldsymbol{x}}(\hat{\boldsymbol{x}}^i_k))\Delta\hat{\boldsymbol{x}}_k \quad , \end{aligned} \tag{26}$$

where $e_{k+1}(\tilde{\boldsymbol{x}}(\boldsymbol{x}_k))$ is defined as

$$e_{k+1}(\tilde{\boldsymbol{x}}(\boldsymbol{x}_k)) = \begin{cases} 0 & \tilde{\boldsymbol{x}}(\boldsymbol{x}_k) \notin \boldsymbol{j}_{k+1} \\ 1 & \tilde{\boldsymbol{x}}(\boldsymbol{x}_k) \in \boldsymbol{j}_{k+1} \end{cases} , \tag{27}$$

$\hat{\boldsymbol{x}}_k^i$ (i = 1,…, N) are points selected in cell $\boldsymbol{j}_k$, and $\Delta\hat{\boldsymbol{x}}_k^i$ is the small volume that surrounds $\hat{\boldsymbol{x}}_k^i$. In measure theory, $e_{k+1}(\tilde{\boldsymbol{x}}(\boldsymbol{x}_k))$ is called the indicator[27] of $\tilde{\Omega}_{k+1}$ for $\tilde{\boldsymbol{x}}(\boldsymbol{x}_k) \in \tilde{\Omega}_{k+1}$. The $e_{k+1}(\tilde{\boldsymbol{x}}(\boldsymbol{x}_k))$ is not Borel measurable if $\tilde{\Omega}_{k+1}$ is not a Borel set, which would mean that the integral over cell $\boldsymbol{j}_{k+1}$ in Eq. (26) might have not existed for some nonlinear systems if the integration were carried over $\tilde{\Omega}_{k+1}$ rather than cell $\boldsymbol{j}_{k+1}$. Carrying the integration over cell $\boldsymbol{j}_{k+1}$ assures the existence of the integral as discussed above with regard to proposition 1 and Eq. (22); however, it may lead to loss of resolution in the estimate as will be indicated below.

Further simplification of Eq. (26) can be made by assuming that the probability $p(\hat{\boldsymbol{x}}_k^i|\bar{\boldsymbol{y}}_k)$ is constant over $\Delta\hat{\boldsymbol{x}}_k^i$ and selecting the points $\hat{\boldsymbol{x}}_k^i$ equally spaced inside the cell; then,

$$\frac{p(\hat{\boldsymbol{x}}_k^i|\bar{\boldsymbol{y}}_k)}{\displaystyle\int_{\boldsymbol{j}_k} p(\boldsymbol{x}_k|\bar{\boldsymbol{y}}_k)\,d\boldsymbol{x}_k} = \frac{p(\hat{\boldsymbol{x}}_k^i|\bar{\boldsymbol{y}}_k)}{Np(\hat{\boldsymbol{x}}_k^i|\bar{\boldsymbol{y}}_k)\Delta\hat{\boldsymbol{x}}_k} = \frac{1}{N\Delta\hat{\boldsymbol{x}}_k} = \frac{1}{V_k} , \tag{28}$$

where V_k is the volume of cell $\boldsymbol{j}_k$ (i.e., the product $\Delta_{1,j_1}\Delta_{2,j_2}\ldots\Delta_{L,j_L}$) and Eq. (26) becomes

$$\begin{aligned} g(\boldsymbol{j}_{k+1}|\boldsymbol{j}_k) = & \int_{\boldsymbol{j}_k} f_w(\boldsymbol{y}_{k+1} - \boldsymbol{h}(\tilde{\boldsymbol{x}}(\boldsymbol{x}_k))) \\ & \times \frac{p(\boldsymbol{x}_k|\bar{\boldsymbol{y}}_k)}{\displaystyle\int_{\boldsymbol{j}_k} p(\boldsymbol{x}_k|\bar{\boldsymbol{y}}_k)\,d\boldsymbol{x}_k} e_{k+1}(\tilde{\boldsymbol{x}}(\boldsymbol{x}_k))\,d\boldsymbol{x}_k \\ \approx & \sum_{i=1}^{N} f_w(\boldsymbol{y}_{k+1} - \boldsymbol{h}(\tilde{\boldsymbol{x}}(\hat{\boldsymbol{x}}_k^i))) \\ & \times \frac{p(\hat{\boldsymbol{x}}_k^i|\bar{\boldsymbol{y}}_k)}{Np(\hat{\boldsymbol{x}}_k^i|\bar{\boldsymbol{y}}_k)\Delta\hat{\boldsymbol{x}}_k} e_{k+1}(\tilde{\boldsymbol{x}}(\hat{\boldsymbol{x}}_k^i))\Delta\hat{\boldsymbol{x}}_k \\ = & \sum_{i=1}^{N} \frac{1}{N} f_w(\boldsymbol{y}_{k+1} - \boldsymbol{h}(\tilde{\boldsymbol{x}}(\hat{\boldsymbol{x}}_k^i))) \\ & \times e_{k+1}(\tilde{\boldsymbol{x}}(\hat{\boldsymbol{x}}_k^i)) . \end{aligned} \tag{29}$$

Equations (23) and (24) are similar to the recursive estimation rule reported in Ref. 20 on which the DSD software package is based. However, the definition of the cell-to-cell transition probabilities through Eq. (23) differs from this rule in the following respects:

1. The rule in Ref. 20 assumes there is no model uncertainty (except possibly small random fluctuations in system parameters that are contained within cells $\boldsymbol{V}_j$). Equation (23) allows representing arbitrary distributions of the model uncertainties through the term $p(\boldsymbol{x}_{k+1}|\boldsymbol{x}_k)$.

2. The rule in Ref. 20 assumes that only the state variables are directly measured; i.e.,

$$\boldsymbol{y}_k = \begin{bmatrix} y_1 \\ y_2 \\ \vdots \\ y_i \end{bmatrix}_k = \begin{bmatrix} x_1 \\ x_2 \\ \vdots \\ x_i \end{bmatrix}_k + \begin{bmatrix} w_1 \\ w_2 \\ \vdots \\ w_i \end{bmatrix}_k \quad k = 1,2,\ldots$$

$$\Rightarrow \boldsymbol{y}_k = [1 \quad 0] \begin{bmatrix} \hat{\boldsymbol{x}} \\ \bar{\boldsymbol{x}} \end{bmatrix}_k + \boldsymbol{w}_k ,$$

where $\hat{\boldsymbol{x}} = [x_1, x_2, \ldots, x_i]$ is the vector whose elements are the monitored state variables and $\bar{\boldsymbol{x}} = [x_{i+1}, x_{i+2}, \ldots, x_L]$ is the vector whose elements are the unmonitored state variables. Hence, Eq. (23) allows arbitrary observers, whereas Ref. 20 is restricted to the directly measured components of the state variable vector.

3. The rule in Ref. 20 assumes that $\boldsymbol{w}_k$ is uniformly distributed; i.e.,

$$f_w(\boldsymbol{w}_k) = \begin{cases} 1 & |\boldsymbol{w}_k| \le \lambda \\ 0 & \text{otherwise} \end{cases} , \tag{30}$$

while Eq. (23) allows arbitrary distributions of $\boldsymbol{w}_k$ through the term $p(\boldsymbol{y}_{k+1}|\boldsymbol{x}_{k+1})$.

4. In Ref. 20, cells $\hat{\boldsymbol{j}} = \{j_1 j_2 \ldots j_i\}$ and $\bar{\boldsymbol{j}} = \{j_{i+1} j_{i+2} \ldots j_L\}$ are defined in the monitored and unmonitored state variable spaces (i.e., $\boldsymbol{j} = \{\hat{\boldsymbol{j}} \quad \bar{\boldsymbol{j}}\}$), respectively. The cells $\hat{\boldsymbol{j}}$ contain the measured data point $\boldsymbol{y}$, and $\bar{\boldsymbol{j}}$ contain the measurement noise (i.e., $\hat{\boldsymbol{j}}_k = \{\hat{\boldsymbol{x}}_k : |\hat{\boldsymbol{x}}_k - \boldsymbol{y}_k| \le \lambda\}$). The cell-to-cell transition probabilities are calculated from

$$\begin{aligned} g(\boldsymbol{j}_{k+1}|\boldsymbol{j}_k) &\equiv g(\hat{\boldsymbol{j}}_{k+1}, \bar{\boldsymbol{j}}_{k+1}|\hat{\boldsymbol{j}}_k, \bar{\boldsymbol{j}}_k) \\ &= \int_{\boldsymbol{j}_k} \frac{d\boldsymbol{x}_k}{V_k} e_{k+1}(\tilde{\boldsymbol{x}}(\boldsymbol{x}_k)) , \end{aligned} \tag{31}$$

where $\boldsymbol{j}_k$ is the cell containing $\boldsymbol{x}_k$ and V_k is the volume of $\boldsymbol{j}_k$ (i.e., the product $\Delta_{1,j_1}\Delta_{2,j_2}\ldots\Delta_{L,j_L}$) as defined before.

It can be shown that if $\boldsymbol{j}_{s,k}$ denotes the actual cell the system is in at time $t = k\tau$ and $g(\boldsymbol{j}_{k+1}|\boldsymbol{j}_k) < g(\boldsymbol{j}_{s,k+1}|\boldsymbol{j}_k)$ for all $\boldsymbol{j}_{k+1} \neq \boldsymbol{j}_{s,k+1}$, then[20]

$$\lim_{k\to\infty} p(\boldsymbol{j}_{k+1}|\bar{\boldsymbol{y}}_{k+1}) \to \delta_{j_{s,k+1}, j_{k+1}} ,$$

$$\delta_{j_{s,k+1}, j_{k+1}} = \begin{cases} 1 & \text{if } \boldsymbol{j}_{k+1} = \boldsymbol{j}_{s,k+1} \\ 0 & \text{otherwise} \end{cases}$$

irrespective of the choice of $p(\boldsymbol{j}_0|\boldsymbol{y}_0)$; i.e., $p(\boldsymbol{j}_{k+1}|\bar{\boldsymbol{y}}_{k+1})$ converges to the correct cell $\boldsymbol{j}_{s,k+1}$ irrespective of the initial distribution used. The practical implication of this result is that the choice of cells should be such that the correct system trajectory can be adequately represented by the $g(\boldsymbol{j}_{k+1}|\boldsymbol{j}_k)$. Figure 2 illustrates such a

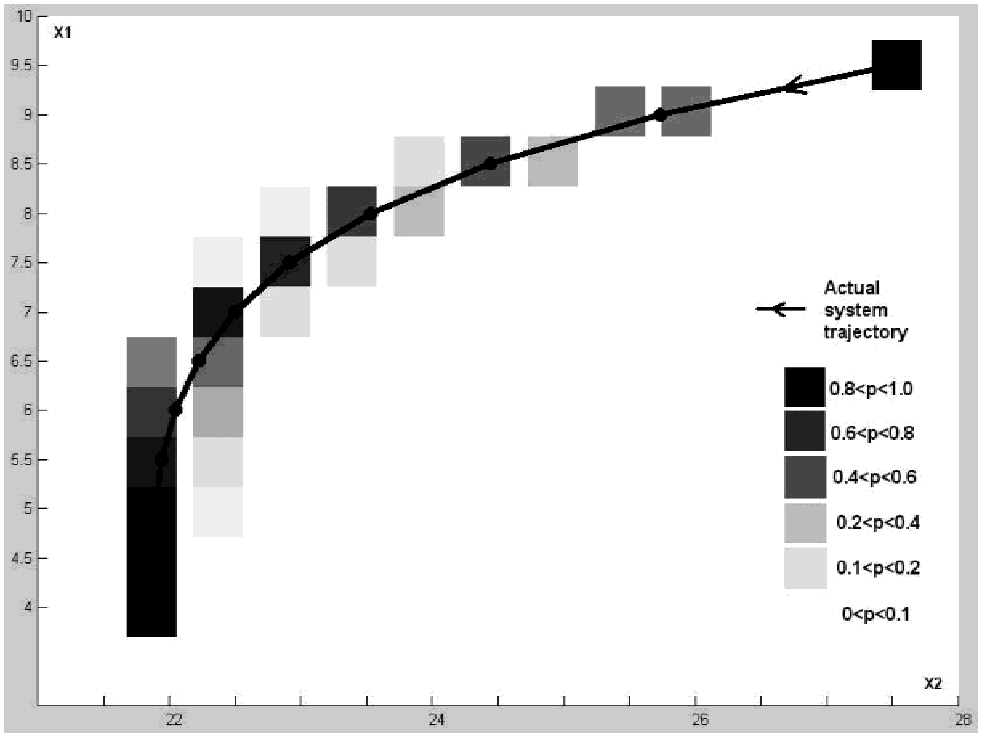

Fig. 2. Approximation of the phase-space trajectory of a hypothetical second-order system by CCMT.

representation for a hypothetical second-order system in its phase-space. Note that the probabilities $p \equiv p(\boldsymbol{j}_{k+1}|\bar{\boldsymbol{y}}_{k+1})$ are highest on or close to the actual trajectory.

While the condition $g(\boldsymbol{j}_{s,k+1}|\boldsymbol{j}_k) > g(\boldsymbol{j}_{k+1}|\boldsymbol{j}_k)$ is practically not convenient for the selection of the cells due to the computational effort required in its implementation, it implies that convergence will be obtained with sufficiently small cells. If the cells are small enough, we will have $g(\boldsymbol{j}_{s,k+1}|\boldsymbol{j}_k) = 1$ if $\boldsymbol{j}_{k+1} = \boldsymbol{j}_{s,k+1}$ and $g(\boldsymbol{j}_{k+1}|\boldsymbol{j}_k) = 0$ otherwise. Since this condition is obtained in Ref. 20 using just the counterpart of Eq. (24) and not Eq. (31), the condition is also valid for Eqs. (23) and (24). Appendix A shows that Eq. (23) reduces to Eq. (31) when differences 1 through 4 are removed.

At this point it should be indicated that both the original DSD algorithm defined through Eqs. (24) and (31) (and subsequently the convergence criteria above) and the improved algorithm defined in Eqs. (23) and (24), in principle, still assume $p(\boldsymbol{x}_k|\bar{\boldsymbol{y}}_k)$ to be measurable over the $\boldsymbol{x}$ range of interest. For the improved algorithm, this assumption is implicit in the steps: (a) replacing integration over the $\boldsymbol{x}$ range of interest in Eq. (6) by a sum of integrals over cells $\boldsymbol{V}_j$ in Eq. (22) and (b) representing $p(\boldsymbol{x}_k|\bar{\boldsymbol{y}}_k)$ over cells $\boldsymbol{V}_j$ through its values at $\hat{\boldsymbol{x}}_k^q$ in Eq. (25), which are assumed to be constant over $\Delta\hat{\boldsymbol{x}}_k^q$. The assumption is carried over to Eq. (31) when differences 1 through 4 are removed. In that respect, refinement of the partitioning scheme (i.e., decreasing the size of $\boldsymbol{V}_j$) or the quadrature scheme [e.g., increasing the number of points $\hat{\boldsymbol{x}}_k^q$ in Eq. (25)], as it is the conventional wisdom for finite difference or finite element techniques, may not lead to better resolution in the estimated quantities if Ω_k containing all possible $\boldsymbol{x}_k$ at time $t = k\tau$ are not measurable sets. A good example is the situation studied in Ref. 29, which uses an algorithm similar to original DSD algorithm to identify the domains of attraction (DOA) of the van der Pol oscillator (a limit cycle and a single point) and calculates the cell-to-cell transition probabilities $g(\boldsymbol{j}_{k+1}|\boldsymbol{j}_k)$ both analytically (exactly) and numerically from the counterpart of Eq. (31). It is shown that the analytical approach [which implicitly assumes that $\tilde{\boldsymbol{x}}(\boldsymbol{x}_k)$ in Eq. (31) is integrable over V_k] leads to loss of resolution in the estimated DOA with respect to the DOA estimated by the numerical approximation of the integral in Eq. (31). The paper shows that the loss of resolution arises from an artificial connectivity between the sets $\tilde{\Omega}_k$ (for which V_k provide a finite subcover) during the determination of $g(\boldsymbol{j}_{k+1}|\boldsymbol{j}_k)$; however, it does not explain the origin of the connectivity. In light of the difference between Eqs. (6) and (22) as explained earlier, the connectivity can be attributed to forcing the originally noncompact $\tilde{\Omega}_k$ to be compact during the analytical determination of $g(\boldsymbol{j}_{k+1}|\boldsymbol{j}_k)$ through integration over the subcover V_k [which is the union of intervals $\Delta_{l,j_l} = \{x_l : a_{l,j_l} \le x_l < a_{l,j_l+1}; a_{l,1} = a_l, a_{l,J_1+1} = b_l\}$ as given by Eq. (18) for some $j_l (j_l = 1,\ldots,J_l; l = 1,\ldots,L)$ and hence connected[30]] rather than $\tilde{\Omega}_k$. Such an explanation has

extended implications[31] regarding previous work on reliability and safety analysis of dynamic systems[32] as well. On the other hand, experience with the original DSD algorithm shows that evaluation of the integral in Eq. (31) using quadratures can often yield successful results even when Ω_k are not measurable, possibly also because $p(\boldsymbol{j}_k|\bar{\boldsymbol{y}}_k)$ provides an outer measure for the set $\tilde{\Omega}_k$ as indicated above in the discussion of the difference between Eqs. (6) and (22). In addition to the problem considered in Ref. 29, a good example is the capability of the original DSD algorithm to determine[33] the bifurcation parameter (which corresponds to the fuel-to-coolant heat transfer coefficient) of the well-known reduced-order boiling water reactor (BWR) model described in Ref. 34 with observed neutron flux, temperature, and pressure. The search in Ref. 23 is carried over a range of the bifurcation parameters in which the BWR behavior can switch from stable to periodic to chaotic. The Ω_k of the system trajectories in neither periodic nor chaotic behavior are Borel measurable, i.e., Ω_k are not closed under finite intersection and union of some open subintervals in the ranges of interest since we cannot define a sequence $z_k^{(s)} \in \Omega_k$ such that $\lim_{s\to\infty} z_k^{(s)} \to x_k \in \Omega_k$.

III. IMPLEMENTATION

This section compares the recursive procedure defined by Eqs. (23) and (24) to the rule reported in Ref. 20 using a xenon evolution model and presents the results.

III.A. System Description

The system under consideration has been proposed by Chernick[35] and consists of three first-order, nonlinear differential equations:

$$\Lambda \frac{d\phi}{dt} = \left(\rho - \frac{\sigma_x}{c\Sigma_f} X - \gamma\phi\right)\phi \ ,$$

$$\frac{dX}{dt} = y_X \Sigma_f \phi - \lambda_x X + \lambda_I I - \sigma_X X\phi \ ,$$

and

$$\frac{dI}{dt} = y_I \Sigma_f \phi - \lambda_I I \ , \tag{32}$$

where

Λ = effective neutron generation time

ϕ = neutron flux

X = ^{135}Xe concentration

I = ^{135}I concentration

c = conversion coefficient from xenon absorption rate to reactivity

ρ = reactivity at zero flux and zero xenon poisoning

σ_X = microscopic absorption cross section for ^{135}Xe

Σ_f = core-averaged macroscopic absorption cross section

γ = flux coefficient of reactivity

λ_X = ^{135}Xe decay coefficient = 0.0753/h

λ_I = ^{135}I decay coefficient = 0.1035/h

y_I = ^{135}I yield = 0.06386

y_X = ^{135}Xe yield = 0.00228

The values for the parameters $\lambda_X, \lambda_I, y_X, y_I$ are generic data. The other model parameters are reactor-specific quantities, and the values obtained from The Ohio State University Research Reactor[36] will be used in this paper (Table I). For the purpose of this study, Eq. (32) is normalized as

$$\Lambda \frac{d\phi}{dt} = \left(\rho - \frac{\sigma_x}{c}\frac{X}{\Sigma_f} - \gamma\phi\right)\phi \ ,$$

$$\frac{d\left(\frac{X}{\Sigma_f}\right)}{dt} = y_X \phi - \lambda_X \frac{X}{\Sigma_f} + \lambda_I \frac{I}{\Sigma_f} - \sigma_X \frac{X}{\Sigma_f}\phi \ ,$$

and

$$\frac{d\left(\frac{I}{\Sigma_f}\right)}{dt} = y_I \phi - \lambda_I \frac{I}{\Sigma_f} \ . \tag{33}$$

The transient considered is a small step insertion of reactivity with $\rho = 0.0005$. Only the flux is assumed to be measured, and the measurement is corrupted by noise; i.e.,

$$y_k = \phi_k + w_k \ ,$$

where y_k is the measurement and w_k is the noise with the pdf $f_w(w_k)$. The subscript k is the time step index. We will assume the noise is white noise and f_w has the same functional form for all $t = k\tau$.

TABLE I

Reactor-Dependent Parameters of Eq. (32)

c	γ (cm$^2\cdot$s)	σ_x (cm^2)	Λ (s)
1.2384	3.97×10^{-16}	1.984×10^{-18}	0.083

TABLE II

Data Used for Simulation of Xenon Evolution for Case 1

Initial Value of ϕ	Initial Value of X/Σ_f	Initial Value of I/Σ_f	Time Step τ (h)	Mean of the Noise	Standard Deviation of the Noise
0.01×10^{13}	0.4×10^{13}	0.5×10^{13}	0.015	0	0.0012×10^{13}

Two cases will be considered in this section:

1. Given $f_w(w_k)$ to be white Gaussian noise, estimate X/Σ_f, I/Σ_f.

2. Given $f_w(w_k)$ to be uniformly distributed, estimate X/Σ_f, I/Σ_f.

Sections III.B and III.C describe the results for cases 1 and 2, respectively.

III.B. Estimation Results with Gaussian Noise (Case 1)

Table II shows the data used in case 1 for the simulation of the measured flux. The simulated system evolution is shown in Fig. 3. The results for the actual flux were obtained from the integration of Eq. (33) using a fourth-order Runge-Kutta scheme. The results for the measured flux y_k at time $t = k\tau$ $(k = 0,1,2,\ldots)$ were obtained by sampling from a normal distribution with mean zero and standard deviation 0.0012×10^{13} (see Table II) using a random number generator and algebraically adding the result to those obtained for the flux $\phi(t)$. Since the noise is assumed to be Gaussian, it cannot be contained within a single cell $\boldsymbol{V}_j$, and the procedure described in Ref. 20 does not converge. In order to apply the new procedure described in Sec. II, the partitioning data used are shown in Table III.

Since there is no model uncertainty, the transition probabilities $g(\boldsymbol{j}_{k+1}|\boldsymbol{j}_k)$ are calculated from Eq. (26) [and subsequently from Eq. (29)] with $\boldsymbol{h}(\bar{x}(\boldsymbol{x}_k)) = \bar{x}(\boldsymbol{x}_k)$ and f_w having 0 mean and 0.0012×10^{13} standard variation. The total number of quadrature points $\hat{\boldsymbol{x}}_k^i$ $(i = 1,\ldots,N)$ selected in the approximation of $g(\boldsymbol{j}_{k+1}|\boldsymbol{j}_k)$ through Eq. (29) is $N = 3 \times 3 \times 3 = 9$.

The estimated 99.99% credibility interval as a function of time for the measured values of flux and the estimated value of X/Σ_f, I/Σ_f are shown, respectively, in Figs. 4, 5, and 6. From Fig. 4, we can see that the estimated intervals for flux (denoted by vertical bars) contain the measured data y_k at all time points. Since the estimation process cross-correlates the measured data in view of the given pdf for w_k [i.e., through $p(\boldsymbol{y}_{k+1}|\boldsymbol{x}_{k+1})$ in Eq. (23)] and the system model (i.e., through $p(\boldsymbol{x}_k|\bar{\boldsymbol{y}}_k)$) in the determination of $g(\boldsymbol{j}_{k+1}|\boldsymbol{j}_k)$, Fig. 4 implies that the improved estimation procedure described by Eqs. (23) and (24) [or Eqs. (24) and (26) when there is no modeling uncertainty] can be also used for model uncertainty/noise reduction in the measured data as will be shown

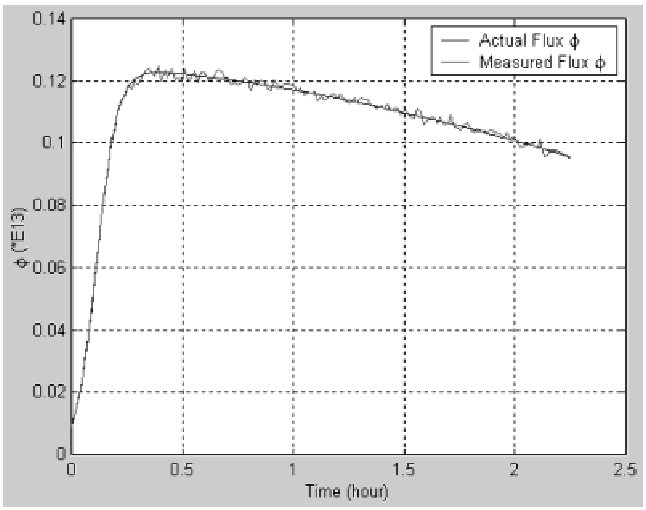

Fig. 3. Actual flux ϕ and its measured value (both simulated) for case 1.

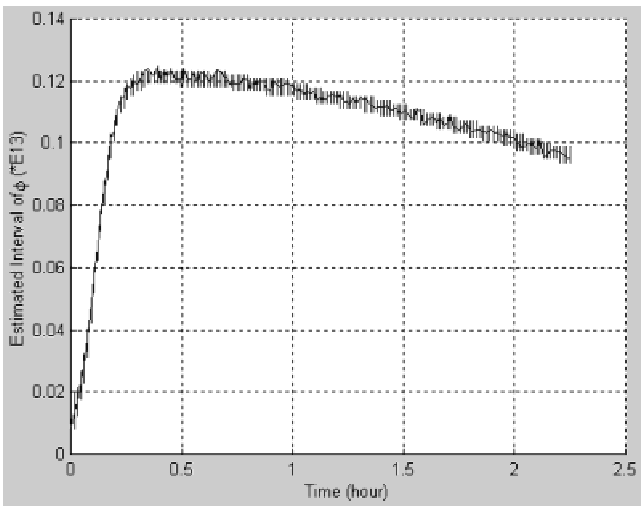

Fig. 4. Estimated interval of flux ϕ as a function of time (solid line indicates the measured value of flux).

TABLE III

The Partitioning Data Used for Case 1

Variables	Possible Maximum Value	Possible Minimum Value	Number of Cells	Number of Quadrature Points $\hat{x}_k^i$ $(i = 1, \ldots, N)$ in Eq. (26)
ϕ	0.14×10^{13}	0	103	3
X/Σ_f	10×10^{13}	0.397×10^{13}	303	3
I/Σ_f	60×10^{13}	0.397×10^{13}	303	3

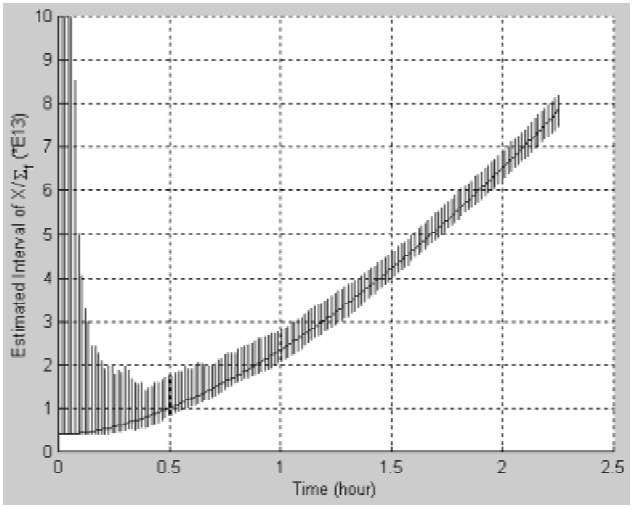

Fig. 5. Estimated interval of X/Σ_f as a function of time.

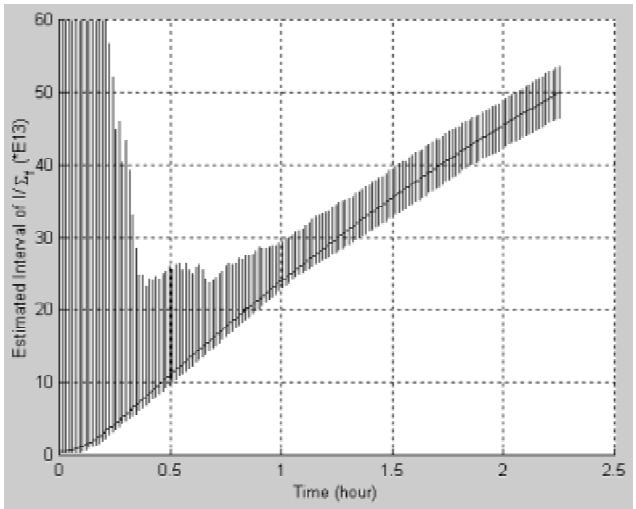

Fig. 6. Estimated interval of I/Σ_f as a function of time.

below. While the estimated interval for X/Σ_f, I/Σ_f is still large after 40 time steps (see Figs. 5 and 6), the mean of the estimated distributions for ϕ and X/Σ_f, I/Σ_f are close to their true values at all times as shown in Figs. 7, 8, and 9, respectively. Figure 10 shows the ratio of the posterior standard deviation over the noise standard deviation $(\sigma_{estimate}/\sigma_{noise})$ for the flux. Together with Fig. 7, which shows that the posterior mean converges to the true flux value, Figs. 7 and 10 demonstrate that the improved estimation procedure can reduce the uncertainty on the measurements by a factor of $\sigma_{estimate}/\sigma_{noise} = 60\%$ for ϕ after about 0.5 h.

Figures 11 and 12, respectively, show the evolution of the posterior variance for X/Σ_f, I/Σ_f for case 1 using $\tau = 0.015$ h and the partitioning data in Table III. The respective posterior standard deviations in the estimated values of X/Σ_f, I/Σ_f are $\sigma_X = 2.7597 \times 10^{13}$ and $\sigma_I = 17.1913 \times 10^{13}$ at the first time step. This uncertainty

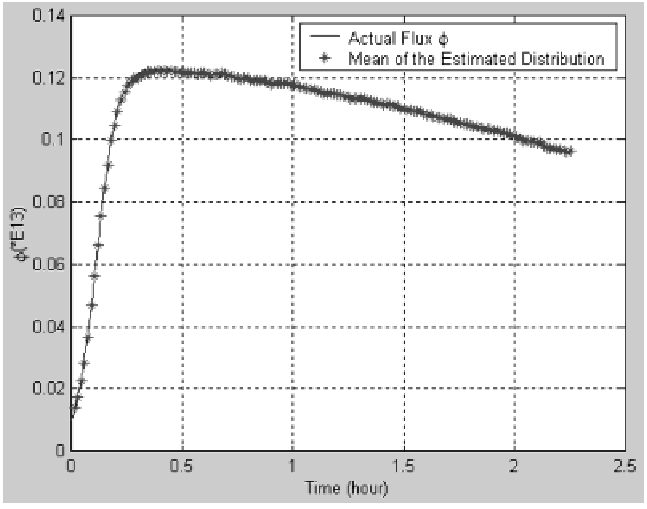

Fig. 7. Mean value of the estimated distribution of ϕ for case 1 (solid line indicates the true value).

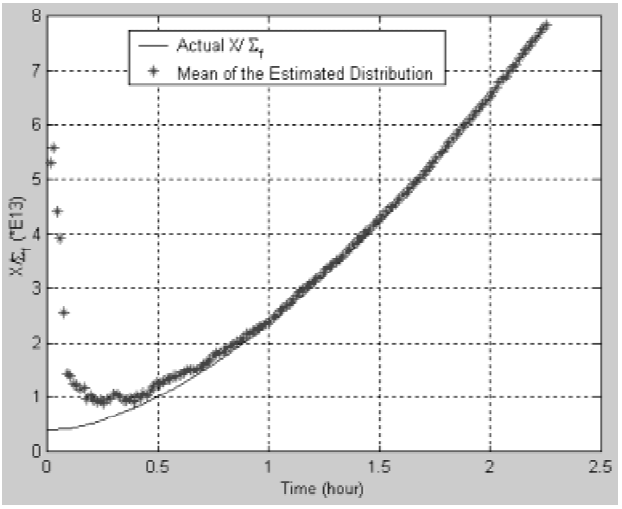

Fig. 8. Mean value of the estimated distribution of X/Σ_f for case 1 (solid line indicates the true value).

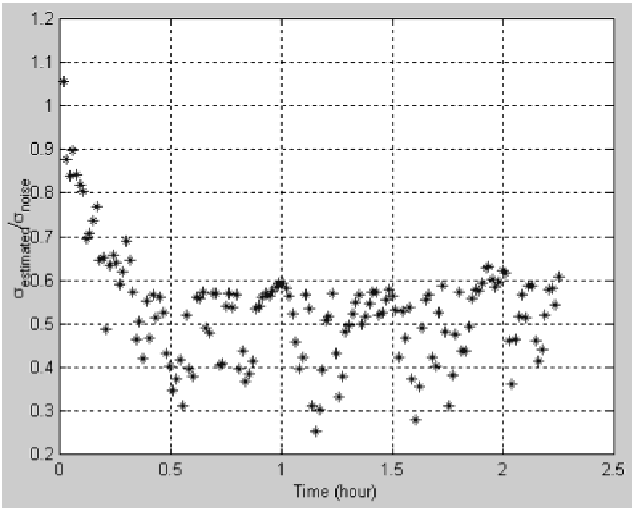

Fig. 10. The ratio of the estimated posterior standard deviation and the noise standard deviation for ϕ.

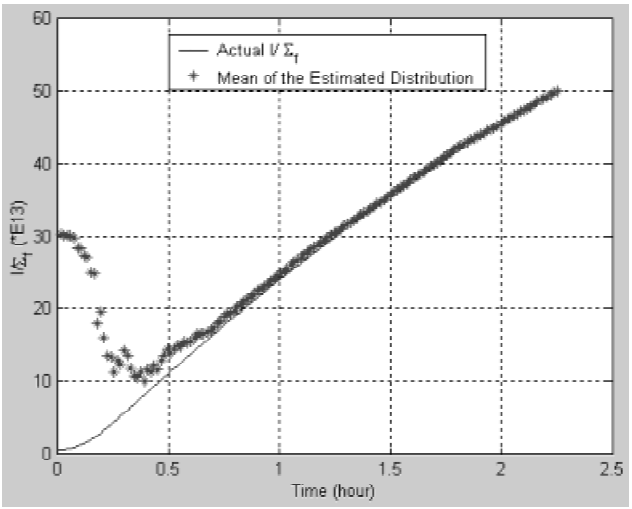

Fig. 9. Mean value of the estimated distribution of I/Σ_f for case 1(solid line indicates the true value).

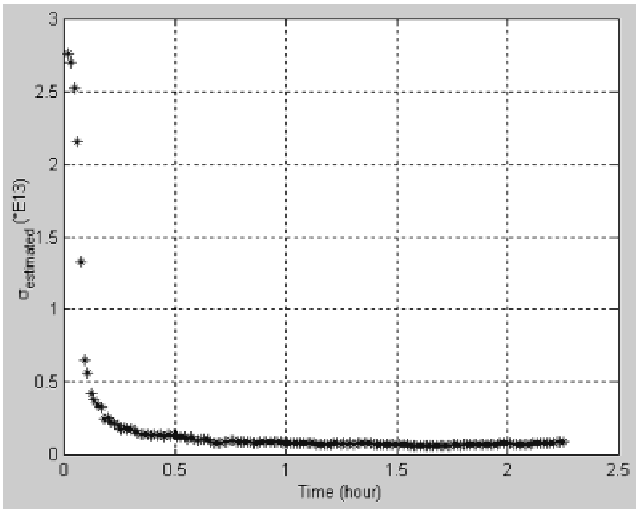

Fig. 11. The evolution of posterior variance for X/Σ_f for case 1.

decreases to $\sigma_X = 0.1781 \times 10^{13}$ and $\sigma_I = 6.1055 \times 10^{13}$ at $t = 20\tau$ (or 0.3 h) and stabilizes around $\sigma_X = 0.08 \times 10^{13}$ and $\sigma_I = 0.8 \times 10^{13}$ after $t = 65\tau$ (or 1 h).

III.C. Estimation Results with Uniform Noise (Case 2)

Table IV shows the data used in case 2 for the simulation of measured values of ϕ. The simulated system evolution is shown in Fig. 13.

The measured data were simulated by using the procedure described for case 1 in Sec. III.B with the data listed in Table IV. The unknown state variables X/Σ_f, I/Σ_f are estimated by two methods: (a) using the improved procedure through Eqs. (24) and (26) and (b) the previous DSD algorithm reported in Ref. 20. Both methods use the partitioning data listed in Table V. The evolution of the estimated 99.99% credibility intervals for ϕ, X/Σ_f, I/Σ_f using the improved procedure is shown in Figs. 14, 15, and 16, respectively, and the corresponding expected values are shown in Figs. 17, 18, and 19. Figures 14 through 19 show that again the measured data are within the expected uncertainty margins and convergence is rapid. Figure 14 also illustrates the signal validation capability of the improved procedure. The flux ϕ is estimated as $0.1183 \times 10^{13} \leq \phi \leq 0.1237 \times 10^{13}$ with

TABLE IV

Data Used for Simulation of System Evolution for Case 2

Initial Value of ϕ	Initial Value of X/Σ_f	Initial Value of I/Σ_f	Time Step τ (h)	Uncertainty Level $\lambda \times 10^{13}$ [see Eq. (30)]
0.01×10^{13}	0.4×10^{13}	0.5×10^{13}	0.015	0.012

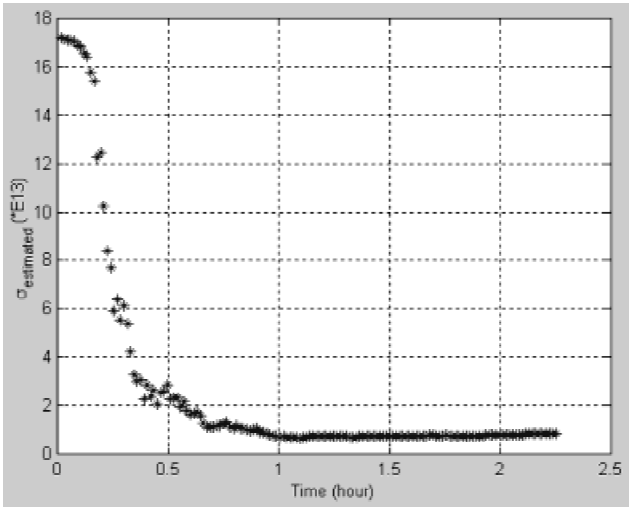

Fig. 12. The evolution of posterior variance for I/Σ_f for case 1.

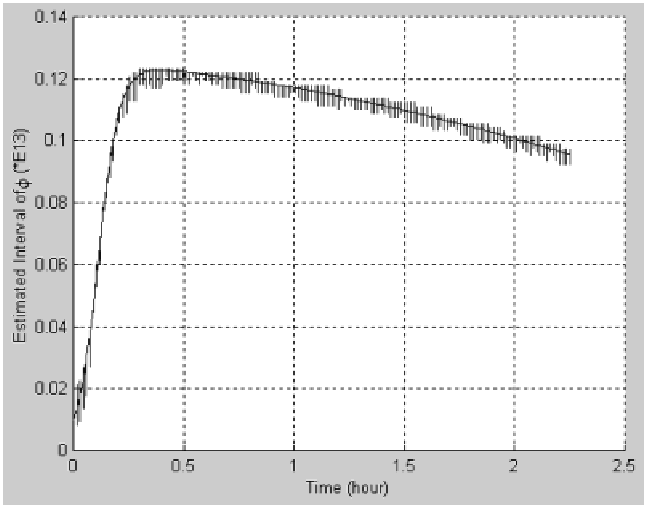

Fig. 14. Estimated interval of flux ϕ as a function of time using Eqs. (24) and (26) for case 2 (solid line indicates the measured value of flux).

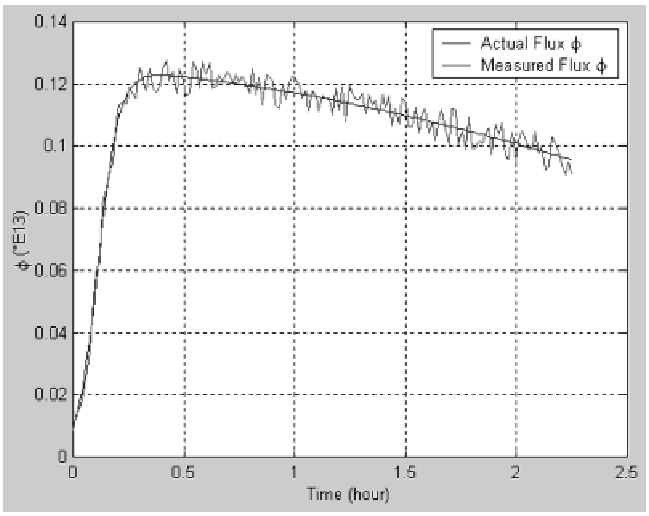

Fig. 13. Actual flux ϕ and its measured value $y(t)$ (both simulated) for case 2.

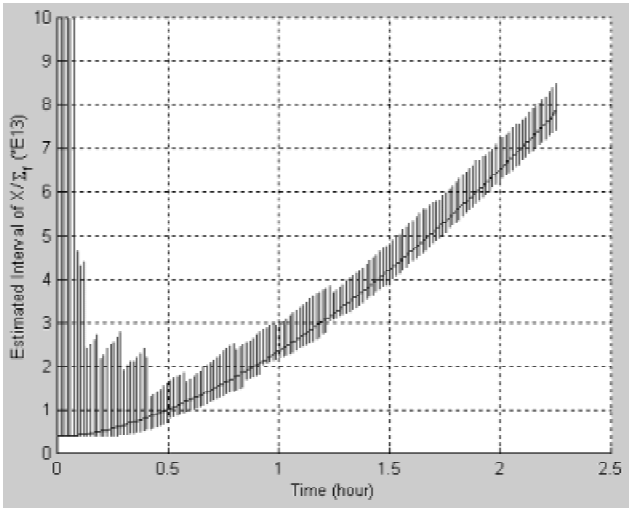

Fig. 15. Estimated interval of X/Σ_f as a function of time using Eqs. (24) and (26) for case 2 (solid line indicates the measured value).

TABLE V

The Partitioning Data Used for Case 2

Variables	Possible Maximum Value	Possible Minimum Value	Number of Cells	Number of Quadrature Points $\hat{x}_k^i$ $(i = 1, \ldots, N)$ in Eq. (26)
ϕ	0.14×10^{13}	0	103	5
X/Σ_f	10×10^{13}	0.397×10^{13}	303	3
I/Σ_f	60×10^{13}	0.397×10^{13}	303	3

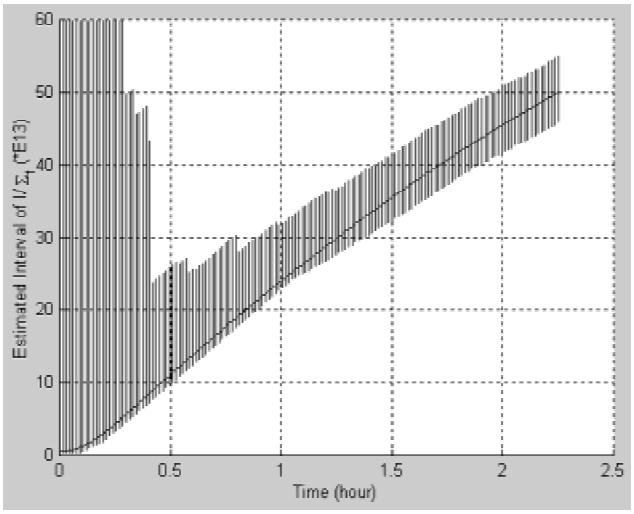

Fig. 16. Estimated interval of I/Σ_f as a function of time using Eqs. (24) and (26) for case 2 (solid line indicates the measured value).

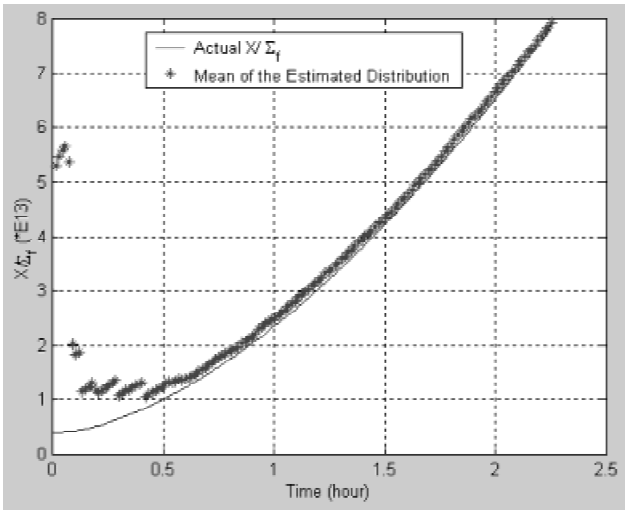

Fig. 18. Mean value of the estimated distribution of X/Σ_f for case 2.

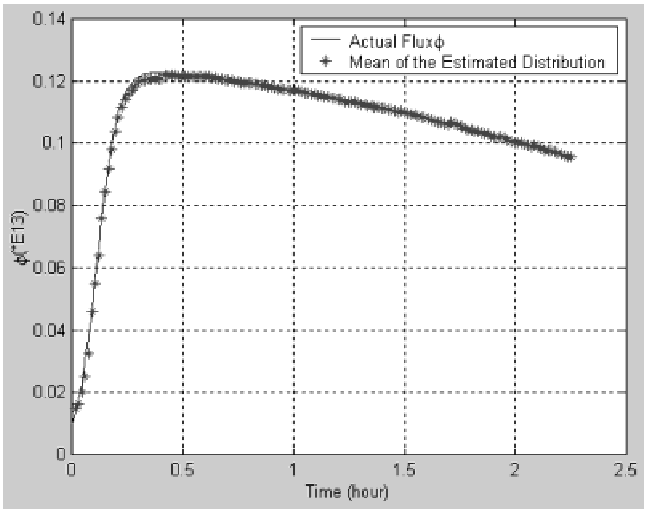

Fig. 17. Mean value of the estimated distribution of ϕ for case 2.

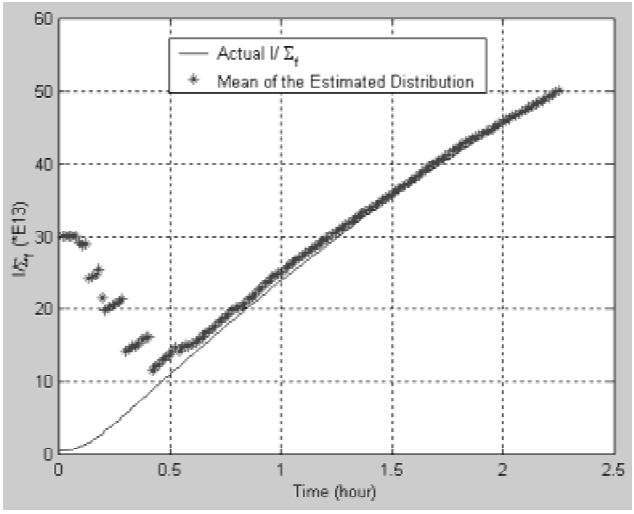

Fig. 19. Mean value of the estimated distribution of I/Σ_f for case 2.

99.99% confidence at time $t = 20\tau$ (or 0.3 h), which is $1 - (0.1237 - 0.1183)/0.012 = 55\%$ smaller than the measurement uncertainty level (see Table IV). Similarly, at time $t = 150\tau$ (or 2.25 h), the flux ϕ is estimated as $0.0924 \times 10^{13} \leq \phi \leq 0.0979 \times 10^{13}$, which is also $1 - (0.0979 - 0.0924)/0.012 = 54\%$ reduction of the measurement noise. These results again show that Eqs. (24) and (26) can be also used to reduce the uncertainty in the measurements for noisy data.

Figures 20 through 23 show the estimation results for case 2 using the DSD algorithm in Ref. 20 with the same partitioning data listed in Table V. Comparing Figs. 20 through 23 to their respective counterparts, Figs. 15, 16, 18, and 19, shows that better estimation results are obtained by using Eqs. (24) and (26) than the previous DSD algorithm. The estimation process converges faster and provides smaller credibility intervals for the unknown variables.

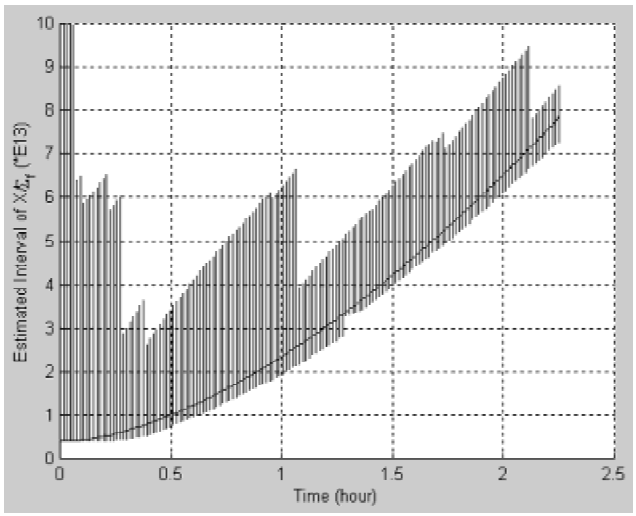

Fig. 20. Estimated interval of X/Σ_f as a function of time using the rules in Ref. 20 for case 2.

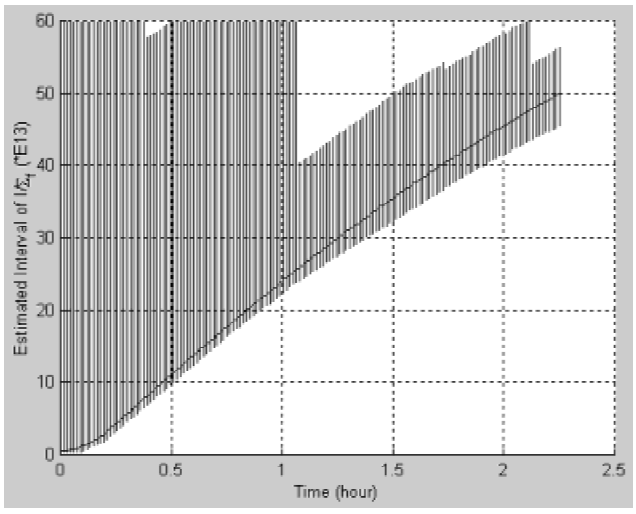

Fig. 21. Estimated interval of I/Σ_f as a function of time using the rules in Ref. 20 for case 2.

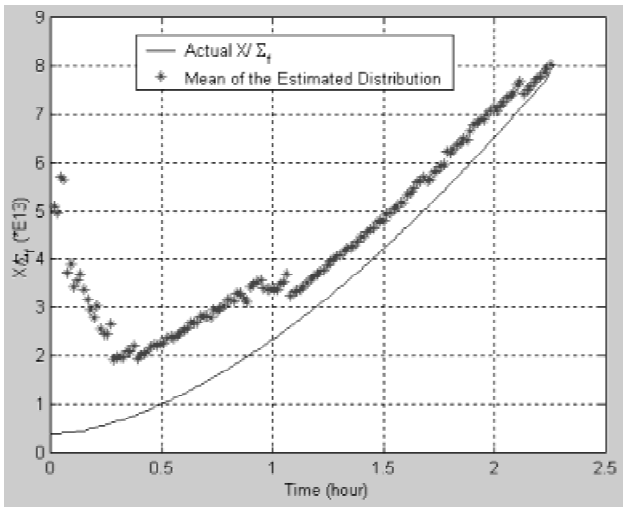

Fig. 22. Mean value of the estimated distribution of X/Σ_f using the rules in Ref. 20 for case 2.

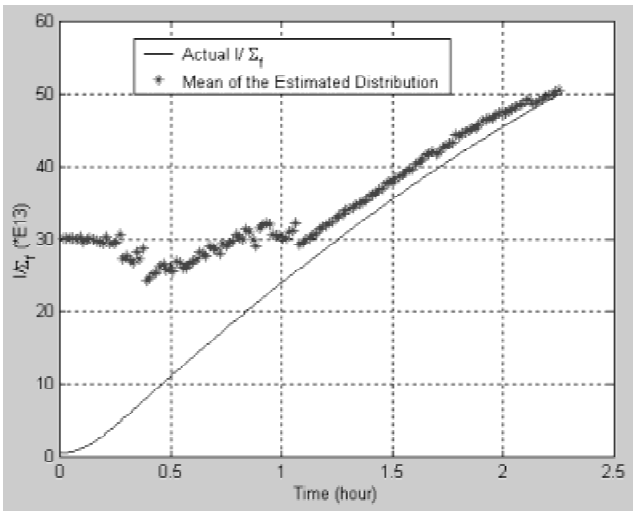

Fig. 23. Mean value of the estimated distribution of I/Σ_f using the rules in Ref. 20 for case 2.

IV. THE RELATIONSHIP OF THE CCMT-BASED STATE/PARAMETER ESTIMATION TO CONVENTIONAL TECHNIQUES

As indicated in Sec. I, the original DSD algorithm is based on the Chapman-Kolmogorov equation, which does

not provide a convenient framework to investigate the relationship of DSD to conventional state/parameter estimation techniques. On the other hand, Sec. II.B shows that the DSD algorithm is a special case of the hierarchical Bayes rule defined through Eq. (6) where the priors $p(\boldsymbol{x}_k|\bar{\boldsymbol{y}}_k)$ are recursively determined from

$$
\begin{aligned}
&p(\boldsymbol{x}_{k+1}|\bar{\boldsymbol{y}}_{k+1}) \\
&\quad = \frac{L(\boldsymbol{x}_{k+1}|\boldsymbol{y}_{k+1})p^{prior}(\boldsymbol{x}_{k+1}|\bar{\boldsymbol{y}}_k)}{\int_{\Omega_{k+1}} d\boldsymbol{x}_{k+1} L(\boldsymbol{x}_{k+1}|\boldsymbol{y}_{k+1})p^{prior}(\boldsymbol{x}_{k+1}|\bar{\boldsymbol{y}}_k)} \\
&\quad = \frac{\int_{\Omega_k} p(\boldsymbol{y}_{k+1}|\boldsymbol{x}_{k+1})p(\boldsymbol{x}_{k+1}|\boldsymbol{x}_k)p(\boldsymbol{x}_k|\bar{\boldsymbol{y}}_k)\,d\boldsymbol{x}_k}{\int_{\Omega_{k+1}} d\boldsymbol{x}_{k+1} p(\boldsymbol{y}_{k+1}|\boldsymbol{x}_{k+1}) \int_{\Omega_k} p(\boldsymbol{x}_{k+1}|\boldsymbol{x}_k)p(\boldsymbol{x}_k|\bar{\boldsymbol{y}}_k)\,d\boldsymbol{x}_k} \\
&\quad = \frac{p(\boldsymbol{y}_{k+1}|\boldsymbol{x}_{k+1})p(\boldsymbol{x}_{k+1}|\bar{\boldsymbol{y}}_k)}{p(\boldsymbol{y}_{k+1}|\bar{\boldsymbol{y}}_k)} \qquad (34)
\end{aligned}
$$

$$
\Rightarrow p(\boldsymbol{x}_{k+1}|\bar{\boldsymbol{y}}_k) = \int p(\boldsymbol{x}_{k+1}|\bar{\boldsymbol{y}}_{k+1})p(\boldsymbol{y}_{k+1}|\bar{\boldsymbol{y}}_k)\,d\boldsymbol{y}_{k+1} \ . \qquad (35)
$$

Equation (35) assumes that $\boldsymbol{y}_k$ as well as $\boldsymbol{x}_k \in \Omega_k$ at each $t = k\tau$ constitute measurable sets. This assumption is realistic since the pdf for $\boldsymbol{w}_k = \boldsymbol{y}_k - \boldsymbol{h}(\boldsymbol{x}_k)$ is often described through a measurable function (e.g., uniform, Gaussian). Then, for a stationary process (e.g., constant parameter vector $\boldsymbol{\theta} = [\theta_1 \theta_2 \ldots \theta_M]$ to be estimated) with the range of interest covering all possible values of $\boldsymbol{\theta}$ under consideration, the following can be shown[37]:

1. There is a unique solution $p(\boldsymbol{\theta})$ to Eq. (34).

2. The sequence $p(\boldsymbol{x}_k)$ converges monotonically in L_1 norm to $p(\boldsymbol{\theta})$.

3. $\int |p(\boldsymbol{x}_k) - p(\boldsymbol{\theta})|\,d\boldsymbol{x}_k \to 0$ exponentially with increasing k.

Other implications of Eq. (6) from estimation theory are as follows:

Implication 1: For a set of constant parameters $\boldsymbol{\theta} = [\theta_1 \theta_2 \ldots \theta_M]$, the mode of $p(\boldsymbol{\theta}|\bar{\boldsymbol{y}}_k)$ yields the maximum likelihood estimate (MLE) of $\boldsymbol{\theta}$ (Ref. 38).

Implication 2: For a set of constant parameters $\boldsymbol{\theta} = [\theta_1 \theta_2 \ldots \theta_M]$ and for $\boldsymbol{w}_k$ being white Gaussian noise, the MLE of $\boldsymbol{\theta}$ is the least-squares estimate (LSE) of $\boldsymbol{\theta}$ (Ref. 39). Therefore, under these assumptions, the mode of $p(\boldsymbol{\theta}|\bar{\boldsymbol{y}}_k)$ is also the LSE of $\boldsymbol{\theta}$.

Implication 3: If $\boldsymbol{w}_k$ and $\boldsymbol{v}$ in Eq. (1) are both white Gaussian noise and $\boldsymbol{f}(\boldsymbol{x}), \boldsymbol{h}(\boldsymbol{x})$ are linear in $\boldsymbol{x}$, then the mean and covariance of $p(\boldsymbol{x}_k|\bar{\boldsymbol{y}}_k)$ obtained from Eq. (6) are equivalent to those obtained from a Kalman filter.[38]

Subsequently, Eqs. (23) and (24), which constitute the improved DSD algorithm and are equivalent to Eq. (6) when the system evolution is represented using CCMT, provide a practical state/parameter estimation procedure that yields the same results as

1. the Kalman filter approach for linear dynamical systems when the modeling uncertainties (i.e., $\boldsymbol{v}$) and measurement noise (i.e., $\boldsymbol{w}_k$) have white Gaussian pdf's
2. the MLE for algebraic systems with constant parameters
3. the LSE for algebraic systems with constant parameters when the measurement noise is white Gaussian.

It should be emphasized, however, the improved DSD algorithm contains the Kalman filter, MLE, and LSE as special cases and has a broader range of applicability than any one of these methods. Section IV.B illustrates implications 1, 2, and 3 using the constant temperature power sensor described in Sec. IV.A.

IV.A. Constant Temperature Power Sensor

The following notation is used in Secs. IV.A and IV.B:

M_i = mass of node i ($i = 1,2$) (kg)

C_i = specific heat capacity of node i ($i = 1,2$) (J/kg·K)

A_i = external area of node i ($i = 1,2$) (m^2)

T_{is} = steady-state temperature of node i ($i = 1,2$) (K)

U_1 = node-1-to-coolant heat transfer coefficient ($W/m^2 \cdot K$)

U_2 = node-2-to-node-1 heat transfer coefficient ($W/m^2 \cdot K$)

T_∞ = coolant temperature (K)

T_h = sensor heater wire reference temperature (K)

i_h = electric current input into the heater wire (A)

α = heater wire temperature coefficient of resistance (1/K)

R_h = heater wire reference resistance (Ω)

$\dot{q}_n$ = nuclear energy input rate into node 2 (W/kg).

A recently developed in-core calorimetric instrument called constant temperature power sensor[40,41] (CTPS) can directly measure the local nuclear energy deposition and heat transfer rate. The direct measurement of the local nuclear energy deposition and the local heat transfer rate reduces the uncertainty in the predicted thermal margins, resulting in improvement in performance and

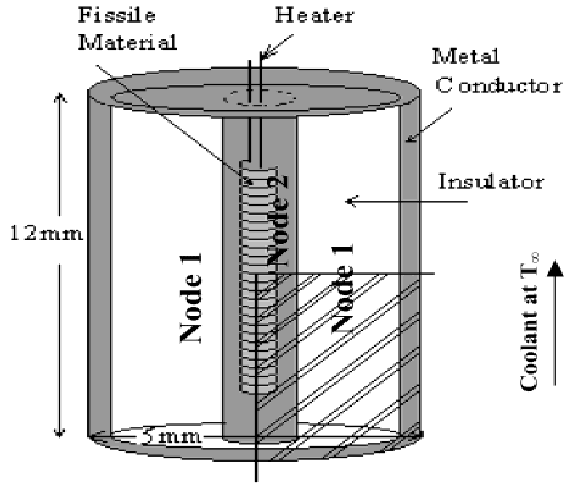

Fig. 24. The constant temperature power sensor.

economy of new reactor designs. This design concept is based on the idea of adding heat through resistive dissipation of input electrical energy, to a small mass of actual reactor fuel analogue (mode 1). The CTPS (Fig. 24) consists of a highly enriched UO_2 core (node 2) surrounded by electrical heating resistance wire. The core is contained in an alumina-based ceramic thermal insulator (node 1). The sensor core and the insulator are coated with thin layers of copper. Heat is lost from the insulator to the surrounding coolant. A feedback control loop is used to provide the exact amount of input electrical energy in order to keep the fuel mass at a constant temperature regardless of the nuclear energy generated in node 2. In steady state (i.e., mode 1), the input electrical energy required will be related to the actual nuclear energy deposition, given the assumption that the external heat transfer rate remains constant; i.e.,

$$M_2\dot{q}_n + [i_h^2 R_h(1+\alpha(T_{2s}-T_h))] = A_2U_2(T_{2s}-T_{1s}) = A_1U_1(T_{1s}-T_\infty) \ . \quad (36)$$

Equation (36) is simply an energy balance between the sensor nodes and surrounding coolant, where $\dot{q}_n$, U_1, U_2, and T_∞ are unknown. The T_{1s} is a known function of T_∞ and T_{2s} (which is measured). The estimation process consists of the following steps:

1. Supply i_h until steady-state conditions are reached (mode 1).

2. Take the sensor temporarily out of the control loop (mode 2), or practically, reduce the supplied electrical current i_h to 1% of the steady-state value in mode 1. In mode 2, the variation of the node 2 temperature T_2 as a function of time t can be represented as[40]

$$T_2(t) = T_\infty + \theta_1 e^{-\theta_2 t} + \theta_3 e^{-\theta_4 t} + w \ , \quad (37)$$

where the exponents θ_2 and θ_2 are related through

$$\theta_2+\theta_4 = -\frac{C_2M_2(U_2A_2+U_1A_1)+C_1M_1(-10^{-4}i_h^2R_h\alpha+U_2A_2)}{C_1M_1C_2M_2}$$

and

$$\theta_2\theta_4 = \frac{-10^{-4}i_h^2R_h\alpha U_2A_2+U_1A_1(-10^{-4}i_h^2R_h\alpha+U_2A_2)}{C_1M_1C_2M_2} \ . \quad (38)$$

In Eq. (37), the quantity w represents model/measurement uncertainty as in Eq. (1). Equation (38) is obtained from the two-node, lumped parameter representation of CTPS under the assumption that the deviation of the node temperatures in mode 2 from their steady-state values in mode 1 is small enough to allow linearization around these mode 1 temperatures.

3. Measure $T_2(t)$ [which also yields T_∞ after the exponentials in Eq. (37) die out] and estimate θ_i $(i=1,\ldots,4)$ through Eqs. (24) and (26).

4. Solve for U_1 and U_2 from Eq. (38) with θ_i $(i=1,2)$ obtained in step 3.

5. Using the T_∞ obtained in step 3 and U_i $(i=1,2)$ found in step 4, solve for $\dot{q}_n$ from Eq. (36).

Work to date shows that the CTPS model parameters can be estimated using the improved procedure through Eqs. (24) and (26), even when the sensor behavior is represented through coupled nonlinear differential equations[42] rather than a single algebraic equation such as Eq. (37).

IV.B. Illustrations

Table VI summarizes the results of the comparison of DSD with LSE, MLE, and Kalman filters using the CTPS described in Sec. IV.A. The LSE results were obtained by minimizing the objective function

TABLE VI

Comparison of the Results for Different Estimators

Parameter/Estimator	$\hat{\theta}_1$	$\hat{\theta}_2$	$\hat{\theta}_3$	$\hat{\theta}_4$
LSE	5.4854	0.2833	19.6994	2.7906
MLE	5.4825	0.2831	19.7017	2.7897
Kalman filter	6.9525	0.3464	18.4278	3.2104
DSD (mode)[a]	5.4663	0.2865	19.7247	2.7978
DSD (mean)[b]	5.4787	0.2829	19.6954	2.7865

[a]For comparison to LSE and MLE.
[b]For comparison to Kalman filter.

$$\sum_{k=1}^{N} [T_{2,k} - T_\infty - \hat{\theta}_1 e^{-\hat{\theta}_2 t_k} - \hat{\theta}_3 e^{-\hat{\theta}_4 t_k}]^2 \quad (39)$$

with respect to $\hat{\theta}_1, \hat{\theta}_2, \hat{\theta}_3, \hat{\theta}_4$, where $T_{2,k} = T_2(t_k)$. The likelihood function used for MLE was

$$\left[\frac{1}{\sqrt{2\pi(0.1)}}\right]^N \exp\left[-\frac{\sum_{k=1}^{N}(T_{2,k} - T_\infty - \hat{\theta}_1 e^{-\hat{\theta}_2 t_k} - \hat{\theta}_3 e^{-\hat{\theta}_4 t_k})^2}{0.2}\right] . \quad (40)$$

The Kalman filter results were found from

$$\hat{\boldsymbol{\theta}}_k = \hat{\boldsymbol{\theta}}_{k-1} + \boldsymbol{K}_k(T_{2,k} - T_\infty - \hat{\theta}_{1,k-1} e^{-\hat{\theta}_{2,k-1} t_k} - \hat{\theta}_{3,k-1} e^{-\hat{\theta}_{4,k-1} t_k}) , \quad (41)$$

where

$$\hat{\boldsymbol{\theta}}_k = [\hat{\theta}_{1,k} \quad \hat{\theta}_{2,k} \quad \hat{\theta}_{3,k} \quad \hat{\theta}_{4,k}] ,$$

$$\boldsymbol{H}_k^T = \begin{bmatrix} e^{-\hat{\theta}_{2,k} t_k} \\ -\hat{\theta}_{1,k} t_k e^{-\hat{\theta}_{2,k} t_k} \\ e^{-\hat{\theta}_{4,k} t_k} \\ -\hat{\theta}_{3,k} t_k e^{-\hat{\theta}_{4,k} t_k} \end{bmatrix} ,$$

$$\boldsymbol{K}_k = \boldsymbol{P}_{k-1} \boldsymbol{H}_k^T (\boldsymbol{H}_k \boldsymbol{P}_{k-1} \boldsymbol{H}_k^T + 0.1)^{-1} ,$$

and

$$\boldsymbol{P}_k = (\boldsymbol{I} - \boldsymbol{K}_k \boldsymbol{H}_k) \boldsymbol{P}_{k-1} \quad (42)$$

with $\boldsymbol{I}$ representing a 4×4 unit matrix and $\boldsymbol{P}_0 = 10\,\boldsymbol{I}$. The partitioning data used for the DSD estimation are shown in Table VII. In all cases, the noise $\boldsymbol{w}_k$ in Eq. (1) was assumed to be Gaussian noise with mean 0, and the variance was calculated by the sample variance of $T_{2,k}$ as 0.1. The data $T_{2,k} = T_2(t_k)$ with $k = 1,\ldots,250$ were generated using the more detailed finite element CTPS model described in Ref. 40.

Table VI shows that there is good agreement among the DSD, LSE, and MLE results, as expected. In general, the differences among the DSD, LSE, and MLE are small (within 0.1 to 1.2%). In order to investigate the origin of the larger differences between the Kalman filter and other estimator results, another set of data $T_{2,k} = T_2(t_k)$ with $k = 1,\ldots,250$ generated using Eq. (37) and the measurement noise was simulated by sampling again from a normal distribution with mean 0 and variance 0.1 using a random number generator (see Table VIII). The estimation results are shown in Table IX, which indicates that with the data generated by Eq. (37) and Gaussian noise, the difference between the DSD and Kalman filter is reduced to $<2.5\%$. The MLE and LSE results are in good agreement with the DSD results in both Tables VI and IX because, as indicated above, for a set of constant parameters $\boldsymbol{\theta} = [\theta_1 \theta_2 \ldots \theta_M]$, (a) the mode of $p(\boldsymbol{\theta}|\bar{\boldsymbol{y}}_k)$ yields the MLE of $\boldsymbol{\theta}$ and (b) if $\boldsymbol{w}_k$ is white Gaussian noise, the MLE of $\boldsymbol{\theta}$ is the LSE of $\boldsymbol{\theta}$. The explanation of the reduction of the difference between the DSD and Kalman filter results from Tables VI through IX is that the data generated from the finite element model of Ref. 40 do not conform to the functional form of Eq. (37). Subsequently, $\boldsymbol{w}_k$ in Eq. (37) is not strictly Gaussian as assumed by the Kalman filter approach [see implication 3 following Eq. (35)].

TABLE VII

DSD Partitioning Data Used for the CTPS Model

Parameter	θ_1	θ_2	θ_3	θ_4
Maximum	7	0.6	22	3.5
Minimum	4	0.0	17	2.5
Number of cells	89	89	89	89
Number of quadrature points $\hat{x}_k^i$ $(i = 1,\ldots,N)$ in Eq. (26)	3	3	3	3

TABLE VIII

Parameter Used for Simulation of Measured Temperature from Eq. (37)

Parameter	θ_1	θ_2	θ_3	θ_4	Mean of the Noise	Variance of the Noise
Value	5.4	0.28	19.7	2.8	0.0	0.1

TABLE IX

Comparison of the Results for Different Estimators for Data Simulated from Eq. (37) and Gaussian Noise

Parameter/Estimator	θ_1	θ_2	θ_3	θ_4
LSE	5.8026	0.2904	19.0819	2.9245
MLE	5.7935	0.2900	19.0888	2.9223
Kalman filter	5.8972	0.2948	18.9750	2.9163
DSD (mode)[a]	5.8061	0.3000	19.1939	2.9388
DSD (mean)[b]	5.7775	0.2889	19.0978	2.9174

[a]For comparison to LSE and MLE.
[b]For comparison to Kalman filter.

V. CONCLUSION

This study shows that the CCMT-based state/parameter estimation procedure, originally based on the Chapman-Kolmogorov equation[20](or in its algorithmic form, DSD), is equivalent to a recursive Bayesian

estimator in the discretized system state/parameter space. This Bayesian interpretation of the DSD algorithm

1. increases the applicability of methodology to arbitrary observers and arbitrary noise distributions in the monitored data as well as to arbitrary uncertainties in the model parameters
2. leads to improvements in the estimation speed and accuracy, as illustrated using the Chernick model[35] of xenon evolution with temperature feedback
3. establishes a link to conventional estimation schemes such as MLE, LSE, and Kalman filter as illustrated by the CTPS model.[40]

The improved DSD algorithm contains MLE, LSE, and the Kalman filter as special cases and has a broader range of applicability than any one of these methods regarding system representation, modeling uncertainties and measurement noise again as illustrated by the CTPS example. The Bayesian interpretation also provides a possible explanation for the origins of some unexplained phenomena encountered in previous work.[29]

APPENDIX A

DERIVATION OF EQ. (31) FROM EQ. (23)

First, using Eq. (30) and noting that $\boldsymbol{y}_{k+1} = \hat{\boldsymbol{x}}_{k+1} + \boldsymbol{w}_{k+1}$ from difference 2, we have

$$p(\boldsymbol{y}_{k+1}|\boldsymbol{x}_{k+1}) = f_w(\boldsymbol{y}_{k+1} - \hat{\boldsymbol{x}}_{k+1}) = \begin{cases} 1 & |\hat{\boldsymbol{x}}_{k+1} - \boldsymbol{y}_{k+1}| \le \lambda \\ 0 & \text{else} \end{cases} = \begin{cases} 1 & \hat{\boldsymbol{x}}_{k+1} \in \hat{\boldsymbol{j}}_{k+1} \\ 0 & \hat{\boldsymbol{x}}_{k+1} \notin \hat{\boldsymbol{j}}_{k+1} \end{cases} . \tag{A.1}$$

Recalling that $\boldsymbol{j} = \{\hat{\boldsymbol{j}} \quad \bar{\boldsymbol{j}}\}$ and $\boldsymbol{x} = \{\hat{\boldsymbol{x}} \quad \bar{\boldsymbol{x}}\}$, the transition probability $g(\hat{\boldsymbol{j}}_{k+1}, \bar{\boldsymbol{j}}_{k+1}|\hat{\boldsymbol{j}}_k, \bar{\boldsymbol{j}}_k)$ can be written from Eq. (23) as the following:

$$\begin{aligned} g(\boldsymbol{j}_{k+1}|\boldsymbol{j}_k) \equiv g(\hat{\boldsymbol{j}}_{k+1}, \bar{\boldsymbol{j}}_{k+1}|\hat{\boldsymbol{j}}_k, \bar{\boldsymbol{j}}_k) &= \iint_{\hat{j}_{k+1}, \bar{j}_{k+1}} \iint_{\hat{j}_k, \bar{j}_k} p(\boldsymbol{y}_{k+1}|\hat{\boldsymbol{x}}_{k+1}, \bar{\boldsymbol{x}}_{k+1}) p(\hat{\boldsymbol{x}}_{k+1}, \bar{\boldsymbol{x}}_{k+1}|\hat{\boldsymbol{x}}_k, \bar{\boldsymbol{x}}_k) \\ &\quad \times \frac{p(\hat{\boldsymbol{x}}_k, \bar{\boldsymbol{x}}_k|\bar{\boldsymbol{y}}_k)}{\int_{j_k} p(\boldsymbol{x}_k|\bar{\boldsymbol{y}}_k)\, d\boldsymbol{x}_k} d\hat{\boldsymbol{x}}_k\, d\bar{\boldsymbol{x}}_k\, d\hat{\boldsymbol{x}}_{k+1}\, d\bar{\boldsymbol{x}}_{k+1} \\ &= \iint_{\hat{j}_{k+1}, \bar{j}_{k+1}} \iint_{\hat{j}_k, \bar{j}_k} f_w(\boldsymbol{y}_{k+1} - \hat{\boldsymbol{x}}_{k+1}) p(\hat{\boldsymbol{x}}_{k+1}, \bar{\boldsymbol{x}}_{k+1}|\hat{\boldsymbol{x}}_k, \bar{\boldsymbol{x}}) \\ &\quad \times \frac{p(\hat{\boldsymbol{x}}_k, \bar{\boldsymbol{x}}_k|\bar{\boldsymbol{y}}_k)}{\int_{j_k} p(\boldsymbol{x}_k|\bar{\boldsymbol{y}}_k)\, d\boldsymbol{x}_k} d\hat{\boldsymbol{x}}_k\, d\bar{\boldsymbol{x}}_k\, d\hat{\boldsymbol{x}}_{k+1}\, d\bar{\boldsymbol{x}}_{k+1} , \end{aligned} \tag{A.2}$$

where $\hat{\boldsymbol{x}}_k$ and $\bar{\boldsymbol{x}}_k$ denote the location of the monitored and unmonitored system variables in their respective spaces. Using Eq. (A.1), Eq. (A.2) becomes

$$\begin{aligned} g(\boldsymbol{j}_{k+1}|\boldsymbol{j}_k) &= g(\hat{\boldsymbol{j}}_{k+1}, \bar{\boldsymbol{j}}_{k+1}|\hat{\boldsymbol{j}}_k, \bar{\boldsymbol{j}}_k) \\ &= \iint_{\hat{j}_{k+1}, \bar{j}_{k+1}} \iint_{\hat{j}_k, \bar{j}_k} p(\hat{\boldsymbol{x}}_{k+1}, \bar{\boldsymbol{x}}_{k+1}|\hat{\boldsymbol{x}}_k, \bar{\boldsymbol{x}}_k) \frac{p(\hat{\boldsymbol{x}}_k, \bar{x}_k|\bar{\boldsymbol{y}}_k)}{\int_{j_k} p(\hat{\boldsymbol{x}}_k, \bar{x}_k|\bar{\boldsymbol{y}}_k)\, d\hat{\boldsymbol{x}}_k\, d\bar{x}_k} d\hat{\boldsymbol{x}}_k\, d\bar{\boldsymbol{x}}_k\, d\hat{\boldsymbol{x}}_{k+1}\, d\bar{\boldsymbol{x}}_{k+1} \\ &= \iint_{j_{k+1}, j_k} p(\boldsymbol{x}_{k+1}|\boldsymbol{x}_k) \frac{p(\boldsymbol{x}_k|\bar{\boldsymbol{y}}_k)}{\int_{j_k} p(\boldsymbol{x}_k|\bar{\boldsymbol{y}}_k)\, d\boldsymbol{x}_k} d\boldsymbol{x}_{k+1}\, d\boldsymbol{x}_k , \end{aligned} \tag{A.3}$$

where $\boldsymbol{j}_{k+1} = \{\hat{\boldsymbol{j}}_{k+1} \quad \bar{\boldsymbol{j}}_{k+1}\}$ and $\boldsymbol{j}_k = \{\hat{\boldsymbol{j}}_k \quad \bar{\boldsymbol{j}}_k\}$. If there is no modeling uncertainty (i.e., difference 1 above), Eq. (16) holds, and Eq. (A.3) becomes

$$g(\hat{\boldsymbol{j}}_{k+1}, \bar{\boldsymbol{j}}_{k+1} | \hat{\boldsymbol{j}}_k, \bar{\boldsymbol{j}}_k) = \iint\limits_{j_{k+1},\, j_k} p(\boldsymbol{x}_{k+1}|\boldsymbol{x}_k) \frac{p(\boldsymbol{x}_k|\bar{\boldsymbol{y}}_k)}{\int_{j_k} p(\boldsymbol{x}_k|\bar{\boldsymbol{y}}_k)\, d\boldsymbol{x}_k} d\boldsymbol{x}_{k+1}\, d\boldsymbol{x}_k$$

$$= \iint\limits_{j_{k+1},\, j_k} \delta(\boldsymbol{x}_{k+1} - \tilde{\boldsymbol{x}}(\boldsymbol{x}_k)) \frac{p(\boldsymbol{x}_k|\bar{\boldsymbol{y}}_k)}{\int_{j_k} p(\boldsymbol{x}_k|\bar{\boldsymbol{y}}_k)\, d\boldsymbol{x}_k} d\boldsymbol{x}_{k+1}\, d\boldsymbol{x}_k$$

$$= \int_{j_k} \frac{p(\boldsymbol{x}_k|\bar{\boldsymbol{y}}_k)}{\int_{j_k} p(\boldsymbol{x}_k|\bar{\boldsymbol{y}}_k)\, d\boldsymbol{x}_k} e_{k+1}(\tilde{\boldsymbol{x}}(\boldsymbol{x}_k))\, d\boldsymbol{x}_k \ , \tag{A.4}$$

where $e_{k+1}(\tilde{\boldsymbol{x}}(\boldsymbol{x}_k))$ is as defined in Eq. (27). Finally, by assuming that the system location is uniformly distributed over the cell $\boldsymbol{j}_k$ and using Eq. (28),

$$\frac{p(\boldsymbol{x}_k|\bar{\boldsymbol{y}}_k)}{\int_{j_k} p(\boldsymbol{x}_k|\bar{\boldsymbol{y}}_k)\, d\boldsymbol{x}_k} = \frac{1}{V_k} \ . \tag{A.5}$$

Then,

$$g(\hat{\boldsymbol{j}}_{k+1}, \bar{\boldsymbol{j}}_{k+1} | \hat{\boldsymbol{j}}_k, \bar{\boldsymbol{j}}_k) = \frac{1}{V_k} \int_{j_k} e_{k+1}(\tilde{\boldsymbol{x}}(\boldsymbol{x}_k))\, d\boldsymbol{x}_k \ , \tag{A.6}$$

which is the same as Eq. (31).

REFERENCES

1. D. J. MOOK, "Estimation and Identification of Nonlinear Dynamic Systems," *AIAA J.*, **27**, 968 (1989).

2. J. S. ALBUQUERQUE and L. T. BIEGLER, "Decomposition Algorithm for On-Line Estimation with Nonlinear Models," *Comput. Chem. Eng.*, **19**, *10*, 1031 (1995).

3. M. GUAY and D. D. McLEAN, "Optimization and Sensitivity Analysis for Multiresponse Parameter Estimation in Systems of Ordinary Differential Equations," *Comput. Chem. Eng.*, **19**, 1271 (1995).

4. K. D. HJELMSTAD and M. R. BANAN, "Time-Domain Parameter Estimation Algorithm for Structures. I: Computational Aspects," *J. Eng. Mech.*, **121**, 424 (1995).

5. Z.-S. LIU, "QR Methods of O(N) Complexity in Adaptive Parameter Estimation," *IEEE Trans. Signal Processing*, **43**, 720 (1995).

6. D. DIMOGIANOPOULOS and R. LOZANO, "Adaptive Control for Linear Slowly Time Varying Systems Using Direct Least-Squares Estimation," *Automatica*, **37**, 251 (2001).

7. M. A. HOPKINS and H. F. VAN LANDINGHAM, "Optimal Nonlinear Estimation of Linear Stochastic Systems," *J. Dynamic Syst. Measurement Control*, **116**, 529 (1994).

8. M. A. HOPKINS and H. F. VAN LANDINGHAM, "Optimal Nonlinear Estimation of Linear Stochastic Systems: The Multivariable Extension," *J. Dynamic Syst. Measurement Control*, **118**, 350 (1996).

9. J. L. DOUCE and Q. M. ZHU, "Modeling a Class of Nonlinear Systems," *IEEE Proc.*, **137**, 385 (1990).

10. S. LYASHEVSKIY and Y.-B. CHEN, "Identification of Nonlinear System Parameters Using Describing Function Approach," *Proc. Am. Control Conf.*, Albuquerque, New Mexico, p. 1944 (1997).

11. M. RICARDO and P. TOMEI, "Adaptive Observers with Arbitrary Exponential Rate of Convergence for Nonlinear Systems," *IEEE Trans. Automatic Control*, **40**, 1300 (1995).

12. R. A. McCANN, M. S. ISLAM, and I. HUSAIN, "Application of a Sliding-Mode Observer for Position and Speed Estimation in Switched Reluctance Motor Drives," *IEEE Trans. Industry Applications*, **37**, *1* (2001).

13. P. WANG, T. ALDEMIR, and V. I. UTKIN, "Estimation of Xenon Concentration and Reactivity in Nuclear Reactor Using Sliding Mode Observer," *Proc. 40th IEEE Conf. Decision and Control*, Orlando, Florida, December 2001.

14. Y.-W. KIM, G. RIZZONI, and V. I. UTKIN, "Automotive Engine Diagnosis and Control via Nonlinear Estimation," *IEEE Control Syst.* (Oct. 1998).

15. E. BOLVIKEN, P. J. ACKLAM, N. CHRISTOPHERSEN, and J.-M. STORDAL, "Monte Carlo Filters from Non-Linear State Estimation," *Automatica*, **37**, 177 (2001).

16. C. D. CHARALAMBOUS and A. LOGOTHETIS, "Maximum Likelihood Parameter Estimation from Incomplete Data

via Sensitivity Equations: The Continuous-Time Case," *IEEE Trans. Automatic Control*, **45**, *5* (2000).

17. A. G. PARLOS, A. F. ATIYA, K. T. CHONG, and W. K. TSAI, "Nonlinear Identification of Process Dynamic Using Neural Networks," *Nucl. Technol.*, **97**, 79 (1992).

18. R. J. PATTON, C. J. LOPEZ-TORIBIO, and F. J. UPPAL, "Artificial Intelligence Approaches to Fault Diagnosis for Dynamic Systems," *Int. J. Appl. Math. Comp. Sci.*, **9**, *3*, 471 (1999).

19. M. MARSEGUERRA and E. ZIO, "Genetic Algorithms for Estimating Effective Parameters in a Lumped Reactor Model for Reactivity Predictions," *Nucl. Sci. Eng.*, **139**, 96 (2001).

20. L. DINCA and T. ALDEMIR, "Parameter Estimation Toward Fault Diagnosis in Nonlinear Systems Using a Markov Model of System Dynamics," *Nucl. Sci. Eng.*, **127**, 199 (1997).

21. P. WANG, T. ALDEMIR, and D. W. MILLER, "Reactivity Ramp Rate Estimation Using a Probabilistic Approach," *Trans. Am. Nucl. Soc.*, **78**, 121 (1998).

22. P. WANG and T. ALDEMIR, "Real-Time Xenon Estimation in Nuclear Power Plants," *Trans. Am. Nucl. Soc.*, **81**, 154 (1999).

23. M. GADIOLI, M. MARSEGUERRA, and E. ZIO, "Fast Integration by Neural Nets in DSD: Probabilistic State Estimation," *Trans. Am. Nucl. Soc.*, **81**, 151 (1999).

24. X. M. CHEN, P. WANG, and T. ALDEMIR, "DSD; A Parameter/State Estimation Tool for Model-Based Fault Diagnosis in Non-Linear Dynamic Systems," *Dynamic Reliability: Future Directions, International Workshop Series on Advanced Topics in Reliability and Risk Analysis*, Center for Reliability Engineering, University of Maryland (1999).

25. "Dynamic System Doctor," Interactive Version; available on the Internet at ⟨http://rclsgi.eng.ohio-state.edu/courses/Aldemir/DSDInteractive/index2.htm⟩.

26. H. STARK and J. W. WOODS, *Probability, Random Process and Estimation Theory for Engineers*, 2nd ed., Chap. 11.6, Prentice-Hall, Upper Saddle River, New Jersey (1994).

27. R. B. ASH, *Real Analysis and Probability*, Academic Press, New York (1972).

28. C. W. GARDINER, *Handbook of Stochastic Methods for Physics, Chemistry and the Natural Sciences*, Chap. 1.2, Springer-Verlag, New York (1983).

29. B. TOMBUYSES and T. ALDEMIR, "Continuous Cell-to-Cell Mapping," *J. Sound Vibration*, **202**, *3*, 395 (May 1997).

30. N. B. HAASER and J. A. SULLIVAN, *Real Analysis*, p. 89, Van Nostrand Reinhold Company, New York (1971).

31. T. ALDEMIR, "Some Measure-Theoretic Issues in the Implementation of Dynamic Methodologies for PRA," *Trans. Am. Nucl. Soc.*, **89**, 410 (2003).

32. J. DEVOOGHT and C. SMIDTS, "Probabilistic Reactor Dynamics—I: The Theory of Continuous Event Trees," *Nucl. Sci. Eng.*, **111**, 229 (1992).

33. L. DINCA and T. ALDEMIR, "State/Parameter Estimation in BWR Dynamics," *Trans. Am. Nucl. Soc*, **80**, 124 (1999).

34. J. MARCH-LEUBA, D. G. CACUCI, and R. B. PEREZ, "Nonlinear Dynamics and Stability of Boiling Water Reactors: Part 2—Quantitative Analysis," *Nucl. Sci. Eng.*, **93**, 124 (1986).

35. J. CHERNICK, G. LELLOUCHE, and W. WOLLMAN, "The Effect of Temperature on Xenon Instability," *Nucl. Sci. Eng.*, **10**, 120 (1961).

36. H.-L. JIN, M. GADIOLI, P. WANG, T. ALDEMIR, and D. W. MILLER, "Validation of a Point Reactor Model for Global Xenon Estimation," *Proc. 8th Int. Conf. Nuclear Engineering*, Baltimore, Maryland, April 12–16, 2000 (2000).

37. M. A. TANNER and W. H. WONG, "The Calculation of Posterior Distributions by Data Augmentation," *J. Am. Stat. Assoc.*, **82**, 528 (1987).

38. N. MORRISON, *Introduction to Sequential Smoothing and Prediction*, p. 468, McGraw-Hill Book Company, New York (1969).

39. R. LUPTON, *Statistics in Theory and Practice*, p. 81, Princeton University Press, Princeton, New Jersey (1993).

40. T. D. RADCLIFF, D. W. MILLER, and A. C. KAUFFMAN, "Modeling of a Constant-Temperature Power Sensor," *Proc. 8th Int. Conf. Nuclear Engineering*, Baltimore, Maryland, April 2–6, 2000 (2000).

41. T. D. RADCLIFF, D. W. MILLER, and A. C. KAUFFMAN, "Constant-Temperature Calorimetry for In-Core Power Measurement," *Nucl. Technol.*, **132**, 240 (2000).

42. A. BURGHELEA and T. ALDEMIR, "In-Core Power Detection with CTPS Using a Non-Linear Model," *Trans. Am. Nucl. Soc.*, **88**, 314 (2003).

Probabilistic Safety Assessment and Management: PSAM 7-ESREL'04,
C. Spitzer, U. Schmocker, V. N. Dang (Eds.), 1809-1814, Springer – Verlag, London, U.K. (June 2004)

The DSD and Conventional State/Parameter Estimation

Peng Wang and Tunc Aldemir
The Ohio State University, 206 West 18th Avenue,
Columbus, OH 43210, U.S.A.

Abstract

The DSD (Dynamic System Doctor) is system independent, state/parameter estimation software that can be used for both point and interval estimation. The DSD also yields useful information for risk informed regulation and risk monitoring of nuclear power plants. The relationship of DSD to some conventional estimation techniques is described and illustrated using a linearized model for the on-line calibration of the constant temperature power sensor, recently proposed for direct core power density distribution measurement in Generation IV reactors.

1 Introduction

The DSD (Dynamic System Doctor) is system independent, state/parameter estimation software [1]. The DSD uses a system representation scheme based on the transition probabilities between user specified computational cells that partition the system state space (cell-to-cell mapping). These transition probabilities are obtained from the user supplied system model. The theoretical basis of the DSD and the current DSD algorithm are described in a companion paper [2]. The main advantage of the DSD over conventional estimators is that DSD is both a point and an interval estimator. In addition, the DSD yields the probability distribution of the system variables/parameters within the estimated bounds which provides a probabilistic measure to rank the likelihood of system faults in view of modeling uncertainties and/or signal noise. Such information is particularly useful for risk informed regulation and risk monitoring of nuclear power plants.

The current DSD algorithm is based on the assumptions that: a) the measurement noise is uniformly distributed, and, b) the measured variables are part of the state variable vector. Recent theoretical developments [3] have extended the applicability range of DSD to arbitrarily distributed (but known) signal noise and modeling uncertainties and arbitrary observers. The new theoretical developments have also provided the framework which clarifies the previously unexplained relationship between DSD and conventional state/parameter estimation techniques. The paper describes and illustrates the relationship of DSD to the generalized maximum likelihood estimator (MLE),

least squares estimator (LSE) and the Kalman filter approach.

2 Overview of the Recent Developments

The extended DSD algorithm accepts system equations of the form

$$\boldsymbol{x}_{k+1} = \tilde{\boldsymbol{x}}(\boldsymbol{x}_k) + \boldsymbol{v}_k \quad (k = 0,1,2,\cdots) \tag{1}$$

and observers of the form

$$\boldsymbol{y}_k = \boldsymbol{h}(\boldsymbol{x}_k) + \boldsymbol{w}_k \quad (k = 0,1,2,\cdots) \tag{2}$$

where

$\boldsymbol{x}$ L-dimensional vector whose elements are the state variables or unknown model parameters x_l $(l = 1,...,L)$ of the dynamic system

$\boldsymbol{v}_k$ system noise at time step $k\tau$ $(k = 0,1,2,...)$ (e.g. due to stochastic variation of system parameters) or a measure of modelling uncertainties, in general

$\boldsymbol{x}_k$ state vector at time step $k\tau$ $(k = 0,1,2,...)$

$\boldsymbol{y}_k$ M-dimensional vector whose elements y_k are the measured data at time step $k\tau$ $(k = 0,1,2,...)$

$\boldsymbol{w}_k$ measurement uncertainty

$\tilde{\boldsymbol{x}}$ a L- dimensional rule that maps $\boldsymbol{x}_k$ onto $\boldsymbol{x}_{k+1}$ (such as by the integration of a set of L ordinary differential equations)

$\boldsymbol{h}$ M - dimensional vector whose elements are known nonlinear functions

The estimation process takes place in the discretized state/parameter space partitioned through the user-defined intervals

$$\Delta_{l,j_l} = \{x_l : a_{l,j_l} \le x < a_{l,j_l+1}; a_{l,1} = a_l, a_{l,J_l} = b_l\} \tag{3}$$
$$j_l = 1,...,J_l; l = 1,...,L.$$

The specification of these intervals may be, for example, based on the uncertainty/noise in the monitored x_l. The Δ_{l,j_l} constitute the computational cells $\boldsymbol{V}_j = \{\Delta_{1,j_1}, \Delta_{2,j_2}, ...\Delta_{L,j_L}\}$ $(j = 1,...,J = \prod_{l=1}^{L} J_l)$ which partition the

range of interest $a_l \le x_l \le b_l (l = 1,...,L)$ in the state/parameter space in a similar manner to those used by finite difference and finite element methods. If $\boldsymbol{j} = \{j_1 j_2 ... j_L\}$ denotes the location of the cell $\boldsymbol{V}_j$ in the discretized state-space, then it can be shown that [3] the probability

$$p(\boldsymbol{j}_k | \bar{\boldsymbol{y}}_k) = \int_{\boldsymbol{j}_k} p(\boldsymbol{x}_k | \bar{\boldsymbol{y}}_k) d\boldsymbol{x}_k \tag{4}$$

of finding the system in the cell $\boldsymbol{j}_k$ at time $t = k\tau$ is recursively calculated from

$$p(\boldsymbol{j}_{k+1} | \bar{\boldsymbol{y}}_{k+1}) = \frac{\sum_{\boldsymbol{j}_k} g(\boldsymbol{j}_{k+1} | \boldsymbol{j}_k) p(\boldsymbol{j}_k | \bar{\boldsymbol{y}}_k)}{\sum_{\boldsymbol{j}_{k+1}} \sum_{\boldsymbol{j}_k} g(\boldsymbol{j}_{k+1} | \boldsymbol{j}_k) p(\boldsymbol{j}_k | \bar{\boldsymbol{y}}_k)} \tag{5}$$

$$g(\boldsymbol{j}_{k+1} | \boldsymbol{j}_k) = \iint_{\boldsymbol{j}_{k+1}, \boldsymbol{j}_k} p(\boldsymbol{y}_{k+1} | \boldsymbol{x}_{k+1}) p(\boldsymbol{x}_{k+1} | \boldsymbol{x}_k) \frac{p(\boldsymbol{x}_k | \bar{\boldsymbol{y}}_k)}{\int_{\boldsymbol{j}_k} p(\boldsymbol{x}_k | \bar{\boldsymbol{y}}_k) d\boldsymbol{x}_k} d\boldsymbol{x}_k d\boldsymbol{x}_{k+1} \tag{6}$$

where $g(\boldsymbol{j}_{k+1} | \boldsymbol{j}_k)$ is the probability that the system will move from cell $\boldsymbol{j}_k$ to cell $\boldsymbol{j}_{k+1}$ during $k\tau \le t < (k+1)\tau$. It can be also shown that [3]:

1. Eqs.(5) and (6) constitute a recursive Bayesian estimator (the original DSD algorithm is based on the Chapman-Kolmogorov equation),
2. if $\boldsymbol{j}_{s,k}$ denotes the actual cell the system is in at time $t = k\tau$ and $g(\boldsymbol{j}_{k+1} | \boldsymbol{j}_k) < g(\boldsymbol{j}_{s,k+1} | \boldsymbol{j}_k)$ for all $\boldsymbol{j}_{k+1} \ne \boldsymbol{j}_{s,k+1}$, $p(\boldsymbol{j}_{k+1} | \bar{\boldsymbol{y}}_{k+1})$ converges to the correct cell $\boldsymbol{j}_{s,k+1}$ irrespective of the initial distribution used, and,
3. if
   - $\boldsymbol{v}_k = 0$ for all $k = 0,1,2,\cdots$,
   - the probability $p(\boldsymbol{x}_k | \bar{\boldsymbol{y}}_k)$ is uniform over each cell $\boldsymbol{j}_k$,
   - $\boldsymbol{h}(\boldsymbol{x}_k) = \boldsymbol{x}_k$,
   - the integrals in Eq.(6) are approximated by a quadrature scheme,

   Eqs.(5) and (6) reduce to the current DSD algorithm [2].

The $p(\boldsymbol{j}_k | \bar{\boldsymbol{y}}_k)$ from Eq.(5) can be used to find all the statistical properties of the variables to be estimated at times $t = k\tau$, including expected values, standard deviations and credibility intervals. Item 3 above indicates the limitations of the current DSD algorithm with respect to Eqs.(5) and (6). Item 1 implies that [3]

1. For constant $\boldsymbol{x}_k = \boldsymbol{\theta}$ $(k = 0,1,\cdots)$, the mode of $p(\boldsymbol{\theta} | \bar{\boldsymbol{y}}_k)$ yields the maximum likelihood estimate (MLE) of $\boldsymbol{\theta}$.

2. If in Eq.(1) and $\boldsymbol{w}_k$ in Eq.(2) are both white Gaussian noise and Eq.(1) originates from a linear model for the evolution of $\boldsymbol{x}$, then the mean and covariance of $p(\boldsymbol{x}_k|\bar{\boldsymbol{y}}_k)$ obtained from Eq.(6) are equivalent to those obtained from a Kalman filter.
3. The mean of $p(\boldsymbol{\theta}|\bar{\boldsymbol{y}}_k)$ is also the least-squares estimate (LSE) of $\boldsymbol{\theta}$.

These implications are illustrated below using a linearized version of the model in [2] for the on-line calibration of the constant temperature power sensor (CTPS), proposed for direct core power density distribution measurement in Generation 4 reactors.

3 Implementation and Results

The CTPS [2] can directly measure the local nuclear energy deposition and heat transfer rate. This design concept is based on the idea of adding heat through resistive dissipation of input electrical energy to a small mass of actual reactor fuel pellet analogue which constitutes the sensor core (Node 2). The core is surrounded by ceramacast, which is an alumina based ceramic thermal insulator (Node 1). In Mode 1 operation, Node 2 is kept at constant temperature T_2 by providing the exact amount of input electrical energy q_e (in kW) through a feedback control loop irrespective of the nuclear energy q_n (in kW) generated in Node 2. At steady state [2]

$$q_e + q_n = \frac{T_2 - T_1}{R_1} = \frac{T_1 - T_0}{R_2} = \frac{T_2 - T_0}{R_1 + R_2} \tag{7}$$

where T_i is the Node i (i=1,2) temperature (K), T_0 is the temperature of the surrounding coolant, R_1 (in K/kW) is the contact resistance between Node 1 and Node 2 and R_2 (in K/kW) is the contact resistance between Node 1 and the coolant. In Eq.(7), q_n, R_2 and T_0 are not known. In the current design, only T_2 is measured. The calibration of the senor is accomplished through the determination of R_2 and T_0. Then q_n can be found from Eq.(7) with the measured q_e, T_2 and known R_1. For calibration, the sensor is temporarily taken out of the control loop (Mode 2 operation), or practically, the supplied electrical current is reduced to 1% of the steady state value in Mode 1 operation. Then R_2 and T_0 can be obtained from the dynamic characteristics of the sensor temperature in decaying back from the steady state value in Mode 1 to its original level through [2]

$$T_{2k} \equiv T_2(t_k) = T_0 + \theta_1 e^{-\theta_2 t_k} + \theta_3 e^{-\theta_4 t_k} \tag{8}$$

In Eq.(8), $T_2(t_k)$ is Node 2 temperature at time t_k The parameters θ_1 through θ_4 are known functions of q_n, q_e, sensor properties and Mode 1 node temperatures. Once θ_1 or θ_4 are estimated, then R_2 can be found from [2]

$$\theta_2 = \frac{1}{2}\left[\gamma + \sqrt{\gamma^2 - 4}\right] \qquad \theta_4 = \frac{1}{2}\left[\gamma - \sqrt{\gamma^2 - 4}\right] \tag{9}$$

with

$$\gamma = \frac{1}{C_1 R_1} + \frac{1}{C_2 R_2} + \frac{1}{C_2 R_1}. \tag{10}$$

For this study, the data T_k with k=1,…,250 were generated using a finite element CTPS model [4]. The noise $\boldsymbol{w_k}$ in Eq.(2) was assumed to be Gaussian noise with mean 0 and the variance was calculated by the sample variance of T_k which was found to be 0.1.

Table 1 below summarizes the results of the comparison of DSD with LSE, MLE and Kalman filters.

Parameter/Estimator	$\hat{\theta}_1$	$\hat{\theta}_2$	$\hat{\theta}_3$	$\hat{\theta}_4$
LSE	5.4854	0.2833	19.6994	2.7906
MLE	5.4825	0.2831	19.7017	2.7897
Kalman Filter	6.9525	0.3464	18.4278	3.2104
DSD (Mode)[1]	5.4326	0.2798	19.6685	2.7865
DSD (Mean)[2]	5.4663	0.2865	19.7247	2.7978

[1]For comparison to LSE and MLE [2]For comparison to Kalman Filter

Table 1. Comparison of the Results for Different Estimators

Table 1 shows that there is good agreement between DSD, LSE and MLE results, as expected. In general, the differences between the DSD, LSE and MLE are small (within 0.1% to 1.2%). The larger differences between the Kalman filter and other estimator results originate from the white Gaussian noise requirement of the Kalman filter. The data generated for the estimation process using the finite difference model of [4] do not necessarily conform to the functional form of Eq.(7). Subsequently, the differences between data behaviour and the functional form of Eq.(7) exhibit themselves as correlated noise.

4 Conclusion

The new theoretical developments show that DSD is equivalent to LSE, MLE and Kalman filter approach for stat/parameter estimation under certain conditions.

The advantage of DSD is that it is both a point and interval estimator whereas the other estimators are only point estimators. In addition, the DSD yields the probability distributions of the estimated quantities over their respective intervals which are useful information for risk informed regulation and risk monitoring of nuclear power plants.

References

1. Wang P, Chen X-M, Aldemir T. DSD: a generic software package for model-based fault diagnosis in dynamic systems. Reliab Engn & System Safety 2002; 28, 31-39
2. Burghalea A, Aldemir T. An application of DSD with recursive partitioning scheme to constant temperature power sensors. These proceedings
3. Wang P. Some improvements in state/parameter estimation using the cell to-cell mapping technique. Ph.D. thesis, The Ohio State University, 2002
4. Radcliff TD, Miller DW, Kauffman AC. Modeling of A Constant-Temperature Power Sensor. In: ICONE-8, Proceedings of 8th International Conference on Nuclear Engineering. American Society of Mechanical Engineers, New York, 2000

Probabilistic Safety Assessment and Management: PSAM 7-ESREL'04,
C. Spitzer, U. Schmocker, V. N. Dang (Eds.), 1809-1814, Springer – Verlag, London, U.K. (June 2004)

The DSD and Conventional State/Parameter Estimation

Peng Wang and Tunc Aldemir
The Ohio State University, 206 West 18th Avenue,
Columbus, OH 43210, U.S.A.

Abstract

The DSD (Dynamic System Doctor) is system independent, state/parameter estimation software that can be used for both point and interval estimation. The DSD also yields useful information for risk informed regulation and risk monitoring of nuclear power plants. The relationship of DSD to some conventional estimation techniques is described and illustrated using a linearized model for the on-line calibration of the constant temperature power sensor, recently proposed for direct core power density distribution measurement in Generation IV reactors.

1 Introduction

The DSD (Dynamic System Doctor) is system independent, state/parameter estimation software [1]. The DSD uses a system representation scheme based on the transition probabilities between user specified computational cells that partition the system state space (cell-to-cell mapping). These transition probabilities are obtained from the user supplied system model. The theoretical basis of the DSD and the current DSD algorithm are described in a companion paper [2]. The main advantage of the DSD over conventional estimators is that DSD is both a point and an interval estimator. In addition, the DSD yields the probability distribution of the system variables/parameters within the estimated bounds which provides a probabilistic measure to rank the likelihood of system faults in view of modeling uncertainties and/or signal noise. Such information is particularly useful for risk informed regulation and risk monitoring of nuclear power plants.

The current DSD algorithm is based on the assumptions that: a) the measurement noise is uniformly distributed, and, b) the measured variables are part of the state variable vector. Recent theoretical developments [3] have extended the applicability range of DSD to arbitrarily distributed (but known) signal noise and modeling uncertainties and arbitrary observers. The new theoretical developments have also provided the framework which clarifies the previously unexplained relationship between DSD and conventional state/parameter estimation techniques. The paper describes and illustrates the relationship of DSD to the generalized maximum likelihood estimator (MLE),

least squares estimator (LSE) and the Kalman filter approach.

2 Overview of the Recent Developments

The extended DSD algorithm accepts system equations of the form

$$\boldsymbol{x}_{k+1} = \tilde{\boldsymbol{x}}(\boldsymbol{x}_k) + \boldsymbol{v}_k \quad (k = 0,1,2,\cdots) \tag{1}$$

and observers of the form

$$\boldsymbol{y}_k = \boldsymbol{h}(\boldsymbol{x}_k) + \boldsymbol{w}_k \quad (k = 0,1,2,\cdots) \tag{2}$$

where

$\boldsymbol{x}$ L-dimensional vector whose elements are the state variables or unknown model parameters x_l $(l = 1,...,L)$ of the dynamic system

$\boldsymbol{v}_k$ system noise at time step $k\tau$ $(k = 0,1,2,...)$ (e.g. due to stochastic variation of system parameters) or a measure of modelling uncertainties, in general

$\boldsymbol{x}_k$ state vector at time step $k\tau$ $(k = 0,1,2,...)$

$\boldsymbol{y}_k$ M-dimensional vector whose elements y_k are the measured data at time step $k\tau$ $(k = 0,1,2,...)$

$\boldsymbol{w}_k$ measurement uncertainty

$\tilde{\boldsymbol{x}}$ a L- dimensional rule that maps $\boldsymbol{x}_k$ onto $\boldsymbol{x}_{k+1}$ (such as by the integration of a set of L ordinary differential equations)

$\boldsymbol{h}$ M - dimensional vector whose elements are known nonlinear functions

The estimation process takes place in the discretized state/parameter space partitioned through the user-defined intervals

$$\Delta_{l,j_l} = \{x_l : a_{l,j_l} \le x < a_{l,j_l+1}; a_{l,1} = a_l, a_{l,J_l} = b_l\} \tag{3}$$
$$j_l = 1,...,J_l; l = 1,...,L.$$

The specification of these intervals may be, for example, based on the uncertainty/noise in the monitored x_l. The Δ_{l,j_l} constitute the computational cells $\boldsymbol{V}_j = \{\Delta_{1,j_1}, \Delta_{2,j_2}, ...\Delta_{L,j_L}\}$ $(j = 1,...,J = \prod_{l=1}^{L} J_l)$ which partition the

range of interest $a_l \le x_l \le b_l (l = 1,...,L)$ in the state/parameter space in a similar manner to those used by finite difference and finite element methods. If $\boldsymbol{j} = \{j_1 j_2 ... j_L\}$ denotes the location of the cell $\boldsymbol{V}_j$ in the discretized state-space, then it can be shown that [3] the probability

$$p(\boldsymbol{j}_k | \bar{\boldsymbol{y}}_k) = \int_{\boldsymbol{j}_k} p(\boldsymbol{x}_k | \bar{\boldsymbol{y}}_k) d\boldsymbol{x}_k \tag{4}$$

of finding the system in the cell $\boldsymbol{j}_k$ at time $t = k\tau$ is recursively calculated from

$$p(\boldsymbol{j}_{k+1} | \bar{\boldsymbol{y}}_{k+1}) = \frac{\sum_{\boldsymbol{j}_k} g(\boldsymbol{j}_{k+1} | \boldsymbol{j}_k) p(\boldsymbol{j}_k | \bar{\boldsymbol{y}}_k)}{\sum_{\boldsymbol{j}_{k+1}} \sum_{\boldsymbol{j}_k} g(\boldsymbol{j}_{k+1} | \boldsymbol{j}_k) p(\boldsymbol{j}_k | \bar{\boldsymbol{y}}_k)} \tag{5}$$

$$g(\boldsymbol{j}_{k+1} | \boldsymbol{j}_k) = \iint_{\boldsymbol{j}_{k+1}, \boldsymbol{j}_k} p(\boldsymbol{y}_{k+1} | \boldsymbol{x}_{k+1}) p(\boldsymbol{x}_{k+1} | \boldsymbol{x}_k) \frac{p(\boldsymbol{x}_k | \bar{\boldsymbol{y}}_k)}{\int_{\boldsymbol{j}_k} p(\boldsymbol{x}_k | \bar{\boldsymbol{y}}_k) d\boldsymbol{x}_k} d\boldsymbol{x}_k d\boldsymbol{x}_{k+1} \tag{6}$$

where $g(\boldsymbol{j}_{k+1} | \boldsymbol{j}_k)$ is the probability that the system will move from cell $\boldsymbol{j}_k$ to cell $\boldsymbol{j}_{k+1}$ during $k\tau \le t < (k+1)\tau$. It can be also shown that [3]:

1. Eqs.(5) and (6) constitute a recursive Bayesian estimator (the original DSD algorithm is based on the Chapman-Kolmogorov equation),
2. if $\boldsymbol{j}_{s,k}$ denotes the actual cell the system is in at time $t = k\tau$ and $g(\boldsymbol{j}_{k+1} | \boldsymbol{j}_k) < g(\boldsymbol{j}_{s,k+1} | \boldsymbol{j}_k)$ for all $\boldsymbol{j}_{k+1} \ne \boldsymbol{j}_{s,k+1}$, $p(\boldsymbol{j}_{k+1} | \bar{\boldsymbol{y}}_{k+1})$ converges to the correct cell $\boldsymbol{j}_{s,k+1}$ irrespective of the initial distribution used, and,
3. if
   - $\boldsymbol{v}_k = 0$ for all $k = 0,1,2,\cdots$,
   - the probability $p(\boldsymbol{x}_k | \bar{\boldsymbol{y}}_k)$ is uniform over each cell $\boldsymbol{j}_k$,
   - $\boldsymbol{h}(\boldsymbol{x}_k) = \boldsymbol{x}_k$,
   - the integrals in Eq.(6) are approximated by a quadrature scheme,

   Eqs.(5) and (6) reduce to the current DSD algorithm [2].

The $p(\boldsymbol{j}_k | \bar{\boldsymbol{y}}_k)$ from Eq.(5) can be used to find all the statistical properties of the variables to be estimated at times $t = k\tau$, including expected values, standard deviations and credibility intervals. Item 3 above indicates the limitations of the current DSD algorithm with respect to Eqs.(5) and (6). Item 1 implies that [3]

1. For constant $\boldsymbol{x}_k = \boldsymbol{\theta}$ $(k = 0,1,\cdots)$, the mode of $p(\boldsymbol{\theta} | \bar{\boldsymbol{y}}_k)$ yields the maximum likelihood estimate (MLE) of $\boldsymbol{\theta}$.

2. If in Eq.(1) and $\boldsymbol{w}_k$ in Eq.(2) are both white Gaussian noise and Eq.(1) originates from a linear model for the evolution of $\boldsymbol{x}$, then the mean and covariance of $p(\boldsymbol{x}_k|\bar{\boldsymbol{y}}_k)$ obtained from Eq.(6) are equivalent to those obtained from a Kalman filter.
3. The mean of $p(\boldsymbol{\theta}|\bar{\boldsymbol{y}}_k)$ is also the least-squares estimate (LSE) of $\boldsymbol{\theta}$.

These implications are illustrated below using a linearized version of the model in [2] for the on-line calibration of the constant temperature power sensor (CTPS), proposed for direct core power density distribution measurement in Generation 4 reactors.

3 Implementation and Results

The CTPS [2] can directly measure the local nuclear energy deposition and heat transfer rate. This design concept is based on the idea of adding heat through resistive dissipation of input electrical energy to a small mass of actual reactor fuel pellet analogue which constitutes the sensor core (Node 2). The core is surrounded by ceramacast, which is an alumina based ceramic thermal insulator (Node 1). In Mode 1 operation, Node 2 is kept at constant temperature T_2 by providing the exact amount of input electrical energy q_e (in kW) through a feedback control loop irrespective of the nuclear energy q_n (in kW) generated in Node 2. At steady state [2]

$$q_e + q_n = \frac{T_2 - T_1}{R_1} = \frac{T_1 - T_0}{R_2} = \frac{T_2 - T_0}{R_1 + R_2} \tag{7}$$

where T_i is the Node i (i=1,2) temperature (K), T_0 is the temperature of the surrounding coolant, R_1 (in K/kW) is the contact resistance between Node 1 and Node 2 and R_2 (in K/kW) is the contact resistance between Node 1 and the coolant. In Eq.(7), q_n, R_2 and T_0 are not known. In the current design, only T_2 is measured. The calibration of the senor is accomplished through the determination of R_2 and T_0. Then q_n can be found from Eq.(7) with the measured q_e, T_2 and known R_1. For calibration, the sensor is temporarily taken out of the control loop (Mode 2 operation), or practically, the supplied electrical current is reduced to 1% of the steady state value in Mode 1 operation. Then R_2 and T_0 can be obtained from the dynamic characteristics of the sensor temperature in decaying back from the steady state value in Mode 1 to its original level through [2]

$$T_{2k} \equiv T_2(t_k) = T_0 + \theta_1 e^{-\theta_2 t_k} + \theta_3 e^{-\theta_4 t_k} \tag{8}$$

In Eq.(8), $T_2(t_k)$ is Node 2 temperature at time t_k The parameters θ_1 through θ_4 are known functions of q_n, q_e, sensor properties and Mode 1 node temperatures. Once θ_1 or θ_4 are estimated, then R_2 can be found from [2]

$$\theta_2 = \frac{1}{2}\left[\gamma + \sqrt{\gamma^2 - 4}\right] \qquad \theta_4 = \frac{1}{2}\left[\gamma - \sqrt{\gamma^2 - 4}\right] \tag{9}$$

with

$$\gamma = \frac{1}{C_1 R_1} + \frac{1}{C_2 R_2} + \frac{1}{C_2 R_1}. \tag{10}$$

For this study, the data T_k with k=1,…,250 were generated using a finite element CTPS model [4]. The noise $\boldsymbol{w_k}$ in Eq.(2) was assumed to be Gaussian noise with mean 0 and the variance was calculated by the sample variance of T_k which was found to be 0.1.

Table 1 below summarizes the results of the comparison of DSD with LSE, MLE and Kalman filters.

Parameter/Estimator	$\hat{\theta}_1$	$\hat{\theta}_2$	$\hat{\theta}_3$	$\hat{\theta}_4$
LSE	5.4854	0.2833	19.6994	2.7906
MLE	5.4825	0.2831	19.7017	2.7897
Kalman Filter	6.9525	0.3464	18.4278	3.2104
DSD (Mode)[1]	5.4326	0.2798	19.6685	2.7865
DSD (Mean)[2]	5.4663	0.2865	19.7247	2.7978

[1]For comparison to LSE and MLE [2]For comparison to Kalman Filter

Table 1. Comparison of the Results for Different Estimators

Table 1 shows that there is good agreement between DSD, LSE and MLE results, as expected. In general, the differences between the DSD, LSE and MLE are small (within 0.1% to 1.2%). The larger differences between the Kalman filter and other estimator results originate from the white Gaussian noise requirement of the Kalman filter. The data generated for the estimation process using the finite difference model of [4] do not necessarily conform to the functional form of Eq.(7). Subsequently, the differences between data behaviour and the functional form of Eq.(7) exhibit themselves as correlated noise.

4 Conclusion

The new theoretical developments show that DSD is equivalent to LSE, MLE and Kalman filter approach for stat/parameter estimation under certain conditions.

The advantage of DSD is that it is both a point and interval estimator whereas the other estimators are only point estimators. In addition, the DSD yields the probability distributions of the estimated quantities over their respective intervals which are useful information for risk informed regulation and risk monitoring of nuclear power plants.

References

1. Wang P, Chen X-M, Aldemir T. DSD: a generic software package for model-based fault diagnosis in dynamic systems. Reliab Engn & System Safety 2002; 28, 31-39
2. Burghalea A, Aldemir T. An application of DSD with recursive partitioning scheme to constant temperature power sensors. These proceedings
3. Wang P. Some improvements in state/parameter estimation using the cell to-cell mapping technique. Ph.D. thesis, The Ohio State University, 2002
4. Radcliff TD, Miller DW, Kauffman AC. Modeling of A Constant-Temperature Power Sensor. In: ICONE-8, Proceedings of 8th International Conference on Nuclear Engineering. American Society of Mechanical Engineers, New York, 2000

Trans. Am. Nucl. Soc., 92, 555-557 (June 2005)

Representation of Measurement Uncertainty in Flux/Power Shape Construction From Monitored Data

Aram Hakobyan, Mihaela Biro, Tunc Aldemir

The Ohio State University, Nuclear Engineering Program,
Bldg 1, Rm 130B, Suite 255, 650 Ackerman Road, Columbus, OH 43202

INTRODUCTION

Different techniques have been developed and used to predict the flux/power density between measurement points, namely, using cubic splines to interpolate between measured data [1], fittings by modal expansions [2, 3], artificial neural networks [4], and, finally, least-square fittings [5]. Also, there have been few attempts to directly incorporate the measurement uncertainty into the flux/power shape reconstruction process [6-9].

Recent work [8,9] has described such a one-dimensional (1-D) reconstruction procedure which leads to computational simplicity when there are a large number of observations. This procedure can be also used with a wide range of fitting schemes, from simple linear interpolation between data points to model based fittings, as well as a variety of probability distribution functions (pdfs) to represent the measurement uncertainty.

The objective of this paper is to demonstrate that the 1-D procedures of [8] and [9] can be used for three dimensional (3-D) power/flux shape construction by decomposing the reconstruction process into three 1-D problems locally.

PROCEDURE

Consider a cube whose vertices are detector locations and which also contains another detector at its center. We will assume that thermal neutron flux/power density satisfies the Helmholtz equation within the cube, i.e.

$$\nabla^2\varphi(\boldsymbol{r})+B^2\varphi(\boldsymbol{r})=0 \tag{1}$$

where the vector $\boldsymbol{r}$ denotes the spatial location within the cube and

$$B^2=\frac{\left[\nu\frac{\Sigma_{f,1}}{\Sigma_{a,1}}-1\right]\Sigma_{a,1}+\left[\nu\frac{\Sigma_{f,2}}{\Sigma_{a,2}}-1\right]\Sigma_{1\to 2}}{D_1} \tag{2}$$

for 1 ½ group diffusion theory representation of the flux/power distribution under uniform material composition within the cube (e.g. through a homogenization process). The symbols in Eq.(2) have their conventional definitions. The solution of Eq.(1) using separation of variables yields

$$\begin{aligned}&\left[A_1\cos(B_x x_i)+C_1\sin(B_x x_i)\right]\times\\&\left[A_2\cos(B_y y_i)+C_2\sin(B_y y_i)\right]\times\\&\left[A_3\cos(B_z z_i)+C_3\sin(B_z z_i)\right]=\phi_i\end{aligned} \tag{3}$$

where ϕ_i is the measured flux/power density at detector location i = 1,…,9 and x_i, y_i, z_i are the coordinates of the measurement point i. The other quantities in Eq.(3) are arbitrary constants. These constants are determined from the system of 9 non-linear equations given by Eq(3) using non-linear least squares estimation and the mean values of the measured pdfs for ϕ_i (e.g. by taking repeated measurements for steady-state operation or for slow transients or using the procedure described in [10]). Once these constants are determined, then two methods can be used to move to the probabilistic domain and interpolate between the measured pdfs. Method 1 [8] assumes that the expected value $\varphi(s)$ of the flux/power at a point $0\le s\le d$ between two detector locations i and j satisfies again the Helmholtz equation

$$\nabla^2\varphi(s)+B^2\varphi(s)=0 \tag{4}$$

with ϕ_i and ϕ_j as boundary conditions and: a) $B = B_x$, B_y ,B_z if the detectors are placed on the x-, y-and z-edges of the cube, respectively, b) $B^2=B_x^2+B_y^2$, $B^2=B_x^2+B_z^2$ and $B^2=B_y^2+B_z^2$ if the detectors are placed on the diagonals of the x-y, x-z and y-z surfaces of the cube, respectively, and, c) $B^2=B_x^2+B_y^2+B_x^2$ if the detectors are placed on the diametrically opposite vertices of the cube. For Eq.(4) with ϕ_i and ϕ_j as boundary conditions it can be shown that [8]

$$p(\phi\,|\,w)=\frac{1}{\sin(B)}\begin{bmatrix}p(\phi_i\,|\,0)\sin[B(1-w)]\\+p(\phi_j\,|\,1)\sin(Bw)\end{bmatrix} \tag{5}$$

with $w = s/d$ ($w=0$ at location i), where $p(\phi\,|\,w)$ is the pdf of ϕ at w. Method 2 [9] imposes the additional condition

$$F=\int_0^{\phi_i}d\phi' p(\phi'\,|\,0)=\int_0^{\phi_j}d\phi' p(\phi'\,|\,1)=\int_0^{\phi}d\phi' p(\phi'\,|\,w) \tag{6}$$

for all w, where ϕ_i, ϕ_j and ϕ denote the corresponding quantities in Eq.(5) for specified $0 \le F \le 1$.

IMPLEMENTATION

The hypothetical assembly considered for illustration was a 300X300X300 cm homogeneous cube, placed in vacuum and with diffusion parameters as given in [8]. The overall flux distribution in the cube was determined analytically from Eqs.(1) and (2). Then the ϕ_i in Eq.(3) were determined from this flux distribution for a 30X30X30 cm virtual test cube randomly placed in the assembly.

The comparison of the overall flux/power distribution (S1) with the flux/power distribution obtained from the solution of Eq.(3) (S2) was carried out for a fixed plane 10cm above the mid *x-y* plane. Figure 1 below shows that the maximum relative error (S1-S2)/S1 did not exceed 0.8%.

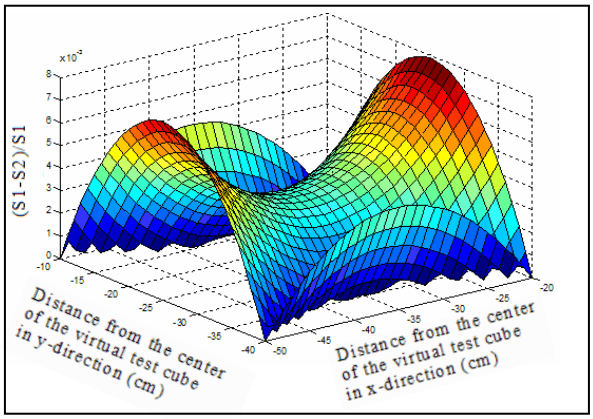

Fig.1: Relative error (S1-S2)/S1 10cm above the mid *x-y* plane of the virtual test cube

Figure 2(a) shows comparison of the solutions obtained from Eqs.(3) and (4) for the *x-y* diagonal on the same plane and indicates good agreement (less than 2.5%) difference between the 3-D and 1-D solutions.

For the $p(\phi \mid w)$, it was assumed that the $p_i(\phi)$ and $p_j(\phi)$ in Eq.(5) are Gaussian with means equal to ϕ_i and ϕ_j, respectively, and 1% standard deviation. Figures 2(b) and 2(c), respectively, show the $p(\phi \mid w)$ obtained from Method 1 and Method 2. The bimodal nature of the pdf obtained from Method 1 in Fig.2(b) and the low probability region between detector locations reflects the large uncertainty in the flux value due to lack of observation in this region. Note that expected value in Fig.2 (b) is still very similar to the local 3D solution shown in Fig.2 (a).

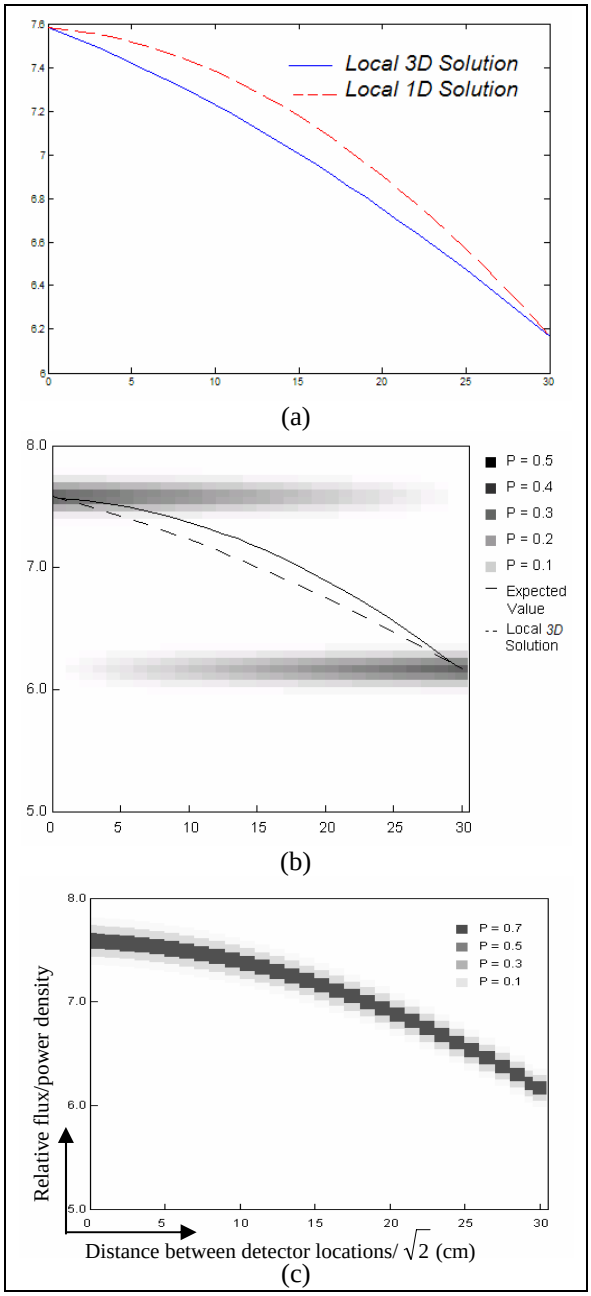

Fig.2: Flux comparison for the *x-y* diagonal direction (a) and corresponding $p(\phi \mid w)$ obtained from Method 1 (b) and Method 2 (c)

The difference between Fig.2(b) and 2(c) results is due to the condition imposed by Eq.(6) which assumes that the cumulative probability distribution of flux/power density is conserved between detector locations. Another interpretation

of this assumption is that the uncertainty in flux/power at the detector locations also propagates according to Eq.(4) between detector locations. The assumption is justified if the uncertainty originates from possible flux/power fluctuations but not if it originates from electronic noise in the detection hardware.

CONCLUSION

This study shows that uncertainty on the flux/power density between detector locations in a 3-D problem can be quantified by:

- locally decomposing in flux/power density construction into three 1-D problems, and,
- using Method 1 or Method 2.

It is not clear at this point in time whether Method 1 or 2 should be the method of choice. Work is underway to study Methods 1 and 2 with simulated data obtained from actual production codes.

REFERENCES

1. S. HAN, U. S. KIM, P. H. SEONG "A Methodology for Benefit Assessment of Using In-core Neutron Detector Signals in Core Protection Calculator System (CPCS) for Korea Standard Nuclear Power Plants (KSNPP)", *Annals of Nuclear Energy*, **26**, 471-488 (1999).
2. M. E. Pomerantz, C.R. Calabrese, C. Grant, "Nuclear Reactor Power and Flux Distribution Fitting from a Diffusion Theory Model and Experimental Data", *Annals of Nuclear Energy*, **29,** 1073–1083 (2002).
3. L. Fu, L. Zhengpei, H. Yongming "Harmonics Synthesis Method for Core Flux Distribution Reconstruction", *Progress in Nuclear Energy*, **31**, 369-372 (1997).
4. G.-C. Lee, W-P. Baek, S. H. Chang. "Improved Methodology for Generation of Axial Flux Shapes in Digital Core Protection Systems", *Annals of Nuclear Energy*, **29**, 805–819 (2002).
5. K. Lee, C. H. Kim, "The Least-Squares Method for Three-Dimensional Core Power Distribution Monitoring in Pressurized Water Reactors"**,** *Nucl.Sci.Eng*, **143,** 268 (2003).
6. J. W. Bryson, J. C. Lee, and J. A. Hassberger, "Optimal Flux Map Generation Through Parameter Estimation Techniques", *Nucl.Sci.Eng*, **114**, 238 (1993).
7. R.A. Bonalumi, N.P.Kherani "Rational Mapping (RAM) of In-Core Data", *Nucl.Sci.Eng*, **90**, 47 (1985).
8. M. Biro, T. Aldemir, "A Model Based Probabilistic Scheme for Flux/Power Shape Construction from Monitored Data**",** *Trans. Am. Nucl. Soc*., **90,** 59-61 (June 2004)
9. M. Biro, T. Aldemir, "Quantifying The Measurement Uncertainty Propagation In Flux/Power Reconstruction", *Proceedings of NPIC&HMIT 2004*, 1246-1253, American Nuclear Society, LaGrange Park, IL (September 2004)
10. A. Burghelea, T. Aldemir, "An Application of DSD with Recursive Partitioning Scheme to Constant Temperature Power Sensors", *Probabilistic Safety Assessment and Management: PSAM 7-ESREL'04*, C. Spitzer, U. Schmocker, V. N. Dang (Eds.), 1821-1827, Springer – Verlag, London, U.K. (June 2004)

Space Technology and Applications International Forum—STAIF 2004,
M. S. El-Genk (Ed.), 582-589, American Institute of Physics, Melville, N.Y. (February 2004)

Direct Estimation of Power Distribution in Reactors for Nuclear Thermal Space Propulsion

Tunc Aldemir, Don W. Miller, and Andrei Burghelea

The Ohio State University, Nuclear Engineering Program, 206 West 18th Avenue, Columbus, Ohio 43210
(614)292-4627; aldemir.1@osu.edu

Abstract. A recently proposed constant temperature power sensor (CTPS) has the capability to directly measure the local power deposition rate in nuclear reactor cores proposed for space thermal propulsion. Such a capability reduces the uncertainties in the estimated power peaking factors and hence increases the reliability of the nuclear engine. The CTPS operation is sensitive to the changes in the local thermal conditions. A procedure is described for the automatic on-line calibration of the sensor through estimation of changes in thermal .conditions.

INTRODUCTION

Substantial effort has been spent since the 1950s on the design and testing of highly enriched uranium fuelled, graphite moderated reactor cores for nuclear thermal space propulsion. Due to their compact size and high operating temperatures, very strong coupling exists between the nuclear and thermal hydraulic behavior of such cores (Aithal, Aldemir, and Vafai, 1994). Accurate modeling of this coupling in both ground testing of the cores and in-flight operation is usually difficult because of the uncertainties in local material compositions, coolant flow paths, reactor operation history and possibly nuclear data. On the other hand, accurate prediction of core power distribution is important to determine the local power peaking factors and hence the operating limits of the nuclear engine. A recently proposed constant temperature power sensor (CTPS) (Radcliff, Miller, and Kauffman, 2000a) has the capability to measure local core power directly. While the measurement process is sensitive to local temperature and flow variations, such variations can be accounted for using the estimation procedure DSD (Dynamic System Doctor) (Wang, Chen, and Aldemir, 2002). This paper describes how the CTPS-DSD combination can be applied to space reactors for accurate prediction of core power distribution. Three important features of the CTPS-DSD combination for space reactors are the following:

- The sensor core can blend with the fuel matrix of a number of reactor concepts proposed for nuclear thermal propulsion, such as the particle bed concept (Powell et al., 1991) or cermet fuel (Kruger, 1991), reducing material compatibility problems at high temperatures and high temperature gradients.
- The measurement procedure is self-calibrating. This feature is particularly important for space reactors where sensor calibration though external means may not be feasible.
- The measurement process yields point estimates for the power densities as well as credibility intervals for these point estimates so that the uncertainty in the estimated quantities is an automatic output of the estimation process. Such data provide useful inputs for pre-launch determination mission reliability and for decision making during the mission.

THE SENSOR

As designed for testing purposes, the sensor consists of a fuel pellet surrounded by electrical heating resistance wire (see Fig.1). (Radcliff, Miller, and Kauffman, 2000a) The pellet and the wire form the sensor core (Node 2). The core is surrounded by ceramacast which is an alumina based ceramic thermal insulator (Node 1). Both the sensor core and the insulator are coated with thin layers of copper. A feedback control loop is used to provide the exact

amount of input electrical energy q_e needed to keep Node 2 temperature T_2 constant in time t, well above the ambient temperature T_0, regardless of nuclear energy deposited (q_n). The CTPS is ideally suited for use in the proposed nuclear thermal space systems in which the sensors need to be an integral part of the core for the mission duration and where sensor calibration though external means may not be feasible.

The sensor operation involves switching between the feedback-controlled constant-temperature mode (Mode 1) and the dynamic temperature decay mode following the opening of the feedback loop (Mode 2) as described by (Burghelea and Aldemir, 2003; Liu, Miller, Li, and Radcliff, 2002; Radcliff, Miller, and Kauffman, 2000a)

$$\begin{aligned} C_1 \frac{dT_2}{dt} &= (q_n + q_e) - \frac{1}{R_1}(T_2 - T_1), \\ C_2 \frac{dT_1}{dt} &= \frac{1}{R_1}(T_2 - T_1) - \frac{1}{R_2}(T_1 - T_0), \\ \frac{1}{R_1} &= \frac{2\pi k(T_2)[h_s - 2(r_o - r_i)]}{\log\left(\frac{r_o}{r_i}\right)} + \frac{2\pi k(T_2)(r_o^2 - r_i^2)}{[h_s - 2(r_o - r_i)]}. \end{aligned} \tag{1}$$

Equation (1) has been validated against the results from a finite element code (Liu, Miller, Li, and Radcliff, 2002).

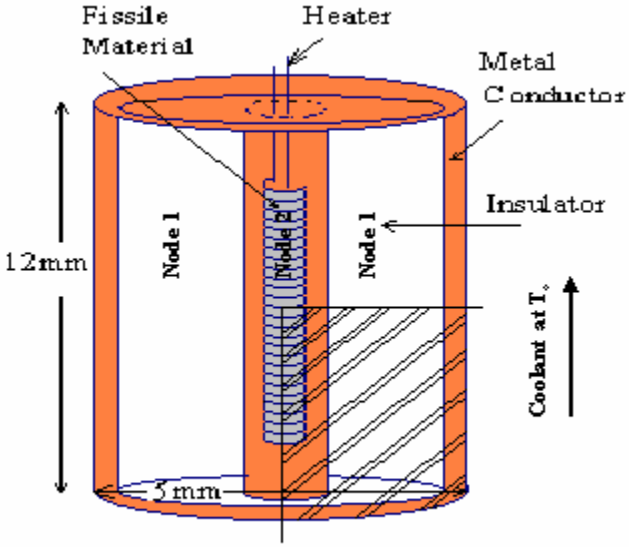

FIGURE 1. The Constant Temperature Power Sensor.

At steady-state Eq.(1) yields:

$$q_n + q_e = \frac{1}{R_2}(T_1 - T_0), \tag{2}$$

which corresponds to the constant temperature mode (i.e. Mode 1) operation of the CTPS. Under linearity assumptions Eq.(1) yields for Mode 2

$$T_2(t) = \theta_0 + \theta_1 e^{-\theta_2 t} + \theta_3 e^{-\theta_4 t}, \tag{3}$$

where θ_0 through θ_4 are known functions of T_0, $T_2(0)$ and the parameters of Eq.(1). In the implementation, C_1, C_2, R_1 in Eq.(1) are assumed to be known. The estimation of q_n consists of the following steps:

1. In Mode 1, measure q_e, $T_1(0)$ and $T_2(0)$
2. Switch to Mode 2 and measure $T_1(t)$, $T_2(t)$
3. Assume a value q_n' for nuclear energy deposition rate.
4. Estimate T_0 and R_2 from Eq.(1) or θ_0 through θ_4 from Eq.(3) using Step 1 through Step 3 results and the estimation software described in the next section. Once θ_0 through θ_4 are estimated, T_0 and R_2 can be determined from these estimates and given C_1, C_2 and R_1 (Radcliff, Miller, and Kauffman, 2000b).
5. Determine q_n from Eq.(2) using Step 4 results.
6. Compare q_n from Step 5 to its Step 3 value q_n'.
7. If $(q_n - q_n')/q_n < 0.01$ stop (convergence), otherwise go to Step 3 with $q_n' = q_n$.

Steps 1 though 4 account for changes in the local temperature and flow variations which affect T_0 and R_2 in Eq.(1) and hence are equivalent to the on-line calibration of the sensor

THE ESTIMATON SOFTWARE

The DSD is based on the representation of the system dynamics in terms of transition probabilities between user specified cells that partition the system parameter/state space during user specified time intervals $k\tau \le t \le (k+1)\tau$ (k = 0, 1, 2, ...), such as between data sampling times. These cells are obtained by partitioning the range of interest $a_l \le x_l \le b_l$ for the state variable $x_l (l = 1, \cdots, L)$ into $j_l = 1, \cdots, J_l - 1$ intervals $a_{l,j_1} \le x < a_{l,j_l+1}$ and the range of interest $\widetilde{a}_m \le \alpha_m \le \widetilde{b}_m$ for the parameter $\alpha_m (m = 1, \cdots, M)$ into $n_m = 1, \cdots, N_m - 1$ intervals $\widetilde{a}_{m,n_m} \le x < \widetilde{a}_{m,n_m+1}$, in a manner similar to those used in finite difference or finite difference methods. The partitionings are provided as user input to DSD. The DSD recursively computes the probability $p_k(j, n \mid J_k)$ that the state variables (e.g. $T_1(t)$, $T_2(t)$) are in cell j ($j = 1,...J=J_1J_2...J_L$) and the unknown parameters (e.g. R_2, T_0) are in cell n ($n = 1,...,N=N_1N_1...N_M$) during $k\tau \le t \le (k+1)\tau$, given that the possible set of cells the state variables can be in at this time is J_k (as observed from the monitored data), from

$$
\begin{aligned}
p_k^*(j,n) &\equiv p_k(j,n \mid J_k) \\
&= \frac{p_k(j,n)}{\sum_{j' \in J_k} \sum_{n'} p_k(j',n')} \quad (j \in J_k), \\
p_k(j,n) &= \sum_{j' \in J_{k-1}} g(j \mid j', n) p_{k-1}^*(j',n'),
\end{aligned}
\tag{4}
$$

where

$$g(j \mid j', n') =$$

$$\begin{cases} \int_{a_1, j_1}^{a_1, j_1+1} \frac{dx'_1}{a_{1,j'_1+1} - a_{1,j'_1}} e_{j_1}(\tilde{\boldsymbol{x}}(\boldsymbol{x}', \boldsymbol{\alpha}_{n'}, \tau)) \ldots \int_{a_L, j_L}^{a_L, j_{L1}+1} \frac{dx'_L}{a_{L,j'_L+1} - a_{L,j'_L}} e_{j_{L1}}(\tilde{\boldsymbol{x}}(\boldsymbol{x}', \boldsymbol{\alpha}_{n'}, \tau)), \\ \quad \text{if} \quad a_l \le x'_l \le b_l \\ \quad 0 \quad \text{otherwise} \end{cases} \tag{5}$$

with

$$e_{j_l} = \begin{cases} 1 & \text{if} \quad a_{1,j_1} \le x \le a_{1,j_1+1}, \\ 0 & \text{otherwise} \end{cases} \tag{6}$$

is the transition probability from state variable cell j' to state variable cell j during the period $k\tau \le t \le (k+1)\tau$ while the system parameters remain within cell n'. The quantity $\tilde{\boldsymbol{x}}(\boldsymbol{x}', \boldsymbol{\alpha}_{n'}, \tau)$ in Eq.(5) indicates the arrival point in the state-space at time $(k+1)\tau$ of the trajectory that has departed at time $k\tau$ from point $\boldsymbol{x}'$ in cell j' with the system parameters at $\boldsymbol{\alpha}_{n'}$ within cell n', as determined from a user provided system model (e.g. Eq.(1)). In applications, the $g(j \mid j', n)$ are usually approximated using a $\tilde{j}'$ -point quadrature scheme, i.e.

1) at time $k\tau$, selecting randomly or otherwise (e.g. equidistant) $\tilde{j}'$ starting points from cell j' for a given n,

2) from the user provided system model, find the number $\tilde{j}$ of trajectories that arrive within cell j at $t = (k+1)\tau$ (e.g. by integrating Eq.(1) over $k\tau \le t \le (k+1)\tau$ for each of the $\tilde{j}'$ initial conditions), and,

3) letting $g(j \mid j', n) = \tilde{j} / \tilde{j}'$.

A graphical illustration of this process, along with an example partitioning scheme, is shown in Fig.2 for a second order system where only one state variable is monitored. Some sufficient conditions for the convergence of Eq.(4) are given in (Wang and Aldemir, 1999) An important advantage of DSD is that it yields point estimates of the system variables to be determined as well as credibility intervals for these point estimates (i.e. state variable and parameter ranges inferred from j and n with $p_k(j, n) \ne 0$) so that the uncertainty in the estimated quantities is an automatic output of the estimation process.

IMPLEMENTATION

The example nuclear thermal propulsion reactor concept chosen to illustrate the utilization of the CTPS/DSD combination is the particle bed reactor (PBR) concept used in (Aithal, Aldemir, and Vafai, 1994). Figures 3 and 4, respectively, show a horizontal cross section of the reactor core and an axial cross section of a PBR fuel element. The PBR uses fuel in the form of small diameter particles (100-500 μm) which consist of a highly enriched uranium kernel surrounded by multiple layers of pyrographite and sometimes additional ZrC or SiC layers. The fuel particles are held between two porous annuli ("frits") to form a fuel element (Fig.4) and the fuel elements are embedded in the moderator block in concentric rings to form the core (Fig.3). The moderator block is surrounded by a pressure vessel, reflected radially and axially for neutron economy. Hydrogen pumped from the propellant tank flows through an annulus located between the radial reflector and the pressure vessel before entering the core. After

entering the core, the coolant first passes through the outer cold frit (Zircaloy 2), then directly over the fuel particles and finally through the inner hot frit (ZrC) into the outlet plenum to be ejected through a nozzle to develop thrust. Partial reactivity control is achieved by varying the hydrogen mass flow rate in the annulus.

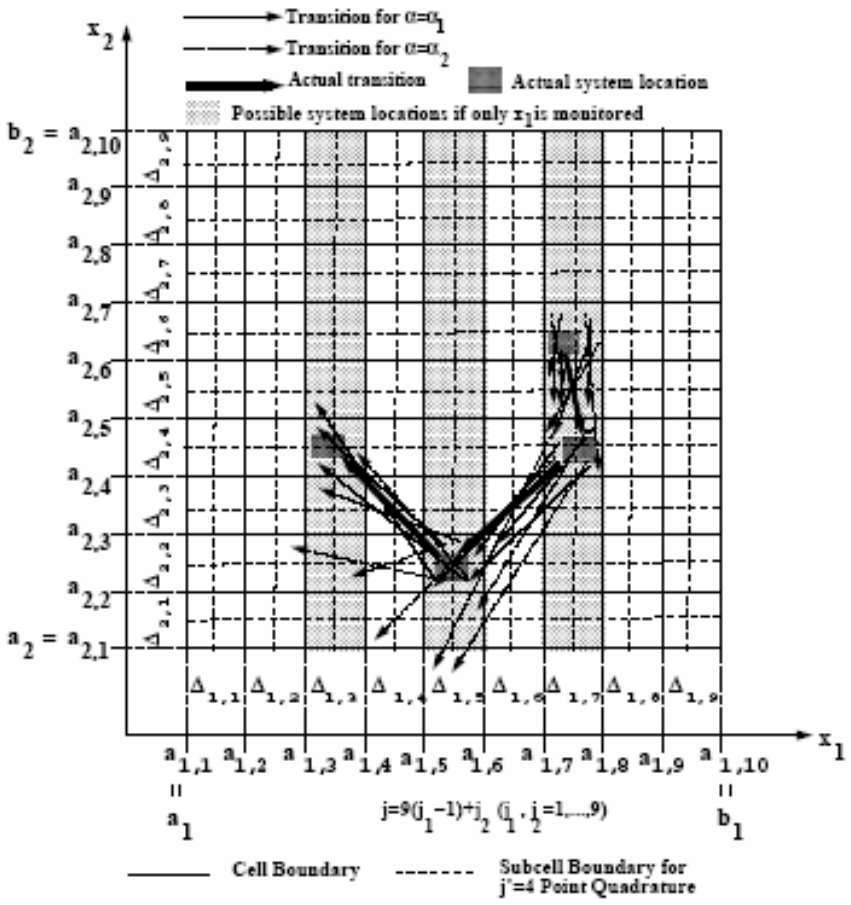

$$g(58 \mid 29,1) = 3/4 = 0.75,\ g(58 \mid 29,2) = 0,\ g(29 \mid 22,1) = 2/4 = 0.5,\ g(29 \mid 22,2) = 1/4 = 0.25$$

FIGURE 2. An example partitioning scheme and the illustration of the approximation of *g(j| j', n)* for a hypothetical dynamical system with two state variables x_1, x_2 and one parameter α. The system is in cells $j = 9(j_1 - 1) + j_2 = 60,58,29,22$ at times $k\tau, (k+1)\tau, (k+2)\tau, (k+3)\tau$ respectively. If only x_1 is monitored, the set of possible cells the system can be in are $J_k = J_{k+1} = \{j = 55, \ldots, 63\}$, $J_{k+2} = \{j = 37,\ldots,45\}$ and $J_{k+3} = \{j = 10, \ldots, 18\}$ (adapted from Dinca, 1997).

For the PBR application, the CTPS is assumed to be imbedded in the fuel element between the hot and cold frit with sensor core (i.e. Node 2 in Fig.1) consisting of the same type of particles used in the fuel elements. For the purposes of this illustration, the sensor heater wire and the Node 1 and 2 metal coatings were assumed to be tungsten. Table 1 shows the example power and temperature data used for the illustration. The data in Table 1 have been generated with the MCNP (Breimeister, 1989) and HEATING-5 (Turner, Elrod, and Siman-Tov, 1977) codes. Figure 5 shows the results of the estimation using DSD, assuming that the monitored variables are $T_1(t), T_2(t)$ and $q_e(t)$. The bars in Fig.5 indicate 100% credibility intervals. The data for the estimation process was simulated using Eq.(1) with 1% noise in the monitored variables. Figure 5 indicates that the credibility intervals contain the actual (i.e. simulated data) and also quantify the uncertainty in the estimation process.

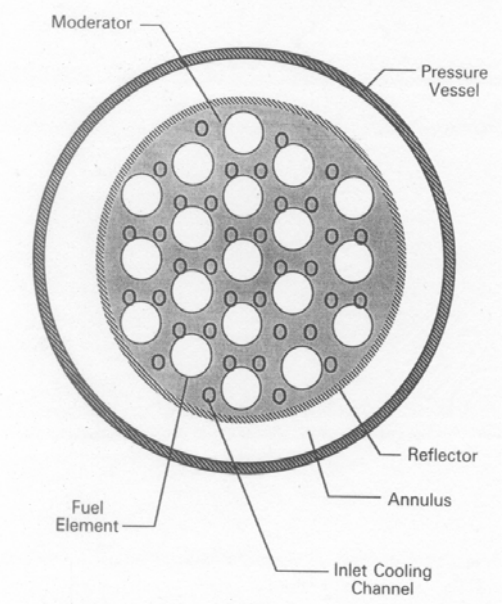

FIGURE 3. The Particle Bed Reactor Core (Aithal, Aldemir, and Vafai, 1994).

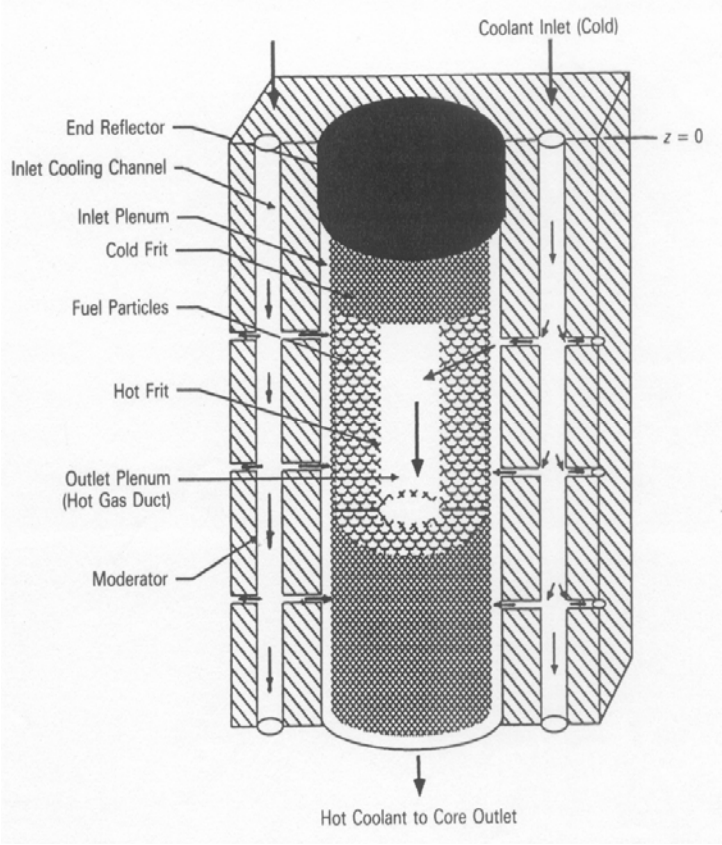

FIGURE 4. A Particle Bed Reactor Fuel Element (Aithal, Aldemir, and Vafai, 1994).

TABLE 1. Example Power and Temperature Data for the Particle Bed Reactor (Aithal, Aldemir, and Vafai, 1994).

Distance from Coolant Inlet (cm)	Power Density q_n (W/cm^3)	Solid Temperature $T_1(0)=T_2(0)$ (K)	Coolant Temperature (K)
5	960	480	455
10	1440	635	610
20	1888	1230	1208
30	2040	1580	1560
40	1888	2104	2085
50	1456	2521	2503
55	976	2968	2950

CONCLUSION

Obtaining accurate power profiles in both ground testing and in-flight operation or reactor cores for nuclear thermal propulsion is usually difficult because the strong neutronic-thermal hydraulic coupling of the cores and uncertainties in local material compositions, coolant flow paths, reactor operation history and possibly nuclear data. This study shows that using CTPS modeled through Eq.(1) and DSD may be a feasible option to obtain direct estimates of the power distribution as well as quantifying the uncertainty in the estimated power profiles. The advantages of the CTPS-DSD combination with respect to space reactors are: a) it reduces material compatibility problems at high

temperatures and high temperature gradients, b) the measurement procedure is self-calibrating, and, c) it provides useful inputs for pre-launch determination mission reliability and for decision making during the mission.

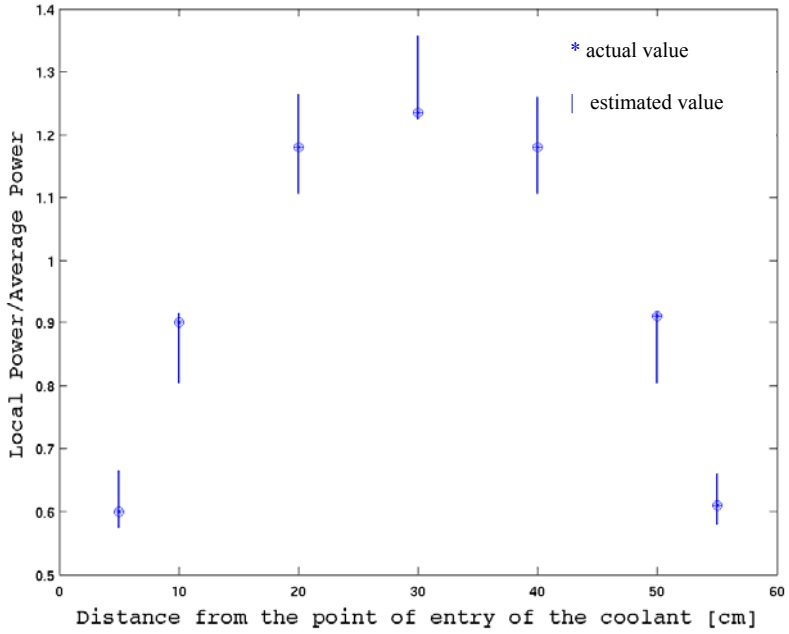

FIGURE 5. Estimated and Actual Values of the Local Power for the Data in Table 1.

NOMENCLATURE

C_i	=	thermal capacitance of Node i (i =1,2) (J/m^{3}K)
$g(j,n\|j',n')$	=	transition probability from cell pair (j',n') to cell pair (j,n) during $k\tau < t < (k+1)\tau$ (k=0,1,2,..)
h	=	sensor height (m)
k	=	thermal conductivity of the contact layer between Node 1 and 2 (W/m.K)
$p_k(j,n)$	=	probability that the system variables are in cell j ($j=1,...,J$) and the system parameters are in cell n ($n=1,...,N$) at time $t=k\tau$
q_n	=	nuclear energy deposition rate (W/m^3)
q_e	=	electrical energy deposition rate (W/m^3)
r_i	=	inner radius of the layer between Node 1 and Node 2(m)
r_0	=	outer radius of the layer between Node 1 and Node 2 (m)
R_1	=	thermal resistance between Node 1 and 2 (K.m^3/W)
R_2	=	thermal resistance between Node 1 and the coolant (K.m^3/W)
t	=	time (s)
T_i	=	temperature of Node i (i =1,2) (K)
T_0	=	coolant temperature (K)
x_l	=	system state variable ($l=1,...,L$)
α_m	=	system parameter ($m=1,...,M$)

REFERENCES

Aithal, S.M., Aldemir, T., and Vafai, K., "Assessment of the Impact of Neutronic/Thermal-Hydraulic Coupling on the Design and Performance of Nuclear Reactors for Space Propulsion," *Nucl. Technol*. 106, 15-30 (1994).

Breimeister, J. S. "MCNP-A General Monte Carlo Code For Neutron and Photon Transport, Version 3B," LA 7396-M, Los Alamos National Laboratory, New Mexico (1989).

Burghelea, A., and Aldemir, T., "In-Core Power Detection with CTPS Using a Non-Linear Model," *Trans. Am. Nucl. Soc*., **88**, 314-316 (2003).

Dinca, L., "A Probabilistic Approach to Parameter Estimation towards Fault Diagnosis in Non-Linear Dynamic Systems," Ph.D Thesis, The Ohio State University (1997).

Kruger,G., "A Cermet Fuel Reactor for Nuclear Thermal Propulsion," *Nuclear Thermal Propulsion*, NASA Conference Publication 10079, 165-184 (1991).

Liu, H.-Y., Miller, D. W., Li, D.-X., and Radcliff, T. D., "A Novel Method to On-Line Monitor Reactor Nuclear Power and In-Core Thermal Environments," *Proceedings of the International Congress on Advanced Nuclear Power Plants (ICAPP),* Paper #1212, CD-ROM, American Nuclear Society, La Grange, IL (2002).

Powell, J., Ludewig, H., Mughabghab, S., Perkins, K. Selcow, E., Schmidt, E., and, Horn, F., "A Nuclear Thermal Rocket Engine Design Based on the Particle Bed Reactor Suitable for a Mars Mission," AIAA-91-3508, AIAA/NASA/OAI Conference on SEI Technologies, Cleveland, Ohio (1991).

Radcliff, T. D., Miller, D. W., and Kauffman, A. C., "Constant-Temperature Calorimetry for In-Core Power Measurement", *Nucl. Technol.,* **132,** 240-255 (2000a).

Radcliff, T. D., Miller, D. W., and Kauffman, A. C., "Modeling Of A Constant-Temperature Power Sensor", *Proceeding of 8th International Conference on Nuclear Engineering (ICONE-8)*, Paper #8098, American Society of Mechanical Engineers, New York, N.Y. (2000b).

Turner, W. D., Elrod, D. C., Siman-Tov, I. I., "HEATING-5," ORNL/CSD/TM-15, Oak Ridge National Laboratory, Oak Ridge, Tennessee (1977).

Wang, P., and Aldemir, T., "Real Time Xenon Estimation in Nuclear Power Plants," *Trans. Am. Nucl. Soc.,* **81**, 154-156 (1999).

Wang, P., Chen, X. M., and Aldemir, T., "DSD: A Generic Software Package For Model-based Fault Diagnosis in Dynamic Systems," *Reliab. Engng & System Safety,* **75**, 31-39 (2002).

Proceedings of NPIC&HMIT 2004, 1246-1253, American Nuclear Society, LaGrange Park, IL (September 2004)

Forth American Nuclear Society International Topical Meeting on Nuclear Plant Instrumentation, Controls and Human-Machine Interface Technologies (NPIC&HMIT 2004), Columbus, Ohio, September, 2004

QUANTIFYING THE MEASUREMENT UNCERTAINITY PROPAGATION IN FLUX/POWER RECONSTRUCTION

Mihaela Biro, Tunc Aldemir
The Ohio State University, Nuclear Engineering Program
Bldg 1, Rm 130B, Suite 255, 650 Ackerman Road, Columbus, OH 43202
biro.6@osu.edu; aldemir.1@osu.edu

Keywords: diffusion theory, core power distribution, probability distribution function

ABSTRACT

This paper presents a theoretical approach combining the 1 ½ group diffusion theory with statistical techniques to estimate the flux/power shape probability distribution based on statistical interpolation between measured data. Two methods for estimating the statistical properties of power density/flux between measurement points are described and illustrated on a hypothetical steady state one-dimensional reactor. Results are reported using simulated measured data from 15 hypothetical power sensors placed within the core.

1. INTRODUCTION

In nuclear reactors, it is important to have knowledge of the power/flux shape at all times during the reactor lifetime. This information is, for example, used for determining fuel burnup history and is strictly necessary for ensuring safe operation of the reactor. Currently, in power reactors, the flux/power map is reconstructed based on the signals from out of core or in-core detectors, using diffusion codes and employing different methods of flux reconstruction, such as: piecewise cubic splines to interpolate between measured data (Han, 1999), fittings based on modal expansions (Pomerantz, 2002; Fu, 1997), artificial neural networks (Lee, 2002) and least-squares fittings (Lee, 2003).

There have been relatively few studies that explicitly consider the probability distribution of the measurement uncertainty in the flux/power shape construction process (Bryson, 1993). The proposed approaches are limited to linear relationships between flux/power and location, often requiring long computation times and large memory (Bryson, 1993).

The objective of this research is to develop an approach that can be used to obtain the probability distribution function (pdf) of the flux/power distribution at all points in the reactor using monitored data from in-core power detectors. The proposed approach yields all the statistical properties of the flux/power distribution in the core, including expected values and credibility intervals. Such data could be useful for risk-informed regulatory process and may allow reduction in operational thermal margins (and

subsequently increasing the power extracted from the core) in view of the reduced uncertainty in the estimated local power densities.

Two possible methods of obtaining the pdfs between detectors locations are investigated in this study, both combining the diffusion theory with statistical techniques.

Section 2 describes the theoretical basis. Application on a hypothetical steady state one-dimensional reactor is presented in Section 3. A discussion of the results is given in Section 4.

2. METHODS

The two methods considered in this study differ in the assumptions made:

- Method 1 assumes that, at every point in the reactor, the expected value of the power density/flux follows the diffusion theory.
- Method 2 imposes the additional constraint that the power density/flux can achieve all possible values at any specified point in the reactor.

2.1 Method 1

Consider a one–dimensional steady state reactor as described by 1 ½ group diffusion theory:

$$\frac{d}{dx}\left[D_1(x)\frac{d\phi_1(x)}{dx}\right] + B^2(x)\phi_1(x) = 0 \tag{1}$$

$$\Sigma_{1\to 2}(x)\phi_1(x) = [\Sigma_{a,2}(x) + \Sigma_b(x)]\phi_2(x)$$

with

$$B^2(x) = \frac{\nu}{D_1}\left[\Sigma_{f,1}(x) + \Sigma_{f,2}(x)\frac{\Sigma_{1\to 2}(x)}{\Sigma_{a,2}(x) + \Sigma_b(x)}\right] - [\Sigma_{a,1}(x) + \Sigma_{1\to 2}(x)] \quad (0 \le x \le L) \tag{2}$$

where $\Sigma_b(x)$ denotes the reactivity control cross section (poison and/or control rods) and all the other symbols have their conventional definitions. Solution of Eq.(1) for constant $B^2(x) > 0$ and $B^2(x) < 0$ (e.g. in the vicinity of a control rod) within $x_n < x < x_{n+1}$ yields the power density $h(y)$ at location

$$y = \frac{x_{n+1} - x}{x_{n+1} - x_n} \tag{3}$$

as

$$h(y)=\begin{cases}\dfrac{1}{\sin(\beta)}\left[h_{n+1}\sin[\beta(1-y)]+h_n\sin(\beta y)\right] & B^2(y)>0\\ \dfrac{1}{\sinh(\beta)}\left[h_{n+1}\sinh[\beta(1-y)]+h_n\sinh(\beta y)\right] & B^2(y)<0\end{cases} \tag{4}$$

where h_n is the measured power density/flux at $x = x_n$ (or $y = 1$), h_{n+1} is the measured power density/flux at $x = x_{n+1}$ (or $y = 0$) and

$$\beta^2 = (x_{n+1} - x_n)^2 B^2 \tag{5}$$

Imposing the condition that the expected values of ϕ_1 and ϕ_2 satisfy Eq.(1), the pdf of the power density/flux, $p(h \mid y)$, for given $p(h \mid 1) = p_n$, $p(h \mid 0) = p_{n+1}$ and at a given $0 < y < 1$ can be written as

$$p(h\mid y)=\begin{cases}\dfrac{1}{\sin(\beta)}\left[p_{n+1}\sin[\beta(1-y)]+p_n\sin(\beta y)\right] & B^2(y)>0\\ \dfrac{1}{\sinh(\beta)}\left[p_{n+1}\sinh[\beta(1-y)]+p_n\sinh(\beta y)\right] & B^2(y)<0\end{cases} \tag{6}$$

It can be seen from Eq.(6) that the resulting inferred pdf of power density/flux at location $x_n < x < x_{n+1}$ is a weighted sum of the pdfs of power density/flux at locations x_n and x_{n+1}. This result may be extended for the multigroup case, where energy discriminant detectors need to be used to determine the boundary conditions.

2.2 Method 2

Integration of Eq.(6) over all possible values of h yields

$$F(\infty \mid y)=\int_0^\infty dh\,p(h\mid y)=\begin{cases}\dfrac{1}{\sin(\beta)}\left[\sin[\beta(1-y)]+\sin(\beta y)\right] & B^2(y)>0\\ \dfrac{1}{\sinh(\beta)}\left[\sinh[\beta(1-y)]+\sinh(\beta y)\right] & B^2(y)<0\end{cases} \tag{7}$$

where $F(h|y)$ is the cumulative distribution function (Cdf) for power density/flux at a specified y. It can be seen from Eq.(7) that, for all y, $F(\infty \mid y) = 1$ only for small β, and not for all β values as would be intuitively expected. Method 2 is a modification of the procedure proposed by Read (1999) to search for neutral and charged Higgs bosons in electron-positron collisions. Adapted to the problem under consideration in this study, it assumes that power density/flux varies linearly between detector locations and imposes the condition that $F(\infty \mid y) = 1$ at all y. The procedure also requires that the Cdfs

$$F(h\mid 1)\equiv F_n(h)=\int_0^h p_n(h')dh' \quad \text{and} \quad F(h\mid 0)\equiv F_{n+1}(h)=\int_0^h p_{n+1}(h')dh' \tag{8}$$

at the two consecutive detector locations x_n and x_{n+1}, respectively, have the same value F as well as at all points between the detector locations, i.e.

$$F_n(h_n) = F_{n+1}(h_{n+1}) = F(h) = F \tag{9}$$

Given $p_n(h)$ and $p_{n+1}(h)$, the $p(h \mid y)$ can then be constructed using the algorithm shown in Fig.1

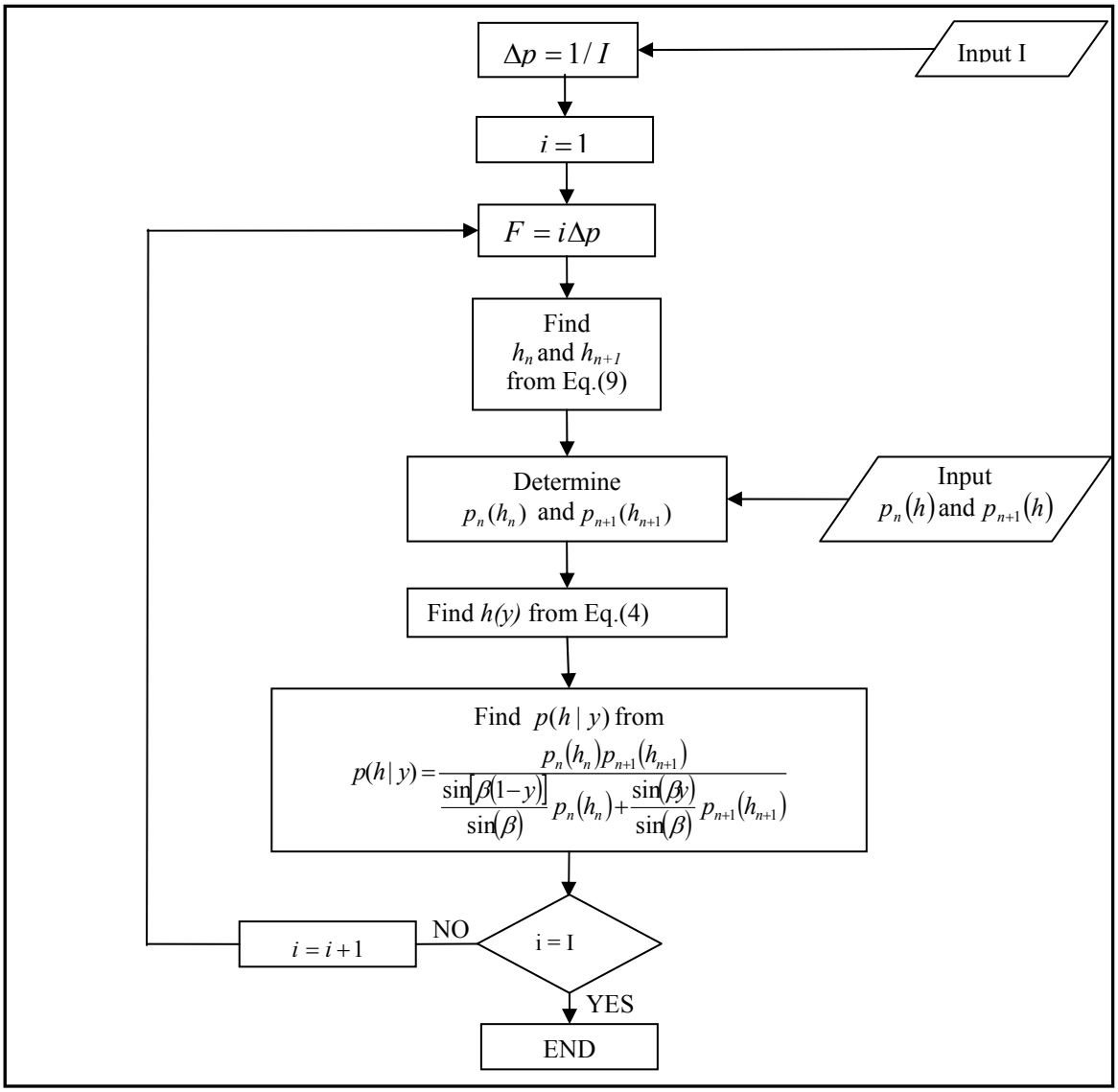

Fig.1: Method 2 Flowchart

3. EXAMPLE RESULTS

A one-dimensional reactor of length $2L$ = 300 cm with material properties given in Table 1 was considered. A gray control rod of thickness 2 cm and transmissivity 0.9

was assumed to be inserted in the reactor at x = 50 cm away from the reactor midplane. Data from detectors placed within the core at every 10 cm starting from the reactor midplane were simulated by solving Eqs.(1) and (2) within $0 \le x \le L$ and with

$$\left.\frac{d\phi_1(x)}{dx}\right|_{x=0} = \left.\frac{d\phi_2(x)}{dx}\right|_{x=0} = 0 \tag{10}$$

$$\phi_1(L) = \phi_2(L) = 0$$

to obtain

$$h(x)/h(0) = \begin{cases} \cos(Bx) & \text{if } x < 49\,\text{cm} \\ 0.488751[\sin(Bx) - \tan(BL)\cos(Bx)] & \text{if } x > 51\,\text{cm} \end{cases} \tag{11}$$

where for criticality we must have B = 0.0242 cm^{-1}.

Table 1 Group constants for the example reactor

Group constant	**Group**	
	1	**2**
$\nu\Sigma_f$ (cm^{-1})	0.008476	0.18514
Σ_a (cm^{-1})	0.01207	0.1210
D (cm)	1.2627	0.3543
$\Sigma_{1->2}$ (cm^{-1})	0.0141	-

The monitored data from the detectors were assumed to be normally distributed with the expected value satisfying Eq.(11) and with a 1% standard deviation. Figure 2(a) shows the probability distributions and the expected values as obtained from Method 1. Figure 2(b) shows the same information, but as obtained by applying Method 2. In the region 40 < x < 60 cm were the existence of a control rod is assumed, the β coefficient in Eq.(4) was obtained through homogenization.

It was noted that although the expected values predicted by both methods matched the simulated data well (see Fig.2), Method 1 may lead to a bimodal distribution and that the predicted expected value between detector locations may fall in a region of low probability. Figures 3 and 4 show the pdfs of reactor power at x = 43 cm and x = 85 cm, respectively. The bimodal shape predicted by Method 1 in Fig.3 has also been observed in other studies (Bursal, 1996) and is due to the fact that $p_n(h)$ and $p_{n+1}(h)$ are being concentrated in different regions of the state space. The unimodal shape of $p(h|y)$ is due to the linearity assumption of Method 2. Figure 4 shows that if the variation in the power density/flux is small with distance (e.g. at x = 85 cm as can be seen from Fig.2)

and subsequently *h(y)* is close to linear, then *p(h|y)* obtained from both Method 1 and Method 2 are similar.

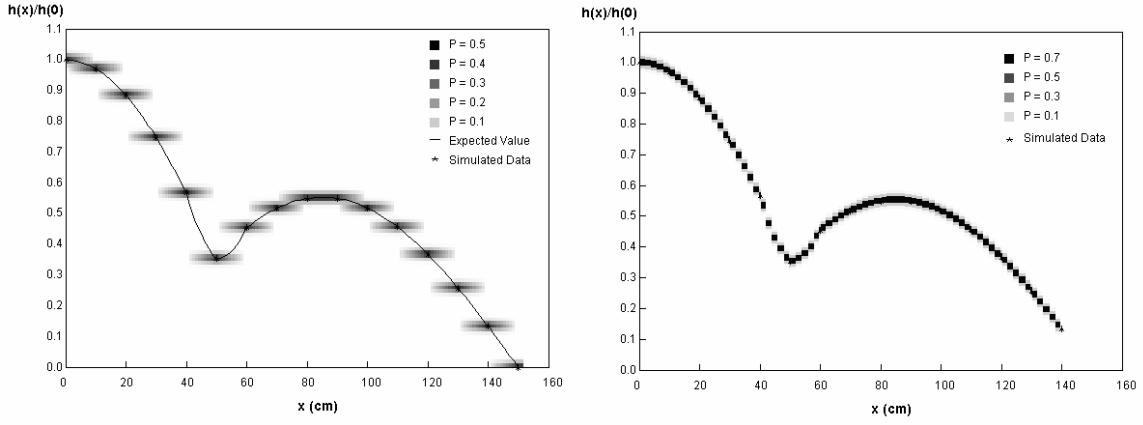

(a) (b)

Fig. 2 Relative power distribution *h(x)/h(0)* for the example reactor: a) Method 1, b) Method 2

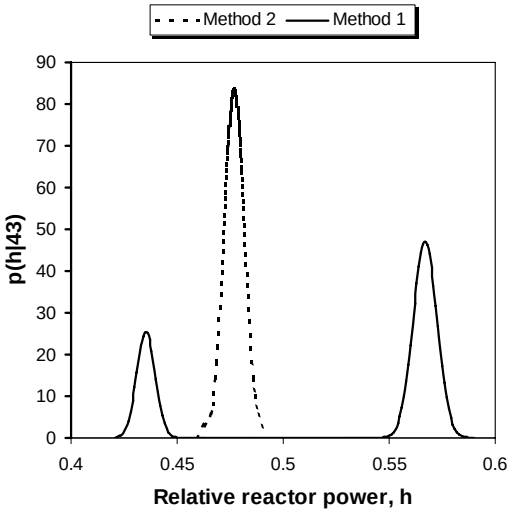

Fig.3 Probability distribution function at location x = 43 cm

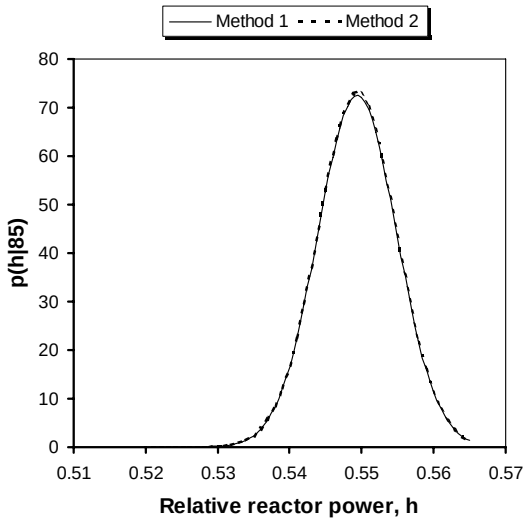

Fig. 4 Probability distribution function at location x = 85 cm

4. CONCLUSIONS

Two methods for estimating the statistical properties of power density/flux between measurement points are described and illustrated in a 1-dimensional reactor assuming steady state behavior and 1 ½ group diffusion theory. Such data may be useful

for risk informed regulation, as well as for establishing meaningful margins on operational power levels and setpoints.

The results of the study show the following:

1. Both Method 1 and Method 2 estimate the expected value of the power density/flux between measurement points well.

2. Method 1 may lead to a bimodal distribution with the uncertainty on the expected value being very large at the midpoint between detector locations.

3. Method 2 always leads to a unimodal distribution with the mode of the distribution close to the expected value.

Considering the fact that the midpoint between detector locations is the one furthest away from the detectors, Result 2 is not counter-intuitive. However, it leads to difficulties from a practical viewpoint since credibility intervals for the expected value of power density/flux in reactor regions away from the detector locations cannot be obtained in a meaningful manner. While Method 2 does not have this problem, it is not clear how the linearity assumption affects the results. One conclusion that arises from these results is that comparison of Method 1 and Method 2 results as a function of x_n allows the optimal choice of detector locations.

NOMENCLATURE

D	diffusion coefficient
ν	number of neutrons emitted per fission
$\phi_i(x)$	neutron flux
$\Sigma_f(x)$	fission cross section
$\Sigma_a(x)$	absorption cross-sections
$\Sigma_{1\to 2}(x)$	group transfer cross-section
$\Sigma_b(x)$	reactivity control cross section
h	power density
p	probability distribution function
F	cumulative distribution function

Subscripts

1	fast neutrons group
2	thermal neutrons group

REFERENCES

J. W. Bryson, J. C. Lee, and J. A. Hassberger, 1993. Optimal Flux Map Generation through Parameter Estimation Techniques, *Nucl.Sci.Eng,* **114**, 238.

F. H. Bursal, 1996. On Interpolating between Probability Distributions, *Applied Mathematics and Computation*, 77, 213-244.

J. J. Duderstadt, L. J. Hamilton, 1976. *Nuclear Reactor Analysis,* John Wiley & Sons.

S. Han, U. S. Kim, P. H. Seong, 1999. A Methodology for Benefit Assessment of Using In-core Neutron Detector Signals in Core Protection Calculator System (CPCS) for Korea Standard Nuclear Power Plants (KSNPP). *Annals of Nuclear Energy*, **26**, 471-488.

G.-C. Lee, W-P. Baek, S. H. Chang, 2002. Improved Methodology for Generation of Axial Flux Shapes in Digital Core Protection Systems, *Annals of Nuclear Energy*, **29**, 805–819.

K. Lee, C. H. Kim, 2003. The Least-Squares Method for Three-Dimensional Core Power Distribution Monitoring in Pressurized Water Reactors**,** *Nucl.Sci.Eng*, **143,** 268.

M. E. Pomerantz, C.R. Calabrese, C. Grant, 2002. Nuclear Reactor Power and Flux Distribution Fitting from a Diffusion Theory Model and Experimental Data, *Annals of Nuclear Energy*, **29,** 1073–1083.

L. Read, 1999. Linear Interpolation of Histograms, *Nuclear Instruments & Methods in Physics Research* A 425, 357-360.

L. Fu, L. Zhengpei, H. Yongming, 1997. Harmonics Synthesis Method for Core Flux Distribution Reconstruction, *Progress in Nuclear Energy*, **31**, 369-372.

Trans. Am. Nucl. Soc., 88, 314-316 (June 2003)

In-Core Power Detection with CTPS Using a Non-Linear Model

Andrei Burghelea, Tunc Aldemir*

The Ohio State University, Nuclear Engineering Program, 206 West 18th Avenue,
Columbus, Ohio 43210

*Author to whom correspondence should be addressed

1. INTRODUCTION

A new in-core reactor power sensor has been under development at The Ohio State University since 1996. This feedback-controlled calorimetric instrument, which is referred to as a constant-temperature power sensor (CTPS), is capable of direct measurement of nuclear energy deposition [1]. The CTPS is ideally suited for use in the proposed Generation IV power systems in which the sensors become an integral part of the fuel for the core lifetime. Previous work [2] to determine the local nuclear energy deposition rate q_n with CTPS has used: a) an algebraic model obtained from the solution of the linearized differential equations describing the CTPS operation, and, b) the software package DSD [3] to estimate the operation dependent model parameters. The results of [2] indicated that the model is very sensitive to model and data uncertainties. This study directly uses the non-linear differential equations describing the CTPS behavior and DSD to estimate the operation dependent model parameters as well q_n. Sections 2 and 3, respectively, describe the sensor model and give an overview of the estimation procedure. Section 4 presents the implementation and results.

2. THE CTPS

The CTPS consists of a UO_2 pellet surrounded by electrical heating resistance wire. The pellet and the wire form the sensor core (Node 2). The core is surrounded by ceramacast which is an alumina based ceramic thermal insulator (Node 1). Both the sensor core and the insulator are coated with thin layers of copper. A feedback control loop is used to provide the exact amount of input electrical energy q_e needed to keep Node 2 temperature T_2 constant in time *(t)*, well above the ambient temperature T_0, regardless of q_n. The sensor operation involves switching between the feedback-controlled constant-temperature mode and the dynamic temperature decay mode following the opening of the feedback loop as described by

$$
\begin{aligned}
C_1 \frac{dT_2}{dt} &= \left(q_n + q_e\right) - \frac{1}{R_1}\left(T_2 - T_1\right) \\
C_2 \frac{dT_1}{dt} &= \frac{1}{R_1}\left(T_2 - T_1\right) - \frac{1}{R_2}\left(T_1 - T_0\right) \\
\frac{1}{R_1} &= \frac{2\pi k_{Cu}(T_2)\left[h_s - 2(r_o - r_i)\right]}{log\left(\frac{r_o}{r_i}\right)} + \frac{2\pi k_{Cu}(T_2)\left(r_o^2 - r_i^2\right)}{\left[h_s - 2(r_o - r_i)\right]}
\end{aligned}
\tag{1}
$$

where k_C , r_o (0.575 mm), r_i (0.3mm) are, respectively, the thermal conductivity, outer and inner radius of the copper layer between Node 1 and Node 2, h_s is the height of the sensor, T_2 is Node 2 temperature, and C_1 and C_2 are, respectively, thermal capacitances of Node 1 and Node 2. Other notation in Eq.(1) are as defined previously. The model described by Eq(1) has been validated against a finite element code [3]. At steady-state Eq.(1) yields

$$
q_n + q_e = \frac{1}{R_2}\left(T_1 - T_0\right) \tag{2}
$$

which corresponds to the constant temperature mode operation of CTPS.

3. AN OVERVIEW OF DSD [4]

The DSD is based on the representation of the system dynamics in terms of transition probabilities between user specified cells that partition the system parameter/state space during user specified time intervals. The DSD recursively computes the probability $p_k(j,n \mid J_k)$ that the state variables (e.g. $T_1(t)$, $T_2(t)$) are in cell j (j = 1,...,J) and the unknown parameters (e.g. R_2, T_0) are in cell n (n = 1,...,N) during the data-sampling time period $k\tau \le t \le (k+1)\tau$ k (k = 0, 1, 2, ...), given that the possible set of cells the state variables can be in at this time is J_k (as observed from the monitored data), from

$$
\begin{aligned}
p_k^*(j,n) &\equiv p_k(j,n \mid J_k) = \frac{p_k(j,n)}{\sum_{j' \in J_k}\sum_{n'} p_k(j',n')} \quad (j \in J_k) \\
p_k(j,n) &= \sum_{j' \in J_{k-1}} g(j \mid j',n)\, p_{k-1}^*(j',n')
\end{aligned}
\tag{3}
$$

where $g(j \mid j',n)$ is the transition probability from state variable cell j' to state variable cell j during the period $k\tau \le t \le (k+1)\tau$ when the system parameters are within cell n. The $g(j \mid j',n)$ can be approximated by: 1) at time $k\tau$, selecting randomly or otherwise (e.g. equidistant) M' starting points from

cell j' for a given n, 2) using the given system model (e.g. Eq.(1)) to find the number M of trajectories that arrive within cell j at $t = (k+1)\tau$ (e.g. by integrating Eq.(1) over $k\tau \le t \le (k+1)\tau$ for each of the $m' = 1, 2, \ldots, M'$ initial conditions), and, c) letting $g(j \mid j', n) = M / M'$. A graphical illustration of this process is given in [5] and some sufficient conditions for the convergence of DSD are given in [6].

4. IMPLEMENTATION AND RESULTS

In the implementation, C_1, C_2, R_1 in Eq.(1) are assumed to be known. T_1, T_2 and q_e are assumed to be measured. The estimation of q_n for each data sampling time $t = k\tau$ (see Section 3) was carried out iteratively through the following steps: 1) Assume q_n; 2) Estimate T_0 and R_2 from Eq.(1); 3) Determine q_n from Eq.(2) using Step 2 results; 4) Compare q_n to its previous value q_n'; 5) If $(q_n - q_n')/q_n < 0.01$ stop (convergence), otherwise go to Step 2 with q_n. The $T_1(t)$ and $T_2(t)$ data for the estimation were generated from Eq.(1) with T_0=700 K, $T_1(0)$=721.095 K, $T_2(0)$=782.538 K, C_1=0.008041 J/K, C_2=0.744024 J/K, R_1=5.41 K/W, R_2=1.85 K/W, q_n=1.68 W q_e=9.6766 W and superimposed 1%random noise on the observed data (i.e. T_1 and T_2). The k_{Cu} as a function of T_2 was represented by a third order polynomial. Figure 1 shows the estimation results, as well as the partitioning scheme used with Eq.(3). Convergence on q_n was obtained in 12 iterations on the average per data sampling interval. The results indicate that the estimation scheme works well for both constant and time-varying ambient temperature T_0.

5. CONCLUSION

The results of the study show that DSD be used with CTPS to estimate the local power density in nuclear reactor cores both for steady-state and transient conditions with noisy data.

REFERENCES

1. T. D. Radcliff, D. W. Miller and A. C. Kauffman, "Modeling of a Constant-Temperature Power Sensor", *ICONE8*, Paper #8263, American Society of Mechanical Engineers, New York, N.Y. (May 2000)
2. I. Munteanu, H.B. Zhou, T. D. Radcliff, T. Aldemir, D. W. Miller, "In-Core Power Detection Using DSD", *Trans. Am. Nucl. Soc*., **83**, 279-281 (November 2000)
3. H.-Y. Liu, D. W. Miller, D.-X. Li, T. D. Radcliff, "A Novel Method to On-Line Monitor Reactor Nuclear Power and In-Core Thermal Environments", *ICAPP: Proceedings of the International Congress on Advanced Nuclear Power Plants,* Paper #1212, CD-ROM, American Nuclear Society, La Grange, IL (June 2002).

4. P. Wang, X. M. Chen, T. Aldemir, "DSD: A Generic Software Package For Model-based Fault Diagnosis in Dynamic Systems", *Reliab. Engng & System Safety*, **75**, 31-39 (January 2002)
5. M. Gadioli, M. Marseguerra, E. Zio, "Fast Integration by Neural Nets in DSD: Probabilistic State Estimation", *Trans. Am. Nucl. Soc., 81*, 151-153 (November 1999)
6. P. Wang, T. Aldemir, "Real Time Xenon Estimation in Nuclear Power Plants", *Trans. Am. Nucl. Soc.,81*, 154-156 (November 1999)

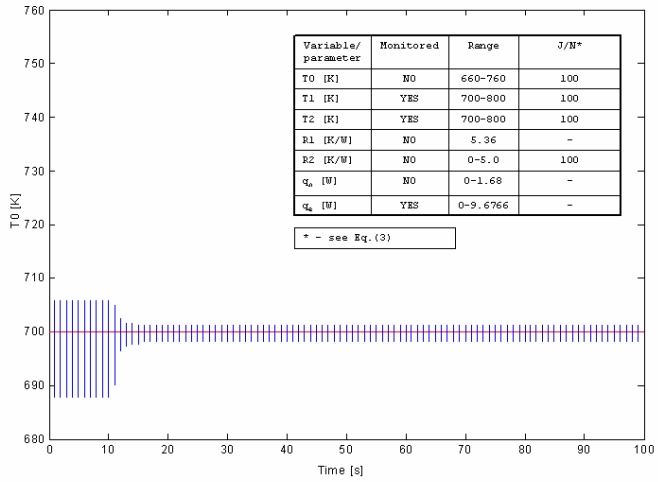

(a)

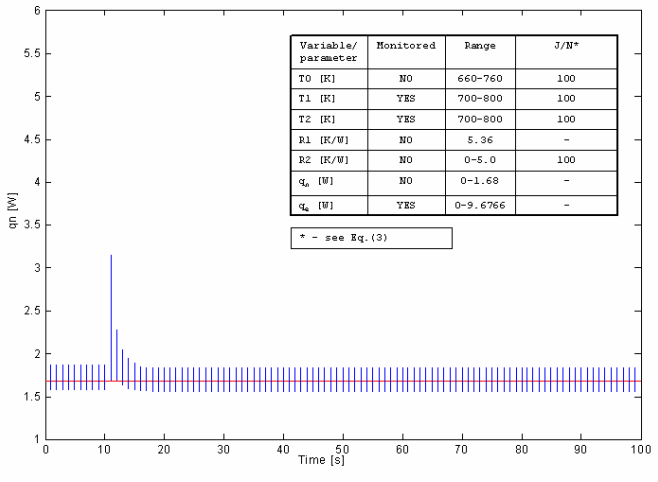

(b)

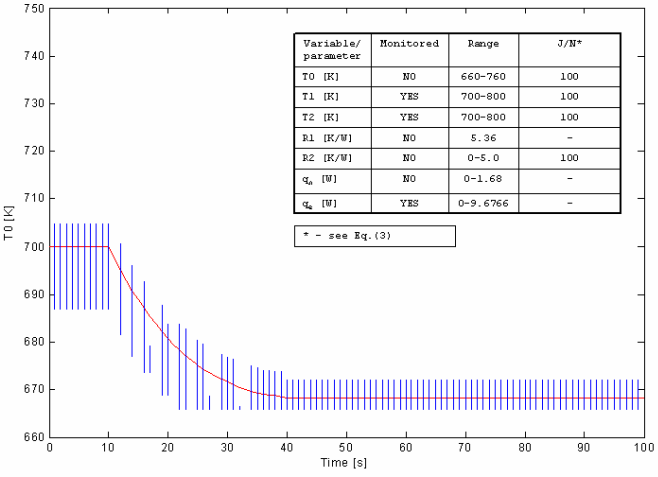

(c)

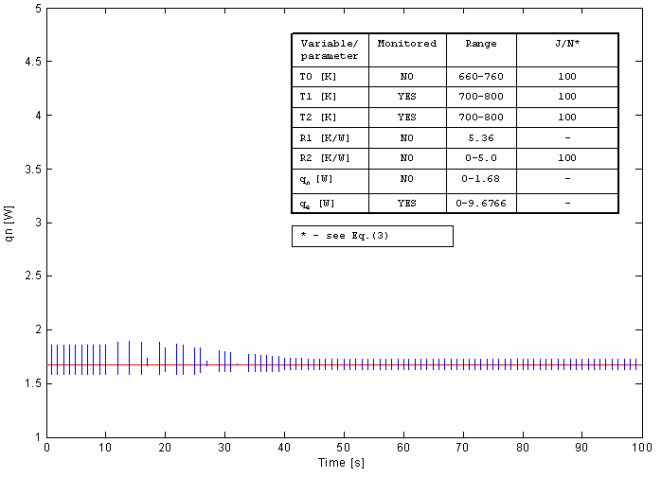

(d)

Fig.1: Estimation results (bars) for constant and time-varying T_0: a) constant T_0; b) q_n for constant T_0; c) time-varying T_0; b) q_n for time-varying T_0. Solid lines indicates the true values.

Trans. Am. Nucl. Soc., 89, 493-495 (November 2003)

A Parametric Investigation of the Recursive Partitioning Approach to DSD for Implementation with CTPS

Andrei Burghelea, Tunc Aldemir*

The Ohio State University, Nuclear Engineering Program, 206 West 18th Avenue, Columbus, Ohio 43210

*Author to whom correspondence should be addressed

INTRODUCTION

The DSD (Dynamic System Doctor) is dynamic system state/parameter estimation software [1] that can automatically account for modeling uncertainties/signal noise in the estimation process. This capability is accomplished through the representation of system evolution in terms of probability of transitions within a user specified time interval τ (e.g. data sampling interval) between sets of user defined parameter/state variable magnitude intervals (or cells) that partition the search space. The DSD yields the probability $p_k(n,j)$ that the parameters are in cell n and the state variables are in cell j at time $t = k\tau$. Then $p_k(n,j)$ can be used to determine the lower and upper bounds on the estimated values of state variables/parameters, as well as their probability distribution within these bounds.

A potential limitation in the implementation of DSD is that excessively long run times and large memory requirements may result for large or rapidly evolving systems if the cell definitions are provided as fixed initial input. Recently a recursive partitioning scheme (RPS) for cell definitions was proposed that substantially reduces the estimation time and memory requirements [2]. This paper investigates the sensitivity of the RPS to the ranges of interest for the state variables/parameters to be estimated using the constant temperature power sensor (CTPS) [3]. The CTPS has been proposed for direct measurement of local power density in nuclear reactor cores and requires the on-line estimation of ambient conditions for reliable operation. A practical implication of such a parametric search is the determination of the power range the CTPS can be operated in.

OVERVIEW OF DSD WITH RPS

The RPS philosophy is to progressively eliminate the regions of the search space where $p_k(n,j) = 0$ through the on-line definition of the cells. Figure 1 shows the DSD algorithm with RPS. The DSD assumes that a system model is available which can be used the system location is state space at time $t = (k+1)\tau$ $(k = 0,1,2\cdots)$ from the knowledge of its location at time $t = k\tau$ and the known values of the system parameters. The algorithm consists of the following steps:

1. *Specify, respectively, the state variable and parameter ranges of interest, RPS stopping rules and monitored data uncertainty*. The parameter and state variable ranges of interest define the search space for the estimation process. The RPS stopping rules define the smallest cell size that needs to be used for the estimation of the unmonitored state variables/parameters. The choice of such a cell is usually based on the accuracy level desired for the variables/parameters to be estimated.
2. *Read data from the monitors* at each time point $t = k\tau$ $(k = 0,1,2\cdots)$.
3. *Define the intervals for the monitored variables* so as to contain the variation/noise on the monitored data, centered on their median values.
4. *Define the intervals for the unmonitored variables and the parameters by bisecting each range of interest*. Along with the intervals defined in Step 3, these intervals form the cells that partition the search space.
5. *Input the initial probability distribution $p_0(n,j)$ to be used to start the estimation process*. The $p_0(n,j)$ is usually chosen as the uniform distribution, however, results of the estimation are not dependent on the choice of $p_0(n,j)$.

6. *Determine the cell-to-cell transition probabilities* $g(j \mid j', n')$ by: a) selecting J' points in cell j' at time $t = k\tau$, b) finding the number of arrival points J in cell j at time $t = (k+1)\tau$ from the system model, assuming that the system parameters remain in their cell n' at time $t = k\tau$, and, c) letting $g(j \mid j', n') = J' / J$.
7. *Find* $p_k(n, j)$ from

$$p_k(n, j) = \sum_{j'} \sum_{n'} g(j \mid j', n') p_{k-1}(n', j')$$

8. *If all* $p_k(n, j) = 0$, *then subdivide each and go to Step 3. Otherwise, normalize* $p_k(n, j)$ *by dividing it by the total probability of finding the system in the search space, increment the time index k and go to Step 2.* The probability of finding the system in the search space is not necessarily 1, because the system may leave the search space during $k\tau \le t < (k+1)\tau$ depending on its location at $t = k\tau$.

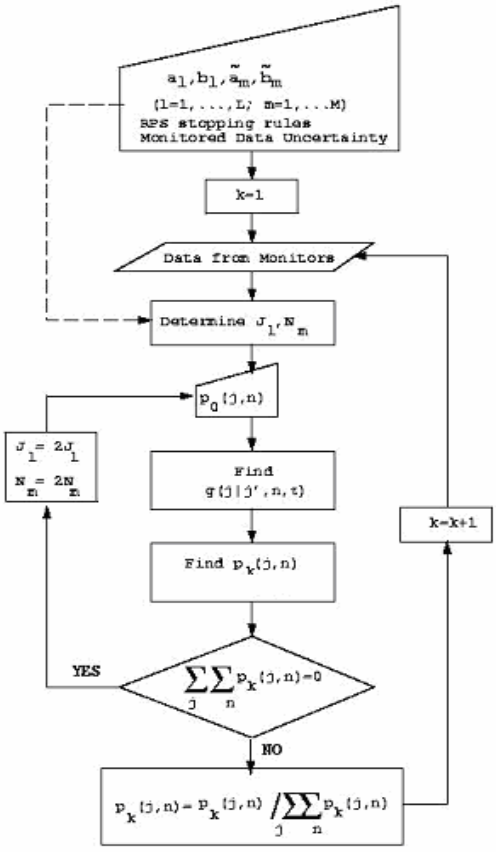

Fig.1: DSD Algorithm with RPS

Steps 2 through 8 are repeated until $p_k(n, j)$ converges in the probability sense, i.e. $p_k(n, j)$ are all zero except for the cells containing the actual system locations in the system state and parameter spaces It should be mentioned at this point that the algorithm may not converge for rapidly evolving systems during one data sampling interval $k\tau \le t < (k+1)\tau$. However, even in this situation, previous work shows that the expected values of the parameters/state variables to be estimated are often found to be close to their actual values [4].

THE CTPS

The CTPS consists of a UO_2 pellet surrounded by electrical heating resistance wire. The pellet and the wire form the sensor core (Node 2). The core is surrounded by ceramacast which is an alumina based ceramic thermal insulator (Node 1). Both the sensor core and the insulator are coated with thin layers of copper. A feedback control loop is used to provide the exact amount of input electrical energy q_e needed to keep Node 2 temperature T_2 constant in time, well above the ambient temperature T_0, regardless of q_n. The sensor operation involves switching between the feedback-controlled constant-temperature mode (Mode 1) and the dynamic temperature decay mode (Mode 2) following the opening of the feedback loop as shown below in Fig.2.

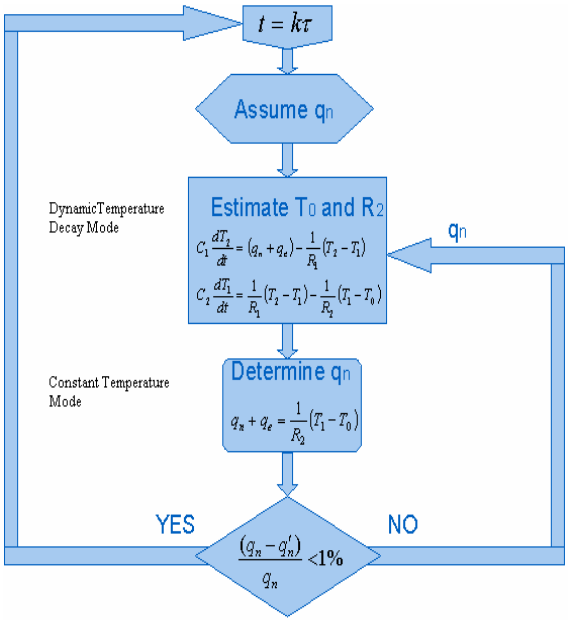

Fig.2: CTPS Operation

The quantities C_1, C_2 and R_1 in Fig.2 are assumed to be known. T_1, T_2 and q_e are assumed to be measured.

IMPLEMENTATION AND RESULTS

In the implementation, the estimation of q_n for each data sampling time $t = k\tau$ was carried out iteratively as shown in Fig.2. The $T_1(t)$ and $T_2(t)$ data for the estimation were generated from the equations describing the dynamic temperature decay mode in Fig. 2 with T_0=700 K, $T_1(0)$=721.095 K, $T_2(0)$=782.538 K, C_1=0.008041 J/K, C_2=0.744024 J/K, R_1=5.41 K/W, R_2=1.85 K/W, q_n=1.68 W q_e=9.6766 W and superimposed 1% random noise on the monitored data (i.e. T_1 and T_2). The noise level is substantially larger than the anticipated measurement uncertainty during the operation of the sensor. The k_{Cu} in Fig.2 as a function of T_2 was represented by a third order polynomial. Table 1 shows the estimation results. The last row shows the average number of switches between Mode 1 and Mode 2 for convergence in q_n and indicates that the computational demand for RPS is relatively insensitive to the size of the search space, however, increases with the refinement of the stopping rule as also expected from DSD applications with progressively refined fixed partitioning schemes.

CONCLUSION

The results of the study show that DSD with RPS be used with CTPS to estimate the local power density in nuclear reactor cores for fuel temperature ranges within 300 K to 1000 K. Similarly, the estimation scheme works within the coolant temperature range of (i.e. T_0) of 300 – 1000K. While these temperatures ranges include most of the operational range of current reactors, further studies are needed to investigate the suitability of measurement scheme to high temperature, gas cooled Generation IV reactors.

Table 1
Estimation Results for RPS

	Case		
	1	2	3
T_0 Range (K)	650-850	500-900	300-1000
T_1/T_2 Range (K)	50-1250	300-900	300-1000
R_2 Range (K/W)	0-5	0-5	0-5
Stopping Rule (%of range)	1	2.0/1.0	1.5
Average Number of Intermodal Iterations	7.25	8.94/11.47	8.63

REFERENCES

1. P. WANG, X. M. CHEN, T. ALDEMIR, "DSD: A Generic Software Package For Model-based Fault Diagnosis in Dynamic Systems", *Reliab. Engng & System Safety*, **75**, 31-39 (January 2002)
2. A. BURGHELEA, I. MUNTEANU, T. ALDEMIR, "A Recursive Partitioning Approach to DSD", *PSA2002: Proceedings of the International Topical Meeting on Probabilistic Safety Assessment, G*. E. Apostolakis, T. Aldemir (Eds), 630-635, American Nuclear Society, La Grange Park, IL (2002)
3. A. BURGHELEA, T. ALDEMIR, "In-Core Power Detection with CTPS Using a Non-Linear Model", *Trans. Am. Nucl. Soc*., **88**, 314-316 (June 2003)
4. P. WANG, T. ALDEMIR, "Some Improvements in State/Parameter Estimation Using the Cell-to-Cell-Mapping Technique", submitted to *Nucl.SciEng* .

TRANSACTIONS

OF THE
AMERICAN NUCLEAR SOCIETY

June 24–28, 2007
Boston Marriott Copley Place
Boston, Massachusetts

Volume 96
TANSAO 96 1–882 (2007)
ISSN: 0003-018X

Raymond T. Klann (ANL)
Technical Program Chair

Stephen P. LaMont (LANL)
Jess Gehin (ORNL)
Assistant Technical Program Chairs

Julie B. Rule (ANS)
Editor

Ellen M. Leitschuh (ANS)
Coordinator

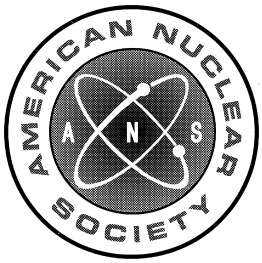

CLICK HERE TO START

AMERICAN NUCLEAR SOCIETY HOME PAGE

Material Identification in Finite Cylindrical Geometries Using the Schwinger Inverse Method, invited

Keith C Bledsoe,* Jeffrey A. Favorite,** and Tunc Aldemir***

*Nuclear Engineering Program, The Ohio State University, Columbus, OH 43210 USA, bledsoe.12@osu.edu
**X-4-TAR, MS T082, Los Alamos National Laboratory, Los Alamos, NM 87545 USA, fave@lanl.gov
***Nuclear Engineering Program, The Ohio State University, Columbus, OH 43210 USA, aldemir.1@osu.edu

INTRODUCTION

The Schwinger inverse method [1], a novel solution method for solving inverse transport problems, was recently developed and tested in one-dimensional spherical geometries [1, 2]. In this paper, the method is applied to solving the inverse problems of source weight fraction identification and shield composition identification in finite two-dimensional cylindrical geometries.

THE SCHWINGER INVERSE METHOD

The Schwinger inverse method [1] was derived from a perturbation-theory approach to the inverse transport problem. Instead of calculating the effect of a system perturbation on a quantity of interest (the usual use of the Schwinger functional), the quantity of interest was assumed to be given (from a measurement) and the Schwinger functional was manipulated to produce an equation for the system perturbation. The equation is applied iteratively. The quantity of interest is the leakage of a discrete gamma-ray line from radioactive decay, which implies that the scattering term in the transport equation can be ignored.

Shield Material Identification

The method was used to derive the following equation for the composition of an unknown shield layer [2]:

$$\Sigma_t'^g = \frac{\int dV \int d\hat{\mathbf{\Omega}} \psi^{*g} q^g}{\int_{V_{unk.}} dV \int d\hat{\mathbf{\Omega}} \psi^{*g} \psi^g} \left(\frac{M^g - M_0^g}{M_0^g} \right) + \Sigma_t^g, \qquad g = 1, \ldots, G. \tag{1}$$

In this equation, Σ_t^g is the total photon cross section in the current iteration for the unknown material at the energy corresponding to line g and $\Sigma_t'^g$ is the updated cross section that will be used in the next iteration. The terms ψ^g, ψ^{*g}, and M^g are the forward flux, adjoint flux, and leakage calculated for line g in the current iteration; q^g is the source for line g (γ/cm^3·s); and M_0^g is the measured leakage for line g. The integral in the numerator in Eq. (1) is over the entire problem, but the integral in the denominator is over the unknown material region only. Once the G macroscopic cross sections are found, the unknown material is identified using cross section tables [2].

Source Weight Fraction Identification

The method was also used to derive an equation for unknown isotope weight fractions in a gamma-emitting source material [1]:

$$\frac{\rho_S N_A}{\left\langle \psi^{*g} q^g \right\rangle} \left[\left(\int_{V_S} dV \int d\hat{\mathbf{\Omega}} \psi^{*g} \psi^g \right) \sum_{j=1}^{J} \frac{\sigma_{t,j}^g}{A_j} \Delta f_j - \left(\frac{M^g}{M_0^g} \frac{q_i^g}{A_i} \int_{V_S} dV \int d\hat{\mathbf{\Omega}} \psi^{*g} \right) \Delta f_i \right] = \frac{M^g - M_0^g}{M_0^g}, \qquad g = 1, \ldots, G. \tag{2}$$

In this equation, ρ_S is the mass density of the source material, N_A is Avogadro's number, $\sigma_{t,j}^g$ is the total microscopic cross section for source isotope j and line energy g, q_i^g is the source strength of isotope i for line g, and A_j is the gram atomic weight of isotope j. The term $\Delta f_j \equiv f_j' - f_j$ is the update to the weight fraction in the current iteration to obtain the weight fraction to use in the next.

TEST PROBLEM

The methods for source and shield identification were tested on the finite cylindrical geometry shown in Fig. 1. A highly enriched uranium source is surrounded by a shield consisting of aluminum on the bottom and side of the cylindrical shield and nickel on the top. The top of the shield is twice as thick as the bottom. This axial asymmetry allows for more physically realistic test problems than were possible with the one-dimensional spherical problems of Refs. 1 and 2.

The quantities of interest were the total leakage (into 4π) of four decay lines from uranium, 144, 186, 766, and 1001 keV. The forward and adjoint angular fluxes of Eqs. (1) and (2) were calculated for each line using the PARTISN discrete-ordinates code [3] with no scattering.

Leakage measurements were simulated in two ways. The first was by using PARTISN with the same angular (S_8) and spatial discretizations as used to calculate the flux in the iterative calculation. Thus, these "measured" and calculated leakages were exactly consistent. The second way of simulating measured leakages was by using a Monte Carlo code, which simulated a real measurement of the total leakage. These measurements are shown in Table I.

Schwinger iterations were run until the calculated line leakages were within 0.01% of the measurements.

RESULTS

Shield Material Identification

Converged cross sections on the left side of Eq. (1) were compared to known cross sections from a library of 40 candidate materials using a root-mean-squared (rms) difference, where the rms difference for material m is

$$(\text{rms})_m = \sqrt{\frac{1}{G}\sum_{g=1}^{G}(\Sigma_t'^g - \Sigma_{t,m}^g)^2}. \quad (3)$$

The materials with the lowest rms differences were considered candidates for the unknown.

When S_8 measurements were used, nickel was successfully identified as the only suitable candidate for the unknown layer, having an rms difference two orders of magnitude smaller than any other material (see Table II). With Monte Carlo measurements, nickel still had the smallest rms difference, but was one of nine possible shield materials.

Source Weight Fraction Identification

Initial guesses for the weight fractions of uranium in the source were ^{235}U: 0.5000, ^{238}U: 0.5000. When S_8 measurements were used, the actual source weight fractions (^{235}U: 0.9473, ^{238}U: 0.0527) were found in one iteration of Eq. (2). With Monte Carlo measurements, slightly less accurate weight fractions of ^{235}U: 0.9300, ^{238}U: 0.0700 were calculated in one iteration.

CONCLUSIONS

The Schwinger inverse method has previously been applied to the separate problems of determining unknown source [1] and shield compositions [2] in one-dimensional spherical geometries. In this paper, the method was successfully applied to these problems in a more physically realistic two-dimensional cylindrical geometry.

In this work, the total leakage into 4π was the quantity of interest. To model more realistic scenarios, the quantity of interest should be the gamma-ray flux at a particular detector location outside the object. We are currently studying ways to mitigate the discrete-ordinates ray effects in order to allow such calculations to be made accurately.

REFERENCES

1. J. A. FAVORITE, "Using the Schwinger Variational Functional for the Solution of Inverse Transport Problems," *Nucl. Sci. Eng.*, **146**, 51-70 (2004).
2. J. A. FAVORITE and K.C. BLEDSOE, "Identification of an Unknown Material in a Radiation Shield Using the Schwinger Inverse Method," *Nucl. Sci. Eng.*, **152**, 106-117 (2006).
3. R. E. ALCOUFFE et al., "PARTISN," LA-CC-98-62, Los Alamos National Laboratory (1997).

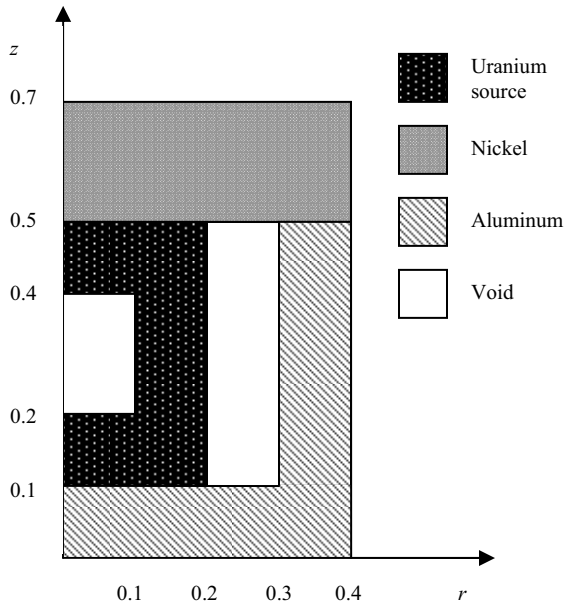

Fig. 1. Geometry for numerical test problems. Dimensions are in cm.

TABLE I. Measured Leakages.

Line (keV)	S_8	Monte Carlo
144	4.58897E+2	4.274E+2 ± 7.79%
186	4.54920E+3	4.577E+3 ± 5.40%
766	1.22674E+0	1.193E+0 ± 2.15%
1001	3.47231E+0	3.393E+0 ± 2.06%

TABLE II. Materials with the Lowest rms Difference in the Shield Identification Problem (Actual Material Was Nickel, Initial Guess Was Lead).

	S_8 Measurements			Monte Carlo Measurements	
1	Nickel	8.612E-04	1	Nickel	1.636E-01
2	Copper	2.952E-02	2	Copper	1.694E-01
3	Cobalt	8.705E-02	3	Cobalt	1.831E-01
4	SS316	1.967E-01	4	SS316	2.191E-01
5	Iron	2.390E-01	5	Cadmium	2.193E-01
			6	Iron	2.287E-01
			7	SS304	2.293E-01
			8	Carbon Steel	2.321E-01
			9	Silver	2.781E-01

Trans. Am. Nucl. Soc., 93, 575-577 (November 2006)

Implementation of an on-line reactor power monitoring system using CTPS

Mihaela Biro, Tunc Aldemir*

T*he Ohio State University, Nuclear Engineering Program, 650 Ackerman Road, Columbus, Ohio 43202*

*Author to whom correspondence should be addressed

INTRODUCTION

The constant-temperature power sensor (CTPS) [1, 2] is a feedback-controlled calorimetric instrument capable of direct measurement of nuclear energy deposition. A conceptual system for power measurements in reactor cores using such sensors has been developed using DSD [3]. The DSD is state/parameter estimation technique for dynamic systems. It yields the probability distribution functions (pdfs) of the quantities to be estimated in their discretized space from a user-provided system model and using monitored system data along with their associated uncertainties. The data uncertainties provide inputs for the discretization process which partitions space of the quantities to be estimated into computational cells, in a similar manner to those used by the finite difference or finite element methods. It has been shown that a probabilistic map of core power distribution can be constructed with DSD using simulated signals from an array of sensors distributed in a hypothetical reactor core [4].

This paper investigates the computational feasibility of the estimation algorithm proposed in [4]. The goal is to have an estimation engine able to construct the probabilistic map of core power distribution in real-time. Parallel implementation of the algorithm is investigated on multiple processors, attempting to determine the minimum number of processors necessary to run the estimation algorithm under real-time constraints.

THE CTPS

The CTPSs [1, 2] are sensors capable of direct measurement of nuclear power density (q_n). The CTPS concept is based on control of the energy balance about a small mass of fissionable material. The sensor core is a UO_2 pellet (Node 2) surrounded by an insulator material (Node 1). An electrical heating resistance wire is wound on Node 2. A feedback control loop is provided that adjusts the necessary input of electrical energy (q_e) such that the Node 2 temperature is maintained constant.

The sensor behavior is described by [5]:

$$C_1\frac{dT_2}{dt} = (q_n + q_e) - \frac{1}{R_1}(T_2 - T_1)$$
$$C_2\frac{dT_1}{dt} = \frac{1}{R_1}(T_2 - T_1) - \frac{1}{R_2}(T_1 - T_0) \quad (1)$$

where T_1 and T_2 are the temperatures of Node 1 and Node 2, respectively, T_0 is the temperature of the coolant in contact with Node 1, C_1 and C_2 are the thermal capacitances of Nodes 1 and Node 2, respectively, R_1 is the thermal resistance between Node 2 and Node 1 and R_2 is the thermal resistance between Node 1 and the coolant.

At steady-state conditions, the energy balance around Node 2 is described by

$$q_n + q_e = (T_2 - T_0)/(R_1 + R_2). \quad (2)$$

By measuring q_e and T_2, q_n can be estimated from Eq. (2) if R_2 and T_0 are known.

As can be seen from Eq. (2), an accurate estimation of q_n in the measuring mode depends on the accurate estimation of T_0 and R_2. The CTPS has two modes of operation: i) power measurement mode when q_e is measured and q_n is estimated using Eq.(2), and, ii) calibration mode during which R_2 and T_0 are estimated from Eq.(1). In the power measurement mode, q_e is such that T_1 and T_2 are constant. In the calibration mode, q_e is interrupted. Then T_1 and T_2 decrease to steady-state values as described by Eq.(1). In Eq.(1), T_1, T_2 and q_e are measured quantities. The R_2, T_0 and q_n parameters are to be estimated. All the other quantities in Eq.(1) are assumed to be known (e.g. through previous off-line measurements)

THE DSD

The DSD uses a representation of system evolution in time in terms of probability of transitions between sets of magnitude intervals of system state-variables (i.e. T_1 and T_2 for Eqs.(1) and (2)) and parameters (i.e. R_2,T_0, q_n for Eqs.(1) and (2)) within the user specified

time intervals $k\tau \le t \le (k+1)\tau$ $(k=0,1,..)$. These sets form computational cells that partition the system state and parameter spaces. If location of the system in the state-space is known for specified system parameters (such as for the problem under consideration since T_1 and T_2 are measured), the DSD generates the transition probability $g(j \mid j', n, \tau)$ from cell j' to j in the state-space within $k\tau \le t \le (k+1)\tau$ given that the system parameters are in cell n at time $k\tau$ from

$$g(j \mid j', n, \tau) = \frac{1}{v_{j'}} \frac{1}{v_n} \int_n d\boldsymbol{\alpha} \int_{j'} d\boldsymbol{x}' e_j[\tilde{\boldsymbol{x}}(\boldsymbol{x}', \boldsymbol{\alpha}, k\tau)]$$
$$e_j(\boldsymbol{x}) = \begin{cases} 1 & \text{if } \boldsymbol{x} \text{ is within } j \\ 0 & \text{otherwise} \end{cases} \quad (3)$$

In Eq.(3), the elements of the vectors $\boldsymbol{x}$ and $\boldsymbol{\alpha}$ are the state variables and system parameters, respectively. The vector $\tilde{\boldsymbol{x}}(\boldsymbol{x}', \boldsymbol{\alpha}, k\tau)$ denotes the location of the system in the state-space at time $t = (k+1)\tau$ given that it departed from point $\boldsymbol{x}'$ at time $t = k\tau$ for specified $\boldsymbol{\alpha}$, $v_{j'}$ is the volume of cell j' and v_n is the volume of cell n. The point $\tilde{\boldsymbol{x}}(\boldsymbol{x}', \boldsymbol{\alpha}, k\tau)$ is determined from a user provided system model describing system evolution in time, such as Eqs.(1) and (2). If the system parameters do not change within $k\tau \le t \le (k+1)\tau$, the DSD determines the joint pdf $p_k(j,n)$ for the mean value of the state-variables and parameters over cell pair j,n at time $t = k\tau$ recursively from

$$p_k(j,n) = \sum_{j'} g(j \mid j', n, \tau) p_{k-1}(j', n) \quad (k = 0,1,\cdots). \quad (4)$$

DETERMINATION OF POWER DISTRIBUTION

Figure 1 shows schematically the procedure for the determination of power distribution. First, the $g(j \mid j', n, \tau)$ in Eq.(4) are determined from Eqs.(1) and (3), monitored $T_1(k\tau)$, $T_2(k\tau)$ and q_e. Then the joint pdf $p_k(R_2, T_0, q_n) \equiv p_k(\hat{j}, n)$, where n denotes the cells in the R_2-T_0-q_n space, and $\hat{j}$ denotes the observed system location in the discretized T_1-T_2 space, is updated using Eq.(4). The following steps are used for the estimation of q_n at each CTPS location:

1. $p(R_2, T_0, q_n)$ is integrated (or summed in the discretized R_2-T_0-q_n space) over all possible values of q_n to obtain the joint pdf $p(R_2, T_0)$.
2. $p(R_2, T_0)$ from Step 1 yields a probability for R_2 and T_0 being in each set of intervals partitioning the R_2-T_0 space.
3. Using the boundaries of these intervals as inputs for Eq.(2), upper and lower bounds are found for q_n for the probabilities identified in Step 2.
4. Superimposition of the intervals and the corresponding probabilities from Step 3 yields the pdf for q_n.

Once the pdfs for q_n is found at CTPS locations, the approach described in [6] can be used to generate the pdfs for q_n between these locations.

PARALLEL IMPLEMENTATION

Parallel implementation of the above-described monitoring scheme was investigated on multiple processors, attempting to determine the minimum number of processors necessary to run the estimation algorithm under the real-time constraints. The algorithm was implemented in C/C++ and ran on multiple processors using Message Passing Interface (MPI) directives for assigning jobs and coordinating communication between the parallel processes. Computation time measurements were taken by running the algorithm on the Pentium IV Cluster of the Ohio Supercomputing Center for different problem sizes (i.e. the number of cells partitioning the estimated parameter space) and for different numbers of processors.

The power monitoring scheme was implemented on an example application taken from [5]. It consisted of seven sensors axially distributed within a cylindrical reactor core of a pebble bed type reactor. A reactor transient in which the coolant temperature decreases exponentially with 1 hour period was assumed.

RESULTS

The computation time needed for the estimation algorithm was assumed to be 6 seconds of real time (duration of the calibration mode). For a problem size of 64x64x64 cells partitioning the R_2-T_0-q_n space, the computation time was 23 s for 1 processor, 15 s on 2 processors, 7 s on 4 processors and 4 s on 8 processors. At the same time, the parallelization efficiency (serial time/parallel time/number of processors) decreased from about 80% on 2 processors to about 70% on 8 processors.

CONCLUSION

This study shows that the DSD algorithm is computationally feasible for implementation for an on-line, real-time power monitoring system using parallel processing.

The optimum number of processors needed depends on how fast the sensors need to be calibrated and on the available processor resources. For 4 processors, the computation time is the nearest to real-time for the assumed transient used for this study, but fewer number processors may be adequate for steady-state operation where the parameters to be estimated would not change rapidly.

REFERENCES

1. T. D. RADCLIFF, S. P LIU, D. W. MILLER, "Modeling and Optimization of a Constant-Temperature In-Core Power Sensor", *Nuclear Technology*, **140**, 209-221 (2002).
2. T. D. RADCLIFF, D. W. MILLER, A. C. KAUFFMAN, Constant-Temperature Calorimetry for In-Core Power Measurement", *Nuclear Technology*, **132**, 40-254 (2000).
3. P. WANG, X. M. CHEN, T. ALDEMIR, "DSD: A Generic Software Package For Model-based Fault Diagnosis in Dynamic Systems", *Reliab. Engng & System Safety*, **75**, 1-39 (2002).
4. M. BIRO, T. ALDEMIR, "The Development of a Self-Calibrating Power Monitoring System for Nuclear Reactors", *Proc.ISAS-CITSA 2005*, II, J. Aguilar, H.-A. Chu, E. D. Gugiu, I. Miloucheva, N. Rishe (Eds.), 4-8, International Institute of Informatics and Systemics, Orlando, FL (July 2005)
5. T. ALDEMIR, D. W. MILLER, A. BURGHELEA, "Direct Estimation of Power Distribution in Reactors for Nuclear Thermal Space Propulsion", *Space Technology and Applications International Forum—STAIF 2004*, M. S. El-Genk (Ed.), 582-589, American Institute of Physics, Melville, N.Y. (February 2004).
6. M. BIRO, T. ALDEMIR, "Quantifying the Measurement Uncertainty Propagation In Flux/Power Reconstruction", *Proceedings of NPIC&HMIT 2004*, 1246-1253, American Nuclear Society, LaGrange Park, IL (September 2004)

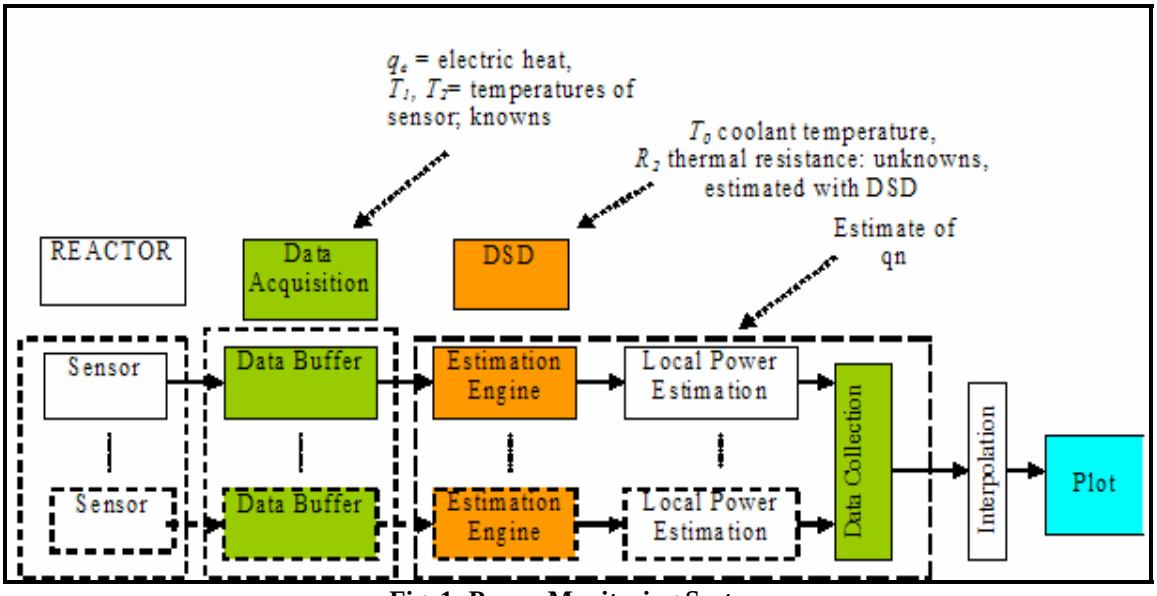

Fig. 1: Power Monitoring System

Trans. Am. Nucl. Soc., 90, 59-61 (June 2004)

A Model Based Probabilistic Scheme for Flux/Power Shape Construction from Monitored Data

Mihaela Biro, Tunc Aldemir*

T*he Ohio State University, Nuclear Engineering Program,*
Bldg 1, Rm 130B, Suite 255, 650 Ackerman Road, Columbus, OH 43202.

*Author to whom correspondence should be addressed

INTRODUCTION

The evolution of flux and power distributions in nuclear reactor cores is usually tracked using diffusion codes. Due to modeling as well as operational uncertainties, it is often necessary to validate/improve the predicted distributions through in-core flux and temperature measurements. A variety of techniques have been developed for this purpose, including using cubic splines to interpolate between measured data [1], fittings based on modal expansions [2,3], artificial neural networks [4] and least-squares fittings [5].

There have been few attempts to directly incorporate the measurement uncertainty into flux/power shape construction process [6, 7]. This paper describes a procedure which approaches the problem in the spirit of [6] and explicitly represents measurement uncertainty through user specified probability distribution functions (pdfs) in the construction process. The difference is that the procedure presented here is a probabilistic interpolation scheme rather than fitting scheme which maximizes the conditional pdf of the estimated flux/power shape given the observations [6]. The proposed procedure is not restricted to linear relationships between flux/power and location [6] and also leads to computational simplicity for a large number of observations. The procedure can be also used with a wide range of approaches to power/flux shape construction, from simple linear interpolation between data points to model based fittings, as well as a variety of pdfs to represent measurement uncertainty. The procedure is illustrated using 1½ group diffusion theory model for a hypothetical one-dimensional reactor.

THE PROCEDURE

Consider a one dimensional reactor with length 2*L* whose steady-state neutronic behavior is described by 1½ group diffusion theory, i.e.

$$\frac{d}{dx}\left[D_1(x)\frac{d\phi_1(x)}{dx}\right]+B^2(x)\phi_1(x)=0$$
$$\Sigma_{1\to2}(x)\phi_1(x)=[\Sigma_{a,2}(x)+\Sigma_b(x)]\phi_2(x) \quad (1)$$
$$B^2(x)=\nu\left[\Sigma_{f,1}(x)+\Sigma_{f,2}(x)\frac{\Sigma_{1\to2}(x)}{\Sigma_{a,2}(x)+\Sigma_b(x)}\right]$$
$$-[\Sigma_{a,1}(x)+\Sigma_{1\to2}(x)] \quad (0\le x\le L)$$

where $\Sigma_b(x)$ indicates the control poison cross section at location *x* and the rest of the symbols have their conventional definitions. We will assume that: 1) group parameters of Eq.(1) are known functions of *x*, 2) the pdfs $p(\phi_1 \mid x_n)=p_n(\phi_1)$ of $\phi_1(x_n)$ at x_n are known for n = 1,…,N on $0\le x\le 2L$, and, 3) expected value

$$<\phi_1(x)>=\int d\phi_1\ \phi_1\ p(\phi_1 \mid x) \quad (2)$$

of $\phi_1(x)$ satisfies Eq.(1). Then it can be shown that

$$\int d\phi_1\ \phi_1\left\{\begin{matrix}\frac{\partial}{\partial x}\left[D(x)\frac{\partial p(\phi_1 \mid x)}{\partial x}\right]+\\ B^2(x)\,p(\phi_1 \mid x)\end{matrix}\right\}=0 \quad (3)$$

which means that a sufficient condition for $p(\phi_1 \mid x)$ to satisfy is

$$\frac{\partial}{\partial x}\left[D(x)\frac{\partial p(\phi_1 \mid x)}{\partial x}\right]+B^2(x)\,p(\phi_1 \mid x)=0 \quad (4)$$

The solution of Eq.(4) with specified $p(\phi_1 \mid x_n)=p_n(\phi_1)$ and $p(\phi_1 \mid x_{n+1})=p_{n+1}(\phi_1)$ yields $\phi_1(x)$ in $x_n<x\le x_{n+1}$ (n = 1,…,N-1). If power is directly measured [8], it can be also shown from Eq.(1)in a similar manner that , for

constant material properties within $x_n < x \le x_{n+1}$,

$$\frac{\partial^2 p(h \mid y)}{\partial y^2} + \beta^2 p(h \mid y) = 0$$

$$\beta^2 = (x_{n+1} - x_n)^2 \frac{B^2}{D_1} \qquad (0 \le y \le 1) \quad (5)$$

$$y = \frac{x_{n+1} - x}{x_{n+1} - x_n}$$

where $p(h \mid y)$ is the pdf of power density h at y. For specified $p(h \mid 0) = p_{n+1}(h)$ and $p(h \mid 1) = p_n(h)$ we get

$$p(h \mid y) = \frac{1}{\sin(\beta)} \begin{bmatrix} p_{n+1}(h) \sin[\beta(1-y)] \\ + p_n(h) \sin(\beta y) \end{bmatrix} \quad (6)$$

or

$$< h(y) >= \frac{1}{\sin(\beta)} \begin{bmatrix} < h(0) > \sin[\beta(1-y)] \\ + < h(1) >= \sin(\beta y) \end{bmatrix} (7)$$

for the expected value $< h(y) >$ of power density at y. For small β (e.g. small interval $[x_{n+1}, x_n]$), Eq.(6) yields

$$p(h \mid y) \approx p_{n+1}(h)(1-y) + p_n(h) y \qquad (8)$$

which is the result from the statistics literature for $< h(y) >$ varying linearly within $0 \le y \le 1$ [11].

Although Eqs.(4) and (5) are in principle partial differential equations, they become ordinary differential equations once the numerical values of the boundary conditions are specified and subsequently can be solved using standard code packages for non-uniform material distributions. It is not difficult to see that equations similar to Eq.(4) can be generated for a multi-group counterpart of Eq.(1). In the multi-group case, energy discriminant sensors need to be used to determine the boundary conditions, such as the SiC detectors developed by Westinghouse [10].

AN EXAMPLE ILLUSTRATION

For the purposes of illustration, we will assume that power density is directly measured in a hypothetical, one dimensional reactor placed in vacuum with uniform material distribution as given in Table 1 and L = 150 cm.

From Eq.(1) and the relationship between power and flux, we have

$$h(x) = h(0) \cos(\beta x) \qquad (0 \le x \le L) \quad (9)$$

For criticality, we must have $\beta \approx \pi / 300\ \text{cm}^{-1}$ (or $\Sigma_b = 0.0707\ \text{cm}^{-1}$ from Eq.(4) and Table 1 data).

Table 1
Group Constants for the Example Reactor [11]

Group Constant	Group	
	1	2
$\nu\Sigma_f$ (cm^{-1})	0.008476	0.18514
Σ_a (cm^{-1})	0.01207	0.1210
D (cm)	1.2627	0.3543
$\Sigma_{1->2}$ (cm^{-1})	0.0141	-

Figure 1 shows: a) the data $h_1, h_2, \cdots h_{10}$ from 10 hypothetical power sensors placed at $0 \le x_1 < x_2 < \cdots x_{10} \le L$, generated from Eq.(9) assuming 1% random error, b) $p(h \mid x)$ obtained from Eqs.(5) and (6) assuming

$$p_n(h) = \frac{1}{0.01\sqrt{2\pi}} \exp\left(-\frac{(h - h_n)^2}{2(0.01)^2} \right), \qquad (10)$$

$$(n = 1, \cdots, 10)$$

and, c) $< h(x) >$ obtained from Eqs.(5) and (7).

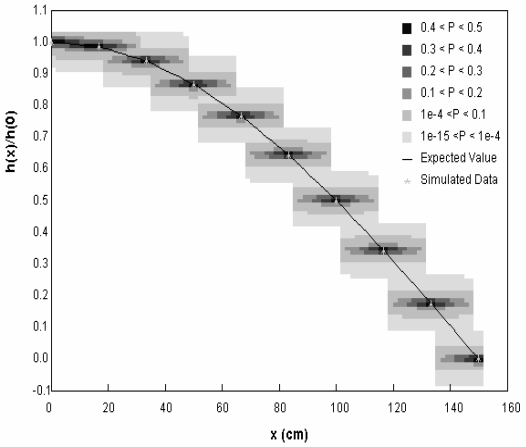

Fig.1: Relative Power Distribution *h(x)/h*(0) for the Example Reactor

Figure 1 indicates that the match between the simulated data and $< h(x) >$ is excellent. Figure 1 also shows how the $p(h \mid y)$ yields the uncertainty ranges for the estimated power between measurement points. The $p(h \mid y)$ can be used to obtain other statistical properties of $h(x)$ as well. For example, the probability that power is within 10% of the expected value can be found from

$$\int_{09<h(y)>}^{1.1<h(y)>} dh\, p(h \mid y) .$$

Similarly, 90% confidence interval for the expected value of power at y can be found from the solution of $p(< h >| y) = 0.9$ for $<h>$.

CONCLUSION

The proposed procedure provides a fast way to estimate the expected value as well as all other statistical properties of power/flux between measurement points. The accuracy of estimation depends on the assumed pdfs at the measurement points and the core model used with the procedure (i.e. Eq.(5))

REFERENCES

1. S. HAN, U. S. KIM, P. H. SEONG "A Methodology for Benefit Assessment of Using In-core Neutron Detector Signals in Core Protection Calculator System (CPCS) for Korea Standard Nuclear Power Plants (KSNPP)", *Annals of Nuclear Energy*, **26**, 471-488 (1999).
2. M. E. Pomerantz, C.R. Calabrese, C. Grant, "Nuclear Reactor Power and Flux Distribution Fitting from a Diffusion Theory Model and Experimental Data", *Annals of Nuclear Energy*, **29,** 1073–1083 (2002).
3. L. Fu, L. Zhengpei, H. Yongming "Harmonics Synthesis Method for Core Flux Distribution Reconstruction", *Progress in Nuclear Energy*, **31**, 369-372 (1997).
4. G.-C. Lee, W-P. Baek, S. H. Chang. "Improved Methodology for Generation of Axial Flux Shapes in Digital Core Protection Systems", *Annals of Nuclear Energy*, **29**, 805–819 (2002).
5. K. Lee, C. H. Kim, "The Least-Squares Method for Three-Dimensional Core Power Distribution Monitoring in Pressurized Water Reactors"**,** *Nucl.Sci.Eng*, **143,** 268 (2003).
6. J. W. Bryson, J. C. Lee, and J. A. Hassberger, "Optimal Flux Map Generation Through Parameter Estimation Techniques", *Nucl.Sci.Eng*, **114**, 238 (1993).
7. R.A. Bonalumi, N.P.Kherani "Rational Mapping (RAM) of In-Core Data", *Nucl.Sci.Eng*, **90**, 47 (1985).
8. T. D. Radcliff, D. W. Miller, A. C. Kauffman,"Constant - Temperature Calorimetry for In-Core Power Measurement", *Nucl. Technol*., **132**, 240-255 (2000).
9. F. H. Bursal, "On Interpolating between Probability Distributions", *Applied Mathematics and Computation*, **77**, 213-244 (1996).
10. F. H. Ruddy, A. R. Dulloo, J. G. Seidel, F. W. Hantz, L. R. Grobmyer, "Nuclear Reactor Power Monitoring Using Silicon Carbide Semiconductor Radiation Detectors", *Nucl. Technol*., **140**, 198-208 (2002).
11. J. J. Duderstadt and L. J. Hamilton, *Nuclear Reactor Analysis*, John Wiley & Sons (1976).

Proc.ISAS-CITSA 2005, II, J. Aguilar, H.-A. Chu, E. D. Gugiu, I. Miloucheva,
N. Rishe (Eds.), 4-8, International Institute of Informatics and Systemics, Orlando, FL (July 2005)

The Development of a Self-Calibrating Power Monitoring System for Nuclear Reactors

Mihaela Biro, Tunc Aldemir
Nuclear Engineering Program, The Ohio State University
Columbus, OH 43202, U.S.A.

ABSTRACT

The constant-temperature power sensor (CTPS) is a feedback-controlled calorimetric instrument capable of direct measurement of nuclear energy deposition. The CTPS simulates a section of the nuclear fuel element. The sensor operation is sensitive to the ambient coolant temperature and contact resistance. A procedure is described which estimates these quantities on-line for an array of sensors and constructs a map of probabilistic core power distribution.

Keywords: nuclear reactors, power distribution, parameter estimation.

1. INTRODUCTION

The constant-temperature power sensor (CTPS) [1] is a feedback-controlled calorimetric instrument capable of direct measurement of nuclear energy deposition. The CTPS simulates a section of the nuclear fuel element. In that respect, is especially suitable for high temperature environments of the planned Generation IV reactors and reactors for nuclear thermal propulsion.

This paper describes a conceptual system for power measurements in the reactor core using such sensors. The monitoring system will process sensor signals from the reactor core in such a manner that probabilistic information, in the form of probability distribution function (pdf) of reactor power density (q_n) is obtained at the sensor location. This signal processing would be in addition and independent of the normal signal processing that is normally performed in a nuclear power plant, and it would be used for informational purposes only, to assist the operator; it would not have any control over the reactor core.

The paper shows how a map of probabilistic core power distribution can be constructed using simulated signals from an array of sensors distributed in a hypothetical reactor core. An estimation algorithm, called DSD (Dynamic System Doctor) [2] is implemented that processes the sensor signals to obtain the power density pdfs at sensor locations.

2. THE MONITORING SYSTEM

The monitoring system will consist of: (a) an array of sensors distributed in the reactor core and associated circuitry, (b) an estimation engine, (c) a module to interpolate the pdf for q_n between sensors locations [3], and, (d) a scheduler to manage data acquisition and multi-thread/distributed processing. All the components of the monitoring system except the interpolation module presented in an earlier publication [3] are described below.

Sensor – The CTPS

The CTPS concept is based on control of the energy balance about a small mass of fissionable material. Figure 1 shows the structure of a CTPS for current electricity generating nuclear power plants. The sensor core (Node 2) is UO_2 pellet. An electrical heating resistance wire surrounds the core. Energy in the sensor core is deposited through nuclear interactions and from resistive dissipation through the wire, while energy is removed through conductive and convective heat transfer to the reactor coolant. A feedback control loop is provided that adjusts the necessary input of electrical energy such that the Node 2 temperature is maintained constant. At steady-state conditions, the energy balance around the core is described by

$$q_n + q_e = (T_2 - T_0)/R_2 \qquad (1)$$

where q_n denotes the nuclear energy deposited (or the reactor power density), q_e is the electrical energy input, R_2 is the thermal resistance between sensor and coolant, T_2 is the temperature of Node 2 and T_0 is the coolant temperature. By measuring q_e and T_2, q_n can be estimated from Eq. (1) above if R_2 and T_0 are known.

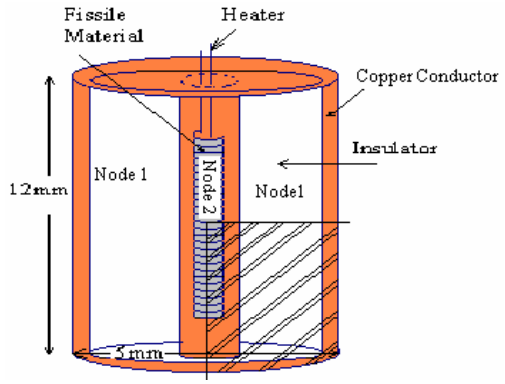

Fig. 1 Constant Temperature Power Sensor

The CTPS has two modes of operation: i) power measurement mode when q_e is measured and q_n is

estimated using Eq.(1), and, ii) calibration mode during which R_2 and T_0 are estimated.

As it can be seen from Eq. (1), an accurate estimation of q_n in the measuring mode depends on the accurate estimation of T_0 and R_2. Coolant temperature T_0 is typically measured at coolant inlet and outlet from the reactor core and it is not measured at each sensor location. The thermal resistance R_2 depends on the coolant temperature, flow speed and local geometry and it is impossible to be measured directly. The calibration mode is designed to provide information on these two variables.

In the calibration mode, the electrical current through the resistive wire that surrounds the sensor core is interrupted. The sensor temperature then decreases to a steady-state value directly dictated by the input of nuclear energy, the coolant temperature and the thermal resistance between the sensor and coolant. T_0 and R_2 are estimated by observing the dynamic behavior of Node 1 and Node 2 temperatures.

The estimation is done through DSD [4,5] which uses a representation of system evolution in time in terms of probability of transitions between sets of magnitude intervals of system state-variables within the user specified time intervals $k\tau \le t \le (k+1)\tau$ $(k=0,1,..)$. These sets form computational cells that partition the system state-space in a similar manner to those used by finite difference and finite element methods. The DSD generates the transition probability $g(j \mid j', \tau)$ from cell j' to j from

$$g(j \mid j', \tau) = \frac{1}{v_{j'}} \int_{j'} d\mathbf{x}' e_j[\tilde{\mathbf{x}}(\mathbf{x}', k\tau)]$$
$$e_j(\mathbf{x}) = \begin{cases} 1 & \text{if } \mathbf{x} \text{ is within } j \\ 0 & \text{otherwise} \end{cases} \quad (2)$$

In Eq.(2), the elements of the vector $\mathbf{x}$ are the state variables, $\tilde{\mathbf{x}}(\mathbf{x}', k\tau)$ denotes the location of the system in the state-space at time $t = (k+1)\tau$ given that it departed from point $\mathbf{x}'$ at time $t = k\tau$ and $v_{j'}$ is the volume of cell j'. The point $\tilde{\mathbf{x}}(\mathbf{x}', k\tau)$ is determined from a user provided system model describing system evolution in time. The DSD determines the joint pdf $p_k(j)$ for the mean value of the state-variables over cell j at time $t = k\tau$ recursively from

$$p_k(j) = \sum_{j'} g(j \mid j', \tau) p_{k-1}(j') \quad (k = 0,1,\cdots). \quad (3)$$

A two node lumped parameter model has been developed for the CTPS [3], representing Node 1 and 2 (see Fig.1) temperature behavior during the calibration mode. By writing the energy conservation equations for the two nodes, the system equations are obtained as [3]:

$$C_1 \frac{dT_2}{dt} = (q_n + q_e) - \frac{1}{R_1}(T_2 - T_1)$$
$$C_2 \frac{dT_1}{dt} = \frac{1}{R_1}(T_2 - T_1) - \frac{1}{R_2}(T_1 - T_0) \quad (4)$$

where T_1 indicates Node 1 temperature; C_1, C_2 are, respectively, thermal capacitance of Nodes 1 and 2; R_1 is the thermal resistance between Node 2 and Node 1. The other notation in Eq.(2) is as defined previously.

Estimation Engine

In Eq.(4) all the variables except R_2, T_0 and q_n are assumed to be known. A flowchart of the estimation engine for these parameters is shown in Fig. 2.

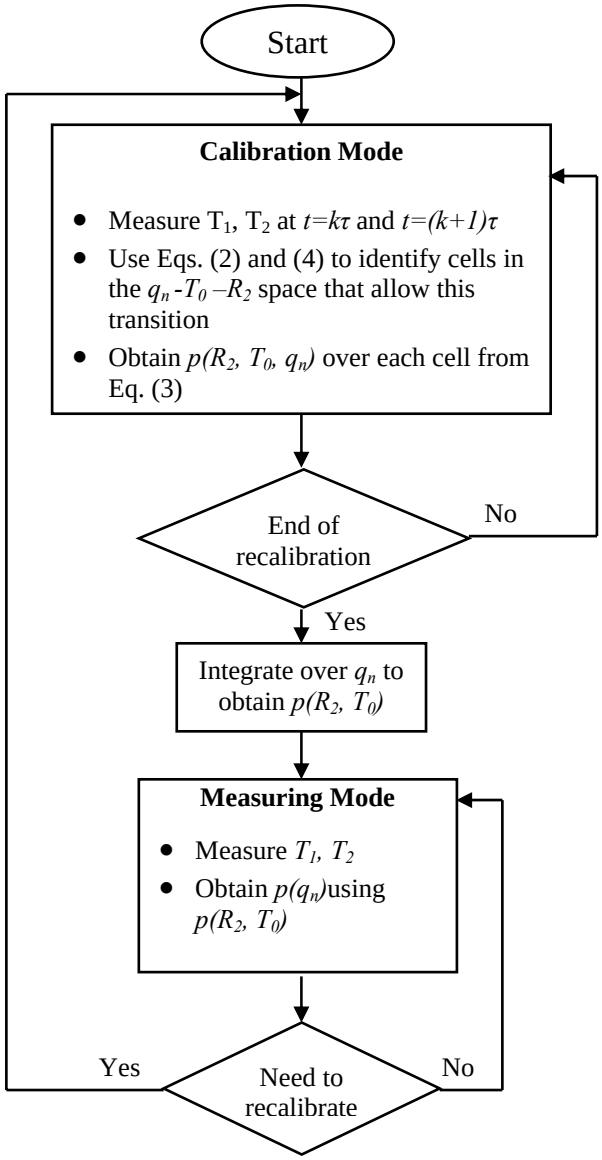

Fig. 2 Estimation engine

In the calibration mode, DSD is run to estimate the values for T_0, R_2 and q_n, in terms of joint pdf $p(R_2,T_0, q_n)$ over the discretized R_2-T_0-q_n space by measuring T_1 and T_2 and using Eqs.(2)-(4). At the end of calibration, $p(R_2,T_0, q_n)$ is integrated over all values of q_n to obtain joint pdf of $p(R_2,T_0)$.

Before the actual algorithm is started, the following are defined for each of the three unknown parameters (R_2, T_0, q_n): a) the ranges of interest (minimum and maximum values $R_{2,min}$, $R_{2,max}$, $T_{0,min}$, $T_{0,max}$, $q_{n,min}$, $q_{n,max}$), b) the number of intervals for each range that will discretize the q_n-T_0-R_2 space into cells, and, c) error σ for the temperature measurements T_1 and T_2. A three dimensional matrix which represents the cells in terms of cell-centered values of R_2, T_0, q_n and which will store $p_k(j)$ (see Eq.(3)) is created and initialized to a uniform distribution $p_0(j)$ (Figure 3(a)).

At t = 0, the sensor starts in the calibration mode trying to estimate the values for T_0, R_2, q_n. Values of T_1, T_2 and q_e for $t=0$ and $t=1$ seconds are read from an input file that simulates the actual sensor signals. Since CTPS is in the calibration mode, q_e = 0 in Eq.(4). Using the simulated $T_1(0)$, $T_2(0)$, $T_1(1)$ and $T_2(1)$, the DSD then searches for the cells that would make this transition possible within the error σ for the temperature measurements from Eqs.(2) - (4) using an equal-weight 4-point quadratures scheme to evaluate the integral in Eq.(2).

The algorithm continues for t = 2, 3... 6 seconds. The temperature signals are read again, the cell—to-cell transition probabilities are recomputed from Eq.(2) based on the current time step and used for recalculating the cell-averaged values of p_k (R_2, T_0, q_n) from Eq.(3) for k=2, 3…6. After each time step the probabilities are rescaled such that they sum to unity over all cells. After 6 seconds, the sensor is switched back to the measurement mode.

At the end of calibration mode, cell-averaged values of $p(R_2, T_0, q_n)$ for each cell j in the q_n-T_0-R_2 space are obtained in the form of $p_6(j)$ from Eq.(3). Integration of $p(R_2, T_0, q_n)$ over q_n yields the joint pdf for R_2 and T_0.

Using this probability distribution function of R_2 and T_0 obtained at the end of the calibration mode, a probability distribution function of q_n can be obtained. By using the minimum and maximum values for R_2 and T_0 in a cell of nonzero probability P, the cell minimum and maximum values for q_n ($q_{n,min}$ and $q_{n,max}$) can be obtained from Eq. (1). It results that q_n is in interval ($q_{n,min}$, $q_{n,max}$) with a probability P. Repeating the calculation for all cells in the R_2 - T_0 space, a pdf of q_n is derived.

Fig.3 shows graphically how this estimation engine works in the discretized q_n-T_0-R_2 space. Fig. 3(a) shows the initial q_n-T_0-R_2 space, where all cells have assigned equal nonzero probabilities (i.e. $p_0(j)$). Then using Eqs.(2) – (4) at successive time steps, the number of cells that have nonzero probabilities narrows down (Fig. 3(b) and Fig. 3(c)).

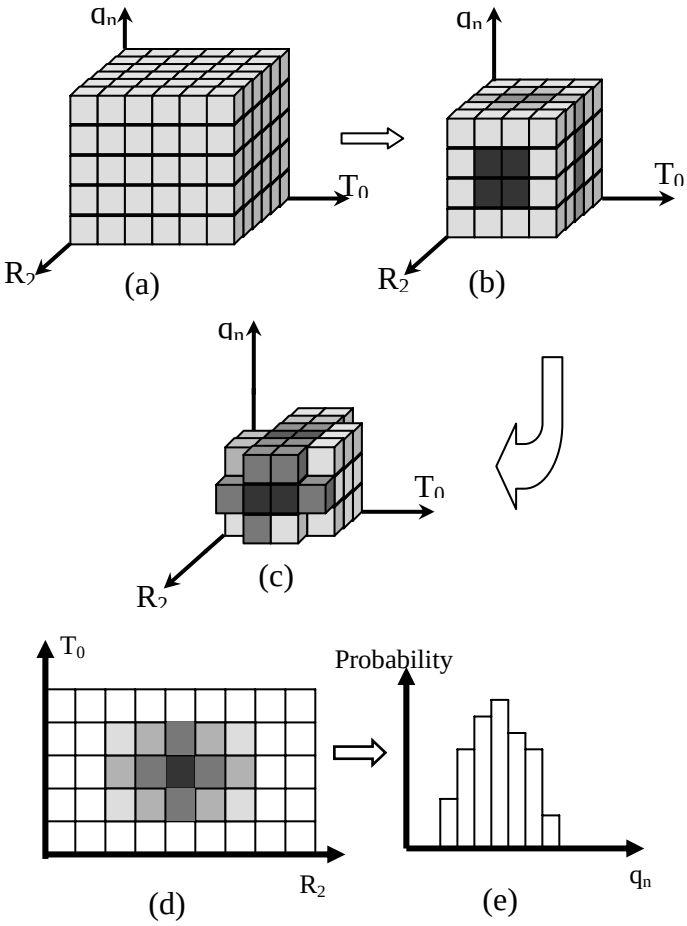

Fig. 3 A graphical illustration of the estimation engine

The different shades of gray represent different probabilities, darker gray represent higher probability than lighter gray. Figure 3(d) shows the probability distribution function of R_2 and T_0 that is obtained at the end of calibration mode and which is used for obtaining the pdf $p(q_n)$ in the measuring mode (Fig. 3(e)).

Scheduler

The estimation engine has been implemented in Java, taking advantage of the modularization capabilities of object-oriented programming. A thread class, running the estimation engine was created. The purpose of the scheduler is synchronize the threads such that data for all sensors at same moment in time can be collected, put together, analyzed and interpolated. Figure 4 shows the conceptual scheduler structure as it would be implemented in a plant. The pdf for q_n between sensor locations (local power estimation) will be estimated using the procedure described in [3].

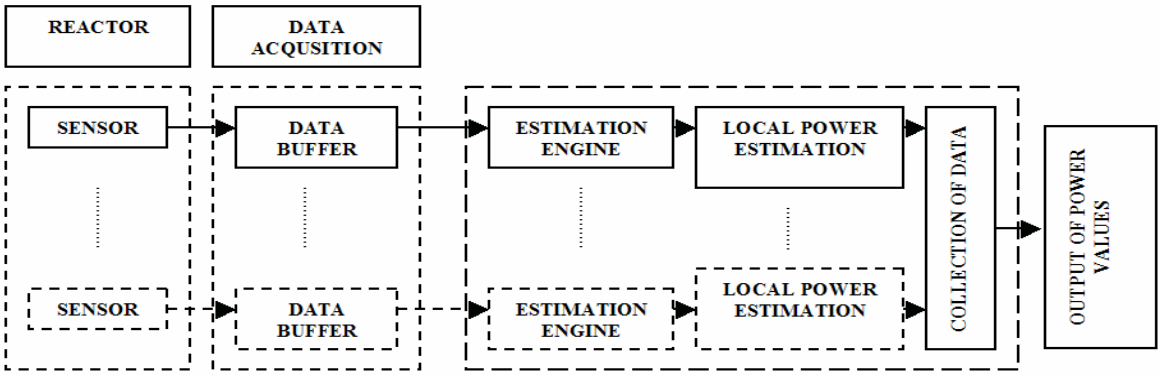

Fig.4 The conceptual scheduler structure

3. EXAMPLE SYSTEM AND RESULTS

Since real sensor data cannot be obtained at this point of the research, a simulation of sensors signals was performed. It was assumed that seven sensors are axially distributed within the core of a pebble bed type reactor [6]. The power/flux is assumed to follow a cosine function axially. The coolant temperature increases continuously from the inlet to the outlet. Data for steady-state power conditions were taken from [6] and are shown in Table 1. The sensors locations and normal power densities and coolant temperatures are shown in Table 1.

Sensor #	Distance from Coolant Inlet (cm)	Deposited Nuclear Energy q_n (W)	Coolant Temperature (K)
1	5	3.09	455
2	10	4.63	610
3	20	6.07	1208
4	30	6.56	1560
5	40	6.07	2085
6	50	4.68	2503
7	55	3.14	2950

Table 1 Simulated data for the example system

From steady-state conditions, it is assumed that a cooling transient occurs in which the coolant temperature start decreasing, while the power density q_n and the thermal resistance R_2 remain constant. The coolant temperature follows

$$T_0(t) = T_0(0)\, e^{-(t-10)/3600} \qquad (5)$$

where the time t is given in seconds [6].

The sensor recalibration is performed every minute, for a six seconds time interval. During these six seconds $q_e = 0$. Since the thermal energy input to the sensor core consists only of the nuclear heat, decay in the sensor temperature will be observed. After the decay, the electric current is switched on again, the sensor temperature increases back to its setpoint value (which is indicated in the last column of Table 1).

The estimation engine was run with 7 parallel threads, each thread handling one sensor. Because of the relatively long computation times, a parallel implementation on multiple processors of the estimation algorithm was also created, this time using C++ and MPI. It was observed that reasonable computation times were achieved when the estimation algorithm it is run on more than two processors.

The results in terms of pdfs of q_n are shown in Fig. 6 and 7. Figure 6 shows a sample pdf for all sensors at a given moment in time. Fig. 7 shows the pdf for Sensor 1 at different moments in time. Both figures represent results for a transient in which the nuclear energy remains constant, while the coolant temperature decreases. In both cases, it can be seen that the probability distribution functions are centered around the expected value for q_n (listed in column 3 of Table 1). In Figure 6, it can be seen that since q_n at detector locations do not vary with time, neither do the pdf's.

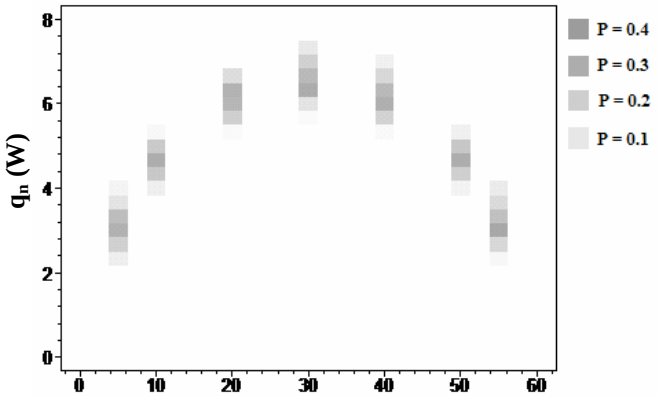

Fig. 5 Pdf of power density at all sensor locations, at $t=7$ seconds

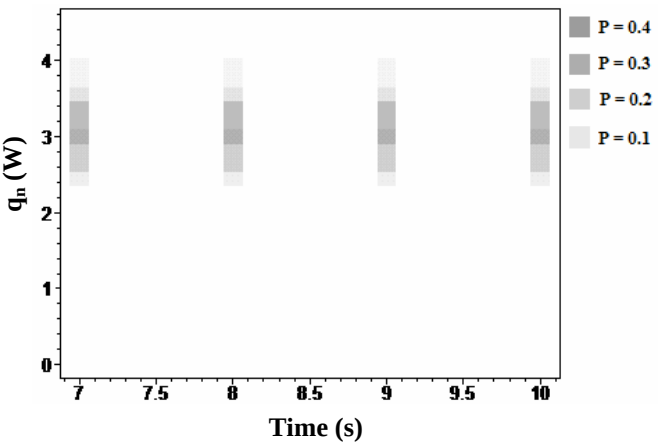

Fig 6 Evolution in time of pdf of power density for Sensor #1

4. CONCLUSIONS

This study illustrates how the CTPS can be used with DSD for an array of sensors to construct a probabilistic map of power distribution in a nuclear reactor. The study also extends the work reported in [6] from the estimation of R_2 and T_0 to the estimation of q_n as well as R_2 and T_0 using Eq.(2). The results of the study indicate that the estimation engine described in Fig.2 can be implemented in a computationally feasible manner to obtain probabilistic maps of power distribution in nuclear reactor under steady-state operation as well as transients.

5. REFERENCES

[1] T. D. Radcliff, S. Liu, D. Miller, "Modeling and Optimization of a Constant-Temperature In-Core Power Sensor", **Nuclear Technology**, Vol. 140, 2002, pp. 209-221.

[2] P. Wang, X. M. Chen, T. Aldemir, "DSD: A Generic Software Package For Model-based Fault Diagnosis in Dynamic Systems", **Reliab. Engng & System Safety**, Vol. 75, January 2002, pp. 1-39.

[3] M. Biro, T. Aldemir, "Quantifying the Measurement Uncertainty Propagation In Flux/Power Reconstruction", **Proceedings of NPIC&HMIT 2004**, pp. 1246-1253, American Nuclear Society, LaGrange Park, IL (September 2004)

[4] I. Munteanu, H.B. Zhou, T. D. Radcliff, T. Aldemir, D. W. Miller, "In-Core Power Detection Using DSD", **Trans. Am. Nucl. Soc**., Vol. 83, November 2000, pp. 279-281.

[5] A. Burghelea, T. Aldemir "A Parametric Investigation of the Recursive Partitioning Approach to DSD for Implementation with CTPS", **Trans. Am. Nucl. Soc.**, Vol. 89**,** November 2003, pp. 493-495.

[6] T. Aldemir, D. W, Miller, A. Burghelea, "Direct Estimation of Power Distribution in Reactors for Nuclear Thermal Space Propulsion", **Space Technology and Applications International Forum—STAIF 2004**, M. S. El-Genk (Ed.), pp. 582-589, American Institute of Physics, Melville, N.Y. (February 2004)

Probabilistic Safety Assessment and Management: PSAM 7-ESREL'04,
C. Spitzer, U. Schmocker, V. N. Dang (Eds.), 1821-1827, Springer – Verlag,
London, U.K. (June 2004)

An Application of DSD with Recursive Partitioning Scheme to Constant Temperature Power Sensors

Andrei Burghelea and Tunc Aldemir
The Ohio State University, 206 West 18th Avenue,
Columbus, OH 43210, U.S.A.

Abstract

The DSD (Dynamic System Doctor) is system independent, state/parameter estimation software. The DSD is based on the modeling of system evolution in terms of probability of transitions within user specified time intervals between sets of user defined parameter/state variable magnitude intervals that partition the system state space. Recently a recursive partitioning scheme has been developed for DSD that reduces the estimation time and memory requirements, as well as making DSD more user friendly. The scheme is illustrated using a non-linear model for the constant temperature power sensor, proposed for direct core power distribution monitoring in Generation 4 nuclear power reactors

1 Introduction

The DSD (Dynamic System Doctor) is a system independent, state/parameter estimation software [1] based on the cell-to-cell mapping technique (CCMT). The CCMT models the system evolution in terms of probability of transitions in time between sets of user defined parameter/state variable magnitude intervals (cells) within a user specified time interval (e.g. data sampling interval). It yields the lower and upper bounds on the estimated values of system variables/parameters (which may be important in the determination of the operational safety margins for the system), as well as the probability distribution of the variables/parameters within these bounds which provides a probabilistic measure to rank the likelihood of system faults in view of modeling uncertainties and/or signal noise.

The original DSD algorithm requires the cell definitions as input to the estimation process which may lead to long run times and large memory requirements. Recently a recursive scheme for cell definitions was proposed for DSD that reduces the estimation time and memory requirements [2]. This paper illustrates the estimation time and memory savings using a non-linear model for

the constant temperature power sensor (CTPS), proposed for direct core power distribution monitoring in Generation 4 nuclear power reactors [3].

2 Overview of the DSD Algorithm with Recursive Partitioning [2]

The DSD estimation algorithm is based on the representation of the system dynamics in terms of transition probabilities between user specified cells that partition the system parameter/state space during user specified time intervals $k\tau \le t < (k+1)\tau$ (k = 0, 1,…). These cells are obtained by dividing the range of interest $a_l \le x_l \le b_l$ for the state variable $x_l (l = 1,\cdots,L)$ into $j_l = 1,\cdots,J_l$ intervals Δ_{l,j_l} and the range of interest $\tilde{a}_m \le \alpha_m \le \tilde{b}_m$ for the parameter $\alpha_m (m = 1,\cdots,M)$ into $n_m = 1,\cdots,N_m$ intervals $\tilde{\Delta}_{m,n_m}$, in a manner similar to those used in finite difference or finite element methods. Such partitionings are provided as user input to DSD. A sample partitioning for a second order system where only one of the state variables is monitored is shown in [2], as well as how the cell-to-cell transition probability $g(j \mid j',n',\tau)$ from cell j' to cell j during $k\tau \le t < (k+1)\tau$ while the system parameters remain in cell n' can be approximated using a 4-point quadrature scheme. The DSD yields the *a posteriori* probabilities $p_{k+1}(j,n)$ that $x_l[(k+1)\tau] \in \Delta_{l,j_l}$ and $\alpha_m \in \tilde{\Delta}_{m,n_m}$ at $t = (k+1)\tau$ $(j_l = 1,...,J_l; l = 1,...L)$ from

$$p_{k+1}(j,n) = \frac{\sum_{j' \in J_k} g(j \mid j',n',\tau)\, p_k(j',n')}{\sum_{n'} \sum_{j' \in J_k} p_k(j',n')} \quad (j \in J_{k+1})(k = 0,1,...) \qquad (1)$$

using the $p_k(j,n)$ estimated at time $t = k\tau$ as *a priori* probabilities The $p_k(j,n)$ determined from Eq.(1) can then be used to determine all the statistical properties of the system state, such as expected values and credibility intervals of the system variables.

If the values of the system parameters change in time, the estimation procedure may lose track of the variables to be estimated, i.e. all the $p_k(j,n)$ obtained from Eq.(1) will be zero. In the original DSD algorithm with this fixed partitioning scheme (FPS), the estimation process will reinitialize itself in this situation by starting from the initial probability $p_0(j,n)$ and estimate the new parameter by the recursive use of Eq.(1) again by searching over all the cells. This approach may lead to excessive computational time if there are frequent parameter changes during system evolution and a large number of variables/parameters to be estimated. The recursive partitioning scheme (RPS)

reduces the computational time for reinitialization (as well as overall memory requirements for DSD) through following steps:

1. Input parameter and state variable ranges of interest (i.e. $a_l \le x_l \le b_l$ and $\tilde{a}_m \le \alpha_m \le \tilde{b}_m$), RPS stopping rules and monitored data uncertainty. Read data from the monitors.
2. Define the intervals Δ_{l,j_l} for the monitored variables so as to contain the variation/noise on the monitored data, centred on their median values. Define the cells for the unmonitored variables by bisecting each state variable range of interest $a_l \le x_l \le b_l$ and each parameter range of interest $\tilde{a}_m \le \alpha_m \le \tilde{b}_m$ (i.e. $J_l = 2, N_m = 2$ for all l and m to be estimated).
3. Specify $p_0(n, j)$ to be used to start the estimation process (usually uniform)
4. Determine the cell-to-cell transition probabilities $g(j \mid j', n', \tau)$ by quadratures or by sampling over the cells specified in Step 2.
5. Find $p_k(n, j)$ from Eq.(1).
6. If all $p_k(n, j) = 0$, then bisect each Δ_{l,j_l} and go to Step 3. Otherwise, normalize $p_k(n, j)$ by dividing it by the total probability of finding the system in the search space, increment the time index *k* and go to Step 2.

Steps 2 through 6 are repeated until convergence, i.e. $p_k(n, j)$ are all zero except for the cells containing the actual system locations. It should be mentioned at this point that the algorithm may not converge for rapidly evolving systems during one data sampling interval $k\tau \le t < (k+1)\tau$. However, even in this situation, previous work a with reduced order reactor dynamics model shows that the expected values of the parameters/state variables to be estimated are often found to be close to their actual values [4].

3 The CTPS

The CTPS consists of a UO_2 pellet surrounded by an electrical heating resistance wire. The pellet and the wire form the sensor core (Node 2). The core is surrounded by ceramacast, which is an alumina based ceramic thermal insulator (Node 1). Both the sensor core and the insulator are coated with thin layers of copper to provide a pathway for heat transfer from the sensor core to the surrounding coolant. A feedback control loop is used to provide the exact amount of input electrical energy q_e (in kW) needed to keep the temperature T_2 (in K) of the Node 2 constant in time (*t*), well above the surrounding coolant temperature T_0 (in K), regardless of the nuclear energy q_n (in kW) deposited into Node 2 (Mode 1 operation). In Mode 1 operation we have

$$q_e + q_n = \frac{T_2 - T_1}{R_1} = \frac{T_1 - T_0}{R_2} = \frac{T_2 - T_0}{R_1 + R_2} \tag{2}$$

where T_1 is the temperature of the ceramacast insulator, R_1 (in K/kW) is the contact resistance between Node 1 and Node 2 and R_2 (in K/kW) is the contact resistance between Node 1 and the coolant.

A mode-switching algorithm has been proposed to accomplish the compensation of the change in the sensor response with the change in R_2 as a function of T_0 and other coolant properties. In Mode 2 operation, the sensor is temporarily taken out of the control loop, or practically, the supplied electrical current is reduced to 1% of the steady state value. In this mode of operation, the time rates of change in Node 1 and Node 2 temperatures are described by

$$C_1 \frac{dT_2}{dt} = (q_n + q_e) - \frac{1}{R_1}(T_2 - T_1)$$

$$C_2 \frac{dT_1}{dt} = \frac{1}{R_1}(T_2 - T_1) - \frac{1}{R_2}(T_1 - T_0) \qquad (3)$$

where C_i is the thermal capacitance (in KJ/K) of Node i (i=1,2). For constant q_n, q_e, C_i and R_i, Eq.(3) yields

$$T_i(t) = T_0 + \theta_{1i} e^{-\theta_2 t} + \theta_{3i} e^{-\theta_4 t} \quad (i = 1,2) \qquad (4)$$

where θ_{1i} and θ_{3i} are known functions of q_n, q_e, sensor properties and Mode 1 sensor temperatures,

$$\theta_2 = \frac{1}{2}\left[\gamma + \sqrt{\gamma^2 - 4}\right] \qquad \theta_4 = \frac{1}{2}\left[\gamma - \sqrt{\gamma^2 - 4}\right] \qquad (5)$$

with

$$\gamma = \frac{1}{C_1 R_1} + \frac{1}{C_2 R_2} + \frac{1}{C_2 R_1}. \qquad (6)$$

The resistance R_1 and the capacitances C_1 and C_2 is a function of the sensor properties only and can be determined off-line. Then the nuclear energy deposition rate q_n and the resistance R_2 can be estimated directly through Eq.(3) and measured $T_i(t)$ (i =1 and/or 2) and q_e or, for constant sensor properties, through Eqs.(4), (5) (6) and the measured $T_i(t)$ and q_e. The sensor operation

involves switching between the feedback-controlled constant-temperature mode (i.e. Mode 1) and the dynamic temperature decay mode following the opening of the feedback loop (i.e. Mode 2).

4 Implementation and Results

Two cases were considered, one of normal operation with a switch between the operation modes of the sensor with constant coolant temperature T_0 (Case 1), and a second one, a slow transient with decreasing T_0 (Case 2). Node 1 and 2 temperatures for the estimation process were simulated using Eq.(3) with the parameter values given in Table 1.

T_0(K)	T_2(K)	C_1(J/K)	C_1(J/K)	R_1(K/W)	R_2(K/W)	q_n(W)	q_e(W)
1000.0	1085.9	0.00804	0.744	5.709	1.857	1.68	9.67

Table 1. Steady-State Parameter Values Used for the Generation of Simulated CTPS Data

The choice of the temperature data in Table 1 reflects the expected steady-state operational conditions in Generation 4 gas cooled reactors.

Figures 1 and 2, respectively, show the estimation results for Case 1 and Case 2 using RPS. The spikes starting at around t=10 s in both Figs.2 and 3 at around indicate the time at which the initial switch from Mode 1 to Mode 2 is made. The figures show that while DSD temporarily looses track of q_n at the time of the switch, recovery is very rapid and DSD with the RPS is able to estimate q_n with the desired accuracy (within 1% of the range of interest) for the rest of the time interval of interest (i.e. until 100 s). Comparison of the run times and memory requirements to obtain the results in Figs.2-4 to those obtained using the original FPS for comparable accuracy indicates a speedup by a factor of 5 in the run time with RPS and a reduction by a factor of 2 in memory requirements.

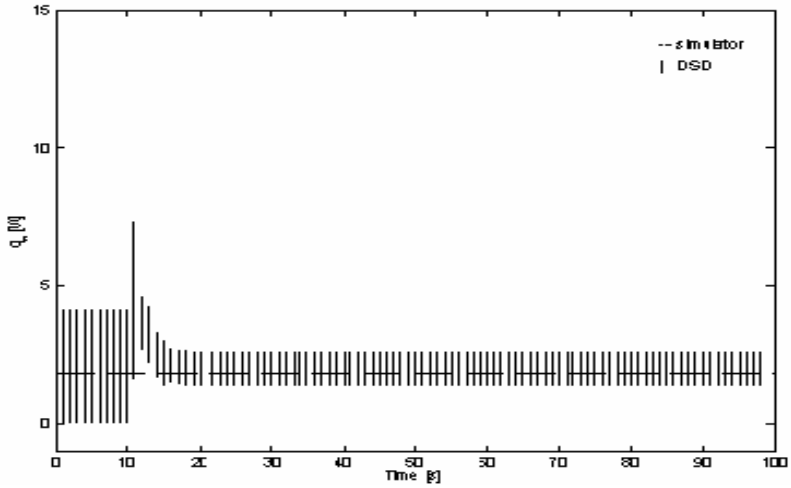

Figure 1. Simulated and Estimated q_n as a Function of Time for Case 1

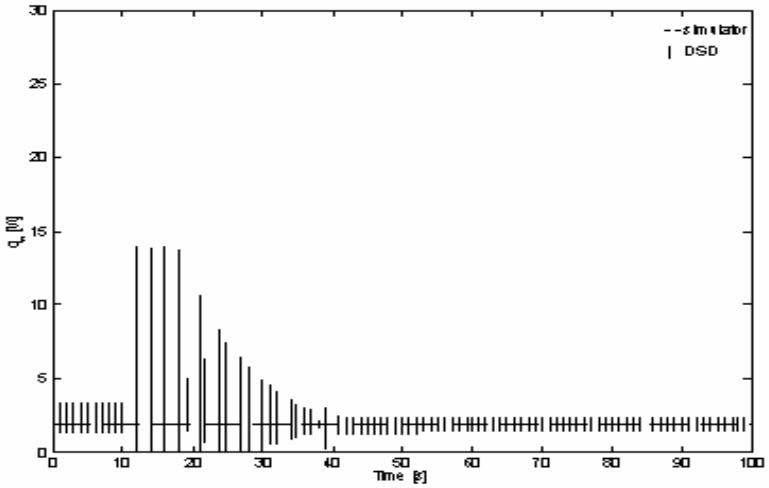

Figure 2. Simulated and Estimated q_n as a Function of Time for Case 2

5 Conclusion

The results of this study show that the DSD with RPS leads to substantial run time and memory savings compared to the original FPS. The results of the study also show that the use of CTPS with DSD may be a feasible option for direct measurement of power distribution in Generation 4 reactors.

References

1. Wang P, Chen X-M, Aldemir T. DSD: a generic software package for model-based fault diagnosis in dynamic systems. Reliab Engn & System Safety 2002; 28, 31-39
2. Burghelea A, Munteanu I, Aldemir T. A Recursive Partitioning Approach to DSD”**,** *PSA2002:* Proceedings of the International Topical Meeting on Probabilistic Safety Assessment, Apostolakis G E, Aldemir T (Eds), 630-635, American Nuclear Society, La Grange Park, IL , 2002
3. Radcliff TD, Miller DW, Kauffman AC. Modeling of A Constant-Temperature Power Sensor. In: ICONE-8, Proceedings of 8th International Conference on Nuclear Engineering. American Society of Mechanical Engineers, New York, 2000
4. Wang P. Some improvements in state/parameter estimation using the cell to-cell mapping technique. Ph.D. thesis, The Ohio State University, 2002

NUCLEAR SCIENCE AND ENGINEERING: **147**, 1–25 (2004)

Some Improvements in State/Parameter Estimation Using the Cell-to-Cell Mapping Technique

Peng Wang and Tunc Aldemir*

The Ohio State University
206 West 18th Avenue
Columbus, Ohio 43210

Received May 6, 2002
Accepted November 3, 2003

Abstract—*The cell-to-cell-mapping technique (CCMT) models system evolution in terms of probability of transitions within a user-specified time interval (e.g., data-sampling interval) between sets of user-defined parameter/state variable magnitude intervals (cells). The cell-to-cell transition probabilities are obtained from the given linear or nonlinear plant model. In conjunction with monitored data and the plant model, the Dynamic System Doctor (DSD) software package uses the CCMT to determine the probability of finding the unmonitored parameter/state variables in a given cell at a given time recursively from a Markov chain. The most important feature of the methodology with regard to model-based fault diagnosis is that it can automatically account for uncertainties in the monitored system state, inputs, and modeling uncertainties through the appropriate choice of the cells, as well as providing a probabilistic measure to rank the likelihood of faults in view of these uncertainties. Such a ranking is particularly important for risk-informed regulation and risk monitoring of nuclear power plants. The DSD estimation algorithm is based on the assumptions that (a) the measurement noise is uniformly distributed and (b) the measured variables are part of the state variable vector. A new theoretical basis is presented for CCMT-based state/parameter estimation that waives these assumptions using a Bayesian interpretation of the approach and expands the applicability range of DSD, as well as providing a link to the conventional state/parameter estimation schemes. The resulting improvements are illustrated using a point reactor xenon evolution model in the presence of thermal feedback and compared to the previous DSD algorithm. The results of the study show that the new theoretical basis (a) increases the applicability of methodology to arbitrary observers and arbitrary noise distributions in the monitored data, as well as to arbitrary uncertainties in the model parameters; (b) leads to improvements in the estimation speed and accuracy; and (c) allows the estimator to be used for noise reduction in the monitored data. The connection between DSD and conventional state/parameter estimation schemes is shown and illustrated for the least-squares estimator, maximum likelihood estimator, and Kalman filter using a recently proposed scheme for directly measuring local power density in nuclear reactor cores.*

I. INTRODUCTION

State/parameter estimation techniques play an important role in dynamic system analysis for fault detection, system identification, and adaptive control. Although parameter estimation in linear systems is by now a well-established field, nonlinear system parameter estimation is still a popular research area.

Among the large number of conventional parameter estimation techniques used for nonlinear dynamic systems, the largest category is based on optimizing the value of the estimates by minimizing a predefined objective function or loss function (i.e., least squares, weighted least square, minimum mean square error). These techniques usually involve solving a linear or nonlinear minimization problem with or without constrains. Closed-form solution of the nonlinear minimization problem is often not available, and numerical methods (e.g., dynamic programming, discrete Euler-Lagrange equations, the

*E-mail: aldemir.1@osu.edu

Gauss-Newton method) have been proposed and widely used in parameter estimation. Mook[1] considers the optimal state and parameter estimation under model error for nonlinear dynamic systems. The unknown parameters are estimated using the least-squares method by minimizing the model error estimate. The minimization problem is solved as a two-point boundary-value problem. The method is shown to be accurate and robust with respect to large errors in system model and measured data, but the model error estimate may contain discontinuities in case of noisy measurement. In Albuquerque and Biegler's[2] paper, the objective function is defined as the sum of a set of functions that depend on the states and inputs at one time, and the constrains are differential equations. A nonlinear dynamic programming (NLP) problem is defined by discretizing the differential equations. Even though the paper presents a faster solver for the NLP problem, the major limitation of this approach is that the size of the NLP problems grows linearly with the number of data sets and the heavy computational load makes it difficult to solve larger problems directly. Guay and McLean[3] present a method for estimation of parameters in nonlinear dynamic systems described by a set of ordinary differential equations by optimization of the Box and Draper (or least-squares) criterion. The decoupled direct method is applied to evaluate the gradient and Hessian matrix of the objective function with respect to the parameters. The authors state that using second-order sensitivity coefficients to evaluate the Hessian matrix can lead to more accurate and reliable results. However, the computation of higher-order sensitivity coefficients increases drastically the computational time and storage. The computational load and storage are also the major problem associated with Hjelmstad's method[4] in order to obtain acceptable accuracy. Another least-squares method, developed by Liu,[5] includes a fast adaptive least-squares algorithm for parameter estimation that is based on Householder transformations. The author indicates that this algorithm requires computation and storage load in the order of $O(N)$ instead of $O(N^2)$, where N is the number of parameters to be estimated. One limitation of this algorithm is that it requires the system to be linear with respect to the unknown parameters. In addition, the estimated parameters may not converge to the true value in case of correlated noise. Dimogianopoulos and Lozano[6] propose a least-squares–based nonrecursive identification algorithm in their paper. The authors chose the L_2 norm of the identification error with a forgetting factor as the minimization criterion. This technique is capable of dealing with slowly time-varying parameters without explicit knowledge of the noise bound or the region where the true parameters lie. However, the bounds on the noise and the parameter variations should be small to obtain meaningful properties of the estimates.

Another widely used technique in parameter estimation problems is to use linearized system models about an operating point. Hopkins and Van Landingham[7,8] propose a method of simultaneous parameter and state estimation called pseudolinear identification (PLID) for stochastic linear time-invariant discrete-time systems with single input single output[7] and multiple inputs multiple outputs.[8] The authors state that the PLID is known to converge, but in the presence of a large amount of noise, this convergence may be practically impossible or so slow as to be useless. Douce and Zhu[9] describe a method for the modeling of nonlinear single-input single-output systems using a modified least-squares method. The application of this method requires that the nonlinear systems be perturbed only in a restricted operating range and the system can be linearized inside this operating range. An autoregressive moving average model is used in order to approximate a wide range of nonlinear systems. A weighted least-squares algorithm for parameter estimation is proposed in order to handle the nonlinearity of the dynamic system. Recently, Lyashevskiy and Chen[10] have developed an innovative identification procedure by applying the harmonic linearization method. Using this technique, the nonlinearity of the system is replaced by a set of harmonic linearized elements, which is obtained through the describing function method. The unknown parameters are solved from a set of algebraic equations that are obtained from the self-oscillations. One limitation of this technique is that it can be applied only for dynamic systems with limit cycles.

A technique that can perform parameter estimation and also deal with unobservable states and variables in nonlinear dynamic systems is to generate observers. Ricardo and Tomei[11] demonstrate adaptive observers that guarantee fast exponential convergence. However, the method is only applicable for a class of nonlinear dynamic systems that are linear with respect to unknown parameters, and the construction of the observers requires the system to be in adaptive observer form. Sliding-mode control and estimation techniques have also been shown to be an effective tool in parameter/state estimation problems. The sliding-mode approach to state/parameter estimation in nonlinear dynamic systems consists of designing the model with discontinuous parameters and enforcing sliding modes such that the model and plant outputs coincide. Then, the average values of the discontinuous parameters depend on the unknown states/parameters and can be used for their evaluation. McCann and Islam[12] have applied the sliding-mode observer method to the operation of a switched reluctance motor to estimate the rotor position and velocity. Sliding-mode observers have also been used in nuclear reactivity and xenon concentration estimation problems by Wang, Aldemir, and Utkin.[13] Kim, Rizzoni, and Utkin[14] apply the sliding-mode estimation idea to an automotive engine diagnosis and control problem. The unknown charge efficiency, mean mass flow rate of air, and throttle angle are estimated through a well-designed sliding-mode observer. The results show that

the observer estimates the actual states within reasonable accuracy.

Statistical parameter estimation methods are also used in dynamic system analysis. The advantage of statistical methods is that these methods deal with uncertainty and noise directly. One commonly used statistical parameter estimation technique is Bayesian estimation. Bolviken et al.[15] use Bayesian state estimation in nonlinear systems. The unknown state vectors are drawn many times from the posterior distribution, and the average is used to be the approximate of the posterior mean. The authors apply the Monte Carlo technique to randomly select points in the range of interest and argue that the Monte Carlo uncertainty is small compared to the inherent uncertainty in the optimal Bayesian estimate. A limitation of this technique is that it gives only sample points of the posterior distribution; the actual posterior distribution is unavailable. Charalambous and Logothetis[16] apply the maximum-likelihood idea to the nonlinear stochastic system parameter estimation problems. The expectation maximization algorithm, an interactive numerical method, is used to generate the parameter estimates by computing the log-likelihood ratio restricted to the measured data. However, the technique is still a point estimator without providing an efficient way to evaluate the uncertainty of the estimation results. Also, the estimation algorithm is system specific and needs to be individually set up for a given system.

Expert systems, neural networks and genetic algorithms have been also used for parameter estimation. Parlos and Atiya[17] use artificial neural networks for the identification of a nonlinear model for a U-tube steam generator. The system identification consists of estimating unknown parameters and/or system variables, which cannot be monitored, in order to obtain a complete model for the system. A similar work by Patton, Lopez-Toribio, and Uppal[18] uses artificial intelligence techniques for fault detection and identification in process systems. Marseguerra and Zio[19] apply a genetic algorithm for estimating the effective nuclear parameters and the initial conditions in tracking xenon evolution using measured power and reactivity. The authors state that the estimation results given by this approach are very close to the true values.

The literature survey shows that the parameter/state estimation of nonlinear systems seems to have the following difficulties:

1. Heavy computational load and large computer memory are required if accurate estimates of the parameters are desired. This requirement usually reduces the capability of most methods for on-line implementation.

2. Noise is difficult to handle, especially when the noise is large.

3. Most methods cannot account for random variations in the parameters.

4. Most estimators are point estimators without providing likelihood of possible parameter values, which renders their implementation difficult for probabilistic risk analysis.

5. Often, the algorithms are system specific and need to be designed for the given system.

The recent developments in state/parameter estimation show that the representation of system dynamics via the cell-to-cell mapping technique[20] (CCMT) may reduce these difficulties. The CCMT models the system evolution in terms of probability of transitions in time between sets of user-defined parameter/state variable magnitude intervals (cells) within a user-specified time interval (e.g., data-sampling interval). The cell-to-cell transition probabilities are obtained from the given system model. Then, using the Chapman-Kolmogorov equation, the probability of finding the system in a given cell at a given time interval is recursively determined from a Markov chain. The most important feature of the methodology with regard to model-based fault diagnosis is that it can automatically account for uncertainties in the monitored system state, inputs, and modeling uncertainties through the appropriate choice of the cells, as well as providing a probabilistic measure to rank the likelihood of faults in view of these uncertainties. Such a ranking is particularly important for risk-informed regulation and risk monitoring of nuclear power plants. Other important features of this methodology are as follows:

1. It does not require a linearization of the system.

2. It allows flexibility in system representation. Differential or difference equations[21,22] as well as almost any type of input/output model (e.g., neural net,[23] response surface) can be used to generate the cell-to-cell transition probabilities.

3. The discrete-time nature of the methodology is directly compatible with a lookup table implementation, which is very convenient for the use of data that may be available from tests or actual incidents.

4. It does not require model inversion (which may lead to singularity problems) or inverse models (which usually have a limited range of applicability).

5. It is both an interval and a point estimator. Subsequently, it yields the lower and upper bounds on the estimated values of state variables/parameters as well as their expected values. A knowledge of such bounds is particularly important in the determination of safety margins during operation.

The Dynamic System Doctor[24] (DSD) software package has been developed for the on-line implementation of this methodology in a system-independent and user-transparent manner. The software has been successfully

tested on a variety of nuclear and mechanical dynamic systems.[20–22] An interactive demonstration version of DSD is available from the internet.[25]

The DSD estimation algorithm is based on the assumptions that the measurement noise is uniformly distributed and the measured variables are among the state variables. From an implementation viewpoint, this assumption implies that arbitrary observers and measurement noise or model uncertainties with arbitrary distributions are not allowed. This paper presents a new theoretical basis for the DSD algorithm that waives these assumptions using a Bayesian interpretation of CCMT-based state/parameter estimation (Sec. II). The new theoretical basis expands the applicability range of DSD and leads to improvements in the estimation algorithm (Sec. III), as well as providing a better understanding of the relationship of CCMT-based state/parameter estimation to conventional state/parameter estimation techniques (Sec. IV) and of the origins of some unexplained phenomena encountered in previous work (Sec. II.B). Section V gives the conclusions of the study.

II. A NEW THEORETICAL BASIS FOR CCMT-BASED STATE/PARAMETER ESTIMATION

The new theoretical basis is developed in two steps. In Sec. II.A, a continuous Bayesian state/parameter estimator is presented for an arbitrary dynamical system. Section II.B applies this Bayesian estimator to a discretized representation of the system used by CCMT and develops a generalized algorithm applicable to arbitrary stochastic variations in the dynamical system variables and parameters. Section II.B also shows that this generalized algorithm reduces to the previous DSD algorithm under the assumptions that the measured variables are part of the state variable vector and the measurement noise is uniformly distributed.

II.A. A Continuous Bayesian Estimator

Consider the dynamic system

$$\dot{\boldsymbol{x}} = \boldsymbol{f}(\boldsymbol{x}) + \boldsymbol{v}$$

and

$$\boldsymbol{y}_k = \boldsymbol{h}(\boldsymbol{x}_k) + \boldsymbol{w}_k \quad (k = 0,1,2,\ldots) \ , \tag{1}$$

where

$\boldsymbol{x}$ = L-dimensional vector whose elements are the state variables $x_l (l = 1,\ldots,L)$ of the dynamic system

$\boldsymbol{v}$ = system noise (e.g., due to stochastic variation of system parameters) or a measure of modeling uncertainties, in general

$\boldsymbol{x}_k$ = state vector at time step $k\tau$ $(k = 0,1,2,\ldots)$

$\boldsymbol{y}_k$ = M-dimensional vector whose elements $y_{m,k}$ $(m = 1,2,\ldots,M)$ are the measured data at time step $k\tau$ $(k = 0,1,2,\ldots)$

$\boldsymbol{w}_k$ = measurement uncertainty

$\boldsymbol{h}$ = M-dimensional vector whose elements are known nonlinear functions

$\boldsymbol{f}$ = L-dimensional vector whose elements are known nonlinear functions.

Equation (1) does not exclude parameter estimation problems because we can always define an unknown set of constant parameters $\boldsymbol{\theta}$ as a set of state variables that satisfy the equation

$$\dot{\boldsymbol{\theta}} = 0 \ . \tag{2}$$

Similarly, systems whose dynamics explicitly depend on time can be described by Eq. (1) by regarding time as another state variable satisfying

$$\dot{t} = 1 \ . \tag{3}$$

Subsequently, Eqs. (1) and (2) allow system parameters that are functions of time. Then, by defining the following new state variables:

$$\boldsymbol{z} = \begin{bmatrix} \boldsymbol{x} \\ \boldsymbol{\theta} \end{bmatrix} \ , \tag{4}$$

the new dynamic system can be described as

$$\dot{\boldsymbol{z}} = \begin{bmatrix} \dot{\boldsymbol{x}} \\ \dot{\boldsymbol{\theta}} \end{bmatrix} = \begin{bmatrix} \boldsymbol{f}(\boldsymbol{x}) + \boldsymbol{v} \\ \boldsymbol{0} \end{bmatrix}$$

and

$$\boldsymbol{y}_k = \boldsymbol{h}(\boldsymbol{C}\boldsymbol{z}_k) + \boldsymbol{w}_k \quad (k = 0,1,2\ldots) \ , \tag{5}$$

where $\boldsymbol{C}$ is a matrix with $\boldsymbol{C} = [\boldsymbol{I} \quad \boldsymbol{0}]$ and $\boldsymbol{I}$ is the $L \times L$ identity matrix.

Let $\boldsymbol{x}_k$ denote the state variable value at time step $t = k\tau$. The estimation problem is stated as the following:

> Given an initial guess $p(\boldsymbol{x}_0|\boldsymbol{y}_0)$ of the probability distribution function (pdf) of the unknown state variable vector $\boldsymbol{x}_0$ at time $t = 0$, estimate the conditional distribution $p(\boldsymbol{x}_k|\boldsymbol{y}_k,\boldsymbol{y}_{k-1},\ldots,\boldsymbol{y}_0) = p(\boldsymbol{x}_k|\bar{\boldsymbol{y}}_k)$ of $\boldsymbol{x}_k$ given the measurements $\boldsymbol{y}_k$ from time step $t = 0$ until time step $t = k\tau$. The $\bar{\boldsymbol{y}}_k = [\boldsymbol{y}_k\boldsymbol{y}_{k-1}\ldots\boldsymbol{y}_0]$ is called the information vector that includes all the measurements from the initial time step until time step $t = k\tau$.

While the main motivation for this problem statement is to lay the groundwork for a more generalized theoretical basis for DSD that will be developed in Sec. II.B, the problem statement also addresses the issue of signal validation as will be illustrated later in this section.

Proposition 1:

Assume

1. $p(\boldsymbol{y}_{k+1}|\boldsymbol{x}_{k+1})$ and $p(\boldsymbol{x}_{k+1}|\boldsymbol{x}_k)$ are, respectively, known pdf's for $\boldsymbol{w}_k$ and for $\boldsymbol{v}$ in Eq. (1) or (5) .

2. $\boldsymbol{w}_k$ are statistically independent for all k.

3. $\boldsymbol{v}$ does not depend on the system history.

4. $p(\boldsymbol{y}_{k+1}, \boldsymbol{x}_{k+1}|\bar{\boldsymbol{y}}_k)$ are Borel measurable over $\boldsymbol{x}_{k+1} \in \Omega_{k+1}$, and $p(\boldsymbol{x}_k|\bar{\boldsymbol{y}}_k)$ are Borel measurable over $\boldsymbol{x}_k \in \Omega_k$, where Ω_k is the set of all possible $\boldsymbol{x}_k$ at time step $k\tau (k = 0,1,2\ldots)$.

Then, $p(\boldsymbol{x}_k|\bar{\boldsymbol{y}}_k)$ can be recursively determined from

$$p(\boldsymbol{x}_{k+1}|\bar{\boldsymbol{y}}_{k+1}) = \frac{\displaystyle\int_{\Omega_k} p(\boldsymbol{y}_{k+1}|\boldsymbol{x}_{k+1})p(\boldsymbol{x}_{k+1}|\boldsymbol{x}_k)p(\boldsymbol{x}_k|\bar{\boldsymbol{y}}_k)\, d\boldsymbol{x}_k}{\displaystyle\int_{\Omega_{k+1}} d\boldsymbol{x}_{k+1} p(\boldsymbol{y}_{k+1}|\boldsymbol{x}_{k+1}) \int_{\Omega_k} p(\boldsymbol{x}_{k+1}|\boldsymbol{x}_k)p(\boldsymbol{x}_k|\bar{\boldsymbol{y}}_k)\, d\boldsymbol{x}_k} \quad , \tag{6a}$$

or since $L(\boldsymbol{x}_{k+1}|\boldsymbol{y}_{k+1}) \equiv p(\boldsymbol{y}_{k+1}|\boldsymbol{x}_{k+1})$ can be regarded also as the likelihood of $\boldsymbol{x}_{k+1}$ given the observation $\boldsymbol{y}_{k+1}$, equivalently,

$$p(\boldsymbol{x}_{k+1}|\bar{\boldsymbol{y}}_{k+1}) = \frac{L(\boldsymbol{x}_{k+1}|\boldsymbol{y}_{k+1})p^{prior}(\boldsymbol{x}_{k+1}|\bar{\boldsymbol{y}}_k)}{\displaystyle\int_{\Omega_{k+1}} d\boldsymbol{x}_{k+1} L(\boldsymbol{x}_{k+1}|\boldsymbol{y}_{k+1})p^{prior}(\boldsymbol{x}_{k+1}|\bar{\boldsymbol{y}}_k)} \tag{6b}$$

with

$$p^{prior}(\boldsymbol{x}_{k+1}|\bar{\boldsymbol{y}}_k) = \int_{\Omega_k} p(\boldsymbol{x}_{k+1}|\boldsymbol{x}_k)p(\boldsymbol{x}_k|\bar{\boldsymbol{y}}_k)\, d\boldsymbol{x}_k \quad ,$$

where $\bar{\boldsymbol{y}}_{k+1} = [\boldsymbol{y}_{k+1}\boldsymbol{y}_k \ldots \boldsymbol{y}_0]$.

A practically important situation that satisfies assumptions 1, 2, and 3 is when $\boldsymbol{v}$ represents random fluctuations in system parameters and $\boldsymbol{w}_k$ corresponds to white noise. However, these assumptions do not exclude correlated noise since correlated noise can be regarded as the transformation of a white noise process through a linear filter (when the power spectral density of the correlated noise is in rational form).[26] Assumption 4 implies that

1. all $\Omega_{k+1}\, k = 0,1,\ldots$ must be closed under finite intersection and union of some open subintervals in the ranges of interest $a_l \le x_l \le b_l\ (l = 1,\ldots,L)$ for the state variables/parameters

2. for a given $0 < p(\boldsymbol{y}_{k+1}, \boldsymbol{x}|\bar{\boldsymbol{y}}_k) < 1, \boldsymbol{x} \in \Omega_{k+1}$

and is important for the existence of the integrals in Eq. (6). Since for given initial conditions within the ranges of interest $a_l \le x_l \le b_l$, the system motion is restricted to trajectories generated by Eq. (1), neither of these implications may need be true in the case of nonlinear systems.

Proof:

From the definition of conditional probability and the information vector $\bar{\boldsymbol{y}}_k$,

$$p(\boldsymbol{y}_{k+1}, \boldsymbol{x}_{k+1}|\bar{\boldsymbol{y}}_k) = \frac{p(\boldsymbol{y}_{k+1}, \boldsymbol{x}_{k+1}, \bar{\boldsymbol{y}}_k)}{p(\bar{\boldsymbol{y}}_k)} = \frac{p(\boldsymbol{x}_{k+1}, \bar{\boldsymbol{y}}_{k+1})}{p(\bar{\boldsymbol{y}}_k)} \tag{7}$$

$$p(\boldsymbol{y}_{k+1}|\bar{\boldsymbol{y}}_k) = \frac{p(\bar{\boldsymbol{y}}_{k+1})}{p(\bar{\boldsymbol{y}}_k)}$$

$$\Rightarrow p(\boldsymbol{x}_{k+1}|\bar{\boldsymbol{y}}_{k+1}) = \frac{p(\boldsymbol{y}_{k+1}, \boldsymbol{x}_{k+1}|\bar{\boldsymbol{y}}_k)}{\displaystyle\int_{\Omega_{k+1}} p(\boldsymbol{y}_{k+1}, \boldsymbol{x}_{k+1}|\bar{\boldsymbol{y}}_k)\, d\boldsymbol{x}_{k+1}} \quad . \tag{8}$$

Assumption 4 needs to be used[27] in the decomposition of $p(\bar{\boldsymbol{y}}_{k+1}|\bar{\boldsymbol{y}}_k)$ to obtain Eq. (8) from Eq. (7). Now, consider the following conditional pdf's:

$$p(\boldsymbol{y}_{k+1}|\boldsymbol{x}_{k+1}, \boldsymbol{x}_k, \bar{\boldsymbol{y}}_k) = \frac{p(\boldsymbol{y}_{k+1}, \boldsymbol{x}_{k+1}, \boldsymbol{x}_k, \bar{\boldsymbol{y}}_k)}{p(\boldsymbol{x}_{k+1}, \boldsymbol{x}_k, \bar{\boldsymbol{y}}_k)} \quad ,$$

$$p(\boldsymbol{x}_{k+1}|\boldsymbol{x}_k, \bar{\boldsymbol{y}}_k) = \frac{p(\boldsymbol{x}_{k+1}, \boldsymbol{x}_k, \bar{\boldsymbol{y}}_k)}{p(\boldsymbol{x}_k, \bar{\boldsymbol{y}}_k)} \quad ,$$

and

$$p(\boldsymbol{x}_k|\bar{\boldsymbol{y}}_k) = \frac{p(\boldsymbol{x}_k,\bar{\boldsymbol{y}}_k)}{p(\bar{\boldsymbol{y}}_k)} \quad . \tag{9}$$

From Eq. (8) and assumption 4, the joint pdf $p(\boldsymbol{y}_{k+1},\boldsymbol{x}_{k+1}|\bar{\boldsymbol{y}}_k)$ can be written as

$$\begin{aligned} p(\boldsymbol{y}_{k+1},\boldsymbol{x}_{k+1}|\bar{y}_k) &= \int_{\Omega_k} p(\boldsymbol{y}_{k+1},\boldsymbol{x}_{k+1},\boldsymbol{x}_k|\bar{\boldsymbol{y}}_k)\,d\boldsymbol{x}_k \\ &= \int_{\Omega_k} \frac{p(\boldsymbol{y}_{k+1},\boldsymbol{x}_{k+1},\boldsymbol{x}_k,\bar{\boldsymbol{y}}_k)}{p(\bar{\boldsymbol{y}}_k)}\,d\boldsymbol{x}_k \\ &= \int_{\Omega_k} \frac{p(\boldsymbol{y}_{k+1},\boldsymbol{x}_{k+1},\boldsymbol{x}_k,\bar{\boldsymbol{y}}_k)}{p(\boldsymbol{x}_{k+1},\boldsymbol{x}_k,\bar{\boldsymbol{y}}_k)}\,\frac{p(\boldsymbol{x}_{k+1},\boldsymbol{x}_k,\bar{\boldsymbol{y}}_k)}{p(\boldsymbol{x}_k,\bar{\boldsymbol{y}}_k)}\,\frac{p(\boldsymbol{x}_k,\bar{\boldsymbol{y}}_k)}{p(\bar{\boldsymbol{y}}_k)}\,d\boldsymbol{x}_k \\ &= \int_{\Omega_k} p(\boldsymbol{y}_{k+1}|\boldsymbol{x}_{k+1},\boldsymbol{x}_k,\bar{\boldsymbol{y}}_k)p(\boldsymbol{x}_{k+1}|\boldsymbol{x}_k,\bar{\boldsymbol{y}}_k)p(\boldsymbol{x}_k|\bar{\boldsymbol{y}}_k)\,d\boldsymbol{x}_k \quad . \end{aligned} \tag{10}$$

Note that the conditional probabilities in Eq (9) have the following properties:

$$p(\boldsymbol{y}_{k+1}|\boldsymbol{x}_{k+1},\boldsymbol{x}_k,\bar{\boldsymbol{y}}_k) = p(\boldsymbol{y}_{k+1}|\boldsymbol{x}_{k+1})$$

and

$$p(\boldsymbol{x}_{k+1}|\boldsymbol{x}_k,\bar{\boldsymbol{y}}_k) = p(\boldsymbol{x}_{k+1}|\boldsymbol{x}_k) \quad . \tag{11}$$

Equation (11) holds because $\boldsymbol{y}_{k+1}$ only depends on the value of $\boldsymbol{x}_{k+1}$ and $\boldsymbol{w}_{k+1}$ by Eq. (1). When $\boldsymbol{x}_{k+1}$ is given, the probability of $\boldsymbol{y}_{k+1}$ will be determined by the value of $\boldsymbol{w}_{k+1}$, whose value does not depend on any previous system states by assumption 2. Similarly, $p(\boldsymbol{x}_{k+1}|\boldsymbol{x}_k)$ only depends on $\boldsymbol{x}_k$ and $\boldsymbol{v}$ by Eq. (1), and $\boldsymbol{v}$ is independent of system history by assumption 3. Using Eqs. (10) and (11), Eq. (8) can be written as

$$p(\boldsymbol{x}_{k+1}|\bar{\boldsymbol{y}}_{k+1}) = \frac{\displaystyle\int_{\Omega_k} p(\boldsymbol{y}_{k+1}|\boldsymbol{x}_{k+1})p(\boldsymbol{x}_{k+1}|\boldsymbol{x}_k)p(\boldsymbol{x}_k|\bar{\boldsymbol{y}}_k)\,d\boldsymbol{x}_k}{\displaystyle\int_{\Omega_{k+1}} d\boldsymbol{x}_{k+1}\,p(\boldsymbol{y}_{k+1}|\boldsymbol{x}_{k+1})\int_{\Omega_k} p(\boldsymbol{x}_{k+1}|\boldsymbol{x}_k)p(\boldsymbol{x}_k|\bar{\boldsymbol{y}}_k)\,d\boldsymbol{x}_k} \quad ,$$

which completes the proof.

Equation (6) constitutes a Bayesian rule for recursive determination of $p(\boldsymbol{x}_{k+1}|\bar{\boldsymbol{y}}_{k+1})$ for known $p(\boldsymbol{y}_{k+1}|\boldsymbol{x}_{k+1})$ and $p(\boldsymbol{x}_{k+1}|\boldsymbol{x}_k)$. Convergence properties of Eq. (6) will be discussed within the context of its discrete formulation in Sec. II.B and also in Sec. IV. Note that if $\boldsymbol{h}(\boldsymbol{x}_k) = \boldsymbol{x}_k$, then Eq. (6) can be used as a recursive rule for signal validation as illustrated in Secs. III.B and III.C. Also, as indicated in Proposition 1, a practically important situation is when the modeling uncertainties and the measurement uncertainties are represented by zero mean random white Gaussian noise. In this situation,

$$\boldsymbol{x}_{k+1} = \tilde{\boldsymbol{x}}(\boldsymbol{x}_k) + \Delta\boldsymbol{B}_\tau \quad , \tag{12}$$

where

$$\Delta\boldsymbol{B}_\tau = \int_{k\tau}^{(k+1)\tau} d\boldsymbol{B}_t = \int_{k\tau}^{(k+1)\tau} \boldsymbol{v}(t)\,dt$$

$$\tilde{\boldsymbol{x}}(\boldsymbol{x}_k) = \int_{k\tau}^{(k+1)\tau} \boldsymbol{f}(\boldsymbol{x}(s))\,ds + \boldsymbol{x}_k$$

and $\mathbf{B}_t$ denotes the Brownian motion[28] whose pdf is the joint normal distribution of the elements of $\Delta\boldsymbol{B}_\tau$. Then, from Eq. (12) we have

$$p(\boldsymbol{x}_{k+1}|\boldsymbol{x}_k) = \frac{1}{(2\pi\sigma_p^2)^{L/2}}\,e^{-\frac{(\boldsymbol{x}_{k+1}-\tilde{\boldsymbol{x}}(\boldsymbol{x}_k))'(\boldsymbol{x}_{k+1}-\tilde{\boldsymbol{x}}(\boldsymbol{x}_k))}{2\sigma_p^2}} \quad , \tag{13}$$

where σ_p is the standard deviation of the modeling uncertainty. Similarly, when $\boldsymbol{w}_k$ is white Gaussian noise, from Eq. (1) we can write

$$p(\boldsymbol{y}_{k+1}|\boldsymbol{x}_{k+1}) = \frac{1}{(2\pi\sigma_m^2)^{M/2}}\,e^{-\frac{(\boldsymbol{y}_{k+1}-\boldsymbol{h}(\boldsymbol{x}_{k+1}))'(\boldsymbol{y}_{k+1}-h(\boldsymbol{x}_{k+1}))}{2\sigma_m^2}} \quad , \tag{14}$$

where again σ_m is the standard deviation of the noise. In Eqs. (13) and (14), the standard deviations σ_p and σ_m are assumed to be constant for all $k\tau$ $(k = 0,1,2,\ldots)$. Substituting Eqs. (13) and (14) into Eq. (6) yields the Bayesian rule for the recursive estimation of the conditional distribution $p(\boldsymbol{x}_k|\bar{\boldsymbol{y}}_k)$ when the modeling and measurement uncertainties are random white Gaussian noise:

$$
\begin{aligned}
&p(\boldsymbol{x}_{k+1}|\bar{\boldsymbol{y}}_{k+1}) \\
&= \frac{\dfrac{1}{(2\pi\sigma_p^2)^{L/2}(2\pi\sigma_m^2)^{M/2}} \displaystyle\int_{\Omega_k} e^{-\left[\frac{(\boldsymbol{x}_{k+1}-\tilde{\boldsymbol{x}}(\boldsymbol{x}_k))'(\boldsymbol{x}_{k+1}-\tilde{\boldsymbol{x}}(\boldsymbol{x}_k))}{2\sigma_p^2}+\frac{(\boldsymbol{y}_{k+1}-\boldsymbol{h}(\boldsymbol{x}_{k+1}))'(\boldsymbol{y}_{k+1}-\boldsymbol{h}(\boldsymbol{x}_{k+1}))}{2\sigma_m^2}\right]} p(\boldsymbol{x}_k|\bar{\boldsymbol{y}}_k)\,d\boldsymbol{x}_k}{\dfrac{1}{(2\pi\sigma_p^2)^{L/2}(2\pi\sigma_m^2)^{M/2}} \displaystyle\int_{\Omega_{k+1}} d\boldsymbol{x}_{k+1} \int_{\Omega_k} e^{-\left[\frac{(\boldsymbol{x}_{k+1}-\tilde{\boldsymbol{x}}(\boldsymbol{x}_k))'(\boldsymbol{x}_{k+1}-\tilde{\boldsymbol{x}}(\boldsymbol{x}_k))}{2\sigma_p^2}+\frac{(\boldsymbol{y}_{k+1}-\boldsymbol{h}(\boldsymbol{x}_{k+1}))'(\boldsymbol{y}_{k+1}-\boldsymbol{h}(\boldsymbol{x}_{k+1}))}{2\sigma_m^2}\right]} p(\boldsymbol{x}_k|\bar{\boldsymbol{y}}_k)\,d\boldsymbol{x}_k} \\
&\equiv \frac{\dfrac{1}{(2\pi\sigma_m^2)^{M/2}} e^{-\left[\frac{(\boldsymbol{y}_{k+1}-\boldsymbol{h}(\boldsymbol{x}_{k+1}))'(\boldsymbol{y}_{k+1}-\boldsymbol{h}(\boldsymbol{x}_{k+1}))}{2\sigma_m^2}\right]} p^{prior}(\boldsymbol{x}_{k+1}|\bar{\boldsymbol{y}}_k)}{\dfrac{1}{(2\pi\sigma_m^2)^{M/2}} \displaystyle\int_{\Omega_{k+1}} d\boldsymbol{x}_{k+1} e^{-\left[\frac{(\boldsymbol{y}_{k+1}-\boldsymbol{h}(\boldsymbol{x}_{k+1}))'(\boldsymbol{y}_{k+1}-\boldsymbol{h}(\boldsymbol{x}_{k+1}))}{2\sigma_m^2}\right]} p^{prior}(\boldsymbol{x}_{k+1}|\bar{\boldsymbol{y}}_k)}
\end{aligned}
\tag{15}
$$

with

$$
p^{prior}(\boldsymbol{x}_{k+1}|\bar{\boldsymbol{y}}_k) = \frac{1}{(2\pi\sigma_p^2)^{L/2}} \int_{\Omega_k} e^{-\left[\frac{(\boldsymbol{x}_{k+1}-\tilde{\boldsymbol{x}}(\boldsymbol{x}_k))'(\boldsymbol{x}_{k+1}-\tilde{\boldsymbol{x}}(\boldsymbol{x}_k))}{2\sigma_p^2}\right]} p(\boldsymbol{x}_k|\bar{\boldsymbol{y}}_k)\,d\boldsymbol{x}_k \ .
$$

In the case there are no system noise and/or modeling uncertainties and $\tilde{\boldsymbol{x}}(\boldsymbol{x}_k)$ [see Eq. (12)] is invertible, then $\boldsymbol{v} = \boldsymbol{0}$ and

$$
p(\boldsymbol{x}_{k+1}|\boldsymbol{x}_k) = \delta(\boldsymbol{x}_{k+1} - \tilde{\boldsymbol{x}}(\boldsymbol{x}_k)) = \delta(l(\boldsymbol{x}_{k+1}) - \boldsymbol{x}_k) \ , \tag{16}
$$

where $l(\boldsymbol{x}_{k+1})$ is the inverse of $\tilde{\boldsymbol{x}}(\boldsymbol{x}_k)$ and δ denotes the Dirac delta function; i.e.,

$$
\int_{\varepsilon} \delta(\boldsymbol{x} - \hat{\boldsymbol{x}})\,d\boldsymbol{x} = 1
$$

with ε as an infinitesimally small ball around $\hat{\boldsymbol{x}}$ and $\delta(\boldsymbol{x} - \hat{\boldsymbol{x}}) = 0$ for $\boldsymbol{x} \neq \hat{\boldsymbol{x}}$. As an example for the inverse function $l(\boldsymbol{x}_{k+1})$ and measurable sets $\boldsymbol{x_k} \in \Omega_k$, consider the system

$$
\dot{x} = x \ .
$$

Then,

$$
x_{k+1} = \tilde{x}(x_k) = \frac{x_k}{e^{t_k}}\, e^{t_{k+1}}
$$

and

$$
x_k = l(x_{k+1}) = \frac{x_{k+1}}{e^{t_{k+1}}}\, e^{t_k} \ .
$$

The sets $\boldsymbol{x_k} \in \Omega_k$ are measurable because each x_k is a continuous function of and any continuous function is (Borel) measurable.[27] Continuing on with the case where there is no system noise/or modeling uncertainties and $\tilde{\boldsymbol{x}}(\boldsymbol{x}_k)$ is invertible, from Eqs. (6) and (16) we have

$$
\begin{aligned}
&p(\boldsymbol{x}_{k+1}|\bar{\boldsymbol{y}}_{k+1}) \\
&= \frac{\displaystyle\int_{\Omega_k} p(\boldsymbol{y}_{k+1}|\boldsymbol{x}_{k+1})p(\boldsymbol{x}_{k+1}|\boldsymbol{x}_k)p(\boldsymbol{x}_k|\bar{\boldsymbol{y}}_k)\,d\boldsymbol{x}_k}{\displaystyle\int_{\Omega_{k+1}} d\boldsymbol{x}_{k+1} p(\boldsymbol{y}_{k+1}|\boldsymbol{x}_{k+1}) \int_{\Omega_k} p(\boldsymbol{x}_{k+1}|\boldsymbol{x}_k)p(\boldsymbol{x}_k|\bar{\boldsymbol{y}}_k)\,d\boldsymbol{x}_k} \\
&= \frac{\displaystyle\int_{\Omega_k} p(\boldsymbol{y}_{k+1}|\boldsymbol{x}_{k+1})\delta(l(\boldsymbol{x}_{k+1}) - \boldsymbol{x}_k)p(\boldsymbol{x}_k|\bar{\boldsymbol{y}}_k)\,d\boldsymbol{x}_k}{\displaystyle\int_{\Omega_{k+1}} d\boldsymbol{x}_{k+1} p(\boldsymbol{y}_{k+1}|\boldsymbol{x}_{k+1}) \int_{\Omega_k} \delta(l(\boldsymbol{x}_{k+1}) - \boldsymbol{x}_k)p(\boldsymbol{x}_k|\bar{\boldsymbol{y}}_k)\,d\boldsymbol{x}_k} \\
&\equiv \frac{L(\boldsymbol{x}_{k+1}|\boldsymbol{y}_{k+1})p^{prior}(l(\boldsymbol{x}_{k+1})|\bar{\boldsymbol{y}}_k)}{\displaystyle\int_{\Omega_{k+1}} L(\boldsymbol{x}_{k+1}|\boldsymbol{y}_{k+1})p^{prior}(l(\boldsymbol{x}_{k+1})|\bar{\boldsymbol{y}}_k)\,d\boldsymbol{x}_{k+1}} \ .
\end{aligned}
\tag{17}
$$

Equation (17) is the special case of Eq. (6) for the situation where there is no model uncertainty [i.e., $\boldsymbol{v} = 0$ in Eq. (1)]. If Eq. (1) has no closed-form solution or the closed-form solution is not invertible, Eq. (6) needs to be evaluated numerically. Section II.B shows how such a numerical evaluation can be performed using the CCMT.

II.B. Application of the Continuous Bayesian Estimator to the Discretized Representation of the System Used by CCMT

The CCMT describes the dynamic system evolution in terms of probability of transitions between user-specified variable magnitude intervals or cells in the system parameter/state-space during user-specified time intervals $k\tau \leq t \leq (k+1)\tau$ $(k = 0,1,2\ldots)$. The cell sizes may correspond to the desired estimation accuracy in

unknown state variables or may be defined to contain the signal noise.

Assume that the l'th component x_l of the state variable vector $\boldsymbol{x} = [x_1, x_2, \ldots, x_L]$ falls within the range of interest $a_l \le x_l \le b_l (l = 1, \ldots, L)$ at all times. This range of interest is partitioned into $J_l (l = 1, \ldots, L)$ user-defined intervals

$$\Delta_{l,j_l} = \{x_l : a_{l,j_l} \le x_l < a_{l,j_l+1}; a_{l,1} = a_l, a_{l,J_l+1} = b_l\}$$
$$j_l = 1, \ldots, J_l; l = 1, \ldots, L \quad . \qquad (18)$$

The sets $\boldsymbol{V}_j = \{\Delta_{1,j_1}, \Delta_{2,j_2}, \ldots, \Delta_{L,j_L}\} (j = 1, \ldots, J = \prod_{l=1}^{L} J_l)$ at locations $\boldsymbol{j} = (j_1, j_2, \ldots, j_L)$ in the discretized L-dimensional state-space constitute computational cells in a similar manner to those used by finite difference and finite element methods. The cell $x_k \in \boldsymbol{V}_{j,k} \equiv \boldsymbol{V}_k$ that the system is in at time $t = k\tau$ contains a subset $\tilde{\Omega}_k$ of Ω_k but may also include points that are not within $\tilde{\Omega}_k$, i.e., points that may not be achievable by the system under any initial condition since $\boldsymbol{V}_k$ consists of a union of semiopen subintervals within $a_l \le x_l \le b_l (l = 1, \ldots, L)$. Figure 1 illustrates such a possible partitioning for a hypothetical second-order system with three trajectories corresponding to three sets of initial conditions and indicates the possible cells the system can be in if one of the state variables is directly measured. As Fig. 1 shows, the set $\tilde{\Omega}_k$ contains the system locations within cell (7,6) for trajectories 1 and 2 at $t = k\tau$ [and possibly other points of cell (7,6) that the system could have reached under other initial conditions]. On the other hand, cell (7,6) may contain points that are never achievable by the system under any initial condition due to the

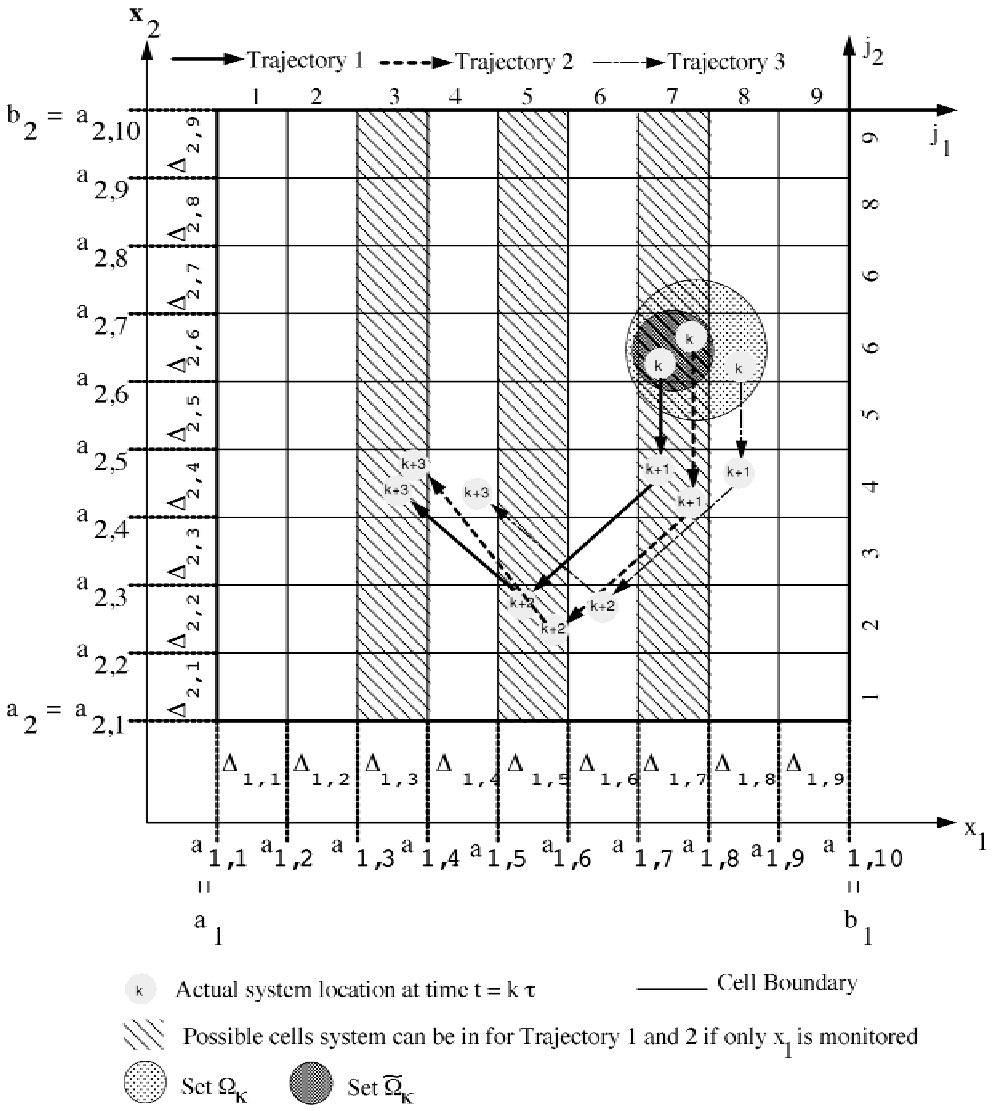

Fig. 1. A possible partitioning for a second-order system.

equations governing the dynamics of the system, just as the trajectory 3 location at $t = k\tau$ is not within cell (7,6) but rather in cell (8,6). Subsequently, cell $\boldsymbol{V}_k$ provides a subcover[27] for $\tilde{\Omega}_k$ (but not for Ω_k).

Integrating both sides of Eq. (6) over the possible cells $\boldsymbol{j}_{k+1}$ where the system might be in at time $t = (k+1)\tau$, we obtain

$$p(\boldsymbol{j}_{k+1}|\bar{\boldsymbol{y}}_{k+1}) = \frac{\displaystyle\int_{\boldsymbol{j}_{k+1}} d\boldsymbol{x}_{k+1} \int_{\Omega_k} d\boldsymbol{x}_k \; p(\boldsymbol{y}_{k+1}|\boldsymbol{x}_{k+1}) p(\boldsymbol{x}_{k+1}|\boldsymbol{x}_k) p(\boldsymbol{x}_k|\bar{\boldsymbol{y}}_k)}{\displaystyle\sum_{\boldsymbol{j}_{k+1}} \int_{\boldsymbol{j}_{k+1}} d\boldsymbol{x}_{k+1} \int_{\Omega_k} d\boldsymbol{x}_k \; p(\boldsymbol{y}_{k+1}|\boldsymbol{x}_{k+1}) p(\boldsymbol{x}_{k+1}|\boldsymbol{x}_k) p(\boldsymbol{x}_k|\bar{\boldsymbol{y}}_k)} \;, \tag{19}$$

where

$$p(\boldsymbol{j}_{k+1}|\bar{\boldsymbol{y}}_{k+1}) = \int_{\boldsymbol{j}_{k+1}} p(\boldsymbol{x}_{k+1}|\bar{\boldsymbol{y}}_{k+1})\, d\boldsymbol{x}_{k+1} \tag{20}$$

is the probability that the system is in cell $\boldsymbol{j}_{k+1}$ at time $(k+1)\tau$. Note that from the definition of $p(\boldsymbol{j}_k|\bar{\boldsymbol{y}}_k)$ in Eq. (20), we can write

$$\int_{\Omega_k} p(\boldsymbol{y}_{k+1}|\boldsymbol{x}_{k+1}) p(\boldsymbol{x}_{k+1}|\boldsymbol{x}_k) p(\boldsymbol{x}_k|\bar{\boldsymbol{y}}_k)\, d\boldsymbol{x}_k = \sum_{\boldsymbol{j}_k} \frac{\displaystyle\int_{\boldsymbol{j}_k} p(\boldsymbol{y}_{k+1}|\boldsymbol{x}_{k+1}) p(\boldsymbol{x}_{k+1}|\boldsymbol{x}_k) p(\boldsymbol{x}_k|\bar{\boldsymbol{y}}_k)\, d\boldsymbol{x}_k}{\displaystyle\int_{\boldsymbol{j}_k} p(\boldsymbol{x}_k|\bar{\boldsymbol{y}}_k)\, d\boldsymbol{x}_k} p(\boldsymbol{j}_k|\bar{\boldsymbol{y}}_k) \;. \tag{21}$$

Substituting Eq. (21) into Eq. (19) we obtain

$$\begin{aligned}
p(\boldsymbol{j}_{k+1}|\bar{\boldsymbol{y}}_{k+1}) &= \frac{\displaystyle\int_{\boldsymbol{j}_{k+1}} d\boldsymbol{x}_{k+1} \int_{\Omega_k} d\boldsymbol{x}_k\, p(\boldsymbol{y}_{k+1}|\boldsymbol{x}_{k+1}) p(\boldsymbol{x}_{k+1}|\boldsymbol{x}_k) p(\boldsymbol{x}_k|\bar{\boldsymbol{y}}_k)}{\displaystyle\sum_{\boldsymbol{j}_{k+1}} \int_{\boldsymbol{j}_{k+1}} d\boldsymbol{x}_{k+1} \int_{\Omega_k} d\boldsymbol{x}_k\, p(\boldsymbol{y}_{k+1}|\boldsymbol{x}_{k+1}) p(\boldsymbol{x}_{k+1}|\boldsymbol{x}_k) p(\boldsymbol{x}_k|\bar{\boldsymbol{y}}_k)} \\
&= \frac{\displaystyle\int_{\boldsymbol{j}_{k+1}} \sum_{\boldsymbol{j}_k} \frac{\displaystyle\int_{\boldsymbol{j}_k} p(\boldsymbol{y}_{k+1}|\boldsymbol{x}_{k+1}) p(\boldsymbol{x}_{k+1}|\boldsymbol{x}_k) p(\boldsymbol{x}_k|\bar{\boldsymbol{y}}_k)\, d\boldsymbol{x}_k}{\displaystyle\int_{\boldsymbol{j}_k} p(\boldsymbol{x}_k|\bar{\boldsymbol{y}}_k)\, d\boldsymbol{x}_k} p(\boldsymbol{j}_k|\bar{\boldsymbol{x}}_k)\, d\boldsymbol{x}_{k+1}}{\displaystyle\sum_{\boldsymbol{j}_{k+1}} \int_{\boldsymbol{j}_{k+1}} \sum_{\boldsymbol{j}_k} \frac{\displaystyle\int_{\boldsymbol{j}_k} p(\boldsymbol{y}_{k+1}|\boldsymbol{x}_{k+1}) p(\boldsymbol{x}_{k+1}|\boldsymbol{x}_k) p(\boldsymbol{x}_k|\bar{\boldsymbol{y}}_k)\, d\boldsymbol{x}_k}{\displaystyle\int_{\boldsymbol{j}_k} p(\boldsymbol{x}_k|\bar{\boldsymbol{y}}_k)\, d\boldsymbol{x}_k} p(\boldsymbol{j}_k|\bar{\boldsymbol{y}}_k)\, d\boldsymbol{x}_{k+1}} \\
&= \frac{\displaystyle\sum_{\boldsymbol{j}_k} p(\boldsymbol{j}_k|\bar{\boldsymbol{y}}_k) \iint_{\boldsymbol{j}_{k+1},\boldsymbol{j}_k} p(\boldsymbol{y}_{k+1}|\boldsymbol{x}_{k+1}) p(\boldsymbol{x}_{k+1}|\boldsymbol{x}_k) \frac{p(\boldsymbol{x}_k|\bar{\boldsymbol{y}}_k)}{\displaystyle\int_{\boldsymbol{j}_k} p(\boldsymbol{x}_k|\bar{\boldsymbol{y}}_k)\, d\boldsymbol{x}_k} d\boldsymbol{x}_k\, d\boldsymbol{x}_{k+1}}{\displaystyle\sum_{\boldsymbol{j}_{k+1}} \sum_{\boldsymbol{j}_k} p(\boldsymbol{j}_k|\bar{\boldsymbol{y}}_k) \iint_{\boldsymbol{j}_{k+1},\boldsymbol{j}_k} p(\boldsymbol{y}_{k+1}|\boldsymbol{x}_{k+1}) p(\boldsymbol{x}_{k+1}|\boldsymbol{x}_k) \frac{p(\boldsymbol{x}_k|\bar{\boldsymbol{y}}_k)}{\displaystyle\int_{\boldsymbol{j}_k} p(\boldsymbol{x}_k|\bar{\boldsymbol{y}}_k)\, d\boldsymbol{x}_k} d\boldsymbol{x}_k\, d\boldsymbol{x}_{k+1}} \;.
\end{aligned} \tag{22}$$

The fundamental difference between Eqs. (6) and (22) is that the integrations in Eq. (6) are carried over the possible system locations at times $t = k\tau$ and $t = (k+1)\tau$ as determined from Eq. (1) and given initial conditions and represented, respectively, by the sets Ω_k and Ω_{k+1}, whereas the integrations in Eq. (22) are carried over cell $\boldsymbol{V}_k$ at $\boldsymbol{j}_k$ and cell $\boldsymbol{V}_{k+1}$ at $\boldsymbol{j}_{k+1}$, which the system is in at these times and which contain the subsets $\tilde{\Omega}_k \subset \Omega_k$ $(k = 0,1,\ldots)$. In view of the explanation given above for the difference between $\boldsymbol{V}_k$ and $\tilde{\Omega}_k$, the $p(\boldsymbol{j}_k|\bar{\boldsymbol{y}}_k)$ as defined by Eq. (20) can be regarded as an outer measure[27] for $\tilde{\Omega}_k$. The limitations and advantages of this approximation will be discussed later in this section.

Now, define the cell-to-cell transition probability as

$$g(\boldsymbol{j}_{k+1}|\boldsymbol{j}_k) = \iint\limits_{\boldsymbol{j}_{k+1},\boldsymbol{j}_k} p(\boldsymbol{y}_{k+1}|\boldsymbol{x}_{k+1})p(\boldsymbol{x}_{k+1}|\boldsymbol{x}_k) \times \frac{p(\boldsymbol{x}_k|\bar{\boldsymbol{y}}_k)}{\int_{\boldsymbol{j}_k} p(\boldsymbol{x}_k|\bar{\boldsymbol{y}}_k)\,d\boldsymbol{x}_k}\,d\boldsymbol{x}_k\,d\boldsymbol{x}_{k+1} \quad . \tag{23}$$

The $g(\boldsymbol{j}_{k+1}|\boldsymbol{j}_k)$ does not include $\boldsymbol{y}_{k+1}$ and $\bar{\boldsymbol{y}}_k$ as arguments for notational simplicity and also because $\boldsymbol{y}_{k+1}$ and $\bar{\boldsymbol{y}}_k$ are measured data points (and hence fixed), whereas $\boldsymbol{j}_{k+1}$ and $\boldsymbol{j}_k$ are arbitrary cells (i.e., variables). Then, Eqs. (22) and (23) yield the discrete counterpart of Eq. (6) as

$$p(\boldsymbol{j}_{k+1}|\bar{\boldsymbol{y}}_{k+1}) = \frac{\sum_{\boldsymbol{j}_k} g(\boldsymbol{j}_{k+1}|\boldsymbol{j}_k)p(\boldsymbol{j}_k|\bar{\boldsymbol{y}}_k)}{\sum_{\boldsymbol{j}_{k+1}}\sum_{\boldsymbol{j}_k} g(\boldsymbol{j}_{k+1}|\boldsymbol{j}_k)p(\boldsymbol{j}_k|\bar{\boldsymbol{y}}_k)} \quad . \tag{24}$$

The cell-to-cell transition probabilities can be calculated numerically from

$$\begin{aligned} g(\boldsymbol{j}_{k+1}|\boldsymbol{j}_k) &= \iint\limits_{\boldsymbol{j}_{k+1}\boldsymbol{j}_k} f_w(\boldsymbol{y}_{k+1} - \boldsymbol{h}(\boldsymbol{x}_{k+1})) \times f_{\Delta B}(\boldsymbol{x}_{k+1} - \tilde{\boldsymbol{x}}(\boldsymbol{x}_k)) \times \frac{p(\boldsymbol{x}_k|\bar{\boldsymbol{y}}_k)}{\int_{\boldsymbol{j}_k} p(\boldsymbol{x}_k|\bar{\boldsymbol{y}}_k)\,d\boldsymbol{x}_k}\,d\boldsymbol{x}_k\,d\boldsymbol{x}_{k+1} \\ &\approx \sum_r\sum_q f_w(\boldsymbol{y}_{k+1} - \boldsymbol{h}(\hat{\boldsymbol{x}}^r_{k+1})) \times f_{\Delta B}(\hat{\boldsymbol{x}}^r_{k+1} - \tilde{\boldsymbol{x}}(\hat{\boldsymbol{x}}^q_k)) \times \frac{p(\hat{\boldsymbol{x}}^q_k|\bar{\boldsymbol{y}}_k)}{\int_{\boldsymbol{j}_k} p(\boldsymbol{x}_k|\bar{\boldsymbol{y}}_k)\,d\boldsymbol{x}_k}\,\Delta\hat{\boldsymbol{x}}^q_k\Delta\hat{\boldsymbol{x}}^r_{k+1} \quad , \end{aligned} \tag{25}$$

where

$f_{\Delta B}, f_w$ = user-specified pdf's for the system noise [e.g., see Eq. (13)] and measurement noise [e.g., see Eq. (14)], respectively

$\hat{\boldsymbol{x}}^q_k$ = quadrature points selected in cell $\boldsymbol{j}_k$ with $\Delta\hat{\boldsymbol{x}}^q_k$ denoting small volumes that surrounds $\hat{\boldsymbol{x}}^q_k$

$\hat{\boldsymbol{x}}^r_{k+1}$ = quadrature points selected in cell $\boldsymbol{j}_{k+1}$ with $\Delta\hat{\boldsymbol{x}}^r_{k+1}$ denoting the small volume that surrounds $\hat{\boldsymbol{x}}^r_{k+1}$.

Equation (25) constitutes a quadrature rule for the numerical approximation of $g(\boldsymbol{j}_{k+1}|\boldsymbol{j}_k)$; however, Monte Carlo sampling can be also used for the approximation of the integrals in Eq. (25). The $\tilde{\boldsymbol{x}}(\hat{\boldsymbol{x}}^q_k)$ can be evaluated by any numerical integration technique from Eq. (1). At this point it should be mentioned that the equations describing the evolution of the system do not have to be differential equations as assumed in Eq. (1). All that is needed is a rule $\tilde{\boldsymbol{x}}(\boldsymbol{x}_k)$ that yields the system location in the state-space at time $(k+1)\tau$ given its location at time $k\tau$, such as difference equations, neural nets, response surfaces, tabular data, or algebraic equations.

If there is no modeling uncertainty, Eq. (25) can be simplified using Eq. (16). In this situation,

$$\begin{aligned} g(\boldsymbol{j}_{k+1}|\boldsymbol{j}_k) &= \iint\limits_{j_{k+1}j_k} p(\boldsymbol{y}_{k+1}|\boldsymbol{x}_{k+1})\delta(\boldsymbol{x}_{k+1} - \tilde{\boldsymbol{x}}(\boldsymbol{x}_k)) \times \frac{p(\boldsymbol{x}_k|\bar{\boldsymbol{y}}_k)}{\int_{j_k} p(\boldsymbol{x}_k|\bar{\boldsymbol{y}}_k)\,d\boldsymbol{x}_k}\,d\boldsymbol{x}_k\,d\boldsymbol{x}_{k+1} \\ &= \int_{j_k} p(\boldsymbol{y}_{k+1}|\tilde{\boldsymbol{x}}(\boldsymbol{x}_k)) \times \frac{p(\boldsymbol{x}_k|\bar{\boldsymbol{y}}_k)}{\int_{j_k} p(\boldsymbol{x}_k|\bar{\boldsymbol{y}}_k)\,d\boldsymbol{x}_k}\,e_{k+1}(\tilde{\boldsymbol{x}}(\boldsymbol{x}_k))\,d\boldsymbol{x}_k \\ &= \int_{j_k} f_w(\boldsymbol{y}_{k+1} - \boldsymbol{h}(\tilde{\boldsymbol{x}}(\boldsymbol{x}_k))) \times \frac{p(\boldsymbol{x}_k|\bar{\boldsymbol{y}}_k)}{\int_{j_k} p(\boldsymbol{x}_k|\bar{\boldsymbol{y}}_k)\,d\boldsymbol{x}_k}\,e_{k+1}(\tilde{\boldsymbol{x}}(\boldsymbol{x}_k))\,d\boldsymbol{x}_k \\ &\approx \sum_i f_w(\boldsymbol{y}_{k+1} - \boldsymbol{h}(\tilde{\boldsymbol{x}}(\hat{\boldsymbol{x}}^i_k))) \times \frac{p(\hat{\boldsymbol{x}}^i_k|\bar{\boldsymbol{y}}_k)}{\int_{j_k} p(\boldsymbol{x}_k|\bar{\boldsymbol{y}}_k)\,d\boldsymbol{x}_k}\,e_{k+1}(\tilde{\boldsymbol{x}}(\hat{\boldsymbol{x}}^i_k))\Delta\hat{\boldsymbol{x}}_k \quad , \end{aligned} \tag{26}$$

where $e_{k+1}(\tilde{\boldsymbol{x}}(\boldsymbol{x}_k))$ is defined as

$$e_{k+1}(\tilde{\boldsymbol{x}}(\boldsymbol{x}_k)) = \begin{cases} 0 & \tilde{\boldsymbol{x}}(\boldsymbol{x}_k) \notin \boldsymbol{j}_{k+1} \\ 1 & \tilde{\boldsymbol{x}}(\boldsymbol{x}_k) \in \boldsymbol{j}_{k+1} \end{cases} , \tag{27}$$

$\hat{\boldsymbol{x}}_k^i$ (i = 1,…, N) are points selected in cell $\boldsymbol{j}_k$, and $\Delta\hat{\boldsymbol{x}}_k^i$ is the small volume that surrounds $\hat{\boldsymbol{x}}_k^i$. In measure theory, $e_{k+1}(\tilde{\boldsymbol{x}}(\boldsymbol{x}_k))$ is called the indicator[27] of $\tilde{\Omega}_{k+1}$ for $\tilde{\boldsymbol{x}}(\boldsymbol{x}_k) \in \tilde{\Omega}_{k+1}$. The $e_{k+1}(\tilde{\boldsymbol{x}}(\boldsymbol{x}_k))$ is not Borel measurable if $\tilde{\Omega}_{k+1}$ is not a Borel set, which would mean that the integral over cell $\boldsymbol{j}_{k+1}$ in Eq. (26) might have not existed for some nonlinear systems if the integration were carried over $\tilde{\Omega}_{k+1}$ rather than cell $\boldsymbol{j}_{k+1}$. Carrying the integration over cell $\boldsymbol{j}_{k+1}$ assures the existence of the integral as discussed above with regard to proposition 1 and Eq. (22); however, it may lead to loss of resolution in the estimate as will be indicated below.

Further simplification of Eq. (26) can be made by assuming that the probability $p(\hat{\boldsymbol{x}}_k^i|\bar{\boldsymbol{y}}_k)$ is constant over $\Delta\hat{\boldsymbol{x}}_k^i$ and selecting the points $\hat{\boldsymbol{x}}_k^i$ equally spaced inside the cell; then,

$$\frac{p(\hat{\boldsymbol{x}}_k^i|\bar{\boldsymbol{y}}_k)}{\displaystyle\int_{\boldsymbol{j}_k} p(\boldsymbol{x}_k|\bar{\boldsymbol{y}}_k)\,d\boldsymbol{x}_k} = \frac{p(\hat{\boldsymbol{x}}_k^i|\bar{\boldsymbol{y}}_k)}{Np(\hat{\boldsymbol{x}}_k^i|\bar{\boldsymbol{y}}_k)\Delta\hat{\boldsymbol{x}}_k} = \frac{1}{N\Delta\hat{\boldsymbol{x}}_k} = \frac{1}{V_k} , \tag{28}$$

where V_k is the volume of cell $\boldsymbol{j}_k$ (i.e., the product $\Delta_{1,j_1}\Delta_{2,j_2}\ldots\Delta_{L,j_L}$) and Eq. (26) becomes

$$\begin{aligned} g(\boldsymbol{j}_{k+1}|\boldsymbol{j}_k) = & \int_{\boldsymbol{j}_k} f_w(\boldsymbol{y}_{k+1} - \boldsymbol{h}(\tilde{\boldsymbol{x}}(\boldsymbol{x}_k))) \\ & \times \frac{p(\boldsymbol{x}_k|\bar{\boldsymbol{y}}_k)}{\displaystyle\int_{\boldsymbol{j}_k} p(\boldsymbol{x}_k|\bar{\boldsymbol{y}}_k)\,d\boldsymbol{x}_k} e_{k+1}(\tilde{\boldsymbol{x}}(\boldsymbol{x}_k))\,d\boldsymbol{x}_k \\ \approx & \sum_{i=1}^{N} f_w(\boldsymbol{y}_{k+1} - \boldsymbol{h}(\tilde{\boldsymbol{x}}(\hat{\boldsymbol{x}}_k^i))) \\ & \times \frac{p(\hat{\boldsymbol{x}}_k^i|\bar{\boldsymbol{y}}_k)}{Np(\hat{\boldsymbol{x}}_k^i|\bar{\boldsymbol{y}}_k)\Delta\hat{\boldsymbol{x}}_k} e_{k+1}(\tilde{\boldsymbol{x}}(\hat{\boldsymbol{x}}_k^i))\Delta\hat{\boldsymbol{x}}_k \\ = & \sum_{i=1}^{N} \frac{1}{N} f_w(\boldsymbol{y}_{k+1} - \boldsymbol{h}(\tilde{\boldsymbol{x}}(\hat{\boldsymbol{x}}_k^i))) \\ & \times e_{k+1}(\tilde{\boldsymbol{x}}(\hat{\boldsymbol{x}}_k^i)) . \end{aligned} \tag{29}$$

Equations (23) and (24) are similar to the recursive estimation rule reported in Ref. 20 on which the DSD software package is based. However, the definition of the cell-to-cell transition probabilities through Eq. (23) differs from this rule in the following respects:

1. The rule in Ref. 20 assumes there is no model uncertainty (except possibly small random fluctuations in system parameters that are contained within cells $\boldsymbol{V}_j$). Equation (23) allows representing arbitrary distributions of the model uncertainties through the term $p(\boldsymbol{x}_{k+1}|\boldsymbol{x}_k)$.

2. The rule in Ref. 20 assumes that only the state variables are directly measured; i.e.,

$$\boldsymbol{y}_k = \begin{bmatrix} y_1 \\ y_2 \\ \vdots \\ y_i \end{bmatrix}_k = \begin{bmatrix} x_1 \\ x_2 \\ \vdots \\ x_i \end{bmatrix}_k + \begin{bmatrix} w_1 \\ w_2 \\ \vdots \\ w_i \end{bmatrix}_k \quad k = 1,2,\ldots$$

$$\Rightarrow \boldsymbol{y}_k = [1 \quad 0] \begin{bmatrix} \hat{\boldsymbol{x}} \\ \bar{\boldsymbol{x}} \end{bmatrix}_k + \boldsymbol{w}_k ,$$

where $\hat{\boldsymbol{x}} = [x_1, x_2, \ldots, x_i]$ is the vector whose elements are the monitored state variables and $\bar{\boldsymbol{x}} = [x_{i+1}, x_{i+2}, \ldots, x_L]$ is the vector whose elements are the unmonitored state variables. Hence, Eq. (23) allows arbitrary observers, whereas Ref. 20 is restricted to the directly measured components of the state variable vector.

3. The rule in Ref. 20 assumes that $\boldsymbol{w}_k$ is uniformly distributed; i.e.,

$$f_w(\boldsymbol{w}_k) = \begin{cases} 1 & |\boldsymbol{w}_k| \le \lambda \\ 0 & \text{otherwise} \end{cases} , \tag{30}$$

while Eq. (23) allows arbitrary distributions of $\boldsymbol{w}_k$ through the term $p(\boldsymbol{y}_{k+1}|\boldsymbol{x}_{k+1})$.

4. In Ref. 20, cells $\hat{\boldsymbol{j}} = \{j_1 j_2 \ldots j_i\}$ and $\bar{\boldsymbol{j}} = \{j_{i+1} j_{i+2} \ldots j_L\}$ are defined in the monitored and unmonitored state variable spaces (i.e., $\boldsymbol{j} = \{\hat{\boldsymbol{j}} \quad \bar{\boldsymbol{j}}\}$), respectively. The cells $\hat{\boldsymbol{j}}$ contain the measured data point $\boldsymbol{y}$, and $\bar{\boldsymbol{j}}$ contain the measurement noise (i.e., $\hat{\boldsymbol{j}}_k = \{\hat{\boldsymbol{x}}_k : |\hat{\boldsymbol{x}}_k - \boldsymbol{y}_k| \le \lambda\}$). The cell-to-cell transition probabilities are calculated from

$$\begin{aligned} g(\boldsymbol{j}_{k+1}|\boldsymbol{j}_k) &\equiv g(\hat{\boldsymbol{j}}_{k+1}, \bar{\boldsymbol{j}}_{k+1}|\hat{\boldsymbol{j}}_k, \bar{\boldsymbol{j}}_k) \\ &= \int_{\boldsymbol{j}_k} \frac{d\boldsymbol{x}_k}{V_k} e_{k+1}(\tilde{\boldsymbol{x}}(\boldsymbol{x}_k)) , \end{aligned} \tag{31}$$

where $\boldsymbol{j}_k$ is the cell containing $\boldsymbol{x}_k$ and V_k is the volume of $\boldsymbol{j}_k$ (i.e., the product $\Delta_{1,j_1}\Delta_{2,j_2}\ldots\Delta_{L,j_L}$) as defined before.

It can be shown that if $\boldsymbol{j}_{s,k}$ denotes the actual cell the system is in at time $t = k\tau$ and $g(\boldsymbol{j}_{k+1}|\boldsymbol{j}_k) < g(\boldsymbol{j}_{s,k+1}|\boldsymbol{j}_k)$ for all $\boldsymbol{j}_{k+1} \neq \boldsymbol{j}_{s,k+1}$, then[20]

$$\lim_{k\to\infty} p(\boldsymbol{j}_{k+1}|\bar{\boldsymbol{y}}_{k+1}) \to \delta_{j_{s,k+1}, j_{k+1}} ,$$

$$\delta_{j_{s,k+1}, j_{k+1}} = \begin{cases} 1 & \text{if } \boldsymbol{j}_{k+1} = \boldsymbol{j}_{s,k+1} \\ 0 & \text{otherwise} \end{cases}$$

irrespective of the choice of $p(\boldsymbol{j}_0|\boldsymbol{y}_0)$; i.e., $p(\boldsymbol{j}_{k+1}|\bar{\boldsymbol{y}}_{k+1})$ converges to the correct cell $\boldsymbol{j}_{s,k+1}$ irrespective of the initial distribution used. The practical implication of this result is that the choice of cells should be such that the correct system trajectory can be adequately represented by the $g(\boldsymbol{j}_{k+1}|\boldsymbol{j}_k)$. Figure 2 illustrates such a

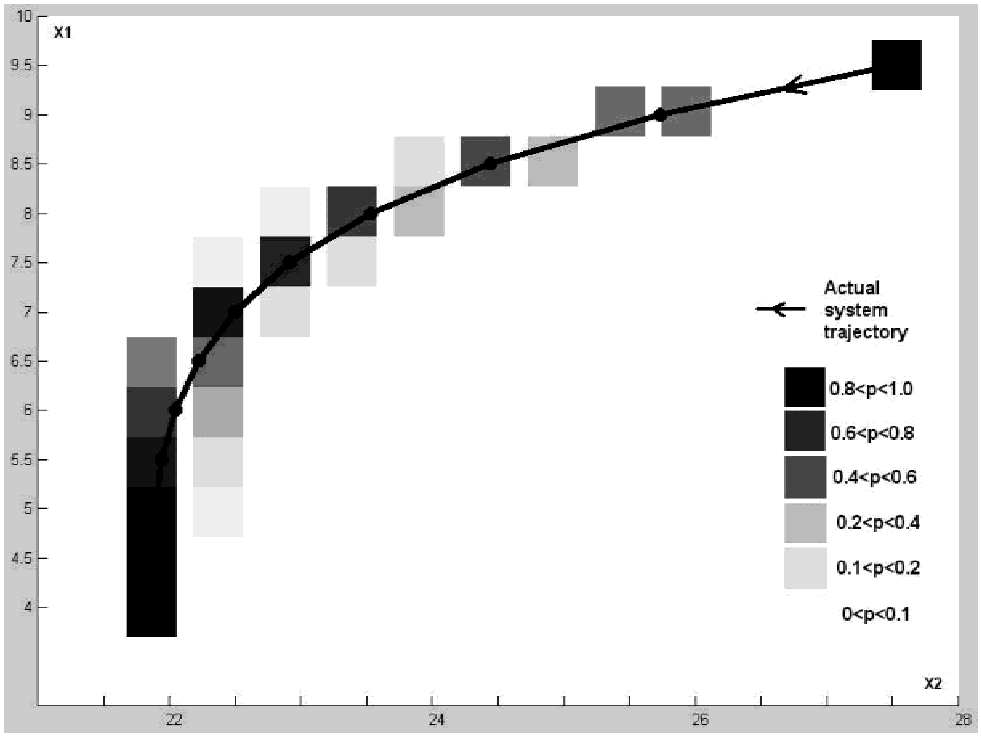

Fig. 2. Approximation of the phase-space trajectory of a hypothetical second-order system by CCMT.

representation for a hypothetical second-order system in its phase-space. Note that the probabilities $p \equiv p(\boldsymbol{j}_{k+1}|\bar{\boldsymbol{y}}_{k+1})$ are highest on or close to the actual trajectory.

While the condition $g(\boldsymbol{j}_{s,k+1}|\boldsymbol{j}_k) > g(\boldsymbol{j}_{k+1}|\boldsymbol{j}_k)$ is practically not convenient for the selection of the cells due to the computational effort required in its implementation, it implies that convergence will be obtained with sufficiently small cells. If the cells are small enough, we will have $g(\boldsymbol{j}_{s,k+1}|\boldsymbol{j}_k) = 1$ if $\boldsymbol{j}_{k+1} = \boldsymbol{j}_{s,k+1}$ and $g(\boldsymbol{j}_{k+1}|\boldsymbol{j}_k) = 0$ otherwise. Since this condition is obtained in Ref. 20 using just the counterpart of Eq. (24) and not Eq. (31), the condition is also valid for Eqs. (23) and (24). Appendix A shows that Eq. (23) reduces to Eq. (31) when differences 1 through 4 are removed.

At this point it should be indicated that both the original DSD algorithm defined through Eqs. (24) and (31) (and subsequently the convergence criteria above) and the improved algorithm defined in Eqs. (23) and (24), in principle, still assume $p(\boldsymbol{x}_k|\bar{\boldsymbol{y}}_k)$ to be measurable over the $\boldsymbol{x}$ range of interest. For the improved algorithm, this assumption is implicit in the steps: (a) replacing integration over the $\boldsymbol{x}$ range of interest in Eq. (6) by a sum of integrals over cells $\boldsymbol{V}_j$ in Eq. (22) and (b) representing $p(\boldsymbol{x}_k|\bar{\boldsymbol{y}}_k)$ over cells $\boldsymbol{V}_j$ through its values at $\hat{\boldsymbol{x}}_k^q$ in Eq. (25), which are assumed to be constant over $\Delta\hat{\boldsymbol{x}}_k^q$. The assumption is carried over to Eq. (31) when differences 1 through 4 are removed. In that respect, refinement of the partitioning scheme (i.e., decreasing the size of $\boldsymbol{V}_j$) or the quadrature scheme [e.g., increasing the number of points $\hat{\boldsymbol{x}}_k^q$ in Eq. (25)], as it is the conventional wisdom for finite difference or finite element techniques, may not lead to better resolution in the estimated quantities if Ω_k containing all possible $\boldsymbol{x}_k$ at time $t = k\tau$ are not measurable sets. A good example is the situation studied in Ref. 29, which uses an algorithm similar to original DSD algorithm to identify the domains of attraction (DOA) of the van der Pol oscillator (a limit cycle and a single point) and calculates the cell-to-cell transition probabilities $g(\boldsymbol{j}_{k+1}|\boldsymbol{j}_k)$ both analytically (exactly) and numerically from the counterpart of Eq. (31). It is shown that the analytical approach [which implicitly assumes that $\tilde{\boldsymbol{x}}(\boldsymbol{x}_k)$ in Eq. (31) is integrable over V_k] leads to loss of resolution in the estimated DOA with respect to the DOA estimated by the numerical approximation of the integral in Eq. (31). The paper shows that the loss of resolution arises from an artificial connectivity between the sets $\tilde{\Omega}_k$ (for which V_k provide a finite subcover) during the determination of $g(\boldsymbol{j}_{k+1}|\boldsymbol{j}_k)$; however, it does not explain the origin of the connectivity. In light of the difference between Eqs. (6) and (22) as explained earlier, the connectivity can be attributed to forcing the originally noncompact $\tilde{\Omega}_k$ to be compact during the analytical determination of $g(\boldsymbol{j}_{k+1}|\boldsymbol{j}_k)$ through integration over the subcover V_k [which is the union of intervals $\Delta_{l,j_l} = \{x_l : a_{l,j_l} \le x_l < a_{l,j_l+1}; a_{l,1} = a_l, a_{l,J_1+1} = b_l\}$ as given by Eq. (18) for some $j_l (j_l = 1,\ldots,J_l; l = 1,\ldots,L)$ and hence connected[30]] rather than $\tilde{\Omega}_k$. Such an explanation has

extended implications[31] regarding previous work on reliability and safety analysis of dynamic systems[32] as well. On the other hand, experience with the original DSD algorithm shows that evaluation of the integral in Eq. (31) using quadratures can often yield successful results even when Ω_k are not measurable, possibly also because $p(\boldsymbol{j}_k|\bar{\boldsymbol{y}}_k)$ provides an outer measure for the set $\tilde{\Omega}_k$ as indicated above in the discussion of the difference between Eqs. (6) and (22). In addition to the problem considered in Ref. 29, a good example is the capability of the original DSD algorithm to determine[33] the bifurcation parameter (which corresponds to the fuel-to-coolant heat transfer coefficient) of the well-known reduced-order boiling water reactor (BWR) model described in Ref. 34 with observed neutron flux, temperature, and pressure. The search in Ref. 23 is carried over a range of the bifurcation parameters in which the BWR behavior can switch from stable to periodic to chaotic. The Ω_k of the system trajectories in neither periodic nor chaotic behavior are Borel measurable, i.e., Ω_k are not closed under finite intersection and union of some open subintervals in the ranges of interest since we cannot define a sequence $z_k^{(s)} \in \Omega_k$ such that $\lim_{s\to\infty} z_k^{(s)} \to x_k \in \Omega_k$.

III. IMPLEMENTATION

This section compares the recursive procedure defined by Eqs. (23) and (24) to the rule reported in Ref. 20 using a xenon evolution model and presents the results.

III.A. System Description

The system under consideration has been proposed by Chernick[35] and consists of three first-order, nonlinear differential equations:

$$\Lambda \frac{d\phi}{dt} = \left(\rho - \frac{\sigma_x}{c\Sigma_f} X - \gamma\phi\right)\phi \ ,$$

$$\frac{dX}{dt} = y_X \Sigma_f \phi - \lambda_x X + \lambda_I I - \sigma_X X\phi \ ,$$

and

$$\frac{dI}{dt} = y_I \Sigma_f \phi - \lambda_I I \ , \tag{32}$$

where

Λ = effective neutron generation time

ϕ = neutron flux

X = ^{135}Xe concentration

I = ^{135}I concentration

c = conversion coefficient from xenon absorption rate to reactivity

ρ = reactivity at zero flux and zero xenon poisoning

σ_X = microscopic absorption cross section for ^{135}Xe

Σ_f = core-averaged macroscopic absorption cross section

γ = flux coefficient of reactivity

λ_X = ^{135}Xe decay coefficient = 0.0753/h

λ_I = ^{135}I decay coefficient = 0.1035/h

y_I = ^{135}I yield = 0.06386

y_X = ^{135}Xe yield = 0.00228

The values for the parameters $\lambda_X, \lambda_I, y_X, y_I$ are generic data. The other model parameters are reactor-specific quantities, and the values obtained from The Ohio State University Research Reactor[36] will be used in this paper (Table I). For the purpose of this study, Eq. (32) is normalized as

$$\Lambda \frac{d\phi}{dt} = \left(\rho - \frac{\sigma_x}{c}\frac{X}{\Sigma_f} - \gamma\phi\right)\phi \ ,$$

$$\frac{d\left(\frac{X}{\Sigma_f}\right)}{dt} = y_X \phi - \lambda_X \frac{X}{\Sigma_f} + \lambda_I \frac{I}{\Sigma_f} - \sigma_X \frac{X}{\Sigma_f}\phi \ ,$$

and

$$\frac{d\left(\frac{I}{\Sigma_f}\right)}{dt} = y_I \phi - \lambda_I \frac{I}{\Sigma_f} \ . \tag{33}$$

The transient considered is a small step insertion of reactivity with $\rho = 0.0005$. Only the flux is assumed to be measured, and the measurement is corrupted by noise; i.e.,

$$y_k = \phi_k + w_k \ ,$$

where y_k is the measurement and w_k is the noise with the pdf $f_w(w_k)$. The subscript k is the time step index. We will assume the noise is white noise and f_w has the same functional form for all $t = k\tau$.

TABLE I

Reactor-Dependent Parameters of Eq. (32)

c	γ (cm$^2\cdot$s)	σ_x (cm^2)	Λ (s)
1.2384	3.97×10^{-16}	1.984×10^{-18}	0.083

TABLE II

Data Used for Simulation of Xenon Evolution for Case 1

Initial Value of ϕ	Initial Value of X/Σ_f	Initial Value of I/Σ_f	Time Step τ (h)	Mean of the Noise	Standard Deviation of the Noise
0.01×10^{13}	0.4×10^{13}	0.5×10^{13}	0.015	0	0.0012×10^{13}

Two cases will be considered in this section:

1. Given $f_w(w_k)$ to be white Gaussian noise, estimate X/Σ_f, I/Σ_f.

2. Given $f_w(w_k)$ to be uniformly distributed, estimate X/Σ_f, I/Σ_f.

Sections III.B and III.C describe the results for cases 1 and 2, respectively.

III.B. Estimation Results with Gaussian Noise (Case 1)

Table II shows the data used in case 1 for the simulation of the measured flux. The simulated system evolution is shown in Fig. 3. The results for the actual flux were obtained from the integration of Eq. (33) using a fourth-order Runge-Kutta scheme. The results for the measured flux y_k at time $t = k\tau$ $(k = 0,1,2,\ldots)$ were obtained by sampling from a normal distribution with mean zero and standard deviation 0.0012×10^{13} (see Table II) using a random number generator and algebraically adding the result to those obtained for the flux $\phi(t)$. Since the noise is assumed to be Gaussian, it cannot be contained within a single cell $\boldsymbol{V}_j$, and the procedure described in Ref. 20 does not converge. In order to apply the new procedure described in Sec. II, the partitioning data used are shown in Table III.

Since there is no model uncertainty, the transition probabilities $g(\boldsymbol{j}_{k+1}|\boldsymbol{j}_k)$ are calculated from Eq. (26) [and subsequently from Eq. (29)] with $\boldsymbol{h}(\bar{x}(\boldsymbol{x}_k)) = \bar{x}(\boldsymbol{x}_k)$ and f_w having 0 mean and 0.0012×10^{13} standard variation. The total number of quadrature points $\hat{\boldsymbol{x}}_k^i$ $(i = 1,\ldots,N)$ selected in the approximation of $g(\boldsymbol{j}_{k+1}|\boldsymbol{j}_k)$ through Eq. (29) is $N = 3 \times 3 \times 3 = 9$.

The estimated 99.99% credibility interval as a function of time for the measured values of flux and the estimated value of X/Σ_f, I/Σ_f are shown, respectively, in Figs. 4, 5, and 6. From Fig. 4, we can see that the estimated intervals for flux (denoted by vertical bars) contain the measured data y_k at all time points. Since the estimation process cross-correlates the measured data in view of the given pdf for w_k [i.e., through $p(\boldsymbol{y}_{k+1}|\boldsymbol{x}_{k+1})$ in Eq. (23)] and the system model (i.e., through $p(\boldsymbol{x}_k|\bar{\boldsymbol{y}}_k)$) in the determination of $g(\boldsymbol{j}_{k+1}|\boldsymbol{j}_k)$, Fig. 4 implies that the improved estimation procedure described by Eqs. (23) and (24) [or Eqs. (24) and (26) when there is no modeling uncertainty] can be also used for model uncertainty/noise reduction in the measured data as will be shown

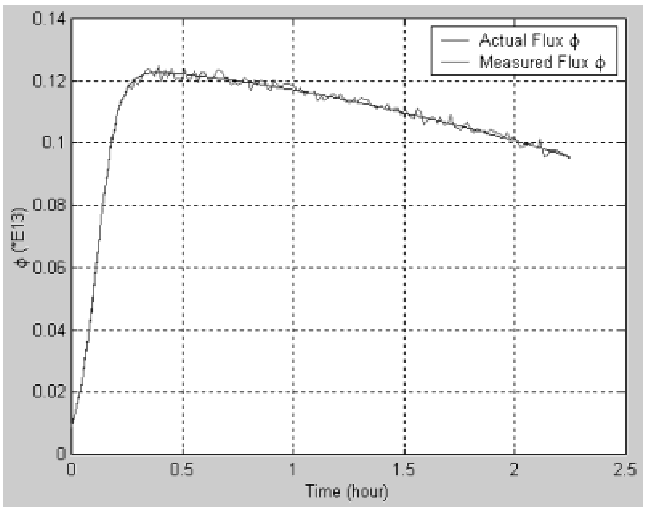

Fig. 3. Actual flux ϕ and its measured value (both simulated) for case 1.

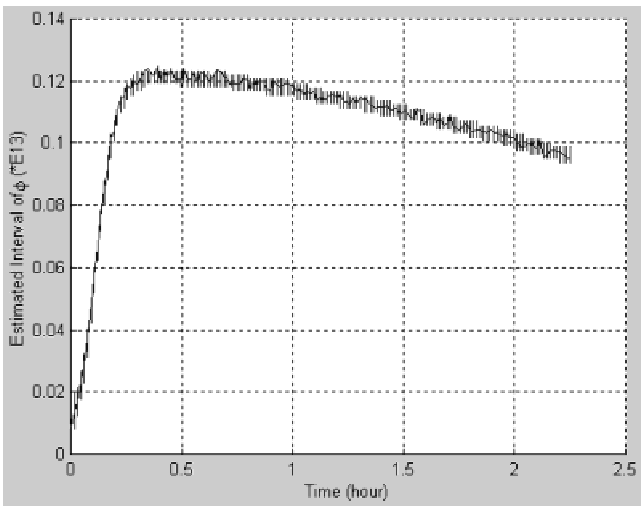

Fig. 4. Estimated interval of flux ϕ as a function of time (solid line indicates the measured value of flux).

TABLE III

The Partitioning Data Used for Case 1

Variables	Possible Maximum Value	Possible Minimum Value	Number of Cells	Number of Quadrature Points $\hat{x}_k^i$ $(i = 1, \ldots, N)$ in Eq. (26)
ϕ	0.14×10^{13}	0	103	3
X/Σ_f	10×10^{13}	0.397×10^{13}	303	3
I/Σ_f	60×10^{13}	0.397×10^{13}	303	3

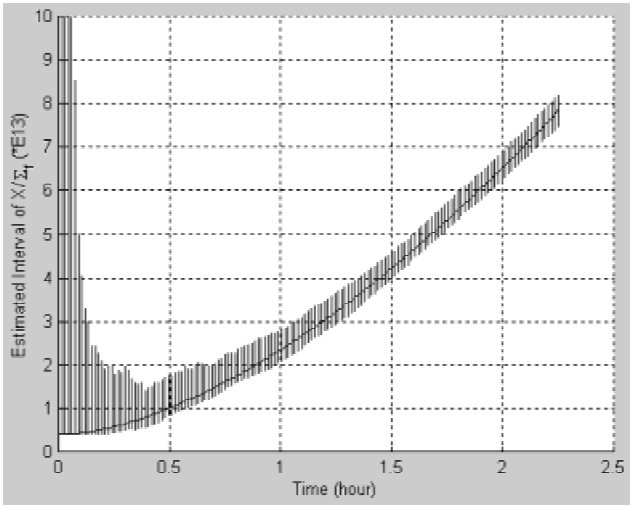

Fig. 5. Estimated interval of X/Σ_f as a function of time.

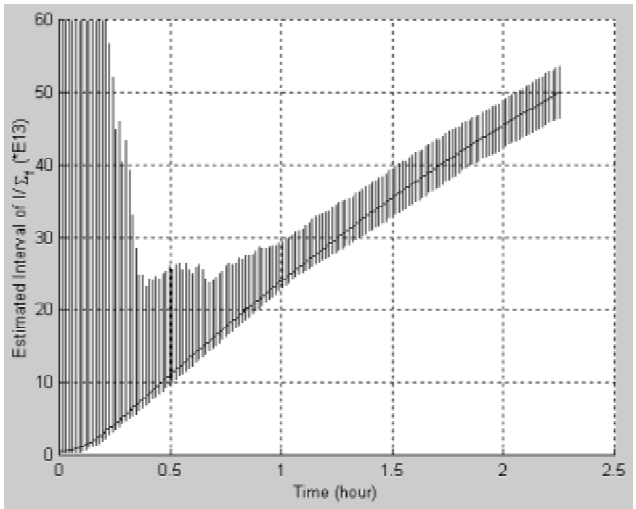

Fig. 6. Estimated interval of I/Σ_f as a function of time.

below. While the estimated interval for X/Σ_f, I/Σ_f is still large after 40 time steps (see Figs. 5 and 6), the mean of the estimated distributions for ϕ and X/Σ_f, I/Σ_f are close to their true values at all times as shown in Figs. 7, 8, and 9, respectively. Figure 10 shows the ratio of the posterior standard deviation over the noise standard deviation $(\sigma_{estimate}/\sigma_{noise})$ for the flux. Together with Fig. 7, which shows that the posterior mean converges to the true flux value, Figs. 7 and 10 demonstrate that the improved estimation procedure can reduce the uncertainty on the measurements by a factor of $\sigma_{estimate}/\sigma_{noise} = 60\%$ for ϕ after about 0.5 h.

Figures 11 and 12, respectively, show the evolution of the posterior variance for X/Σ_f, I/Σ_f for case 1 using $\tau = 0.015$ h and the partitioning data in Table III. The respective posterior standard deviations in the estimated values of X/Σ_f, I/Σ_f are $\sigma_X = 2.7597 \times 10^{13}$ and $\sigma_I = 17.1913 \times 10^{13}$ at the first time step. This uncertainty

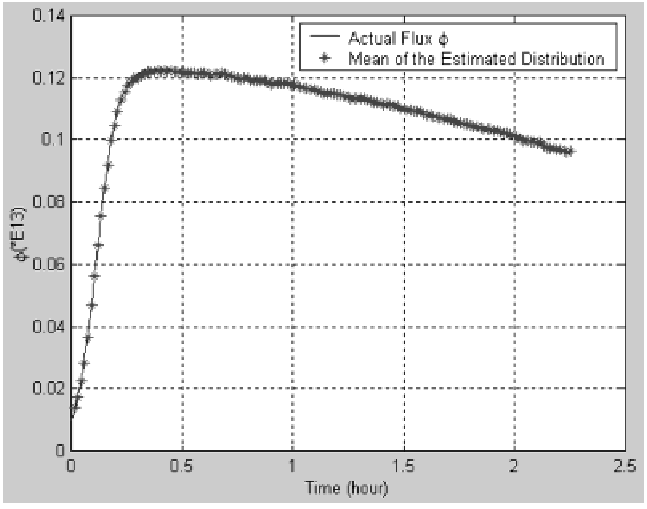

Fig. 7. Mean value of the estimated distribution of ϕ for case 1 (solid line indicates the true value).

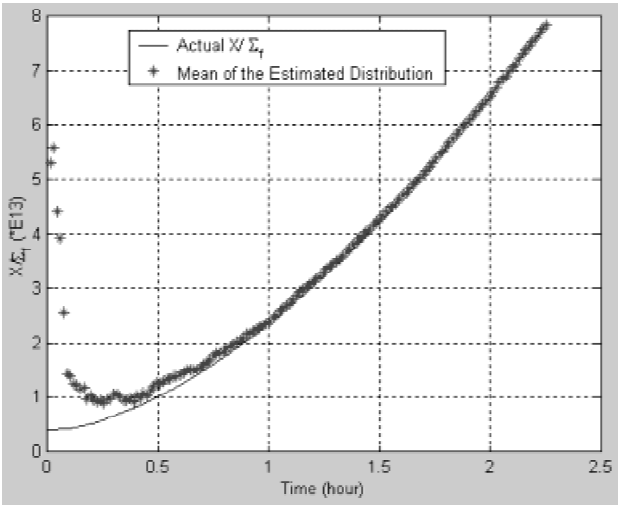

Fig. 8. Mean value of the estimated distribution of X/Σ_f for case 1 (solid line indicates the true value).

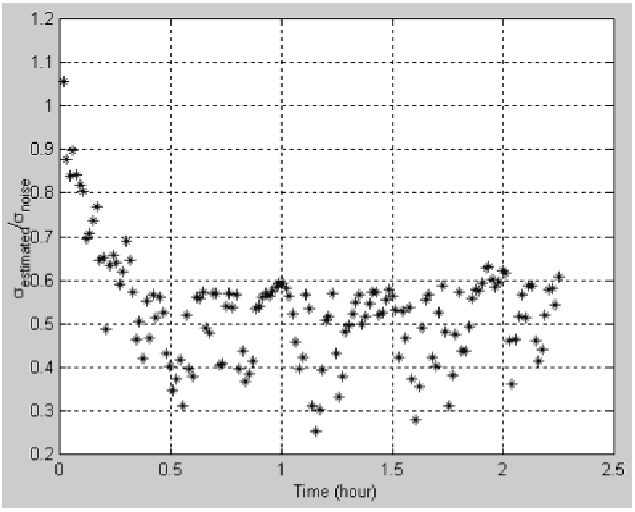

Fig. 10. The ratio of the estimated posterior standard deviation and the noise standard deviation for ϕ.

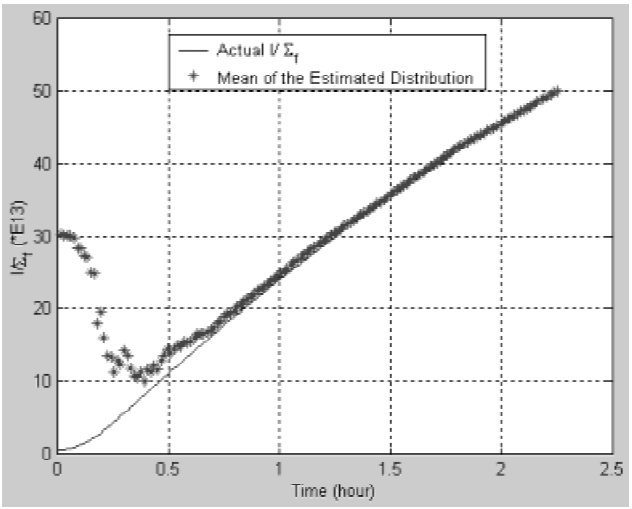

Fig. 9. Mean value of the estimated distribution of I/Σ_f for case 1(solid line indicates the true value).

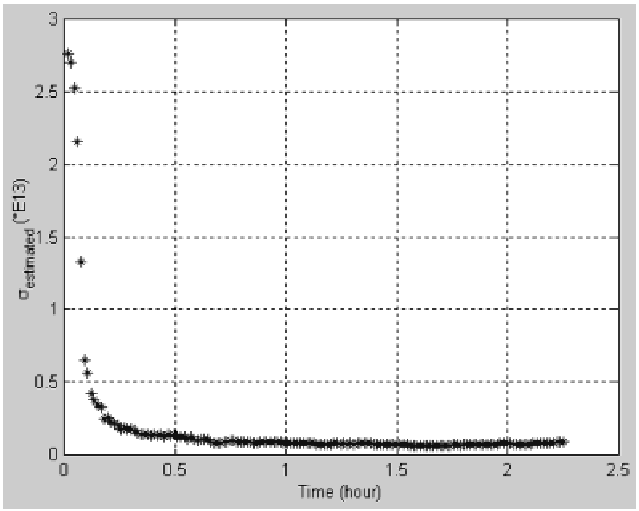

Fig. 11. The evolution of posterior variance for X/Σ_f for case 1.

decreases to $\sigma_X = 0.1781 \times 10^{13}$ and $\sigma_I = 6.1055 \times 10^{13}$ at $t = 20\tau$ (or 0.3 h) and stabilizes around $\sigma_X = 0.08 \times 10^{13}$ and $\sigma_I = 0.8 \times 10^{13}$ after $t = 65\tau$ (or 1 h).

III.C. Estimation Results with Uniform Noise (Case 2)

Table IV shows the data used in case 2 for the simulation of measured values of ϕ. The simulated system evolution is shown in Fig. 13.

The measured data were simulated by using the procedure described for case 1 in Sec. III.B with the data listed in Table IV. The unknown state variables X/Σ_f, I/Σ_f are estimated by two methods: (a) using the improved procedure through Eqs. (24) and (26) and (b) the previous DSD algorithm reported in Ref. 20. Both methods use the partitioning data listed in Table V. The evolution of the estimated 99.99% credibility intervals for ϕ, X/Σ_f, I/Σ_f using the improved procedure is shown in Figs. 14, 15, and 16, respectively, and the corresponding expected values are shown in Figs. 17, 18, and 19. Figures 14 through 19 show that again the measured data are within the expected uncertainty margins and convergence is rapid. Figure 14 also illustrates the signal validation capability of the improved procedure. The flux ϕ is estimated as $0.1183 \times 10^{13} \leq \phi \leq 0.1237 \times 10^{13}$ with

TABLE IV

Data Used for Simulation of System Evolution for Case 2

Initial Value of ϕ	Initial Value of X/Σ_f	Initial Value of I/Σ_f	Time Step τ (h)	Uncertainty Level $\lambda \times 10^{13}$ [see Eq. (30)]
0.01×10^{13}	0.4×10^{13}	0.5×10^{13}	0.015	0.012

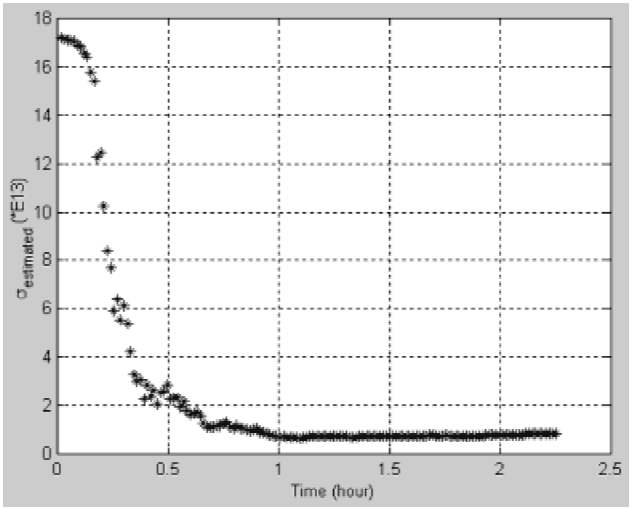

Fig. 12. The evolution of posterior variance for I/Σ_f for case 1.

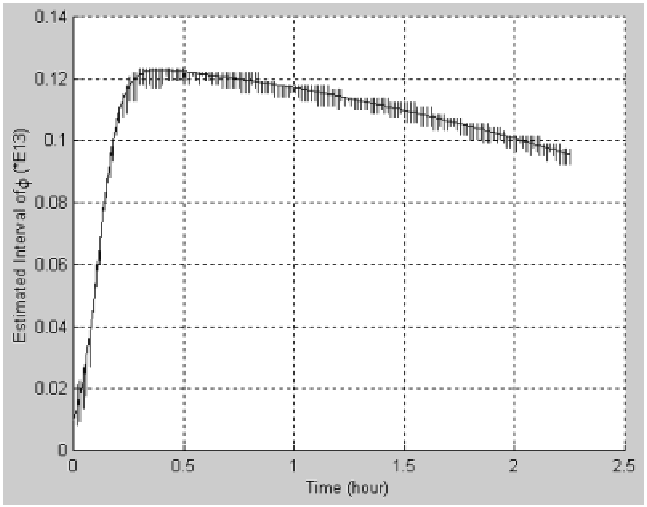

Fig. 14. Estimated interval of flux ϕ as a function of time using Eqs. (24) and (26) for case 2 (solid line indicates the measured value of flux).

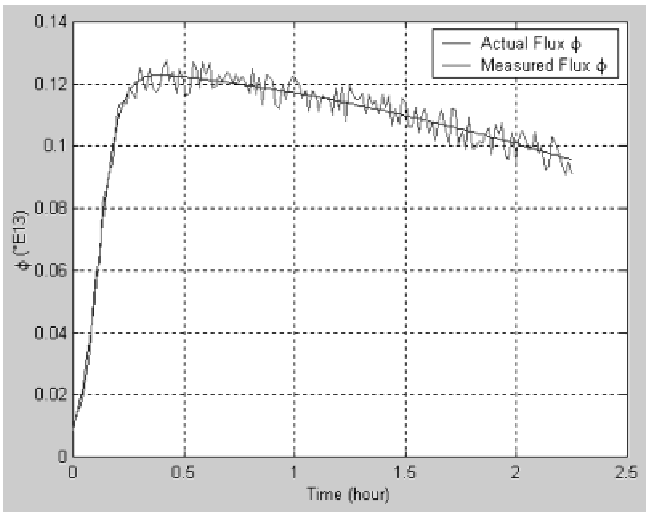

Fig. 13. Actual flux ϕ and its measured value $y(t)$ (both simulated) for case 2.

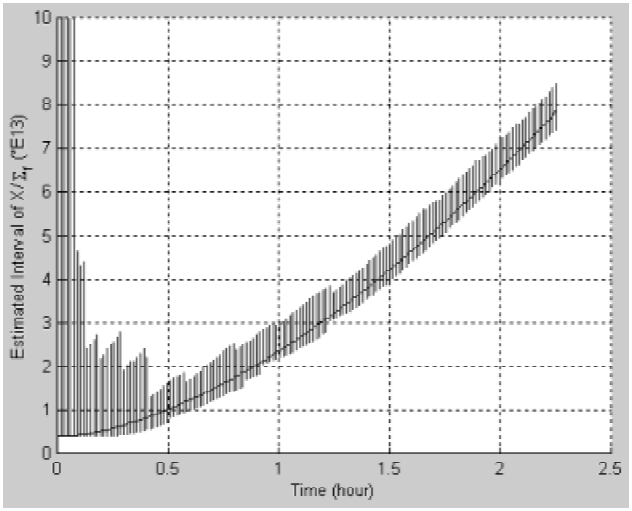

Fig. 15. Estimated interval of X/Σ_f as a function of time using Eqs. (24) and (26) for case 2 (solid line indicates the measured value).

TABLE V

The Partitioning Data Used for Case 2

Variables	Possible Maximum Value	Possible Minimum Value	Number of Cells	Number of Quadrature Points $\hat{x}_k^i$ $(i = 1, \ldots, N)$ in Eq. (26)
ϕ	0.14×10^{13}	0	103	5
X/Σ_f	10×10^{13}	0.397×10^{13}	303	3
I/Σ_f	60×10^{13}	0.397×10^{13}	303	3

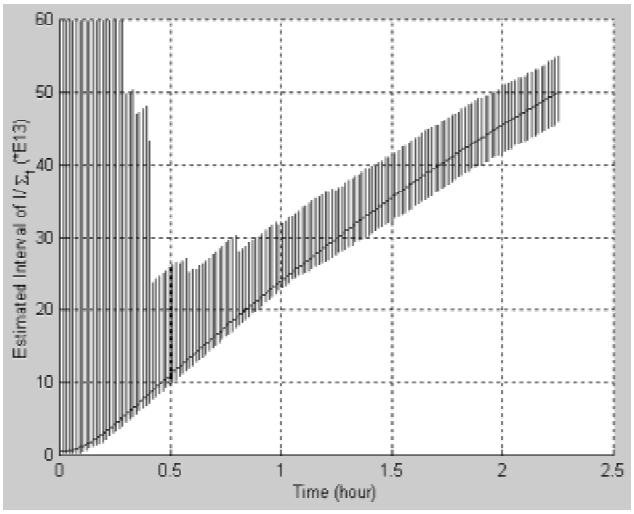

Fig. 16. Estimated interval of I/Σ_f as a function of time using Eqs. (24) and (26) for case 2 (solid line indicates the measured value).

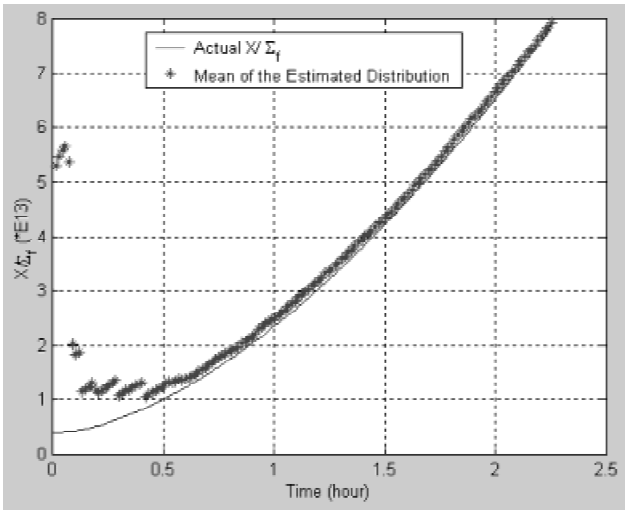

Fig. 18. Mean value of the estimated distribution of X/Σ_f for case 2.

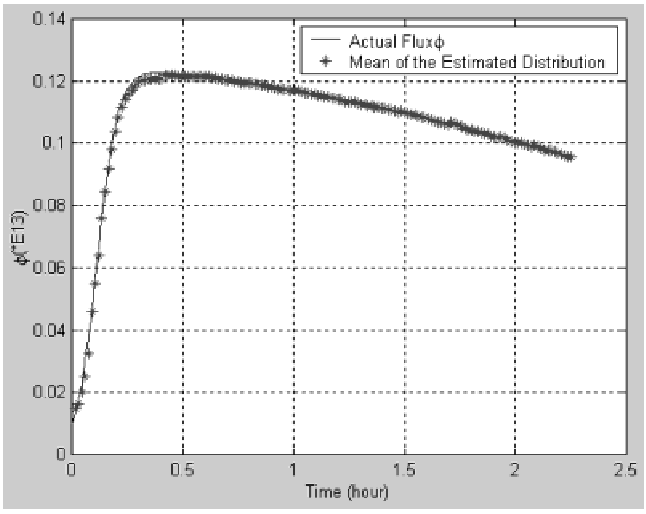

Fig. 17. Mean value of the estimated distribution of ϕ for case 2.

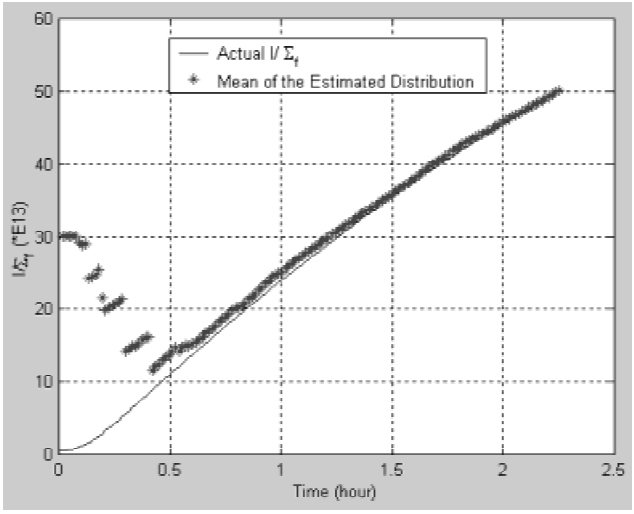

Fig. 19. Mean value of the estimated distribution of I/Σ_f for case 2.

99.99% confidence at time $t = 20\tau$ (or 0.3 h), which is $1 - (0.1237 - 0.1183)/0.012 = 55\%$ smaller than the measurement uncertainty level (see Table IV). Similarly, at time $t = 150\tau$ (or 2.25 h), the flux ϕ is estimated as $0.0924 \times 10^{13} \leq \phi \leq 0.0979 \times 10^{13}$, which is also $1 - (0.0979 - 0.0924)/0.012 = 54\%$ reduction of the measurement noise. These results again show that Eqs. (24) and (26) can be also used to reduce the uncertainty in the measurements for noisy data.

Figures 20 through 23 show the estimation results for case 2 using the DSD algorithm in Ref. 20 with the same partitioning data listed in Table V. Comparing Figs. 20 through 23 to their respective counterparts, Figs. 15, 16, 18, and 19, shows that better estimation results are obtained by using Eqs. (24) and (26) than the previous DSD algorithm. The estimation process converges faster and provides smaller credibility intervals for the unknown variables.

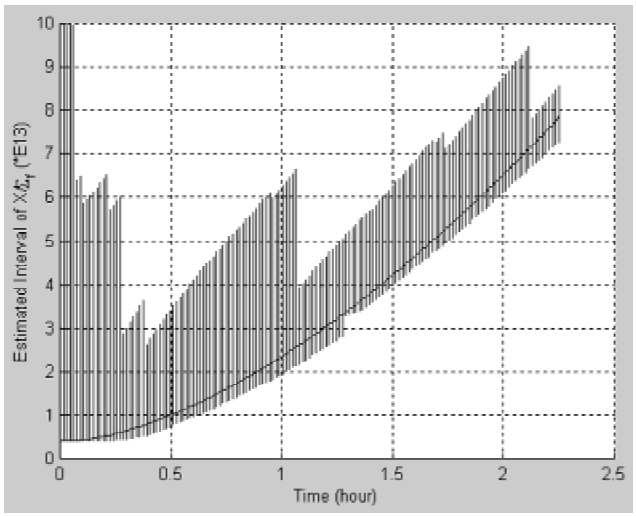

Fig. 20. Estimated interval of X/Σ_f as a function of time using the rules in Ref. 20 for case 2.

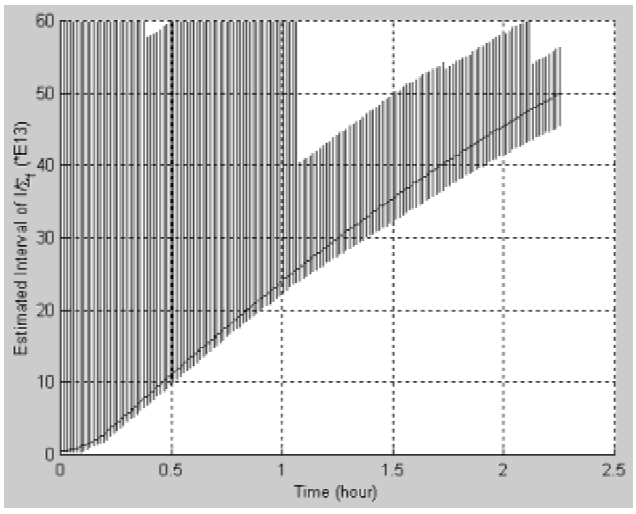

Fig. 21. Estimated interval of I/Σ_f as a function of time using the rules in Ref. 20 for case 2.

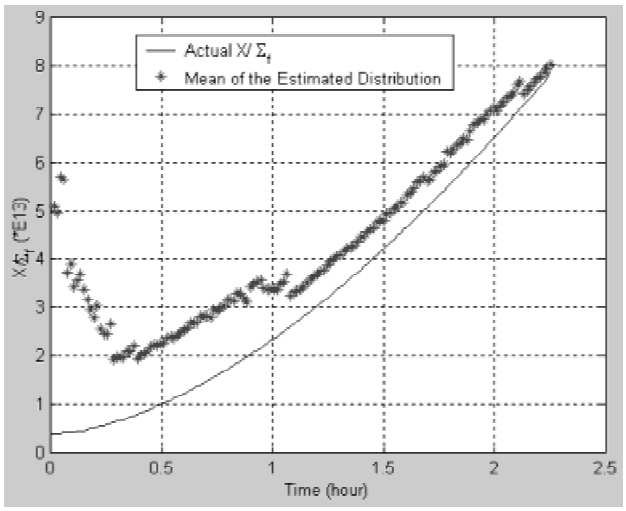

Fig. 22. Mean value of the estimated distribution of X/Σ_f using the rules in Ref. 20 for case 2.

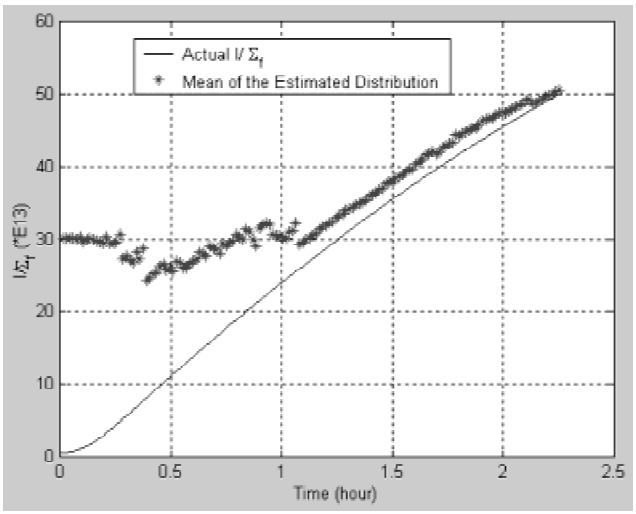

Fig. 23. Mean value of the estimated distribution of I/Σ_f using the rules in Ref. 20 for case 2.

IV. THE RELATIONSHIP OF THE CCMT-BASED STATE/PARAMETER ESTIMATION TO CONVENTIONAL TECHNIQUES

As indicated in Sec. I, the original DSD algorithm is based on the Chapman-Kolmogorov equation, which does

not provide a convenient framework to investigate the relationship of DSD to conventional state/parameter estimation techniques. On the other hand, Sec. II.B shows that the DSD algorithm is a special case of the hierarchical Bayes rule defined through Eq. (6) where the priors $p(\boldsymbol{x}_k|\bar{\boldsymbol{y}}_k)$ are recursively determined from

$$
\begin{aligned}
&p(\boldsymbol{x}_{k+1}|\bar{\boldsymbol{y}}_{k+1}) \\
&\quad = \frac{L(\boldsymbol{x}_{k+1}|\boldsymbol{y}_{k+1})p^{prior}(\boldsymbol{x}_{k+1}|\bar{\boldsymbol{y}}_k)}{\int_{\Omega_{k+1}} d\boldsymbol{x}_{k+1} L(\boldsymbol{x}_{k+1}|\boldsymbol{y}_{k+1})p^{prior}(\boldsymbol{x}_{k+1}|\bar{\boldsymbol{y}}_k)} \\
&\quad = \frac{\int_{\Omega_k} p(\boldsymbol{y}_{k+1}|\boldsymbol{x}_{k+1})p(\boldsymbol{x}_{k+1}|\boldsymbol{x}_k)p(\boldsymbol{x}_k|\bar{\boldsymbol{y}}_k)\,d\boldsymbol{x}_k}{\int_{\Omega_{k+1}} d\boldsymbol{x}_{k+1} p(\boldsymbol{y}_{k+1}|\boldsymbol{x}_{k+1}) \int_{\Omega_k} p(\boldsymbol{x}_{k+1}|\boldsymbol{x}_k)p(\boldsymbol{x}_k|\bar{\boldsymbol{y}}_k)\,d\boldsymbol{x}_k} \\
&\quad = \frac{p(\boldsymbol{y}_{k+1}|\boldsymbol{x}_{k+1})p(\boldsymbol{x}_{k+1}|\bar{\boldsymbol{y}}_k)}{p(\boldsymbol{y}_{k+1}|\bar{\boldsymbol{y}}_k)} \qquad (34)
\end{aligned}
$$

$$
\Rightarrow p(\boldsymbol{x}_{k+1}|\bar{\boldsymbol{y}}_k) = \int p(\boldsymbol{x}_{k+1}|\bar{\boldsymbol{y}}_{k+1})p(\boldsymbol{y}_{k+1}|\bar{\boldsymbol{y}}_k)\,d\boldsymbol{y}_{k+1} \ . \qquad (35)
$$

Equation (35) assumes that $\boldsymbol{y}_k$ as well as $\boldsymbol{x}_k \in \Omega_k$ at each $t = k\tau$ constitute measurable sets. This assumption is realistic since the pdf for $\boldsymbol{w}_k = \boldsymbol{y}_k - \boldsymbol{h}(\boldsymbol{x}_k)$ is often described through a measurable function (e.g., uniform, Gaussian). Then, for a stationary process (e.g., constant parameter vector $\boldsymbol{\theta} = [\theta_1 \theta_2 \ldots \theta_M]$ to be estimated) with the range of interest covering all possible values of $\boldsymbol{\theta}$ under consideration, the following can be shown[37]:

1. There is a unique solution $p(\boldsymbol{\theta})$ to Eq. (34).

2. The sequence $p(\boldsymbol{x}_k)$ converges monotonically in L_1 norm to $p(\boldsymbol{\theta})$.

3. $\int |p(\boldsymbol{x}_k) - p(\boldsymbol{\theta})|\,d\boldsymbol{x}_k \to 0$ exponentially with increasing k.

Other implications of Eq. (6) from estimation theory are as follows:

Implication 1: For a set of constant parameters $\boldsymbol{\theta} = [\theta_1 \theta_2 \ldots \theta_M]$, the mode of $p(\boldsymbol{\theta}|\bar{\boldsymbol{y}}_k)$ yields the maximum likelihood estimate (MLE) of $\boldsymbol{\theta}$ (Ref. 38).

Implication 2: For a set of constant parameters $\boldsymbol{\theta} = [\theta_1 \theta_2 \ldots \theta_M]$ and for $\boldsymbol{w}_k$ being white Gaussian noise, the MLE of $\boldsymbol{\theta}$ is the least-squares estimate (LSE) of $\boldsymbol{\theta}$ (Ref. 39). Therefore, under these assumptions, the mode of $p(\boldsymbol{\theta}|\bar{\boldsymbol{y}}_k)$ is also the LSE of $\boldsymbol{\theta}$.

Implication 3: If $\boldsymbol{w}_k$ and $\boldsymbol{v}$ in Eq. (1) are both white Gaussian noise and $\boldsymbol{f}(\boldsymbol{x}), \boldsymbol{h}(\boldsymbol{x})$ are linear in $\boldsymbol{x}$, then the mean and covariance of $p(\boldsymbol{x}_k|\bar{\boldsymbol{y}}_k)$ obtained from Eq. (6) are equivalent to those obtained from a Kalman filter.[38]

Subsequently, Eqs. (23) and (24), which constitute the improved DSD algorithm and are equivalent to Eq. (6) when the system evolution is represented using CCMT, provide a practical state/parameter estimation procedure that yields the same results as

1. the Kalman filter approach for linear dynamical systems when the modeling uncertainties (i.e., $\boldsymbol{v}$) and measurement noise (i.e., $\boldsymbol{w}_k$) have white Gaussian pdf's
2. the MLE for algebraic systems with constant parameters
3. the LSE for algebraic systems with constant parameters when the measurement noise is white Gaussian.

It should be emphasized, however, the improved DSD algorithm contains the Kalman filter, MLE, and LSE as special cases and has a broader range of applicability than any one of these methods. Section IV.B illustrates implications 1, 2, and 3 using the constant temperature power sensor described in Sec. IV.A.

IV.A. Constant Temperature Power Sensor

The following notation is used in Secs. IV.A and IV.B:

M_i = mass of node i ($i = 1,2$) (kg)

C_i = specific heat capacity of node i ($i = 1,2$) (J/kg·K)

A_i = external area of node i ($i = 1,2$) (m^2)

T_{is} = steady-state temperature of node i ($i = 1,2$) (K)

U_1 = node-1-to-coolant heat transfer coefficient ($W/m^2 \cdot K$)

U_2 = node-2-to-node-1 heat transfer coefficient ($W/m^2 \cdot K$)

T_∞ = coolant temperature (K)

T_h = sensor heater wire reference temperature (K)

i_h = electric current input into the heater wire (A)

α = heater wire temperature coefficient of resistance (1/K)

R_h = heater wire reference resistance (Ω)

$\dot{q}_n$ = nuclear energy input rate into node 2 (W/kg).

A recently developed in-core calorimetric instrument called constant temperature power sensor[40,41] (CTPS) can directly measure the local nuclear energy deposition and heat transfer rate. The direct measurement of the local nuclear energy deposition and the local heat transfer rate reduces the uncertainty in the predicted thermal margins, resulting in improvement in performance and

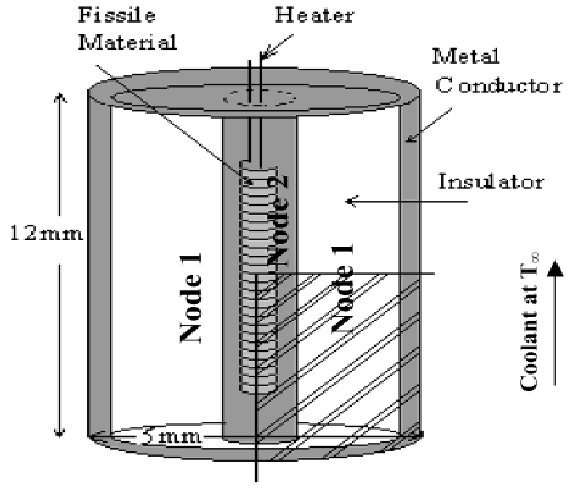

Fig. 24. The constant temperature power sensor.

economy of new reactor designs. This design concept is based on the idea of adding heat through resistive dissipation of input electrical energy, to a small mass of actual reactor fuel analogue (mode 1). The CTPS (Fig. 24) consists of a highly enriched UO_2 core (node 2) surrounded by electrical heating resistance wire. The core is contained in an alumina-based ceramic thermal insulator (node 1). The sensor core and the insulator are coated with thin layers of copper. Heat is lost from the insulator to the surrounding coolant. A feedback control loop is used to provide the exact amount of input electrical energy in order to keep the fuel mass at a constant temperature regardless of the nuclear energy generated in node 2. In steady state (i.e., mode 1), the input electrical energy required will be related to the actual nuclear energy deposition, given the assumption that the external heat transfer rate remains constant; i.e.,

$$M_2\dot{q}_n + [i_h^2 R_h(1+\alpha(T_{2s}-T_h))] = A_2U_2(T_{2s}-T_{1s}) = A_1U_1(T_{1s}-T_\infty) \ . \quad (36)$$

Equation (36) is simply an energy balance between the sensor nodes and surrounding coolant, where $\dot{q}_n$, U_1, U_2, and T_∞ are unknown. The T_{1s} is a known function of T_∞ and T_{2s} (which is measured). The estimation process consists of the following steps:

1. Supply i_h until steady-state conditions are reached (mode 1).

2. Take the sensor temporarily out of the control loop (mode 2), or practically, reduce the supplied electrical current i_h to 1% of the steady-state value in mode 1. In mode 2, the variation of the node 2 temperature T_2 as a function of time t can be represented as[40]

$$T_2(t) = T_\infty + \theta_1 e^{-\theta_2 t} + \theta_3 e^{-\theta_4 t} + w \ , \quad (37)$$

where the exponents θ_2 and θ_2 are related through

$$\theta_2+\theta_4 = -\frac{C_2M_2(U_2A_2+U_1A_1)+C_1M_1(-10^{-4}i_h^2R_h\alpha+U_2A_2)}{C_1M_1C_2M_2}$$

and

$$\theta_2\theta_4 = \frac{-10^{-4}i_h^2R_h\alpha U_2A_2+U_1A_1(-10^{-4}i_h^2R_h\alpha+U_2A_2)}{C_1M_1C_2M_2} \ . \quad (38)$$

In Eq. (37), the quantity w represents model/measurement uncertainty as in Eq. (1). Equation (38) is obtained from the two-node, lumped parameter representation of CTPS under the assumption that the deviation of the node temperatures in mode 2 from their steady-state values in mode 1 is small enough to allow linearization around these mode 1 temperatures.

3. Measure $T_2(t)$ [which also yields T_∞ after the exponentials in Eq. (37) die out] and estimate θ_i $(i=1,\ldots,4)$ through Eqs. (24) and (26).

4. Solve for U_1 and U_2 from Eq. (38) with θ_i $(i=1,2)$ obtained in step 3.

5. Using the T_∞ obtained in step 3 and U_i $(i=1,2)$ found in step 4, solve for $\dot{q}_n$ from Eq. (36).

Work to date shows that the CTPS model parameters can be estimated using the improved procedure through Eqs. (24) and (26), even when the sensor behavior is represented through coupled nonlinear differential equations[42] rather than a single algebraic equation such as Eq. (37).

IV.B. Illustrations

Table VI summarizes the results of the comparison of DSD with LSE, MLE, and Kalman filters using the CTPS described in Sec. IV.A. The LSE results were obtained by minimizing the objective function

TABLE VI

Comparison of the Results for Different Estimators

Parameter/Estimator	$\hat{\theta}_1$	$\hat{\theta}_2$	$\hat{\theta}_3$	$\hat{\theta}_4$
LSE	5.4854	0.2833	19.6994	2.7906
MLE	5.4825	0.2831	19.7017	2.7897
Kalman filter	6.9525	0.3464	18.4278	3.2104
DSD (mode)[a]	5.4663	0.2865	19.7247	2.7978
DSD (mean)[b]	5.4787	0.2829	19.6954	2.7865

[a]For comparison to LSE and MLE.
[b]For comparison to Kalman filter.

$$\sum_{k=1}^{N} [T_{2,k} - T_\infty - \hat{\theta}_1 e^{-\hat{\theta}_2 t_k} - \hat{\theta}_3 e^{-\hat{\theta}_4 t_k}]^2 \quad (39)$$

with respect to $\hat{\theta}_1, \hat{\theta}_2, \hat{\theta}_3, \hat{\theta}_4$, where $T_{2,k} = T_2(t_k)$. The likelihood function used for MLE was

$$\left[\frac{1}{\sqrt{2\pi(0.1)}}\right]^N \exp\left[-\frac{\sum_{k=1}^{N}(T_{2,k} - T_\infty - \hat{\theta}_1 e^{-\hat{\theta}_2 t_k} - \hat{\theta}_3 e^{-\hat{\theta}_4 t_k})^2}{0.2}\right] . \quad (40)$$

The Kalman filter results were found from

$$\hat{\boldsymbol{\theta}}_k = \hat{\boldsymbol{\theta}}_{k-1} + \boldsymbol{K}_k(T_{2,k} - T_\infty - \hat{\theta}_{1,k-1} e^{-\hat{\theta}_{2,k-1} t_k} - \hat{\theta}_{3,k-1} e^{-\hat{\theta}_{4,k-1} t_k}) , \quad (41)$$

where

$$\hat{\boldsymbol{\theta}}_k = [\hat{\theta}_{1,k} \quad \hat{\theta}_{2,k} \quad \hat{\theta}_{3,k} \quad \hat{\theta}_{4,k}] ,$$

$$\boldsymbol{H}_k^T = \begin{bmatrix} e^{-\hat{\theta}_{2,k} t_k} \\ -\hat{\theta}_{1,k} t_k e^{-\hat{\theta}_{2,k} t_k} \\ e^{-\hat{\theta}_{4,k} t_k} \\ -\hat{\theta}_{3,k} t_k e^{-\hat{\theta}_{4,k} t_k} \end{bmatrix} ,$$

$$\boldsymbol{K}_k = \boldsymbol{P}_{k-1} \boldsymbol{H}_k^T (\boldsymbol{H}_k \boldsymbol{P}_{k-1} \boldsymbol{H}_k^T + 0.1)^{-1} ,$$

and

$$\boldsymbol{P}_k = (\boldsymbol{I} - \boldsymbol{K}_k \boldsymbol{H}_k) \boldsymbol{P}_{k-1} \quad (42)$$

with $\boldsymbol{I}$ representing a 4×4 unit matrix and $\boldsymbol{P}_0 = 10\,\boldsymbol{I}$. The partitioning data used for the DSD estimation are shown in Table VII. In all cases, the noise $\boldsymbol{w}_k$ in Eq. (1) was assumed to be Gaussian noise with mean 0, and the variance was calculated by the sample variance of $T_{2,k}$ as 0.1. The data $T_{2,k} = T_2(t_k)$ with $k = 1,\ldots,250$ were generated using the more detailed finite element CTPS model described in Ref. 40.

Table VI shows that there is good agreement among the DSD, LSE, and MLE results, as expected. In general, the differences among the DSD, LSE, and MLE are small (within 0.1 to 1.2%). In order to investigate the origin of the larger differences between the Kalman filter and other estimator results, another set of data $T_{2,k} = T_2(t_k)$ with $k = 1,\ldots,250$ generated using Eq. (37) and the measurement noise was simulated by sampling again from a normal distribution with mean 0 and variance 0.1 using a random number generator (see Table VIII). The estimation results are shown in Table IX, which indicates that with the data generated by Eq. (37) and Gaussian noise, the difference between the DSD and Kalman filter is reduced to $<2.5\%$. The MLE and LSE results are in good agreement with the DSD results in both Tables VI and IX because, as indicated above, for a set of constant parameters $\boldsymbol{\theta} = [\theta_1 \theta_2 \ldots \theta_M]$, (a) the mode of $p(\boldsymbol{\theta}|\bar{\boldsymbol{y}}_k)$ yields the MLE of $\boldsymbol{\theta}$ and (b) if $\boldsymbol{w}_k$ is white Gaussian noise, the MLE of $\boldsymbol{\theta}$ is the LSE of $\boldsymbol{\theta}$. The explanation of the reduction of the difference between the DSD and Kalman filter results from Tables VI through IX is that the data generated from the finite element model of Ref. 40 do not conform to the functional form of Eq. (37). Subsequently, $\boldsymbol{w}_k$ in Eq. (37) is not strictly Gaussian as assumed by the Kalman filter approach [see implication 3 following Eq. (35)].

TABLE VII

DSD Partitioning Data Used for the CTPS Model

Parameter	θ_1	θ_2	θ_3	θ_4
Maximum	7	0.6	22	3.5
Minimum	4	0.0	17	2.5
Number of cells	89	89	89	89
Number of quadrature points $\hat{x}_k^i$ $(i = 1,\ldots,N)$ in Eq. (26)	3	3	3	3

TABLE VIII

Parameter Used for Simulation of Measured Temperature from Eq. (37)

Parameter	θ_1	θ_2	θ_3	θ_4	Mean of the Noise	Variance of the Noise
Value	5.4	0.28	19.7	2.8	0.0	0.1

TABLE IX

Comparison of the Results for Different Estimators for Data Simulated from Eq. (37) and Gaussian Noise

Parameter/Estimator	θ_1	θ_2	θ_3	θ_4
LSE	5.8026	0.2904	19.0819	2.9245
MLE	5.7935	0.2900	19.0888	2.9223
Kalman filter	5.8972	0.2948	18.9750	2.9163
DSD (mode)[a]	5.8061	0.3000	19.1939	2.9388
DSD (mean)[b]	5.7775	0.2889	19.0978	2.9174

[a]For comparison to LSE and MLE.
[b]For comparison to Kalman filter.

V. CONCLUSION

This study shows that the CCMT-based state/parameter estimation procedure, originally based on the Chapman-Kolmogorov equation[20](or in its algorithmic form, DSD), is equivalent to a recursive Bayesian

estimator in the discretized system state/parameter space. This Bayesian interpretation of the DSD algorithm

1. increases the applicability of methodology to arbitrary observers and arbitrary noise distributions in the monitored data as well as to arbitrary uncertainties in the model parameters
2. leads to improvements in the estimation speed and accuracy, as illustrated using the Chernick model[35] of xenon evolution with temperature feedback
3. establishes a link to conventional estimation schemes such as MLE, LSE, and Kalman filter as illustrated by the CTPS model.[40]

The improved DSD algorithm contains MLE, LSE, and the Kalman filter as special cases and has a broader range of applicability than any one of these methods regarding system representation, modeling uncertainties and measurement noise again as illustrated by the CTPS example. The Bayesian interpretation also provides a possible explanation for the origins of some unexplained phenomena encountered in previous work.[29]

APPENDIX A

DERIVATION OF EQ. (31) FROM EQ. (23)

First, using Eq. (30) and noting that $\boldsymbol{y}_{k+1} = \hat{\boldsymbol{x}}_{k+1} + \boldsymbol{w}_{k+1}$ from difference 2, we have

$$p(\boldsymbol{y}_{k+1}|\boldsymbol{x}_{k+1}) = f_w(\boldsymbol{y}_{k+1} - \hat{\boldsymbol{x}}_{k+1}) = \begin{cases} 1 & |\hat{\boldsymbol{x}}_{k+1} - \boldsymbol{y}_{k+1}| \le \lambda \\ 0 & \text{else} \end{cases} = \begin{cases} 1 & \hat{\boldsymbol{x}}_{k+1} \in \hat{\boldsymbol{j}}_{k+1} \\ 0 & \hat{\boldsymbol{x}}_{k+1} \notin \hat{\boldsymbol{j}}_{k+1} \end{cases} . \tag{A.1}$$

Recalling that $\boldsymbol{j} = \{\hat{\boldsymbol{j}} \quad \bar{\boldsymbol{j}}\}$ and $\boldsymbol{x} = \{\hat{\boldsymbol{x}} \quad \bar{\boldsymbol{x}}\}$, the transition probability $g(\hat{\boldsymbol{j}}_{k+1}, \bar{\boldsymbol{j}}_{k+1}|\hat{\boldsymbol{j}}_k, \bar{\boldsymbol{j}}_k)$ can be written from Eq. (23) as the following:

$$\begin{aligned} g(\boldsymbol{j}_{k+1}|\boldsymbol{j}_k) \equiv g(\hat{\boldsymbol{j}}_{k+1}, \bar{\boldsymbol{j}}_{k+1}|\hat{\boldsymbol{j}}_k, \bar{\boldsymbol{j}}_k) &= \iint_{\hat{j}_{k+1}, \bar{j}_{k+1}} \iint_{\hat{j}_k, \bar{j}_k} p(\boldsymbol{y}_{k+1}|\hat{\boldsymbol{x}}_{k+1}, \bar{\boldsymbol{x}}_{k+1}) p(\hat{\boldsymbol{x}}_{k+1}, \bar{\boldsymbol{x}}_{k+1}|\hat{\boldsymbol{x}}_k, \bar{\boldsymbol{x}}_k) \\ &\quad \times \frac{p(\hat{\boldsymbol{x}}_k, \bar{\boldsymbol{x}}_k|\bar{\boldsymbol{y}}_k)}{\int_{j_k} p(\boldsymbol{x}_k|\bar{\boldsymbol{y}}_k)\, d\boldsymbol{x}_k} d\hat{\boldsymbol{x}}_k\, d\bar{\boldsymbol{x}}_k\, d\hat{\boldsymbol{x}}_{k+1}\, d\bar{\boldsymbol{x}}_{k+1} \\ &= \iint_{\hat{j}_{k+1}, \bar{j}_{k+1}} \iint_{\hat{j}_k, \bar{j}_k} f_w(\boldsymbol{y}_{k+1} - \hat{\boldsymbol{x}}_{k+1}) p(\hat{\boldsymbol{x}}_{k+1}, \bar{\boldsymbol{x}}_{k+1}|\hat{\boldsymbol{x}}_k, \bar{\boldsymbol{x}}) \\ &\quad \times \frac{p(\hat{\boldsymbol{x}}_k, \bar{\boldsymbol{x}}_k|\bar{\boldsymbol{y}}_k)}{\int_{j_k} p(\boldsymbol{x}_k|\bar{\boldsymbol{y}}_k)\, d\boldsymbol{x}_k} d\hat{\boldsymbol{x}}_k\, d\bar{\boldsymbol{x}}_k\, d\hat{\boldsymbol{x}}_{k+1}\, d\bar{\boldsymbol{x}}_{k+1} , \end{aligned} \tag{A.2}$$

where $\hat{\boldsymbol{x}}_k$ and $\bar{\boldsymbol{x}}_k$ denote the location of the monitored and unmonitored system variables in their respective spaces. Using Eq. (A.1), Eq. (A.2) becomes

$$\begin{aligned} g(\boldsymbol{j}_{k+1}|\boldsymbol{j}_k) &= g(\hat{\boldsymbol{j}}_{k+1}, \bar{\boldsymbol{j}}_{k+1}|\hat{\boldsymbol{j}}_k, \bar{\boldsymbol{j}}_k) \\ &= \iint_{\hat{j}_{k+1}, \bar{j}_{k+1}} \iint_{\hat{j}_k, \bar{j}_k} p(\hat{\boldsymbol{x}}_{k+1}, \bar{\boldsymbol{x}}_{k+1}|\hat{\boldsymbol{x}}_k, \bar{\boldsymbol{x}}_k) \frac{p(\hat{\boldsymbol{x}}_k, \bar{x}_k|\bar{\boldsymbol{y}}_k)}{\int_{j_k} p(\hat{\boldsymbol{x}}_k, \bar{x}_k|\bar{\boldsymbol{y}}_k)\, d\hat{\boldsymbol{x}}_k\, d\bar{x}_k} d\hat{\boldsymbol{x}}_k\, d\bar{\boldsymbol{x}}_k\, d\hat{\boldsymbol{x}}_{k+1}\, d\bar{\boldsymbol{x}}_{k+1} \\ &= \iint_{j_{k+1}, j_k} p(\boldsymbol{x}_{k+1}|\boldsymbol{x}_k) \frac{p(\boldsymbol{x}_k|\bar{\boldsymbol{y}}_k)}{\int_{j_k} p(\boldsymbol{x}_k|\bar{\boldsymbol{y}}_k)\, d\boldsymbol{x}_k} d\boldsymbol{x}_{k+1}\, d\boldsymbol{x}_k , \end{aligned} \tag{A.3}$$

where $\boldsymbol{j}_{k+1} = \{\hat{\boldsymbol{j}}_{k+1} \quad \bar{\boldsymbol{j}}_{k+1}\}$ and $\boldsymbol{j}_k = \{\hat{\boldsymbol{j}}_k \quad \bar{\boldsymbol{j}}_k\}$. If there is no modeling uncertainty (i.e., difference 1 above), Eq. (16) holds, and Eq. (A.3) becomes

$$g(\hat{\boldsymbol{j}}_{k+1}, \bar{\boldsymbol{j}}_{k+1} | \hat{\boldsymbol{j}}_k, \bar{\boldsymbol{j}}_k) = \iint\limits_{j_{k+1},\, j_k} p(\boldsymbol{x}_{k+1}|\boldsymbol{x}_k) \frac{p(\boldsymbol{x}_k|\bar{\boldsymbol{y}}_k)}{\int_{j_k} p(\boldsymbol{x}_k|\bar{\boldsymbol{y}}_k)\, d\boldsymbol{x}_k} d\boldsymbol{x}_{k+1}\, d\boldsymbol{x}_k$$

$$= \iint\limits_{j_{k+1},\, j_k} \delta(\boldsymbol{x}_{k+1} - \tilde{\boldsymbol{x}}(\boldsymbol{x}_k)) \frac{p(\boldsymbol{x}_k|\bar{\boldsymbol{y}}_k)}{\int_{j_k} p(\boldsymbol{x}_k|\bar{\boldsymbol{y}}_k)\, d\boldsymbol{x}_k} d\boldsymbol{x}_{k+1}\, d\boldsymbol{x}_k$$

$$= \int_{j_k} \frac{p(\boldsymbol{x}_k|\bar{\boldsymbol{y}}_k)}{\int_{j_k} p(\boldsymbol{x}_k|\bar{\boldsymbol{y}}_k)\, d\boldsymbol{x}_k} e_{k+1}(\tilde{\boldsymbol{x}}(\boldsymbol{x}_k))\, d\boldsymbol{x}_k \ , \tag{A.4}$$

where $e_{k+1}(\tilde{\boldsymbol{x}}(\boldsymbol{x}_k))$ is as defined in Eq. (27). Finally, by assuming that the system location is uniformly distributed over the cell $\boldsymbol{j}_k$ and using Eq. (28),

$$\frac{p(\boldsymbol{x}_k|\bar{\boldsymbol{y}}_k)}{\int_{j_k} p(\boldsymbol{x}_k|\bar{\boldsymbol{y}}_k)\, d\boldsymbol{x}_k} = \frac{1}{V_k} \ . \tag{A.5}$$

Then,

$$g(\hat{\boldsymbol{j}}_{k+1}, \bar{\boldsymbol{j}}_{k+1} | \hat{\boldsymbol{j}}_k, \bar{\boldsymbol{j}}_k) = \frac{1}{V_k} \int_{j_k} e_{k+1}(\tilde{\boldsymbol{x}}(\boldsymbol{x}_k))\, d\boldsymbol{x}_k \ , \tag{A.6}$$

which is the same as Eq. (31).

REFERENCES

1. D. J. MOOK, "Estimation and Identification of Nonlinear Dynamic Systems," *AIAA J.*, **27**, 968 (1989).

2. J. S. ALBUQUERQUE and L. T. BIEGLER, "Decomposition Algorithm for On-Line Estimation with Nonlinear Models," *Comput. Chem. Eng.*, **19**, *10*, 1031 (1995).

3. M. GUAY and D. D. McLEAN, "Optimization and Sensitivity Analysis for Multiresponse Parameter Estimation in Systems of Ordinary Differential Equations," *Comput. Chem. Eng.*, **19**, 1271 (1995).

4. K. D. HJELMSTAD and M. R. BANAN, "Time-Domain Parameter Estimation Algorithm for Structures. I: Computational Aspects," *J. Eng. Mech.*, **121**, 424 (1995).

5. Z.-S. LIU, "QR Methods of O(N) Complexity in Adaptive Parameter Estimation," *IEEE Trans. Signal Processing*, **43**, 720 (1995).

6. D. DIMOGIANOPOULOS and R. LOZANO, "Adaptive Control for Linear Slowly Time Varying Systems Using Direct Least-Squares Estimation," *Automatica*, **37**, 251 (2001).

7. M. A. HOPKINS and H. F. VAN LANDINGHAM, "Optimal Nonlinear Estimation of Linear Stochastic Systems," *J. Dynamic Syst. Measurement Control*, **116**, 529 (1994).

8. M. A. HOPKINS and H. F. VAN LANDINGHAM, "Optimal Nonlinear Estimation of Linear Stochastic Systems: The Multivariable Extension," *J. Dynamic Syst. Measurement Control*, **118**, 350 (1996).

9. J. L. DOUCE and Q. M. ZHU, "Modeling a Class of Nonlinear Systems," *IEEE Proc.*, **137**, 385 (1990).

10. S. LYASHEVSKIY and Y.-B. CHEN, "Identification of Nonlinear System Parameters Using Describing Function Approach," *Proc. Am. Control Conf.*, Albuquerque, New Mexico, p. 1944 (1997).

11. M. RICARDO and P. TOMEI, "Adaptive Observers with Arbitrary Exponential Rate of Convergence for Nonlinear Systems," *IEEE Trans. Automatic Control*, **40**, 1300 (1995).

12. R. A. McCANN, M. S. ISLAM, and I. HUSAIN, "Application of a Sliding-Mode Observer for Position and Speed Estimation in Switched Reluctance Motor Drives," *IEEE Trans. Industry Applications*, **37**, *1* (2001).

13. P. WANG, T. ALDEMIR, and V. I. UTKIN, "Estimation of Xenon Concentration and Reactivity in Nuclear Reactor Using Sliding Mode Observer," *Proc. 40th IEEE Conf. Decision and Control*, Orlando, Florida, December 2001.

14. Y.-W. KIM, G. RIZZONI, and V. I. UTKIN, "Automotive Engine Diagnosis and Control via Nonlinear Estimation," *IEEE Control Syst.* (Oct. 1998).

15. E. BOLVIKEN, P. J. ACKLAM, N. CHRISTOPHERSEN, and J.-M. STORDAL, "Monte Carlo Filters from Non-Linear State Estimation," *Automatica*, **37**, 177 (2001).

16. C. D. CHARALAMBOUS and A. LOGOTHETIS, "Maximum Likelihood Parameter Estimation from Incomplete Data

via Sensitivity Equations: The Continuous-Time Case," *IEEE Trans. Automatic Control*, **45**, *5* (2000).

17. A. G. PARLOS, A. F. ATIYA, K. T. CHONG, and W. K. TSAI, "Nonlinear Identification of Process Dynamic Using Neural Networks," *Nucl. Technol.*, **97**, 79 (1992).

18. R. J. PATTON, C. J. LOPEZ-TORIBIO, and F. J. UPPAL, "Artificial Intelligence Approaches to Fault Diagnosis for Dynamic Systems," *Int. J. Appl. Math. Comp. Sci.*, **9**, *3*, 471 (1999).

19. M. MARSEGUERRA and E. ZIO, "Genetic Algorithms for Estimating Effective Parameters in a Lumped Reactor Model for Reactivity Predictions," *Nucl. Sci. Eng.*, **139**, 96 (2001).

20. L. DINCA and T. ALDEMIR, "Parameter Estimation Toward Fault Diagnosis in Nonlinear Systems Using a Markov Model of System Dynamics," *Nucl. Sci. Eng.*, **127**, 199 (1997).

21. P. WANG, T. ALDEMIR, and D. W. MILLER, "Reactivity Ramp Rate Estimation Using a Probabilistic Approach," *Trans. Am. Nucl. Soc.*, **78**, 121 (1998).

22. P. WANG and T. ALDEMIR, "Real-Time Xenon Estimation in Nuclear Power Plants," *Trans. Am. Nucl. Soc.*, **81**, 154 (1999).

23. M. GADIOLI, M. MARSEGUERRA, and E. ZIO, "Fast Integration by Neural Nets in DSD: Probabilistic State Estimation," *Trans. Am. Nucl. Soc.*, **81**, 151 (1999).

24. X. M. CHEN, P. WANG, and T. ALDEMIR, "DSD; A Parameter/State Estimation Tool for Model-Based Fault Diagnosis in Non-Linear Dynamic Systems," *Dynamic Reliability: Future Directions, International Workshop Series on Advanced Topics in Reliability and Risk Analysis*, Center for Reliability Engineering, University of Maryland (1999).

25. "Dynamic System Doctor," Interactive Version; available on the Internet at ⟨http://rclsgi.eng.ohio-state.edu/courses/Aldemir/DSDInteractive/index2.htm⟩.

26. H. STARK and J. W. WOODS, *Probability, Random Process and Estimation Theory for Engineers*, 2nd ed., Chap. 11.6, Prentice-Hall, Upper Saddle River, New Jersey (1994).

27. R. B. ASH, *Real Analysis and Probability*, Academic Press, New York (1972).

28. C. W. GARDINER, *Handbook of Stochastic Methods for Physics, Chemistry and the Natural Sciences*, Chap. 1.2, Springer-Verlag, New York (1983).

29. B. TOMBUYSES and T. ALDEMIR, "Continuous Cell-to-Cell Mapping," *J. Sound Vibration*, **202**, *3*, 395 (May 1997).

30. N. B. HAASER and J. A. SULLIVAN, *Real Analysis*, p. 89, Van Nostrand Reinhold Company, New York (1971).

31. T. ALDEMIR, "Some Measure-Theoretic Issues in the Implementation of Dynamic Methodologies for PRA," *Trans. Am. Nucl. Soc.*, **89**, 410 (2003).

32. J. DEVOOGHT and C. SMIDTS, "Probabilistic Reactor Dynamics—I: The Theory of Continuous Event Trees," *Nucl. Sci. Eng.*, **111**, 229 (1992).

33. L. DINCA and T. ALDEMIR, "State/Parameter Estimation in BWR Dynamics," *Trans. Am. Nucl. Soc*, **80**, 124 (1999).

34. J. MARCH-LEUBA, D. G. CACUCI, and R. B. PEREZ, "Nonlinear Dynamics and Stability of Boiling Water Reactors: Part 2—Quantitative Analysis," *Nucl. Sci. Eng.*, **93**, 124 (1986).

35. J. CHERNICK, G. LELLOUCHE, and W. WOLLMAN, "The Effect of Temperature on Xenon Instability," *Nucl. Sci. Eng.*, **10**, 120 (1961).

36. H.-L. JIN, M. GADIOLI, P. WANG, T. ALDEMIR, and D. W. MILLER, "Validation of a Point Reactor Model for Global Xenon Estimation," *Proc. 8th Int. Conf. Nuclear Engineering*, Baltimore, Maryland, April 12–16, 2000 (2000).

37. M. A. TANNER and W. H. WONG, "The Calculation of Posterior Distributions by Data Augmentation," *J. Am. Stat. Assoc.*, **82**, 528 (1987).

38. N. MORRISON, *Introduction to Sequential Smoothing and Prediction*, p. 468, McGraw-Hill Book Company, New York (1969).

39. R. LUPTON, *Statistics in Theory and Practice*, p. 81, Princeton University Press, Princeton, New Jersey (1993).

40. T. D. RADCLIFF, D. W. MILLER, and A. C. KAUFFMAN, "Modeling of a Constant-Temperature Power Sensor," *Proc. 8th Int. Conf. Nuclear Engineering*, Baltimore, Maryland, April 2–6, 2000 (2000).

41. T. D. RADCLIFF, D. W. MILLER, and A. C. KAUFFMAN, "Constant-Temperature Calorimetry for In-Core Power Measurement," *Nucl. Technol.*, **132**, 240 (2000).

42. A. BURGHELEA and T. ALDEMIR, "In-Core Power Detection with CTPS Using a Non-Linear Model," *Trans. Am. Nucl. Soc.*, **88**, 314 (2003).